Dealing with aversion:

Investigation of the neural substrates for fear and anxiety

Inaugurarldissertion

zur

Erlangung der Würde eines Doktors der Philosophie

vorgelegt der

Philosophisch-Naturrwissenschaftlichen Fakultät

der Universität Basel

von

Zhuoliang Li

Basel, 2021

Genehmigt von der Philosophisch-Naturwissenschaftlichen Fakultät
auf Antrag von

Prof. Dr. Kelly Tan

Prof. Dr. Fiona Doetsch

Prof. Dr. Manuel Mameli

Basel, 22.06.2021

Prof. Dr. Marcel Mayor

Table of Contents

1 Introduction

1.1 Defensive behaviors: necessity for survival

1.1a Fear: a brief overview

1.1b Anxiety: a brief overview

1.1c Fear and anxiety: similarities and differences

1.2 Modeling fear and anxiety in rodents

1.2a Fear conditioning

1.2b Behavioral paradigms for anxiety

1.3 Neural basis for fear and anxiety

1.3a Neural substrates for fear

1.3b Current views on mechanisms underlying learned fear association

1.3c Neural circuitry for fear

1.3d Neural circuitry for anxiety

1.3e Fear and anxiety networks: separate but intertwined

1.4 Gaps in knowledge

1.4a Ventral tegmental area

1.4b Zona Incerta

1.5 Overview of studies

1.5a Lateral ventral tegmental area GABAergic and Glutamatergic modulation of conditioned learning

1.5b Zona Incerta calcium dynamics underlying associative fear learning

1.5c Zona Incerta subpopulations differentially encode and modulate anxiety

2 Studies

2.1 Lateral Ventral Tegmental Area GABAergic and Glutamatergic modulation of conditioned learning

2.2 Zona Incerta calcium dynamics underlying associative fear learning

2.3 Zona Incerta subpopulations differentially encode and modulate anxiety

3 Final comments

3.1 Overview

3.1a Ventral tegmental area and Zona Incerta, new members of the fear network?

3.1b Clinical implications of the role of the Zona Incerta in fear generalization

3.1c Local Zona Incerta circuitry: potential self-regulating network for exploration and avoidance

3.1d Zona Incerta and anxiety: implications for the treatment

3.1e Zona Incerta: independent or intertwined roles in fear and anxiety

3.2 Closing remarks

4 Acknowledgements

Dealing with aversion:

Investigation of the neural substrates for fear and anxiety

Introduction

1.1 Defensive behaviors: necessity for survival

The world is a complex and dynamic system, filled with many threats, rewards, and associated cues. For more than a century, Darwin and many others have postulated that only organisms able to adapt to incoming environmental demands live on and pass their genes to their descendants[1,2]. A substantial part of that is to adequately deal with dangerous threats (ie. predators) that reduce the likelihood of survival. It is no wonder that across species, the nervous system has developed and fine-tuned emotional defensive behavioral responses to actual or potential threats, respectively known as fear and anxiety[2–6]. Furthermore, while it is important to deal with threats directly, it is not enough and often too late. To guarantee survival, it is vitally important to also deal with cues that are predictive of threats[3,5,6].

1.1a Fear: a brief overview

Fear is generally considered as a set of brain states and behavioral instincts towards immediate threats[5–7]. In the case of predator-prey confrontation (a naturalistic scenario that animals and to a much lesser extent humans face on a daily basis) a fearful stimulus (the predator) is detected, integrated with environmental information, assessed (for threat magnitude and avoidability, computed for the most appropriate responses, and finally coordinated actions are generated[5–7]. Multiple systems are important for individual aspects of the fear response. For example, sensory organs detect threat-associated cues while muscles carry out the defensive actions. Importantly the brain is the central driver that integrates these peripheral systems and functionalities into a coordinated response[2,3]. It is generally recognized that fear responses are highly conserved, especially among mammals[3,8,9]. The common behavioral expression of the fear response[6,7] include fight[10], flight[9–11], and freezing[2,5,9]. Though, some has argued that alarm calls[12,13] as well as startle[14] should also be included in this repertoire. Theorists believed that the intensity and immediacy of the incoming threat determines the selection of fear responses undertaken[6,7]. In other words, animals choose to escape when confrontations with predators are avoidable

and stand their ground (to either avoid detection or attack) when interactions with incoming predators are unavoidable.

1.1b Anxiety: a brief overview

Anxiety, on the other hand is more convoluted given the uncertainty with regard to its trigger and differences in opinion as to what should be considered as a "potential" threat[5,6,15,16]. Historically, anxiety has been defined as a set of responses composed of behavioral inhibition, arousal, and vigilance that are impaired with anxiolytic drugs[17]. In other words, anxiety responses can be summarized as risk-assessment behaviors and inhibition of exploration (avoidance) to environments where threats are potentially present. With respect to the predator-prey example, when a faraway (either physically or psychologically distant) threat is perceived, organisms prepare against the predator by putting on-hold their current action, continually assess the environment for any change in threat level, and take steps to reduce confrontation[7,18,19]. Similar to fear responses, anxiety responses are also highly conserved across mammals[16,20].

1.1c Fear and anxiety: similarities and differences

Despite similarities shared between fear and anxiety as well as the concomitance of the two in many cases, it is important to distinguish between the two (for summary, see Table 1). Apart from differences in threat categorization[5,6] with immediate/actual for fear and distant/potential for anxiety, fear and anxiety also differ in their response. Fear responses are generally considered as active avoidance with the behaviroal responses including fight, flight, freeze; while anxiety responses are passive with e.g., reduced exploration[7]. Furthermore, anxiolytic drugs have been widely shown to have little impact on fear responses[7,20]. Speculatively, it could also be argued that the construct of fear is better understood in relation to animal behavior, given the struggles for survival that animals encounter on a daily basis, and translated into human behavior where such clear-cut examples are less common. On the other hand, the construct of anxiety is more subjective and necessities the interpretation of this unpleasant feelings to ambiguous threats, thus perhaps anxiety is better understood in human behavior where communication of this ambiguous state is largely insightful and then translated into animal behavior.

Table 1. Characteristics of fear and anxiety

Dimensionality	**Fear**	**Anxiety**
Emotional valence	Negative	Negative
Threat specificity	Actual	Potential
Threat timing	Immediate	Distant, future
Behavioral response	Fight, flight, freeze	Behavioral inhibition, threat assessment, avoidance
Response to anxiolytics	No effect	Reduced anxiety

1.2 Modeling fear and anxiety in rodents

1.2a Fear conditioning

The highly conserved nature of fear and anxiety led many researchers across the globe to investigate these behaviors in animal models, particularly in rodents[21] due to their structured defensive responses and ease of access. In rodents, fear can be evoked by natural stimuli such as predators, but can also be triggered by unnatural stimuli such as footshocks or artificial representation of predator associated cues[5,6,22,23]. Although some studies investigate the unconditioned fear response[22], particularly with exposure to predators[11,24] or artificial looming cues[25] acting as the trigger, the majority focuses on the conditioned fear response[5,23]. Even though many variations of fear conditioning paradigms exist[5,23], they are all fundamentally similar. Formulated based on the principles of Pavlovian (also known as classical or associative) conditioning (Figure 1A), neutral cues are paired with the unconditioned stimulus (US) that on its own evokes fear such that after learning, the conditioned cue (CS) evokes fear responses, much like the US previously[5,23]. While some investigators prefer natural predator odors as the US[26], they are tricky and inconsistent in eliciting learned fear[27–29]. On the other hand, footshocks robustly drives fear learning and are often preferred[5,23]. Behaviorally speaking, the expression of learned fear under investigation in most cases is freezing[5,23], though some studies also examines flight[30] or potentiated startle reflexes[31]. While fear learning is widely considered as adaptative and necessary for survival[5–8], it can also become maladaptive when it is over-learned. Consequently, fear is generalized to cues that are not predictive of threat and the discrimination between fear predictive and non-predictive cues impaired[32]. To model fear generalization, behavioral paradigms are extended to include neutral cues and contexts that were never associated with the US (see Figure 1B).

Fig 1.

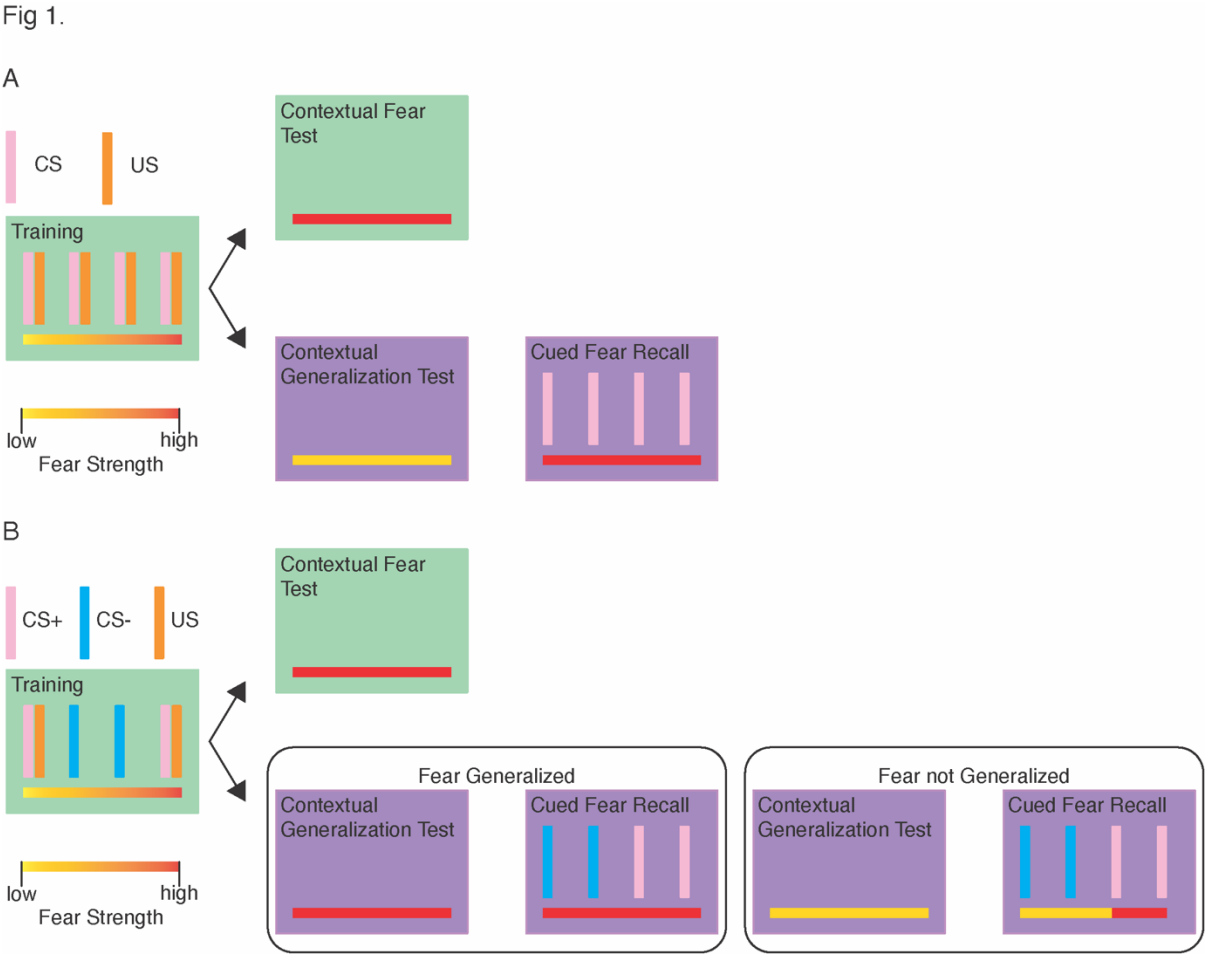

Figure 1. Schematic of Pavlovian fear conditioning.

A) Simple Pavlovian fear conditioning paradigm.

B) Discriminatory Palvovian fear conditioning paradigm with behavioral patterns of fear generalized and not generalized mice.

1.2b Behavioral paradigms for anxiety

In sharp contrast to fear where learned over unconditioned fear is often investigated, research on anxiety mainly focuses on unconditioned anxiety[33,34]. While conditioned anxiety tasks such as conditioned defensive burying of painful (or neutral objects conditioned with painful) stimuli exist[34], these responses tend to be overlooked given the close association with fear responses that may also simultaneously take place. Therefore, anxiety is often studied in the absence of any observable or conditioned threats. The core underlying principle for many popular anxiety tests lie with the instinctive drives for rodents to avoid open lighted areas (considered as potentially threatening given that mice are often hunted by predators during these

environments in the wild) and conflicted by the desire to explore novel environments[33,35–37]. Anxiety is often assessed in terms of the amount of exploration (time or distance) in the anxiogenic (or aversive) open, exposed, and/or lighted areas directly or in relation to exploration in closed, walled, and/or dark places. Common conflict based exploratory tasks[33,35–37] include the elevated mazes[38–40], the light-dark transition test[41,42], and the open field test[43,44]. In addition to these exploration based paradigms, unconditioned defensive burying of neutral objects[45] (such as marbles) and social interaction with familiar and unfamiliar conspecifics[46] have been also used to investigate anxiety.

1.3 Neural basis for fear and anxiety

1.3a Neural substrates for fear

Ever since the early days of behavioral neuroscience where one of the main fundamental goals is to understand the neural substrates for behaviors, researchers across the globe and across generations have diligently worked to uncover how the nervous system encodes and modulates fear and anxiety, key defensive behaviors necessary for survival. In the discussion of the brain circuitry underlying fear, it is almost common knowledge that the amygdala is largely involved. Early lesion studies suggest that the amygdala is necessary for learned fear[47,48], a notion that is corroborated in recent findings where the selective deactivation of synaptic plasticity from sensory inputs onto the amygdala abolished learned fear[49]. On the other side of the coin, amygdala has been shown to be sufficient (in the absence of US) in driving learned fear[50]. Although the amygdala plays an influential role in fear and fear learning, the contribution of other brain areas should not be overlooked. Over the years, many brain regions such as the prefrontal cortex[51,52], the hippocampus[53,54], the hypothalamus[55], and the periaqueductal grey[56] have been shown to play a modulatory role in learned fear.

1.3b Current views on mechanisms underlying learned fear association

Questions still remain as to what are the determining factors that empower brain regions to contribute to fear learning and the relationship between each of these regions in modulating fear. The Hebbian theory[57] has been often used to model the

neural basis underlying fear learning[58,59], meaning the co-activation of neurons to sensory cues related to the CS with the US and the ensuing plasticity afterwards drives fear learning. To that end, there are experimental evidence[49,60] to suggest that this is the case, at least in part. If this is the case, all regions previously mentioned to play a role in learned fear should be modulated by sensory cues and fear evoking stimuli (ie. footshocks). Indeed, most of these regions are activated by footshocks[61] and have access to sensory information[49,62–68]. Despite these indications, it is still yet to be elucidated whether Hebbian plasticity is responsible for fear learning outside of the amygdala, whether modulation by sensory and fear evoking cues are the factors that determine whether brain regions can and do provide the neural basis of fear learning.

1.3c Neural circuitry for fear

Moreover, the second question with regards to the relationship between all brain regions that have thus far shown to play a role in fear learning is an equally important and challenging one. While studies have shown that these brain regions involved in fear are anatomically connected into a "fear network" [5,58] (see Figure 2) and projections between[54,56] and within[69–71] these nodes contribute to fear learning, it is still unclear whether there is a defined hierarchical structure within these components (regions) and whether parallel networks exist.

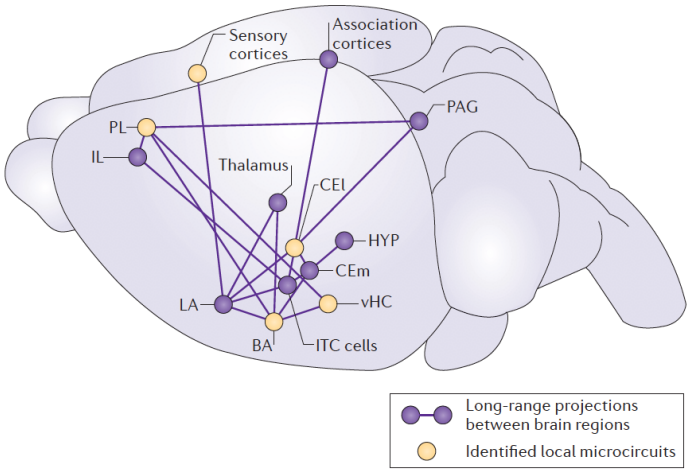

Figure 2. Fear network (extracted from "Neuronal circuits for fear and anxiety"[5]). PL (prelimbic cortex), IL (infralimbic cortex), LA (lateral amygdala), BA (basal amygdala), CEl (lateral central amygdala), CEm (medial central amygdala), ITC (intercalated cells), vHC (ventral hippocampus), HYP (hypothalamus), PAG (periaqueductal gray),

1.3d Neural circuitry for anxiety

Similar to fear, anxiety seems to also be regulated by a number of distributed brain areas[5] (Figure 3). So far, there is substantial evidence to suggest that the amygdala[72–74], the bed nucleus of the stria terminalis (BNST)[74,75], the prefrontal cortex[76,77], the hippocampus[73,77,78], and the hypothalamus[78,79] modulate anxiety. Likewise, these regions are interconnected[5] and the manipulation of pathways between these brain areas differentially influence aspects of anxiety[73,74,77–79]. While many of these regions[74,76,78,79] have been shown to be modulated by cues reflective of differences in anxiety values, it is still unclear what contributing factors determine whether regions are anxiety encoding and modulating. The subjective nature of potential threats and negative feelings that defines anxiety, in part, contributes to the difficulty associated with the investigation of the neural basis for anxiety. Furthermore, it is yet to be elucidated whether other brain structures, particularly ones that are involved in the processing of information carrying negative values can also play a role in anxiety.

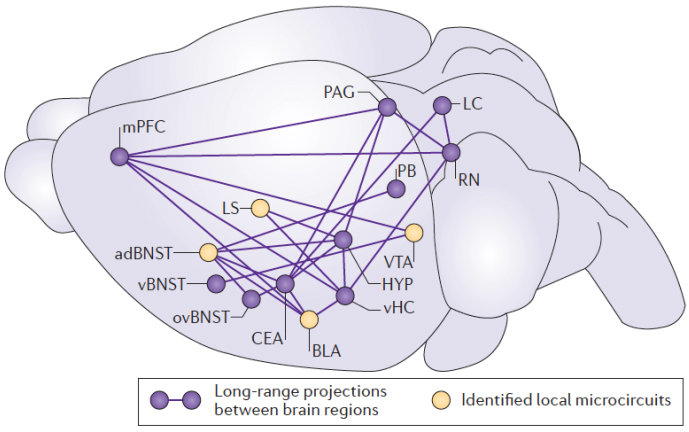

Figure 3. Anxiety network (extracted from "Neuronal circuits for fear and anxiety"[5]). mPFC (medial prefrontal cortex), LS (lateral septum), BNST (bed nucleus of the stria terminalis): ad (anterodorsal), v(ventral), ov(oval), CEA (central amygdala), BLA (basolateral amygdala), vHC (ventral hippocampus), HYP (hypothalamus), VTA (ventral tegmental area), PB (parabrachial nucleus), PAG (periaqueductal gray), RN (raphe nucleus), LC (locus coeruleus)

1.3e Fear and anxiety networks: separate but intertwined

The distributed brain regions shown to be involved in learned fear and anxiety are resoundingly similar. Therefore, one of the glaring questions would be whether learned fear and anxiety share the same network or possess divergent ones. While

this is an area that is largely up to debate and little is definitely known, investigators in the field speculate that they are separate[5,19]. There are a couple lines of evidence that would support this idea. First, anxiolytic drugs have been shown to reduce anxiety-like behaviors while sparing the fear-like ones[21]. Furthermore, there are brain regions such as the BNST that have been shown to be heavily involved in anxiety but studies have largely been unable to show a significant contribution to learned fear[80,81]. If the underlying circuitry behind anxiety and fear are indeed separated, why do some components (brain regions) modulate both fear and anxiety? One possibility would be the diversification of these components into sub-components (ie. different cell populations within the same brain region) and separate but connected sub-components drive fear and anxiety. However, little research has been done to address this point. Recently, a study showed that different amygdala subpopulations encode different behaviors either related to fear (freezing) or anxiety (anxiety-related exploratory behaviors)[82]. However little insights as to whether different cells encode and modulate fear learning and anxiety was provided. While the aforementioned study points in the right direction, much further investigation is necessary to clarify the similarities and differences in the circuitry underlying fear and anxiety.

1.4 Gaps in knowledge

In brief summary, given the importance that defensive behaviors such as fear and anxiety contribute to survival, it is imperative to build a comprehensive understanding of how the nervous system encodes and modulates fear and anxiety. Despite extensive research into the neural substrates underlying fear and anxiety, there are still many open questions left unanswered and aspects unexplored. One such question is whether there are other brain areas that are currently not part of the fear and anxiety networks that play an important role in these responses. In the sub-sections below, the ventral tegmental area (VTA) and the zona incerta (ZI) are introduced. These regions are particularly interesting because preliminary findings implicate them in fear and anxiety responses, thus the VTA and the ZI are the focal points of my investigations.

1.4a Ventral tegmental area

The VTA is a midbrain structure that is well-known for the presence of its dopaminergic (DAergic) neurons. The hallmark of the VTA DAergic neurons is its involvement in reward prediction error[83,84], meaning that these cells are initially activated by rewards and are activated by reward-predicting cues but not expected rewards after learning. Consequently, the phasic activation of VTA DAergic neurons have been shown to promote conditioned preference[85]. In contrast, the other two main cell types of the VTA[86], the gabaergic and glutamatergic neurons have been shown to be activated by negatively valent (in other words, aversive) stimuli[87,88] and drive conditioned[87] and real-time avoidance behaviors[89], respectively.

In terms of connectivity, all three VTA subpopulation receive extensive monosynaptic inputs from across the brain[90–93], including dorsal striatum, nucleus accumbens, BNST, lateral habenula, hypothalamus, amygdala, ZI, and the dorsal raphe nucleus (DR). Likewise, all three subpopulations project to similar targets[92–95], such as the amygdala, prefrontal cortex, dorsal striatum, nucleus accumbens, amygdala, ventral pallidum, PAG, and DR, Furthermore, the gabaergic and glutamatergic but not DAergic subpopulations project to the lateral habenula[93–95]. In addition, VTA gabaergic neurons also project strongly onto the hypothalamus, thalamus, and ZI[94] as well as act as interneurons, inhibiting VTA DAergic neurons[87,96]. It is worth to note that all three VTA subpopulations receive inputs from many regions already mentioned in the fear and anxiety networks.

Given the functional indications and connectivity, it is plausible to speculate that the gabaergic and glutamatergic VTA neurons may play an important role in learned fear. Indeed, the activation of the VTA gabaergic inputs onto the cholinergic interneurons (CINs) of the nucleus accumbens (NAC) has been shown to enhance fear learning[97]. However, it is still unclear whether these VTA subpopulations can encode learned fear and whether anatomically separate pathways contribute to learned fear differently.

1.4b Zona Incerta

As the name implies, the Zona Incerta (ZI) is a region shrouded with mystery. At the junction of the hypothalamus and the thalamus, this string-like structure is

advantageously located anatomically to modulate varying behavioral functions[98]. The ZI is highly complex and heterogenous. In terms of composition, the ZI is made of mainly inhibitory neurons, expressing a wide range of inhibitory markers such as somatostatin, parvalbumin, calbindin, calretinin, and vasoactive intestinal peptide[99–101]. In addition, neuropeptides, glutamatergic markers, and tyrosine hydroxylase (thus potentially dopaminergic neurons) have also been observed in the ZI[99,100].

Similar to its composition, the connectivity of the ZI is highly complex. The ZI seem to be well connected (and often reciprocally) with a wide range of brain areas such the prefrontal cortex, striatum, basal forebrain, thalamus, hypothalamus, septum, BNST, amygdala, substania nigra, superior colliculus, VTA, DR, PAG, and even as far peripherally as the spinal cord[92,102–112]. The diverse connectivity of the ZI suggest that it may be involved in a wide range of functions.

Indeed, over the years, the ZI has been shown to play a modulatory role over a wide range of functions, such as neuronal development[113], hormonal regulation[114,115], ingestion[112,116,117], sleep[118,119], sensory-motor integration[120,121], pain[122], and predatory hunting[111]. Despite the exhaustive list of functions attributed to the ZI, recent studies seem to uncover even more roles. Specifically, the experimental manipulation of the ZI, in terms of its activity or its synaptic transmission, impact fear acquisition[110,123], recall[108,110], and generalization[124]. Given its anatomical proximity to the subthalamic nucleus (a common deep brain stimulation target for the treatment of Parkinson Disease[125]) and its involvement in motor-related functions, the ZI has been at first unintentionally[125–127] and then intentionally targeted by deep brain stimulation (DBS)[128–130]. These studies showed that the DBS of the ZI not only alleviated motor symptoms of Parkinson Disease[128–130] but reduced anxiety[130,131] and enhanced fear recognition[130].

Despite many experimental studies targeting the ZI and implicating the ZI with a role in many functions, there is very little investigation into the physiological activity of the ZI and which stimuli the ZI encodes. Unsurprisingly, this is also the case with learned fear, where very little is known about whether the ZI can even encode fear evoking stimuli or aspects fear learning. More shockingly, the potential role that ZI may play in anxiety has only been observed clinically in a small number of patients, with no

experimental basis or support. There is still much unexplored with the ZI in terms of its roles in fear and anxiety.

1.5 Overview of studies

The studies described in this thesis provide evidence that the neural substrates underlying fear and anxiety are not restricted to the ones previously introduced. By taking a circuit neuroscience approach, we provide evidence that other subcortical brain regions/pathways contribute to the encoding and modulation of fear and/or anxiety. In the following part of the introduction, a brief overview (background, rationale, and main findings) of these studies is introduced and reported in much greater detail in their respective sections.

1.5a Lateral ventral tegmental area GABAergic and Glutamatergic modulation of conditioned learning

The cholinergic interneurons (CINs) of the striatum both the ventral (NAC) as well as the dorsal portions (dSTR), make up a rare neuronal subpopulation that has been heavily implicated in associative learning[132,133]. While the contribution of the cortical[134] and thalamic[134,135] inputs on the involvements of CINs in associative learning has been investigated, little is known about the contribution of other afferent pathways, particularly ones from the midbrain. One potentially interesting input would be the VTA. The VTA gabaergic and glutamatergic neurons project to the dSTR[93–95], but however, it yet elucidated whether they contact the CINs directly. While both VTA gabaergic and glutamatergic neurons have been shown to encode aversive stimuli and promote place avoidance[87,89], little is known about their role in fear. Here, we investigate **whether the VTA gabaergic and glutamatergic neurons can encode learned fear and whether they can act on dSTR CINs to modulate associative fear learning**. Taking a combinational approach with *in-vivo* single cell calcium imaging, monosynaptic retrograde tracing with the pseudotyped rabies virus, *in-vitro* electrophysiology, and optogenetics, we show that the lateral VTA gabaergic and glutamatergic neurons differentially encode aspects of fear learning, provide direct mono-synaptic and indirect (via the thalamus) di-synaptic innervations of the dSTR

CINs, and the manipulation of these pathways differentially modulate fear learning. This study (co-first author) is now published in Cell Reports[136].

1.5b Zona Incerta calcium dynamics underlying associative fear learning

The Zona Incerta (ZI) is reported as a mysterious and complex brain structure where little can be certain. In recent years, the experimental manipulation of the ZI, either in terms of its activity or its synaptic transmission. has been shown to differentially impacts fear acquisition[123,110], recall[108,110], and generalization[124]. Despite these interesting and conflicting experimental findings, there is a glaring gap in knowledge, that is **whether ZI neurons can encode cues that contribute to fear learning as well as fear learning itself**. With *in-vivo* calcium imaging, we provide evidence on both a populational level as well as with longitudinally tracked cells that ZI neurons encode fear learning by showing that they differentially learn to encode auditory cues predictive of footshocks and neutral ones as well as learn to discriminate between the two. In addition, we show that the response profiles of ZI neuronal populations after learning is reflective of the degree mice generalized fear, providing substantial support to the role of the ZI in learned fear and fear generalization. This study (first author) is currently under review.

1.5c Zona Incerta subpopulations differentially encode and modulate anxiety

Despite the many functions that the ZI has been implicated in, the potential link between the ZI and anxiety has almost never been mentioned. That, however, changed with a recent clinical observation, where patients suffering Parkinson's disease receiving an experimental deep brain stimulation treatment in the ZI self-reported lower degrees of anxiety[130,131]. To establish a solid basis for the role of the ZI in anxiety, we examined **whether the ZI can encode anxiety-related information and actively influence anxiety-like behaviors**. An investigation of the immediate early gene expression and *in-vivo* calcium dynamics revealed that ZI neurons encode anxiety-related cues. Furthermore, we show that the ZI neurons and its different subpopulations differentially modulate anxiety-related behaviors with pharmacological and optogenetic manipulations. Our findings in this study considerable experimental

evidence that the ZI can encode and modulate anxiety. This study (co-first author) is currently under review.

References:

1. Charles Darwin. *On the origin of species by means of natural selection, or the preservation of favoured races in the struggle for life*. (John Murray, 1859).

2. LeDoux, J. & Daw, N. D. Surviving threats: neural circuit and computational implications of a new taxonomy of defensive behaviour. *Nat Rev Neurosci* **19**, 269–282 (2018).

3. LeDoux, J. Rethinking the emotional brain. *Neuron* **73**, 653–676 (2012).

4. Mobbs, D., Hagan, C. C., Dalgleish, T., Silston, B. & Prévost, C. The ecology of human fear: survival optimization and the nervous system. *Front Neurosci* **9**, 55 (2015).

5. Tovote, P., Fadok, J. P. & Lüthi, A. Neuronal circuits for fear and anxiety. *Nature Reviews Neuroscience* **16**, 317–331 (2015).

6. Blanchard, D. C. & Blanchard, R. J. Chapter 2.4 Defensive behaviors, fear, and anxiety. in *Handbook of Behavioral Neuroscience* (eds. Blanchard, R. J., Blanchard, D. C., Griebel, G. & Nutt, D.) vol. 17 63–79 (Elsevier, 2008).

7. McNaughton, N. & Corr, P. J. A two-dimensional neuropsychology of defense: fear/anxiety and defensive distance. *Neurosci Biobehav Rev* **28**, 285–305 (2004).

8. LeDoux, J. E. Evolution of human emotion: a view through fear. *Prog Brain Res* **195**, 431–442 (2012).

9. Eilam, D. Die hard: a blend of freezing and fleeing as a dynamic defense--implications for the control of defensive behavior. *Neurosci Biobehav Rev* **29**, 1181–1191 (2005).

10. Lingle, S. & Pellis, S. Fight or flight? Antipredator behavior and the escalation of coyote encounters with deer. *Oecologia* **131**, 154–164 (2002).

11. Wang, W. *et al.* Coordination of escape and spatial navigation circuits orchestrates versatile flight from threats. *Neuron* (2021) doi:10.1016/j.neuron.2021.03.033.

12. Brudzynski, S. M. & Chiu, E. M. Behavioural responses of laboratory rats to playback of 22 kHz ultrasonic calls. *Physiol Behav* **57**, 1039–1044 (1995).

13. Litvin, Y., Blanchard, D. C. & Blanchard, R. J. Rat 22kHz ultrasonic vocalizations as alarm cries. *Behav Brain Res* **182**, 166–172 (2007).

14. Yeomans, J. S., Li, L., Scott, B. W. & Frankland, P. W. Tactile, acoustic and vestibular systems sum to elicit the startle reflex. *Neurosci Biobehav Rev* **26**, 1–11 (2002).

15. Blanchard, D. C. & Blanchard, R. J. Ethoexperimental approaches to the biology of emotion. *Annu Rev Psychol* **39**, 43–68 (1988).

16. McNaughton, N. & Zangrossi Jr., H. Theoretical approaches to the modeling of anxiety in animals. in *Handbook of anxiety and fear.* 11–27 (Elsevier Academic Press, 2008). doi:10.1016/S1569-7339(07)00002-1.

17. Gray, J. A. Précis of The neuropsychology of anxiety: An enquiry into the functions of the septo-hippocampal system. *Behavioral and Brain Sciences* **5**, 469–484 (1982).

18. Fanselow, M. S. Associative vs topographical accounts of the immediate shock–freezing deficit in rats: Implications for the response selection rules governing species-specific defensive reactions. *Learning and Motivation* **17**, 16–39 (1986).

19. Davis, M., Walker, D. L., Miles, L. & Grillon, C. Phasic vs sustained fear in rats and humans: role of the extended amygdala in fear vs anxiety. *Neuropsychopharmacology* **35**, 105–135 (2010).

20. Blanchard, R. J., Griebel, G., Henrie, J. A. & Blanchard, D. C. Differentiation of anxiolytic and panicolytic drugs by effects on rat and mouse defense test batteries. *Neurosci Biobehav Rev* **21**, 783–789 (1997).

21. Blanchard, D. C., Griebel, G. & Blanchard, R. J. Mouse defensive behaviors: pharmacological and behavioral assays for anxiety and panic. *Neurosci Biobehav Rev* **25**, 205–218 (2001).

22. Litvin, Y., Pentkowski, N. S., Pobbe, R. L., Blanchard, D. C. & Blanchard, R. J. Unconditioned models of fear and anxiety. in *Handbook of anxiety and fear.* 81–99 (Elsevier Academic Press, 2008). doi:10.1016/S1569-7339(07)00006-9.

23. Fanselow, M. S. & Ponnusamy, R. The use of conditioning tasks to model fear and anxiety. in *Handbook of anxiety and fear.* 29–48 (Elsevier Academic Press, 2008). doi:10.1016/S1569-7339(07)00003-3.

24. Blanchard, R. J., Fukunaga, K. K. & Blanchard, D. C. Environmental control of defensive reactions to a cat. *Bulletin of the Psychonomic Society* **8**, 179–181 (1976).

25. Shang, C. *et al.* Divergent midbrain circuits orchestrate escape and freezing responses to looming stimuli in mice. *Nat Commun* **9**, 1232 (2018).

26. Takahashi, L. K., Chan, M. M. & Pilar, M. L. Predator odor fear conditioning: current perspectives and new directions. *Neurosci Biobehav Rev* **32**, 1218–1227 (2008).

27. Blanchard, R. J., Yang, M., Li, C. I., Gervacio, A. & Blanchard, D. C. Cue and context conditioning of defensive behaviors to cat odor stimuli. *Neurosci Biobehav Rev* **25**, 587–595 (2001).

28. Blanchard, D. C. *et al.* Failure to produce conditioning with low-dose trimethylthiazoline or cat feces as unconditioned stimuli. *Behav Neurosci* **117**, 360–368 (2003).

29. McGregor, I. S., Schrama, L., Ambermoon, P. & Dielenberg, R. A. Not all 'predator odours' are equal: cat odour but not 2,4,5 trimethylthiazoline (TMT; fox odour) elicits specific defensive behaviours in rats. *Behav Brain Res* **129**, 1–16 (2002).

30. Fadok, J. P. *et al.* A competitive inhibitory circuit for selection of active and passive fear responses. *Nature* **542**, 96–100 (2017).

31. Miserendino, M. J., Sananes, C. B., Melia, K. R. & Davis, M. Blocking of acquisition but not expression of conditioned fear-potentiated startle by NMDA antagonists in the amygdala. *Nature* **345**, 716–718 (1990).

32. Asok, A., Kandel, E. R. & Rayman, J. B. The Neurobiology of Fear Generalization. *Front Behav Neurosci* **12**, 329 (2018).

33. Belzung, C. & Griebel, G. Measuring normal and pathological anxiety-like behaviour in mice: a review. *Behavioural Brain Research* **125**, 141–149 (2001).

34. Anderson, E. M., McWaters, M. L., McFadden, L. M. & Matuszewich, L. Defensive burying as an ethological approach to studying anxiety: Influence of juvenile methamphetamine on adult defensive burying behavior in rats. *Learning and Motivation* **61**, 97–106 (2018).

35. Rodgers, R. J. & Dalvi, A. Anxiety, defence and the elevated plus-maze. *Neurosci Biobehav Rev* **21**, 801–810 (1997).

36. Crawley, J. N. Neuropharmacologic specificity of a simple animal model for the behavioral actions of benzodiazepines. *Pharmacol Biochem Behav* **15**, 695–699 (1981).

37. Crawley, J. N. Exploratory behavior models of anxiety in mice. *Neurosci Biobehav Rev* **9**, 37–44 (1985).

38. Carobrez, A. P. & Bertoglio, L. J. Ethological and temporal analyses of anxiety-like behavior: the elevated plus-maze model 20 years on. *Neurosci Biobehav Rev* **29**, 1193–1205 (2005).

39. Hogg, S. A review of the validity and variability of the elevated plus-maze as an animal model of anxiety. *Pharmacol Biochem Behav* **54**, 21–30 (1996).

40. Shepherd, J. K., Grewal, S. S., Fletcher, A., Bill, D. J. & Dourish, C. T. Behavioural and pharmacological characterisation of the elevated 'zero-maze' as an animal model of anxiety. *Psychopharmacology (Berl)* **116**, 56–64 (1994).

41. Misslin, R., Belzung, C. & Vogel, E. Behavioural validation of a light/dark choice procedure for testing anti-anxiety agents. *Behav Processes* **18**, 119–132 (1989).

42. Arrant, A. E., Schramm-Sapyta, N. L. & Kuhn, C. M. Use of the light/dark test for anxiety in adult and adolescent male rats. *Behav Brain Res* **256**, 119–127 (2013).

43. Choleris, E., Thomas, A. W., Kavaliers, M. & Prato, F. S. A detailed ethological analysis of the mouse open field test: effects of diazepam, chlordiazepoxide and an extremely low frequency pulsed magnetic field. *Neurosci Biobehav Rev* **25**, 235–260 (2001).

44. Carola, V., D'Olimpio, F., Brunamonti, E., Mangia, F. & Renzi, P. Evaluation of the elevated plus-maze and open-field tests for the assessment of anxiety-related behaviour in inbred mice. *Behav Brain Res* **134**, 49–57 (2002).

45. Deacon, R. M. J. Digging and marble burying in mice: simple methods for in vivo identification of biological impacts. *Nat Protoc* **1**, 122–124 (2006).

46. File, S. E. & Hyde, J. R. Can social interaction be used to measure anxiety? *Br J Pharmacol* **62**, 19–24 (1978).

47. Robinson, E. EFFECT OF AMYGDALECTOMY ON FEAR-MOTIVATED BEHAVIOR IN RATS. *J Comp Physiol Psychol* **56**, 814–820 (1963).

48. Goldstein, M. L. EFFECTS OF HIPPOCAMPAL, AMYGDALA, HYPOTHALAMIC AND PARIETAL LESIONS ON A CLASSICALLY CONDITIONED FEAR RESPONSE. *Psychol Rep* **16**, 211–219 (1965).

49. Nabavi, S. *et al.* Engineering a memory with LTD and LTP. *Nature* **511**, 348–352 (2014).

50. Johansen, J. P. *et al.* Optical activation of lateral amygdala pyramidal cells instructs associative fear learning. *Proc Natl Acad Sci U S A* **107**, 12692–12697 (2010).

51. Courtin, J. *et al.* Prefrontal parvalbumin interneurons shape neuronal activity to drive fear expression. *Nature* **505**, 92–96 (2014).

52. Cummings, K. A. & Clem, R. L. Prefrontal somatostatin interneurons encode fear memory. *Nat Neurosci* **23**, 61–74 (2020).

53. Tang, J., Wagner, S., Schachner, M., Dityatev, A. & Wotjak, C. T. Potentiation of amygdaloid and hippocampal auditory-evoked potentials in a discriminatory fear-conditioning task in mice as a function of tone pattern and context. *Eur J Neurosci* **18**, 639–650 (2003).

54. Xu, C. *et al.* Distinct Hippocampal Pathways Mediate Dissociable Roles of Context in Memory Retrieval. *Cell* **167**, 961-972.e16 (2016).

55. Silva, B. A. *et al.* Independent hypothalamic circuits for social and predator fear. *Nat Neurosci* **16**, 1731–1733 (2013).

56. Tovote, P. *et al.* Midbrain circuits for defensive behaviour. *Nature* **534**, 206–212 (2016).

57. Hebb, D. O. *The organization of behavior; a neuropsychological theory.* xix, 335 (Wiley, 1949).

58. Janak, P. H. & Tye, K. M. From circuits to behaviour in the amygdala. *Nature* **517**, 284–292 (2015).

59. Maren, S. & Quirk, G. J. Neuronal signalling of fear memory. *Nat Rev Neurosci* **5**, 844–852 (2004).

60. Johansen, J. P. *et al.* Hebbian and neuromodulatory mechanisms interact to trigger associative memory formation. *Proc Natl Acad Sci U S A* **111**, E5584-5592 (2014).

61. Lin, X. *et al.* c-Fos mapping of brain regions activated by multi-modal and electric foot shock stress. *Neurobiology of Stress* **8**, 92–102 (2018).

62. Moore, T. & Fallah, M. Microstimulation of the frontal eye field and its effects on covert spatial attention. *J Neurophysiol* **91**, 152–162 (2004).

63. Brincat, S. L., Siegel, M., von Nicolai, C. & Miller, E. K. Gradual progression from sensory to task-related processing in cerebral cortex. *Proc Natl Acad Sci U S A* **115**, E7202–E7211 (2018).

64. Fyhn, M., Molden, S., Witter, M. P., Moser, E. I. & Moser, M.-B. Spatial representation in the entorhinal cortex. *Science* **305**, 1258–1264 (2004).

65. Samineni, V. K., Grajales-Reyes, J. G., Sundaram, S. S., Yoo, J. J. & Gereau, R. W. Cell type-specific modulation of sensory and affective components of itch in the periaqueductal gray. *Nat Commun* **10**, 4356 (2019).

66. Bordi, F. & LeDoux, J. Sensory tuning beyond the sensory system: an initial analysis of auditory response properties of neurons in the lateral amygdaloid nucleus and overlying areas of the striatum. *J Neurosci* **12**, 2493–2503 (1992).

67. Koutsikou, S. *et al.* The Periaqueductal Gray Orchestrates Sensory and Motor Circuits at Multiple Levels of the Neuraxis. *J Neurosci* **35**, 14132–14147 (2015).

68. Kaifosh, P., Lovett-Barron, M., Turi, G. F., Reardon, T. R. & Losonczy, A. Septo-hippocampal GABAergic signaling across multiple modalities in awake mice. *Nat Neurosci* **16**, 1182–1184 (2013).

69. Ciocchi, S. *et al.* Encoding of conditioned fear in central amygdala inhibitory circuits. *Nature* **468**, 277–282 (2010).

70. Wolff, S. B. E. *et al.* Amygdala interneuron subtypes control fear learning through disinhibition. *Nature* **509**, 453–458 (2014).

71. Krabbe, S. *et al.* Adaptive disinhibitory gating by VIP interneurons permits associative learning. *Nat Neurosci* **22**, 1834–1843 (2019).

72. Tye, K. M. *et al.* Amygdala circuitry mediating reversible and bidirectional control of anxiety. *Nature* **471**, 358–362 (2011).

73. Felix-Ortiz, A. C. *et al.* BLA to vHPC inputs modulate anxiety-related behaviors. *Neuron* **79**, 658–664 (2013).

74. Kim, S.-Y. *et al.* Diverging neural pathways assemble a behavioural state from separable features in anxiety. *Nature* **496**, 219–223 (2013).

75. Jennings, J. H. *et al.* Distinct extended amygdala circuits for divergent motivational states. *Nature* **496**, 224–228 (2013).

76. Adhikari, A., Topiwala, M. A. & Gordon, J. A. Single units in the medial prefrontal cortex with anxiety-related firing patterns are preferentially influenced by ventral hippocampal activity. *Neuron* **71**, 898–910 (2011).

77. Padilla-Coreano, N. *et al.* Direct Ventral Hippocampal-Prefrontal Input Is Required for Anxiety-Related Neural Activity and Behavior. *Neuron* **89**, 857–866 (2016).

78. Jimenez, J. C. *et al.* Anxiety Cells in a Hippocampal-Hypothalamic Circuit. *Neuron* **97**, 670-683.e6 (2018).

79. Cassidy, R. M. *et al.* A lateral hypothalamus to basal forebrain neurocircuit promotes feeding by suppressing responses to anxiogenic environmental cues. *Sci Adv* **5**, eaav1640 (2019).

80. Avery, S. N., Clauss, J. A. & Blackford, J. U. The Human BNST: Functional Role in Anxiety and Addiction. *Neuropsychopharmacology* **41**, 126–141 (2016).

81. Walker, D. L., Toufexis, D. J. & Davis, M. Role of the bed nucleus of the stria terminalis versus the amygdala in fear, stress, and anxiety. *Eur J Pharmacol* **463**, 199–216 (2003).

82. Gründemann, J. *et al.* Amygdala ensembles encode behavioral states. *Science* **364**, (2019).

83. Schultz, W., Dayan, P. & Montague, P. R. A neural substrate of prediction and reward. *Science* **275**, 1593–1599 (1997).

84. Schultz, W. Dopamine reward prediction-error signalling: a two-component response. *Nature reviews. Neuroscience* **17**, (2016).

85. Tsai, H.-C. *et al.* Phasic firing in dopaminergic neurons is sufficient for behavioral conditioning. *Science* **324**, 1080–1084 (2009).

86. Nair-Roberts, R. G. *et al.* Stereological estimates of dopaminergic, GABAergic and glutamatergic neurons in the ventral tegmental area, substantia nigra and retrorubral field in the rat. *Neuroscience* **152**, 1024–1031 (2008).

87. Tan, K. R. *et al.* GABA neurons of the VTA drive conditioned place aversion. *Neuron* **73**, 1173–1183 (2012).

88. Root, D. H. *et al.* Distinct Signaling by Ventral Tegmental Area Glutamate, GABA, and Combinatorial Glutamate-GABA Neurons in Motivated Behavior. *Cell Rep* **32**, 108094 (2020).

89. Qi, J. *et al.* VTA glutamatergic inputs to nucleus accumbens drive aversion by acting on GABAergic interneurons. *Nat Neurosci* **19**, 725–733 (2016).

90. Watabe-Uchida, M., Zhu, L., Ogawa, S. K., Vamanrao, A. & Uchida, N. Whole-brain mapping of direct inputs to midbrain dopamine neurons. *Neuron* **74**, 858–873 (2012).

91. Beier, K. T. *et al.* Circuit Architecture of VTA Dopamine Neurons Revealed by Systematic Input-Output Mapping. *Cell* **162**, 622–634 (2015).

92. Beier, K. T. *et al.* Topological Organization of Ventral Tegmental Area Connectivity Revealed by Viral-Genetic Dissection of Input-Output Relations. *Cell Rep* **26**, 159-167.e6 (2019).

93. Morales, M. & Margolis, E. B. Ventral tegmental area: cellular heterogeneity, connectivity and behaviour. *Nat Rev Neurosci* **18**, 73–85 (2017).

94. Taylor, S. R. *et al.* GABAergic and glutamatergic efferents of the mouse ventral tegmental area. *J Comp Neurol* **522**, 3308–3334 (2014).

95. Hnasko, T. S., Hjelmstad, G. O., Fields, H. L. & Edwards, R. H. Ventral tegmental area glutamate neurons: electrophysiological properties and projections. *J Neurosci* **32**, 15076–15085 (2012).

96. van Zessen, R., Phillips, J. L., Budygin, E. A. & Stuber, G. D. Activation of VTA GABA neurons disrupts reward consumption. *Neuron* **73**, 1184–1194 (2012).

97. Brown, M. T. C. *et al.* Ventral tegmental area GABA projections pause accumbal cholinergic interneurons to enhance associative learning. *Nature* **492**, 452–456 (2012).

98. Mitrofanis, J. Some certainty for the 'zone of uncertainty'? Exploring the function of the zona incerta. *Neuroscience* **130**, 1–15 (2005).

99. Mitrofanis, J., Ashkan, K., Wallace, B. A. & Benabid, A.-L. Chemoarchitectonic heterogeneities in the primate zona incerta: clinical and functional implications. *J. Neurocytol.* **33**, 429–440 (2004).

100. Kolmac, C. & Mitrofanis, J. Distribution of various neurochemicals within the zona incerta: an immunocytochemical and histochemical study. *Anat. Embryol.* **199**, 265–280 (1999).

101. Watson, C., Lind, C. R. P. & Thomas, M. G. The anatomy of the caudal zona incerta in rodents and primates. *J. Anat.* **224**, 95–107 (2014).

102. Mitrofanis, J. & Mikuletic, L. Organisation of the cortical projection to the zona incerta of the thalamus. *J Comp Neurol* **412**, 173–185 (1999).

103. Heise, C. E. & Mitrofanis, J. Evidence for a glutamatergic projection from the zona incerta to the basal ganglia of rats. *J Comp Neurol* **468**, 482–495 (2004).

104. Kolmac, C. & Mitrofanis, J. Organization of the basal forebrain projection to the thalamus in rats. *Neurosci Lett* **272**, 151–154 (1999).

105. Kolmac, C. I., Power, B. D. & Mitrofanis, J. Patterns of connections between zona incerta and brainstem in rats. *J Comp Neurol* **396**, 544–555 (1998).

106. Power, B. D., Kolmac, C. I. & Mitrofanis, J. Evidence for a large projection from the zona incerta to the dorsal thalamus. *J Comp Neurol* **404**, 554–565 (1999).

107. Shaw, V. E. & Mitrofanis, J. Lamination of spinal cells projecting to the zona incerta of rats. *J Neurocytol* **30**, 695–704 (2001).

108. Chou, X.-L. *et al.* Inhibitory gain modulation of defense behaviors by zona incerta. *Nat Commun* **9**, 1151 (2018).

109. Bolton, A. D. *et al.* A Diencephalic Dopamine Source Provides Input to the Superior Colliculus, where D1 and D2 Receptors Segregate to Distinct Functional Zones. *Cell Rep* **13**, 1003–1015 (2015).

110. Zhou, M. *et al.* A central amygdala to zona incerta projection is required for acquisition and remote recall of conditioned fear memory. *Nat. Neurosci.* **21**, 1515–1519 (2018).

111. Zhao, Z.-D. *et al.* Zona incerta GABAergic neurons integrate prey-related sensory signals and induce an appetitive drive to promote hunting. *Nat. Neurosci.* **22**, 921–932 (2019).

112. Zhang, X. & van den Pol, A. N. Rapid binge-like eating and body weight gain driven by zona incerta GABA neuron activation. *Science* **356**, 853–859 (2017).

113. Chen, J. & Kriegstein, A. R. A GABAergic projection from the zona incerta to cortex promotes cortical neuron development. *Science* **350**, 554–558 (2015).

114. Sanghera, M. K., Anselmo-Franci, J. & McCann, S. M. Effect of medial zona incerta lesions on the ovulatory surge of gonadotrophins and prolactin in the rat. *Neuroendocrinology* **54**, 433–438 (1991).

115. Murray, J. F. *et al.* The effect of leptin on luteinizing hormone release is exerted in the zona incerta and mediated by melanin-concentrating hormone. *J. Neuroendocrinol.* **12**, 1133–1139 (2000).

116. Walsh, L. L. & Grossman, S. P. Zona incerta lesions impair osmotic but not hypovolemic thirst. *Physiol. Behav.* **16**, 211–215 (1976).

117. Stamoutsos, B. A., Carpenter, R. G., Grossman, L. & Grossman, S. P. Impaired feeding responses to intragastric, intraperitoneal, and subcutaneous injections of 2-

deoxy-D-glucose in rats with zona incerta lesions. *Physiol. Behav.* **23**, 771–776 (1979).

118. Liu, M. *et al.* Orexin gene transfer into zona incerta neurons suppresses muscle paralysis in narcoleptic mice. *J. Neurosci.* **31**, 6028–6040 (2011).

119. Liu, K. *et al.* Lhx6-positive GABA-releasing neurons of the zona incerta promote sleep. *Nature* **548**, 582–587 (2017).

120. Trageser, J. C. & Keller, A. Reducing the uncertainty: gating of peripheral inputs by zona incerta. *J. Neurosci.* **24**, 8911–8915 (2004).

121. Urbain, N. & Deschênes, M. Motor cortex gates vibrissal responses in a thalamocortical projection pathway. *Neuron* **56**, 714–725 (2007).

122. Masri, R. *et al.* Zona incerta: a role in central pain. *J. Neurophysiol.* **102**, 181–191 (2009).

123. Loskutova, L. V., Vinnitskii, I. M. & Il'yuchenok, R. Yu. Participation of the zona incerta in mechanisms of the conditioned avoidance reaction. *Neurosci. Behav. Physiol.* **11**, 60–62 (1981).

124. Venkataraman, A. *et al.* Modulation of fear generalization by the zona incerta. *Proc. Natl. Acad. Sci. U.S.A.* **116**, 9072–9077 (2019).

125. Saint-Cyr, J. A. *et al.* Localization of clinically effective stimulating electrodes in the human subthalamic nucleus on magnetic resonance imaging. *J Neurosurg* **97**, 1152–1166 (2002).

126. Zincone, A. *et al.* Physiologic study of the subthalamic volume. *Neurol Sci* **22**, 111–112 (2001).

127. Murata, J. *et al.* Electrical stimulation of the posterior subthalamic area for the treatment of intractable proximal tremor. *J Neurosurg* **99**, 708–715 (2003).

128. Yelnik, J. *et al.* Localization of stimulating electrodes in patients with Parkinson disease by using a three-dimensional atlas-magnetic resonance imaging coregistration method. *J Neurosurg* **99**, 89–99 (2003).

129. Plaha, P., Ben-Shlomo, Y., Patel, N. K. & Gill, S. S. Stimulation of the caudal zona incerta is superior to stimulation of the subthalamic nucleus in improving contralateral parkinsonism. *Brain* **129**, 1732–1747 (2006).

130. Burrows, A. M. *et al.* Limbic and motor function comparison of deep brain stimulation of the zona incerta and subthalamic nucleus. *Neurosurgery* **70**, 125–130; discussion 130-131 (2012).

131. Gourisankar, A. *et al.* Mapping movement, mood, motivation and mentation in the subthalamic nucleus. *R Soc Open Sci* **5**, (2018).

132. Aosaki, T. *et al.* Responses of tonically active neurons in the primate's striatum undergo systematic changes during behavioral sensorimotor conditioning. *J Neurosci* **14**, 3969–3984 (1994).

133. Apicella, P. Tonically active neurons in the primate striatum and their role in the processing of information about motivationally relevant events. *Eur J Neurosci* **16**, 2017–2026 (2002).

134. Doig, N. M., Magill, P. J., Apicella, P., Bolam, J. P. & Sharott, A. Cortical and thalamic excitation mediate the multiphasic responses of striatal cholinergic interneurons to motivationally salient stimuli. *J Neurosci* **34**, 3101–3117 (2014).

135. Matsumoto, N., Minamimoto, T., Graybiel, A. M. & Kimura, M. Neurons in the thalamic CM-Pf complex supply striatal neurons with information about behaviorally significant sensory events. *J Neurophysiol* **85**, 960–976 (2001).

136. Rizzi, G., Li, Z., Hogrefe, N. & Tan, K. R. Lateral ventral tegmental area GABAergic and glutamatergic modulation of conditioned learning. *Cell Rep* **34**, 108867 (2021).

Lateral Ventral Tegmental Area GABAergic and Glutamatergic modulation of conditioned learning

Authors

Giorgio Rizzi[1,2†], Zhuoliang Li[1†], Norbert Hogrefe[1,3] and Kelly R. Tan[1*]

Affiliation

[1]Biozentrum, University of Basel, Klingelbergstrasse 50/70, 4056 Basel, Switzerland.

[2]current affiliation: Inscopix Inc, Palo Alto, California 94303, United States.

[3]current affiliation: Department of Physiology, University of Bern, Buhlplatz 5, 3012 Bern, Switzerland.

[†]These authors contributed equally to the study.

Contact information

Kelly R. Tan

Kelly.tan@unibas.ch

0041 76 441 39

Rizzi*, Li* et al. Graphical Abstract

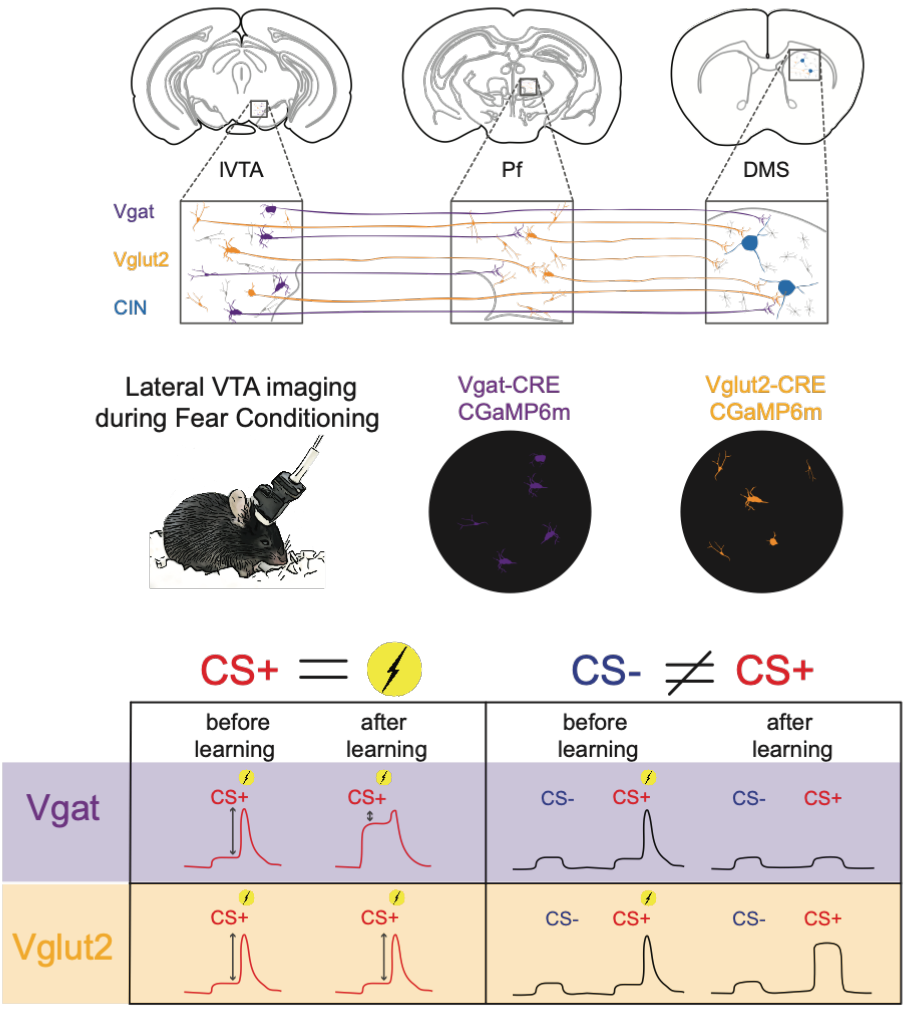

Summary

The firing activity of dorso-medial-striatal-cholinergic interneurons (dmCINs) is a neural correlate of classical conditioning. Tonically active, they pause in response to salient stimuli; mediating the acquisition of the predictive cues/outcome association. Cortical and thalamic inputs represent the rather limited knowledge about the underlying circuitry contributing to this function. Here we aim to dissect the midbrain GABA and Glutamate-to-dmCIN pathways and evaluate how they influence conditioned behavior. We report that midbrain neurons discriminate auditory cues and encode the association of a predictive stimulus with a footshock. Furthermore, GABA and Glutamate cells form selective monosynaptic contacts onto dmCINs and di-synaptic ones via the parafasicular-thalamus. Pathway-specific inhibition of each sub-circuit produces differential impairments of fear-conditioned learning. Finally, Vglut2-expressing cells discriminate between CSs while Vgat-positive neurons associate the predictive cue with the outcome. Overall, these data suggest that each component of such a complex network carries information pertinent to sub-domains of the behavioral strategy.

Introduction

In the Basal Ganglia, dmCINs are a rare neuronal population that exhibits a peculiar firing activity largely recognized as a key component in learning processing. Specifically, they briefly pause their tonic activity in response to salient stimuli and to sensory cues predicting motivationally rewarding and aversive outcomes (Aosaki et al., 1994; Apicella, 2002; Apicella et al., 1997; Zhang and Cragg, 2017). The pause response is hence considered a crucial neural correlate of classical conditioning. The dmCIN pause can be preceded by a short increase in firing and/or followed by a rebound excitation (Zhang and Cragg, 2017). Studies have reported the involvement of glutamatergic cortical (Ding et al., 2008; Doig et al., 2014; Reynolds and Wickens, 2004) and thalamic inputs in the generation of these phases (Lapper and Bolam, 1992; Matsumoto et al., 2001). However, these might not represent the comprehensive input circuitry involved. Here we propose to investigate how the midbrain might play a role in dmCINs function in fear conditioning. Midbrain neurons are heterogenous including Dopamine, GABA and Glutamate releasing cells (Morales and Margolis, 2017). Functionally and conversely to Dopamine neurons, both GABA and Glutamate cells are excited by aversive stimuli (Cohen et al., 2012; de Jong et al., 2019; Root et al., 2014; Tan et al., 2012; Ungless et al., 2004). Furthermore, GABA neurons located in the medial ventral tegmental area send long-range projection to inhibit CINs of the nucleus accumbens. Optogenetic activation of these inputs potentiates the stimulus-outcome association in a fear conditioning task (Brown et al., 2012). Here and with the aim of providing additional insights into midbrain to dmCIN pathways function, we focused on how midbrain GABA and Glutamate neurons modulate CINs response of the dorso-medial striatum (DMS) during fear conditioning. Our data show that the lateral ventral tegmental area (lVTA) neuronal population can discriminate auditory cues and encode the association of a predictive stimulus with a footshock (FS). GABA and Glutamate neurons form selective monosynaptic contacts onto dmCINs as well as di-synaptic preferential ones, via the parafasicular thalamic nucleus (Pf). Each of these pathways is differentially implicated in how mice predict a motivationally relevant stimulus. Indeed, a pathway specific manipulation during the association phase revealed how each component of this circuit contributes to the entire conditioning process and informs the behavioral strategy to deal with external stimuli. Furthermore,

although both Vgat- and Vglut2- expressing cells respond to all stimuli, Vglut2-positive neurons learn to discriminate between the conditioned stimuli while Vgat-positive cells consolidate the association between the predictive one with the FS across days. These results provide important information about lVTA Vgat- / Vglut2- to dmCINs circuitry in conditioned learning. Such knowledge could be instrumental in pathological conditions where associative learning and recall are dysfunctional.

Results

Lateral VTA neurons associate a predictive stimulus with a footshock

To validate our hypothesis that the midbrain critically modulates dmCINs' function in learning, we first assessed their own ability to do so. We imaged the activity of midbrain cells and more specifically from the lVTA while mice performed in a classical fear conditioning task (Figure 1 and Video S1[1]). AAV1-CaMK2a-GCaMP6m was injected in the lVTA and a GRIN-lens implanted above (Ghosh et al., 2011; Grewe et al., 2017) (Figure 1A to 1C). Eight to ten weeks post-surgery, mice underwent a fear conditioning paradigm (Figure 1D). They exhibited low contextual freezing levels to neutral contexts (Figure 1E) and froze significantly more to CS+ as compared to CS- on the test day; hence learning that CS+ is predictive of a FS (Figure 1F, 1G). As a proxy for cellular activation, calcium transients were concomitantly acquired. Cells responding to the cues were sparse and distinct (Figure 1H). All imaged neurons were profiled as responsive if their activity to a stimulus was statistically different from baseline (cue evoked activity vs baseline, ranksum test, $p<0.01$). Throughout the learning phase, the proportion of excited neurons to CS+ increased as did the CS+ evoked-freezing levels (Figure 1I to 1N and 1G). In addition, the amplitude of the calcium responses to CS+ was significantly larger from those of CS- (Figure 1O) and across days CS+ responses were better discriminated from baseline (Figure 1P). On average, lVTA neurons discriminated CS+ from CS- and consolidated this since the discrimination index increased over learning (Figure 1Q). We then examined the FS responses; a large majority of imaged cells were excited and their responses also discriminated from baseline (Figure S1A to S1E). Finally, we assessed the ability of lVTA cells to associate

[1] Supplementary videos for Study 2.1 can be found in the line below
https://www.dropbox.com/sh/867lstc5vaacxdb/AAAqoywmXemEj95ZzXfsu6yYa?dl=0

the predictive cue with the FS and analyzed the similarity between CS+ and FS responses, applying the Euclidean distance analysis. Within a conditioning session, the distance significantly decreased across pairings (Figure S1F to S1I), indicating that the value of CS+ and FS became similar. Most interestingly, it also decreased throughout the learning (Figure S1J and S1K), whether we pool all cells or only look at the FS responsive one. This suggest that the lVTA neurons associate CS+ with FS such that CS+ becomes a predictive stimulus.

Although the calcium indicator was expressed in all cell-types, we believe that the imaged cells were GABA or Glutamate neurons because of the following observations: 1) The large majority of imaged neurons exhibited excitation to FS (Figure S1B) and Dopamine neurons have been reported to respond through an inhibition of their firing activity while in stark contrast GABA and Glutamate cells increase theirs (Morales and Margolis, 2017; Root et al., 2014; Tan et al., 2012; Ungless et al., 2004). 2) Counterstaining of the imaged lVTA tissue revealed that cells located within the imaging field of view are tyrosine hydroxylase (TH) negative, so not dopaminergic (Figure S1L). 3) lVTA-CaMK2a-expressing cells do co-express Vgat or Vglut2 (Figure S2).

These data show that lVTA neurons encode CS+/FS associations in a fear conditioning learning task.

Lateral VTA GABA and Glutamate neurons contact mono-synaptically dmCINs

Because similarly to dmCINs, lVTA cells have the ability to predict the FS; to examine their potential role in dmCIN's function we next verified that they have the anatomical and functional potential to do so. A transsynaptic rabies tracing approach (Wickersham et al., 2007) (injection of AAV2/1-DIO-Ef1α-TVA-T2A-CVS11G and EnvA-coated SADΔG rabies into the DMS in ChAT-cre mice (Leinweber et al., 2017)) was first used to comprehensively explore dmCINs' afferent diversity (Figure 2A). Mouse brains were either processed for tissue clearing (Tainaka et al., 2018) (Figure 2B, Video S2) or sectioned and immuno-stained (Figure 2C). Strong rabies-GCaMP6s labelling was observed in cortical and thalamic regions (Klug et al., 2018; Zhang and Cragg, 2017). Notably, a cluster of neurons was identified in the midbrain and more specifically in the lateral portion of the VTA (Figure 2B to 2D, Video S2). These rabies labelled cells were counter-stained against TH and 96% were TH-negative (Figure 2D), corroborating our

previous assumption that our neuronal population of interest is composed of GABA and Glutamate cells. Furthermore, we verified through fluorescent *in situ* hybridization experiments that the lVTA expresses relatively less TH-positive neurons and that our GABA and Glutamate neuronal sub-populations are pure (Figure 2E). Indeed, not only the sub-nucleus of interest expresses 38.8% of GABA cells, 46.3% of Glutamate neurons and a minority of 11.9% of Dopamine neurons; co-expressors are also rare with less than 1% of the total population (Figure 2F).

We also assessed the lVTA to dmCIN pathway via anterograde tracing and injected AAV1-phSyn1-Flex-tdTomato-T2A-Syp-EGFP in the lVTA of Vgat- and Vglut2-CRE mice (Figure 3A). In both cases, dense labelling was observed in the DMS; with synaptophysin signal apposing ChAT-immuno-positive soma (Figure 3B and 3C).

We next explored the functionality of these pathways through optogenetic-assisted *in vitro* electrophysiology. We expressed ChR2-eYFP in the lVTA of Vgat- and Vglut2-expressing neurons and recorded *in vitro* light-evoked currents from dmCINs. They were identified based on their intrinsic electrophysiological properties (Vm: -49.3 ± 1.4 mV, capacitance: 58.7 ± 3.3 pF , spontaneous firing and Ih current upon hyperpolarization of Vm, Figure 3D (Bennett et al., 2000; Kawaguchi et al., 1997)). In all cases, robust monosynaptic currents were recorded as challenged by the successive bath-applications of TTX and 4AP (Petreanu et al., 2007) (Figure 3E and 3F).

In an independent data set, we recorded from putative non-dmCINs (Figure 3G and 3H). Their identification relied on distinct intrinsic electrophysiological properties from dmCINs e.g.; a smaller capacitance (16 ± 0.728 pF) a more hyperpolarized resting membrane potential (-83 ± 1.4 mV), the absence of Ih current and non-spontaneously firing, Figure 3D). We categorized the cells into two groups based on whether or not they exhibited a post-synaptic current upon light illumination of the DMS slice. In both Vgat- and Vglut2- slice preparations, the majority of the recorded cells displayed no light-evoked current (not connected, NC). Only one (Vgat pathway, Figure 3G) and three cells (Vglut2 pathway, Figure 3H) exhibited a current that was multi-synaptic as they did not reappear with bath application of TTX + 4AP (connected not mono-synaptically, CnM). We attempted to differentiate the NC- from the CnM- cells. In the Vgat pathway, the NC cells seemed to display an input/output curve left-shifted as

compared to the CnM one (Figure 3G). In the Vglut2-related pathway, the NC cells sustain higher firing rate than the CnM ones (Figure 3H).

These data report that lVTA GABA and Glutamate form specific mono-synaptic contacts onto dmCINs.

Lateral VTA GABA and Glutamate neurons contact di-synaptically dmCINs via the Parafascicular Thalamus

While screening our brain slices obtained from the pseudotyped-rabies mapping experiments, we observed as previously reported (Matsumoto et al., 2001) that the Pf are inputs of the dmCINs (Figure 2B, S3A and S3B). Additional mapping experiments were performed where synaptophysin tagged EGFP was expressed in the Pf of Vglut2-CRE mice. Labelled appositions were visualized onto putative dmCINs that were immuno-positive against ChAT (Figure S3C and S3D).

Next, we confirmed that this pathway is functional through *in vitro* patch-clamp recordings of DMS cells (Figure 4A to 4C) while ChR2-EYFP was expressed in the Pf of WT mice. The recorded neurons were identified as previously described in Figure 3. All patched dmCINs displayed mono-synaptic light-evoked currents (Figure 4B). Non-dmCINs were again classified into three categories based on their connectivity. We found that the majority of these cells were not connected (11/19, NC), 4/19 were multi-synaptically connected (CnM) and 4/19 were mono-synaptically connected (CM). We could not clearly identify distinct electrophysiological properties between these 3 groups of cells as reported by the input-output curve (Figure 4C). These data confirm that Pf cells make preferential mono-synaptic contacts onto dmCINs.

Very interestingly, in our anterograde anatomical mapping experiments with synaptophysin expressed in lVTA GABA or Glutamate cells, dense innervation was also evident in the Pf (Figure 4D to 4F). We therefore verified the functionality of these lVTA to Pf sub-pathways and expressed ChR2-EYFP in the lVTA of Vgat- and Vglut2-CRE mice to record potential light-mediated mono-synaptic currents in Pf cells (Figure 4G). In both cases, every single of the patched Pf neurons exhibited light-evoked post-synaptic currents blocked by bath application of TTX, reappearing with 4AP and pharmacologically identified with PTX or KA (Figure 4H and 4I). We then asked whether the Pf neurons receiving monosynaptic inputs from lVTA GABA and Glutamate neurons

are the ones projecting to the DMS. This was assessed by expressing ChR2-EYFP in the lVTA of Vgat- or Vglut2-CRE mice together with red retrobeads injected in the DMS (Figure 4J) and retrogradely labelled cells in the Pf were then patched (Figure 4K and 4L). We found that the large majority (12/13 cells) of Pf cells projecting to the DMS received monosynaptic light-induced currents from lVTA GABA cells (Figure 4M) and lVTA Glutamate neurons (Figure 4N). In each case, only one current was found to be multi-synaptic.

Overall, these anatomical and *in vitro* functional data show that lVTA GABA and Glutamate neurons make a strong di-synaptic connection with dmCINs via the Pf.

Lateral VTA GABA and Glutamate inputs differentially impact discrimination performance

Our next step was to provide experimental evidence that the GABA and Glutamate lVTA to dmCIN sub-pathways are indeed instrumental in fear conditioned learning. We opted for a loss of function optogenetic manipulation of GABA and Glutamate release in the DMS and the Pf. Arch-EYFP was expressed bilaterally in the lVTA of Vgat- and Vglut2-CRE mice and optic fibers implanted in the DMS or the Pf (Figure 5A and 5B). We first verified *in-vitro* that 532nm-green light triggered currents and robust hyperpolarization, as well as blockade of induced-firing in infected neurons (Figure 5C). Mice underwent the fear conditioning task (Figure 5D). Each experimental group (Figure 5E, 5I, 5M, 5Q) showed similar low contextual freezing levels during the first conditioning and test sessions (Figure 5F, 5J, 5N, 5R) and all control mice froze more on the conditioning day 5. This was concomitant to a higher proportion of freezing to CS+ as compared to CS- on the test day (Figure 5G, 5K, 5O, 5S) and reflects association of the CS+ with the FS (Videos S3 and S4).

When light stimulation was applied at GABAergic terminals in the DMS, Arch-mice froze more to CS- as compared to controls, leading to a lower discrimination index between tones (Figure 5G, 5H). This suggests that removal of direct inhibition in the DMS from the lVTA decreases mouse discrimination abilities. When green light was applied at GABAergic terminals in the Pf (allowing a relative increase of excitatory drive from Pf to DMS), Arch-mice exhibited less freezing to CS- hence discriminated better the two stimuli than control mice (Figure 5K, 5L). When modulating excitatory

neurotransmission in the DMS, no difference between mouse groups was observed (Figure 5O and 5P). Interestingly when light stimulation was provided to glutamatergic terminals in the Pf, freezing to both CS+ and CS- was low (Figure 5S). Arch-mice therefore did not associate the CS+ with the FS (Figure 5T).

These experiments confirm that each lVTA pathway, direct or indirect via the Pf, is differentially implicated in associative learning and supply dmCINs with specific information about behaviorally relevant events and strategies.

Lateral VTA GABA and Glutamate neurons contribute differentially to associating a predictive stimulus with a footshock

As a final investigation step, we assessed how lVTA Vgat- and Vglut2-expressing cells encode information during such learning process. Similarly, to the non-specific approach (Figure 1), we injected an AAV8-Dj-Ef1α-DIO-GCaMP6f in the lVTA of Vgat- and Vglut2-CRE mice, implanted a GRIN lens above the infection site (Figure 6A to 6C) and challenged mice in the fear conditioning task. Similarly, to WT mice, both mouse group exhibited low contextual freezing levels to neutral contexts (Figure 6D). On the test day, they froze significantly more to CS+ as compared to CS- hence discriminated between both CSs; learning that CS+ is predictive of the FS (Figure 6E and 6F).

At the ensemble view of the calcium dynamics level; across conditioning sessions and on the test day; both Vgat and Vglut2-expressing cells displayed an overall increased calcium activity at the presentation of CS-, CS+ and FS (Figure S4, Videos S5 and S6). When assessing the responses at the single cell level, the imaged Vgat- and Vglut2-positive cells were either non responsive or responsive through increased or decreased calcium transients (Figure 6G to 6N). Specifically and throughout learning, the proportion of cells responsive to CS- and CS+ increased in both populations at the expense of the non-responsive cells (Vgat- expressing cells; Figure 6G and 6I and Vglut2-expressing neurons; Figure 6K and 6M). In addition, the ability of both populations to discriminate CS+ from the baseline increased over learning (Figure 6O, 6Q) while only the Vglut2- expressing cells were able to learn to discriminate between the CS- and CS+ (Figure 6R and S5).

We also examined the responsiveness of the Vgat- and Vglut2-expressing cells to FS (Figure 7). In both cases, the large majority of neurons were excited (Vgat-expressing

neurons; Figure 7A to 7C and Vglut2-expressing neurons; Figure 7D to 7F) and able to discriminate FS from the baseline (Figure 7G to 7K). Within each conditioning session, the Euclidean distance between the CS+ and FS significantly decreased across successive parings in both populations (Figure 7L to 7Q), indicating an increase in similarity and thus the learning of the association between CS+ and FS. Such decreases were not observed across conditioning sessions (Figure 7R and 7T). However, when we examined specifically the Vgat- and Vglut2- expressing cells that were responsive to FS, we observed a striking difference where an increase in similarity between CS+ and FS responses were observed only in the Vgat-positive population and not the Vglut2- one. These cell-type specific *in vivo* calcium imaging data suggest that the Vglut2-expresssing cell population may represent a component for CSs discrimination while the Vgat-expressing cell population would be responsible for the consolidation of the association between the CS+ and FS.

Discussion

The midbrain encodes reward prediction error and learning (Schultz, 2017; Schultz et al., 1997); here we shed light onto its inhibitory and excitatory components as instrumental for dmCINs-mediated associative learning. Monitoring unspecific lVTA neuronal calcium activity showed that these neurons discriminate salient stimuli and pair predictive cues with aversive outcomes, remarkably reflecting not only the behavioral freezing phenotype but also the cellular activity pattern of dmCINs. We believe that such mirrored activity of lVTA cells and dmCINs is not surprising as they are wired together. Indeed, both GABA and Glutamate lVTA cell types send monosynaptic inputs onto dmCINs. Such functional connectivity is largely specific to dmCINs as rather than other striatal cells. In addition, they also contact the Pf; which itself excites dmCINs (Matsumoto et al., 2001). These indirect pathways via the Pf not only are preferentially targeting the dmCINs but they are di-synaptic; Pf cells receiving mono-synaptic inputs from lVTA neurons, project themselves to the DMS.

Our rabies experiments followed by post-hoc TH staining reveals that lVTA inputs onto dmCINs are rather non dopaminergic. This however, could be due to a lower infection efficiency towards dopaminergic synapses as compared to other ones (Wall et al., 2013) or an impaired protein translation in rabies-infected neurons. Interestingly, our FISH experiments revealed that the lVTA expresses relatively fewer TH- than Vgat or Vglut2-

expressing cells. Furthermore these cells are quite pure relative to the medial VTA (Stamatakis et al., 2013) or the SNc (Tritsch et al., 2016), suggesting a potential role for lVTA GABA and Glutamate modulation in the dmCINs mediated behavioral performances. Our aim here is to highlight the contribution of GABA and Glutamate lVTA inputs in addition to the well characterized and acknowledged Dopamine modulation (Cai and Ford, 2018; Chuhma et al., 2004, 2014).

Furthermore, our optogenetic manipulations during fear conditioning supported by our anatomical and functional mapping observations provide a convincing additional evidence for a role of lVTA Vgat- and Vglut2- projections onto dmCINs' aversive stimuli encoding. Indeed, considering that lVTA Vgat-expressing cells selectively inhibit dmCINs, the increased freezing in response to CS- due to the photoinhibition of lVTA Vgat terminals in the DMS was expected. Furthermore, the di-synaptic pathways via the Pf although preferential onto dmCINs also target non-dmCINs. This implies that photo-inhibition of lVTA-Vgat terminals in the Pf would lead to a differential behavioral outcome as compared to the photo-inhibition directly in the DMS; which is indeed what we observe and report. In addition, the relief of glutamate release in the Pf but not directly in the DMS led to a loss in performance. In other words, the di-synaptic glutamatergic pathway but not the direct one participates in the fear conditioning task. Overall, this suggests that lVTA Vgat- and Vglut2-expressing cells contribute to fear learning through both the direct and indirect (via the Pf) pathways but also involving both dmCINs and non-dmCINs.

Our cell type specific calcium imaging provides important information for the understanding of the relative contribution of lVTA neurons in associative behaviors. First of all, when considering the Vgat and Vglut2-expressing neurons as neuronal ensembles, we confirmed the recent fiber photometry observations that both ensembles are overall excited by CS+ and FS stimuli (Root et al., 2020). We further investigated the heterogeneities in these populations by examining how they behaved at the single cell level. In the naïve state, the majority of recorded cells were non-responsive to auditory cues. Both lVTA Vgat- and Vglut2- expressing cells can clearly discriminate the FS. Throughout learning, both lVTA Vgat- and Vglut2- expressing populations became proportionally more responsive to auditory cues and were able to better discriminate the fear predictive tone. Furthermore, the Vglut2- expressing

neurons were able to learn to discriminate between fear predictive and neutral tones whereas component of the Vgat- positive ones consolidated the association between the fear predictive tone and the unconditioned FS across days. These findings are quite interesting and represent an optimistic start into understanding the differential contribution of each lVTA to CINs pathways (Vgat- direct and di-synaptic versus Vglut2- direct and di-synaptic) have in fear learning. The ability to longitudinally track recorded cells may provide further insights into how each population acquire such defined role and become an individual component of the overall behavioral strategy.

Overall, we provide additional knowledge on the circuitry underlying conditioned fear learning. Inhibitory and excitatory lVTA inputs supply dmCINs with information to create conditioned associations. The modulation of each pathway during learning alters different aspects of the behavioural response as a whole and each cell type contribute distinctly. This suggests that they each contributes to the generation of appropriate behavioural strategies in response to external stimuli. These data may reveal valuable information, specifically when considering circuit-based therapeutical strategies in Basal Ganglia-related cognitive symptoms with impaired associative learning.

Acknowledgments

The authors thank the past and present lab members for constructive input and the team of the Imaging Platform of the Biozentrum. We thank Wolf Heusermann for his technical support in brain clearing and light sheet microscopy. We are grateful to Diane Damez-Wermo, Field Scientist Consultant at Inscopix for her technical support with calcium imaging. This work was supported by the Swiss National Science Foundation grant PP00P3_150683 and BSSGI0-155830. The mouse image for the graphical abstract is courtesy of Inscopix. We thank the team of Georg Keller from the FMI for the viruses used in the rabies tracing experiments.

Author Contributions

G.R. and K.R.T; Conceptualization. G.R, Z.L., N.H and K.R.T.; Methodology, Investigation; G.R, Z.L. and K.R.T Writing and Editing. K.R.T.; Funding, Supervision.

Declaration of Interests

The authors declare no competing interests.

Inclusion and diversity

We worked to ensure sex balance in the selection of non-human subjects. One or more of the authors of this paper self-identifies as an underrepresented ethnic minority in science. The author list of this paper includes contributors from the location where the research was conducted who participated in the data collection, design, analysis, and/or interpretation of the work.

Main figure titles and legends-

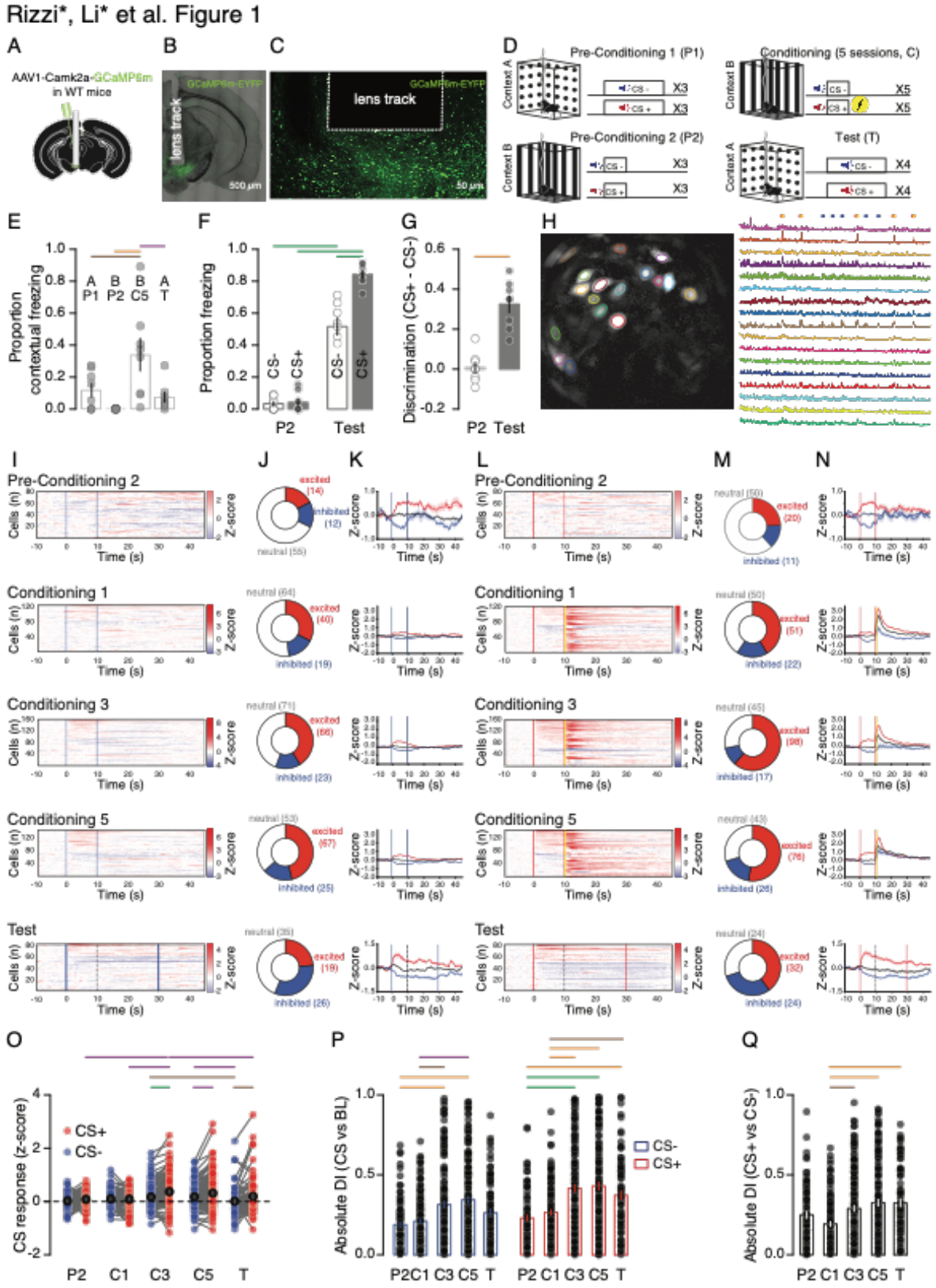

Figure 1: lVTA neurons encode the discrimination of auditory cues in fear conditioning.

(A) Stereotaxic injection of AAV1-CaMK2a-GCaMP6m in the lVTA of WT mice, followed by the implantation of a GRIN lens.

(B) Example confocal image of a coronal lVTA-containing section showing the infected area and the tract left behind by the GRIN lens.

(C) High magnification confocal image from B.

(D) Auditory cued fear conditioning paradigm.

(E) Bar graph of the average proportion of contextual freezing during P1, P2, C5 and the test days.

(F) Bar graph reporting the average proportion of freezing during the presentation of CS- and CS+ on P2 and test days.

(G) Bar graph for the difference of freezing between CS+ and CS- on P2 and test days.

(H) Representative maximal projection image of the field of view obtained from the miniaturized microscope with computationally detected cells labeled in different colors. Calcium transient traces of the colored identified individual cells during C5. Presentations of CS-, CS+ and FS are depicted in blue, red and yellow; respectively. Although the same field of view was imaged across different sessions, different ROIs for cells identification were analyzed on different days.

(I) Z-score heatmaps of average calcium transients at the presentation of the CS- (vertical blue bars) on P2, C1,C3, C5 and T days. The vertical black dashed line depicts the end of the time window used for response classification on the test day.

(J) Pie-chart quantifications of all recorded cells to CS- during P2, C1, C3, C5 and T days.

(K) Z-score curves of the average calcium transients (SEM shaded) of all cells at the CS- presentation on the P2, C1, C3, C5 and T days.

(L) Z-score heatmaps of average calcium transients at CS+ presentation (vertical red bars) and the electric shock (yellow bars) during P2, C1, C3, C5 and test days.

(M) Pie-chart quantification of all recorded cells to the CS+ tone presentation.

(N) Z-score curves of the average calcium transients (SEM shaded) of characterized cells responding to CS+.

(O) Summary graph reporting the Z-score of the tone responses on P2, C1, C3, C5 and T days.

(P) Absolute discrimination index for each tone as compared to baseline; calcium activity on P2, C1, C3, C5 and T days.

(Q) Absolute discrimination index between CS+ and CS- on P2, C1, C3, C5 and T days.

Data are represented as mean +/- SEM. *p<0.05, **p<0.01, ***p<0.001, ****p<0.0001. See also Figure S1, S2, Video S1 as well as Excel Table S1.

n= 8 mice with 80 to 160 cells in total.

Rizzi*, Li* et al. Figure 2

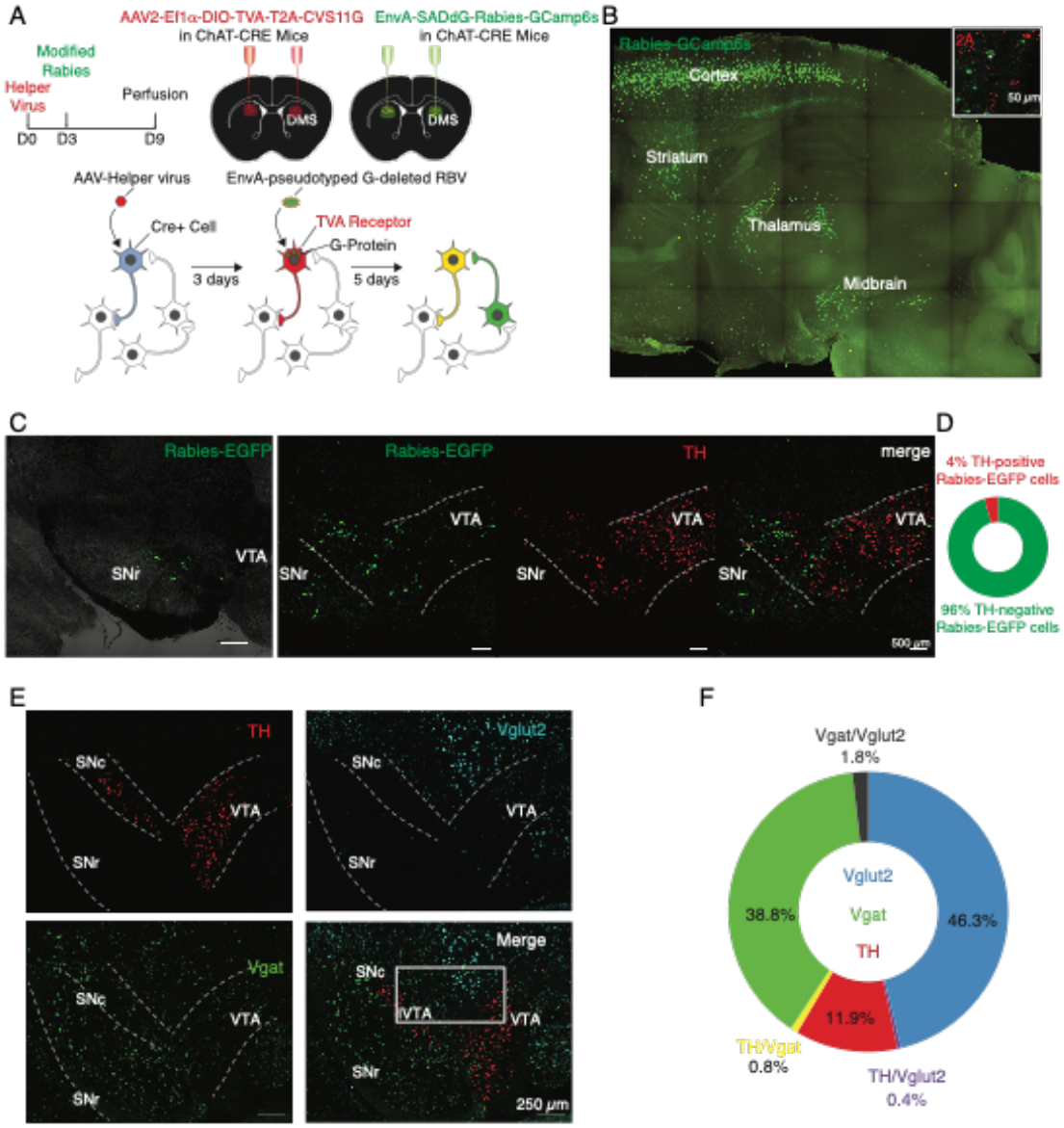

Figure 2: Lateral VTA neurons monosynaptically contact dmCINs.

(A) Experimental design: timeline of the injections for the modified rabies monosynaptic input mapping system, stereotaxic injections of the helper virus AAV2-Ef1α-TVA-T2A-CVS11G in the DMS of ChAT-CRE mice followed by that of the EnVA-SADΔG-Rabies-GCaMP6s, and the mechanistic behind the modified rabies system.

(B) Maximal projection light-sheet image of a CUBIC-cleared hemisphere with the cells that provide monosynaptic inputs onto the DMS ChAT neurons (= dmCINs, Rabies-GCaMP6s, green, n = 3). The inset is an example confocal image illustrating the infection site (peptide 2A, red; * show the starter cells).

(C) Example confocal imaging of a lVTA containing-slice illustrating the location of DMS-ChAT input neurons (Rabies-GCaMP6s, green). The slices were counter-stained against TH (red).

(D) Quantitative pie chart reporting the proportion of rabies labelled input neurons that express TH (red) or not (green).

(E) Confocal images of a representative coronal section containing the lVTA with FISH labeling of the mRNAs for tyrosine hydroxylase TH (red), Vglut2 (cyan), Vgat (green), as well as the merged image of all three. The white rectangle on the merge image delineates the region of interest; the lVTA.

(F) Pie-chart quantification of the lVTA (white rectangle) that expresses mainly either TH, or Vglut2, or Vgat (937 cells, 3 mice).

Rizzi*, Li* et al. Figure 3

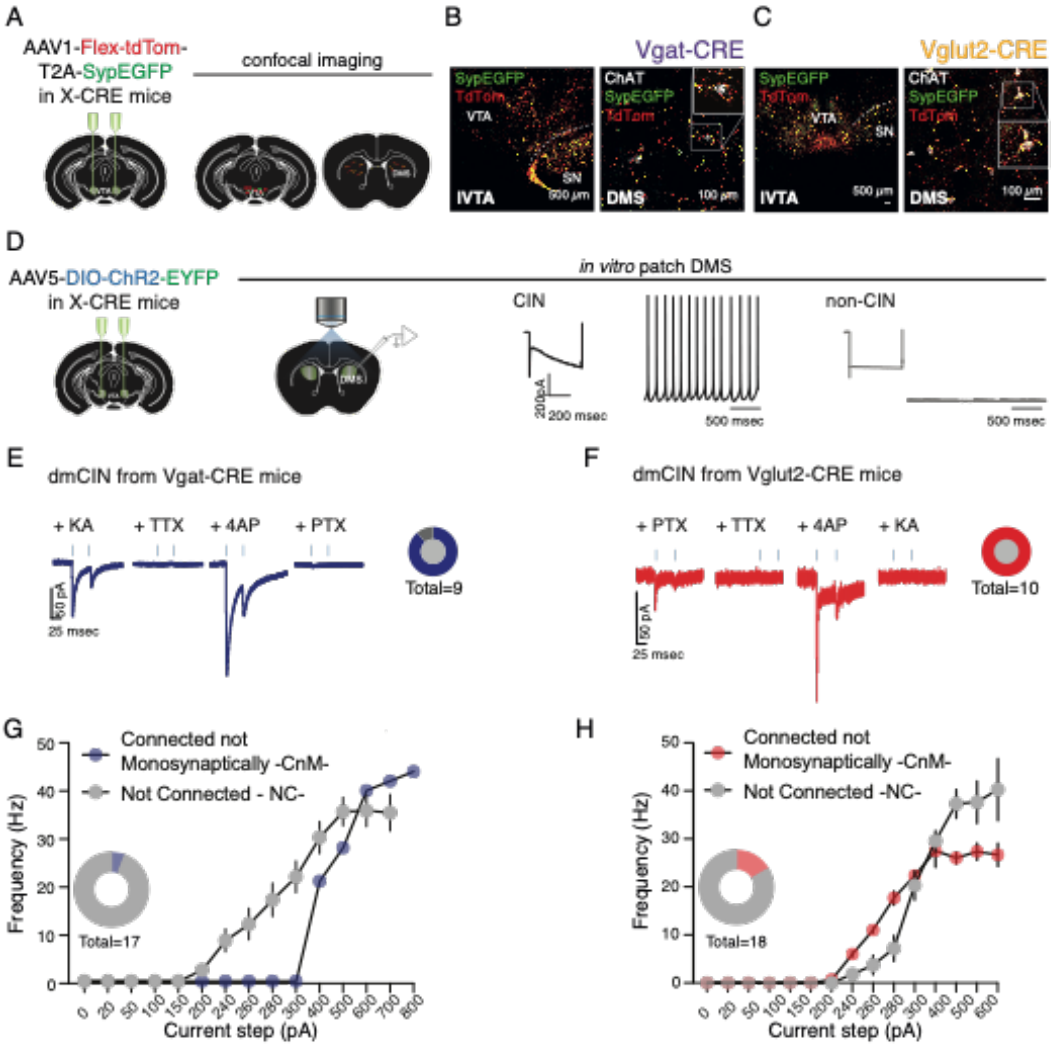

Figure 3: Lateral VTA GABA and Glutamate neurons contact mono-synaptically dmCINs.

(A) Experimental design showing the bilateral injections of AAV1-FLEX-tdTomato-T2A-SypEGFP virus in the lVTA of Vgat- and Vglut2-CRE mice and the sites of confocal imaging in the lVTA and the DMS.

(B) Example confocal images from Vgat-Cre mouse of cytoplasmic Tdtomato signal and synaptophysin-EGFP expression in the lVTA and in the DMS with ChAT immuno-labelling (white).

(C) Same as in B but with a Vglut2-Cre mouse.

(D) Schematic representation of bilateral AAV5-DIO-ChR2-EYFP viral injection in the lVTA of Vgat- and Vglut2-CRE mice and *in vitro* whole-cell patch clamp recordings in the DMS of CINs exhibiting an Ih current as well as spontaneous firing and non-CIN which in stark contrast disply no Ih current and no spontaneous firing activity.

(E) 8 of 9 dmCINs displayed inhibitory currents in the presence of KA (2mM), that were abolished by TTX (500nM), and reappeared with the addition of 4AP (300μM) and blocked by PTX (100μm). (n = 7 mice).

(F) Light-evoked excitatory currents in the presence of PTX were recorded in all dmCINs from Vglut2-CRE mice preparations. This current is monosynaptic, blocked by TTX reappearing in the presence of both TTX and 4AP and finally abolished with KA.

(G) Input/output curves of non-CINs from the Vgat-related preparation. 1 cell was not mono-synaptically connected (CnM, blue) while the remaining 16 were not connected (NC, grey). (n = 6 mice).

(H) Similarly to the lVTA Vgat to DMS projections, in the Vglut2 to DMS pathway, 3 cells were connection but not mono-synaptically (CnM, grey) while the majority of 15 out of 18 cells were not connected (NC, red). (n = 6 mice).

Rizzi*, Li* et al. Figure 4

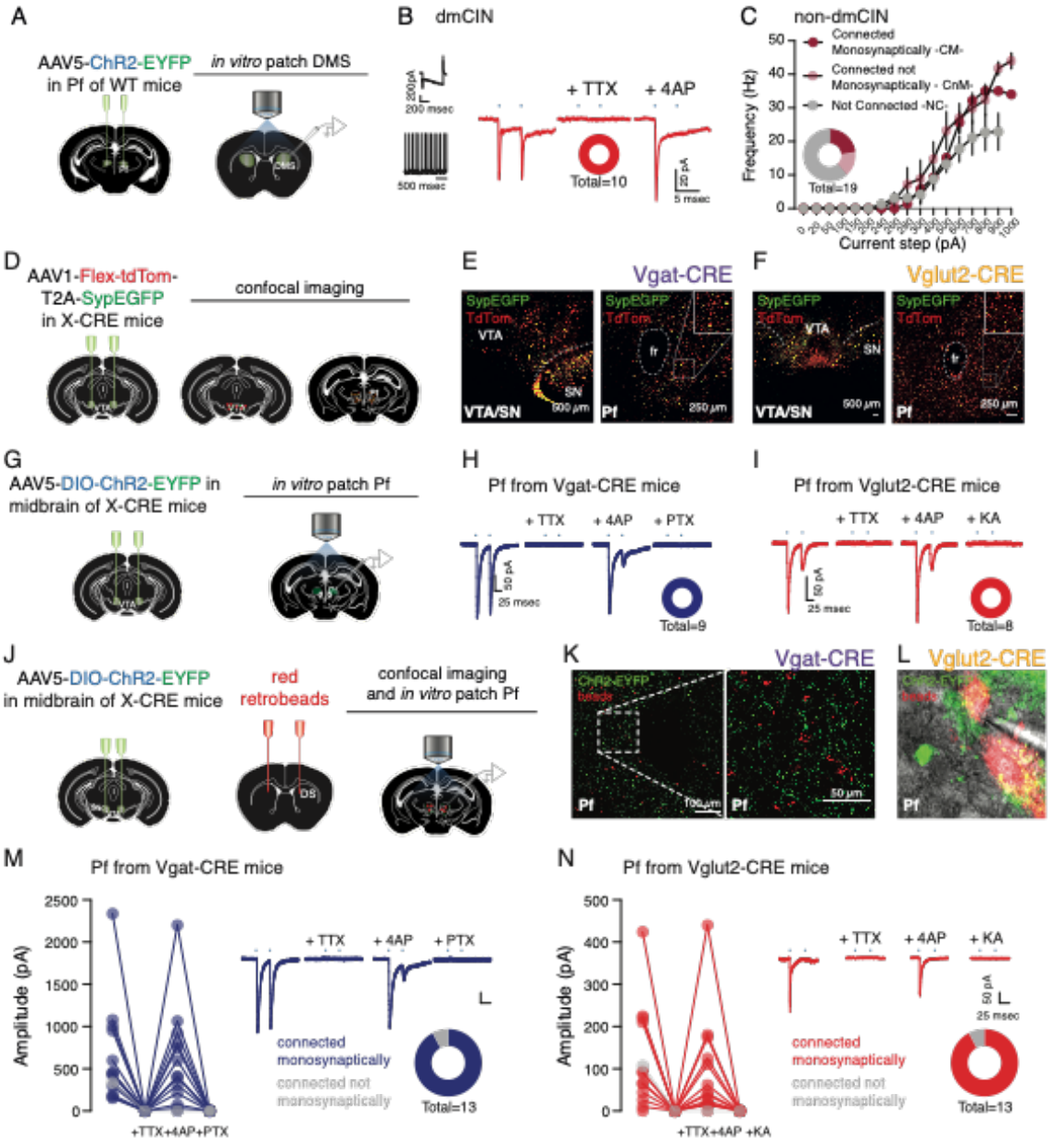

Figure 4: Lateral VTA GABA and Glutamate neurons contact di-synaptically dmCINs via the Parafascicular Thalamus.

(A) Injection of AAV5-ChR2-EYFP in the Pf of WT mice followed by the in vitro patch clamp recording of DMS neurons.

(B) Left, Typical Ih current triggered by a -40mV step in voltage clamp configuration and spontaneous firing recorded at I0. Right, representative light evoked current blocked by TTX but rescued by TTX+4AP bath application. (n = 6 mice and a total of 10 cells).

(C) Among the non-CINs (identified as in Figure 3), we found 4 cells that were mono-synptically connected (CM, dark red) 4 cells that were not mono-synaptically connected (CnM, light red) and the remaining 11 neurons were not connected (NC, grey). Their average input/output curve is depicted. (n = 6 mice and a total of 19 cells).

(D) Experimental design showing the bilateral injections of AAV1-FLEX-tdTomato-T2A-SypEGFP virus in the lVTA of Vgat- and Vglut2-CRE mice and the sites of confocal imaging in the lVTA and the Pf.

(E) Example confocal images from Vgat-Cre mouse of cytoplasmic Tdtomato signal and synaptophysin-EYFP expression in the lVTA (please note that the same image as in Figure 3B is shown) and in the Pf.

(F) Same as in E but for a Vglut2-Cre mouse.

(G) Schematic representation of bilateral AAV5-DIO-ChR2-EYFP viral injections in the lVTA of Vgat- and Vglut2-CRE mice and *in vitro* whole-cell patch clamp recordings of Pf cells.

(H) Pf thalamic neurons also receive functional GABA monosynaptic inputs from the lVTA. Pie charts report that all recorded neurons exhibited a monosynaptic GABAergic transmission, blocked by TTX and reappearing with 4AP.

(I) Monosynaptic glutamatergic currents are also acquired in all recorded Pf thalamic cells.

(J) Schematic illustrating the AAV5-DIO-ChR2-EYFP bilateral injections in the lVTA of Vgat- and Vglut2-CRE mice, followed by the injection of red beads in the DMS and whole cell patch clamp recording of retrogradely labelled Pf neurons.

(K) Example low and high magnification confocal images showing the dense innervation of lVTA Vgat fibers expressing ChR2-EYFP and red retrogradely labeled Pf cells.

(L) Example image from the in vitro set up showing ChR2-EYFP fibers from lVTA Vglut2-expressing neurons, 2 retrogradely Pf cells, among those one is being impaled by a recording pipet.

(M) 12 Pf cells that project to the DMS received mono-synaptic inputs from lVTA Vgat-expresing neurons. Only in one cell the light induced current did not reappear with bath application of 4AP. (n = 6 mice with a total of 13 cells).

(N) 12 Pf cells that project to the DMS generated excitatory light evoked current that were mono-synaptic. (n = 6 mice with a total of 13 cells).

See also Figure S3.

Rizzi*, Li* et al. Figure 5

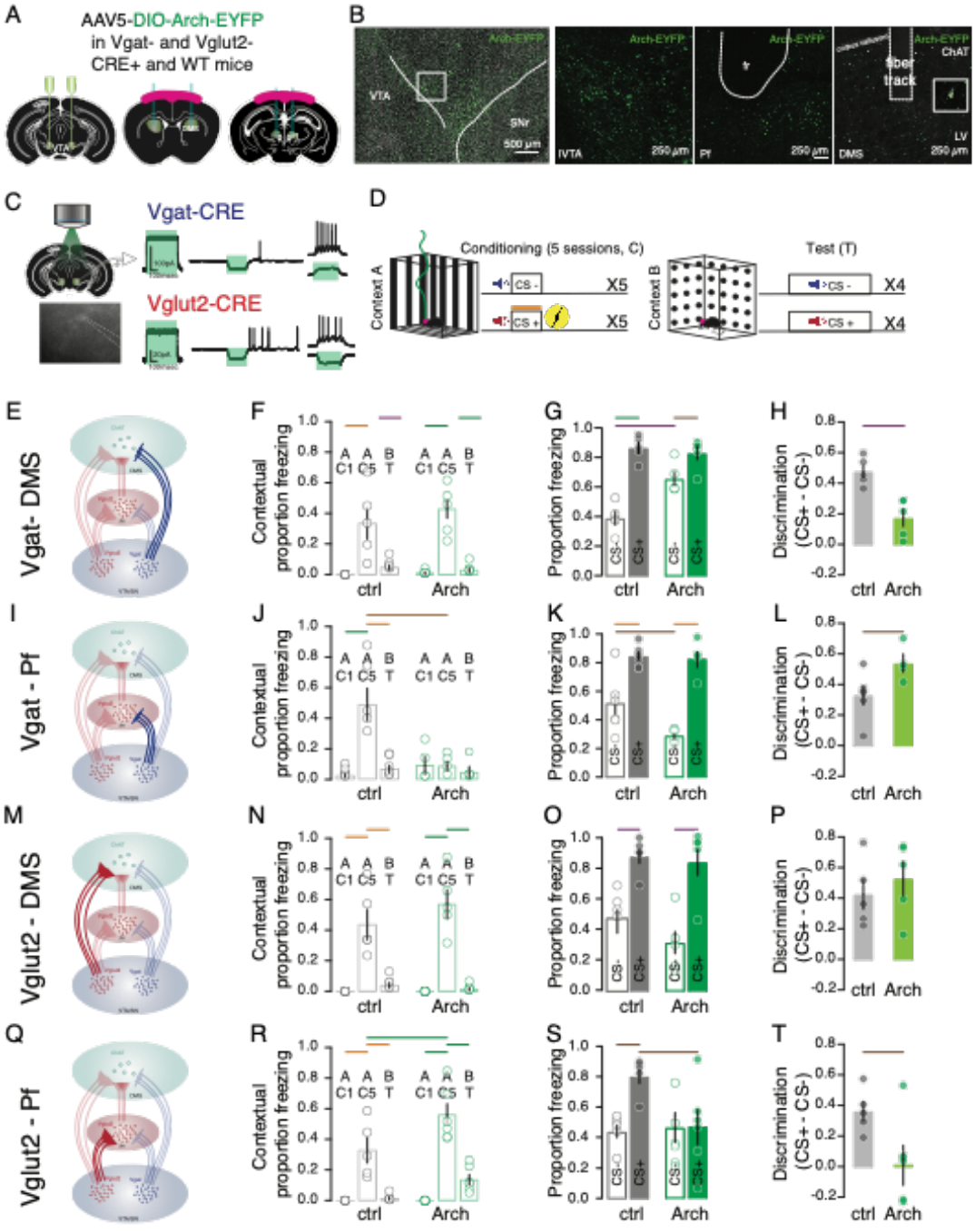

Figure 5: LVTA GABA and Glutamate inputs differentially impact discrimination performance.

(A) Schema of the stereotaxic injections of AAV5-DIO-Arch-EYFP virus in the lVTA of either Vgat-, Vglut2-CRE or WT mice, followed by optic fiber implants above either the DMS or Pf.

(B) Example confocal images of representative brain sections containing the primary infection of the EYFP labeled Arch construct (green, left), a higher magnification exemplifying the somatic expression of Arch-EYFP, the projections in the Pf and in the DMS where the track left behind by optic fiber implant can be observed. ChAT positive cells are revealed by immunostaining (white).

(C) Optogenetic functional validation with the stereotaxic injections of AAV5-DIO-Arch-EYFP in the lVTA of Vgat- or Vglut2-CRE for *in vitro* patch-clamp recordings. Representative fluorescent image of the patched Arch-expressing cell. Representative electrophysiological traces depicting a light-evoked outward current in voltage clamp, the light-evoked reduction of firing activity in current clamp, and inhibition with rebound firing upon the cessation of light presentation in I0, for both Arch infected Vgat (top) and Vglut2 cells.

(D) Schematic of the auditory cued fear conditioning paradigm. Mice were trained (1 session per day over 5 consecutive days) to discriminate between randomly selected auditory CS stimulus that was either paired (CS+, red) with an electric shock or without (CS-, blue) presented in a randomized order. Following conditioning, the animals were tested in a different context by the presentation of 4 CS- and subsequently 4 CS+.

(E) Schematic of the manipulated pathway; lVTA Vgat to DMS.

(F) Bar graph of the proportion of freezing to the context during the C1, C5 and test days in control WT mice (grey) and Arch injected Vgat-CRE (green).

(G) Bar graph of the average proportion of freezing during the presentation of either CS- or CS+ on the test day.

(H) Bar graph reporting the discrimination between the freezing level to CS+ and CS-.

(I) Schematic of the manipulated pathway; lVTA Vgat to Pf.

(J) Bar graph of the freezing proportion to the context during C1, C5, and test days days in Arch injected in WT and Vgat-CRE mice.

(K) Bar graph of the average proportion of freezing during the presentation of CS- or CS+ on the test day.

(L) Discrimination between the CS+ and CS-.

(M) Schematic of the manipulated pathway; lVTA Vglut2 to DMS.

(N) Bar graph of the proportion of freezing to the context during C1, C5, and T in Arch injected in WT and Vglut2-CRE mice.

(O) Bar graph of the average proportion of freezing during the presentation of CS+ or CS- on the test day.

(P) Discrimination between the CS+ and CS-.

(Q) Schematic of the manipulated pathway; lVTA Vglut2 to Pf.

(R) Bar graph of the proportion of freezing to the context during C1, C5, and test days in Arch injected in WT and Vglut2-CRE mice.

(S) Bar graph of the average proportion of freezing during the presentation of either CS+ or CS- on the test days.

(T) Discrimination between the CS+ and CS-.

Data are represented as mean +/- SEM. *p<0.05, **p<0.01, ***p<0.001, ****p<0.0001.

See also Videos S3 and S4 as well as Excel Table S1.

n = 5 to 6 mice in each group.

Rizzi*, Li* et al. Figure 6

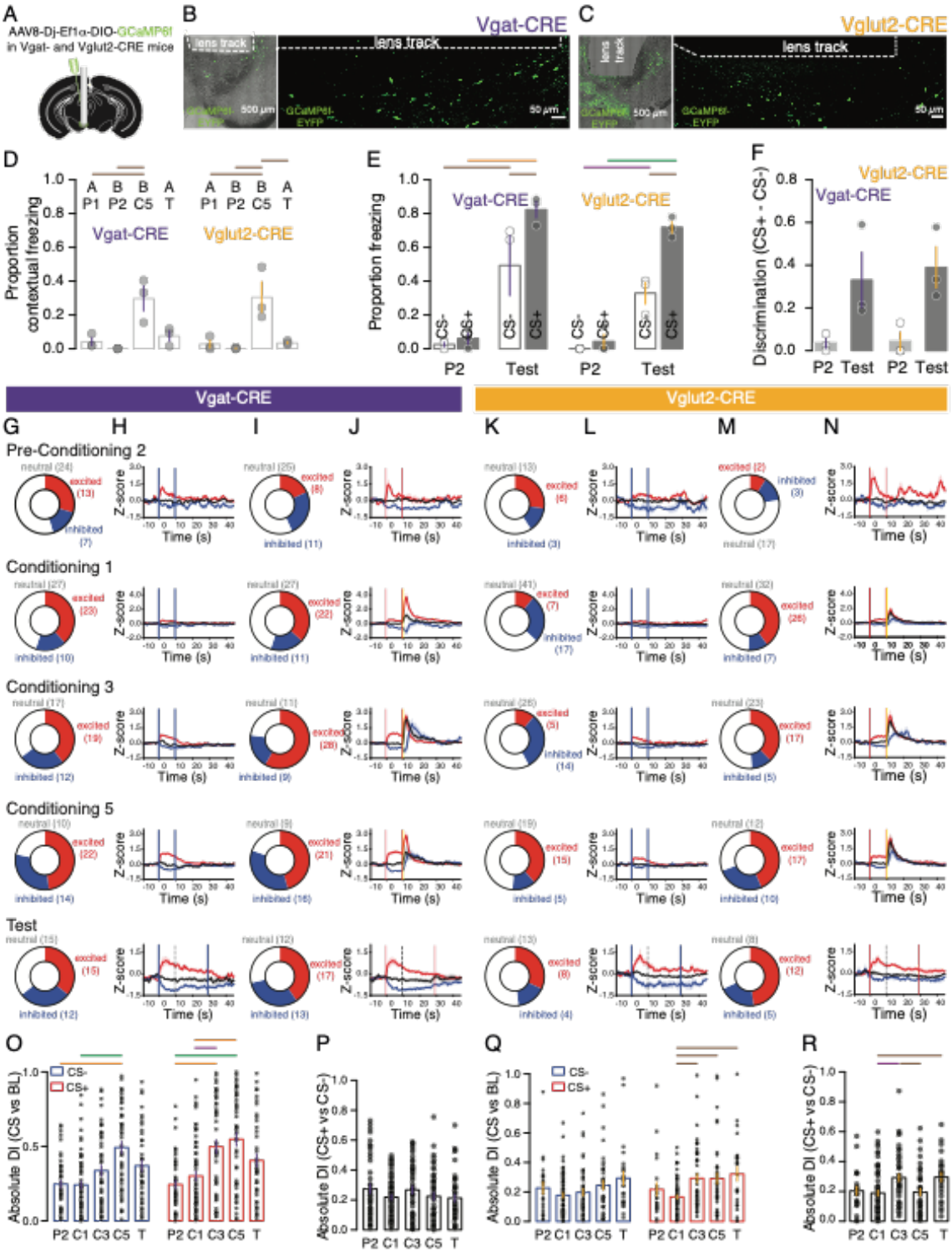

Figure 6: lVTA Vgat- and Vglut2-expressing neurons encode auditory cues but only Vglut2- positive cells learn to discriminate between fear predictive and neutral cues"

(A) Stereotaxic injection of AAV8-Dj-Ef1α-DIO-GCaMP6f in the lVTA of either Vgat- or Vglut2-CRE mice, followed by the implantation of a GRIN lens.

(B) Example confocal image of a coronal lVTA-containing section showing the infected area prepared from Vgat-CRE mice and the tract left behind by the GRIN lens (left) and the high magnification confocal image immediately below the lens track (right).

(C) Example low (left) and high (right) magnification confocal image of the infection and lens track (same as Fig 6B) in brain slices prepared from Vglut2-CRE mice.

(D) Bar graph of the average proportion of contextual freezing during P1, P2, C5 and T days in Vgat-CRE (purple, left) and Vglut2-CRE (orange, right) mice.

(E) Bar graph reporting the average proportion of freezing during the presentation of CS- and CS+ on P2 and T days for both mouse groups.

(F) Bar graph for the difference in freezing between CS+ and CS- on P2 and T days.

(G) Pie-chart quantifications of all recorded lVTA Vgat-expressing cells to CS- during P2, C1, C3, C5 and T days. The excited, inhibited and and non-responsive neurons are depicted in red, blue and white/grey; respectively.

(H) Z-score curves of the average calcium transients (SEM shaded) of characterized Vgat-positive cells at the CS- (vertical blue bars) presentation on the P2, C1, C3, C5 and T days. The vertical black dashed line depicts the end of the time window used for response classification on the test day.

(I) Pie-chart quantifications of all recorded Vgat-expressing cells to CS+ during P2, C1, C3, C5 and T days.

(J) Z-score curves of the average calcium transients (SEM shaded) of characterized Vgat-expressing cells at the CS+ (vertical red bars) presentation on the P2, C1, C3, C5 and T days. The FS applied immediately after the termination of CS+ on C1, C3, and C5 are depicted by the yellow bar.

(K) Pie-chart quantifications of all recorded lVTA Vglut2-expressing cells to CS- during P2, C1, C3, C5 and T days.

(L) Z-score curves of the average calcium transients (SEM shaded) of characterized Vglut2- positive cells at the CS- presentation on the P2, C1, C3, C5 and T days.

(M) Pie-chart quantifications of all Vglut2- expressing cells to CS+ during P2, C1, C3, C5 and T days.

(N) Z-score curves of the average calcium transients (SEM shaded) of characterized Vglut2-positive cells at the CS+ presentation on the P2, C1, C3, C5 and T days.

(O) Absolute discrimination index for CS- or CS+ as compared to baseline calcium activity on P2, C1, C3, C5 and T days for all recorded lVTA Vgat-expressing cells.

(P) Absolute discrimination index between CS- and CS+ on P2, C1, C3, C5 and T days for all recorded Vgat- expressing cells.

(Q) Absolute discrimination index for each tone as compared to baseline calcium activity on P2, C1, C3, C5 and T days for all recorded lVTA Vglut2-expressing cells.

(R) Absolute discrimination index between CS- and CS+ on P2, C1, C3, C5 and Tdays for all Vglut2- positive cells.

42-60 cells (Vgat-CRE) and 22-65 cells (Vglut2-CRE) from 3 mice each.

Data are represented as mean +/- SEM. *p<0.05, **p<0.01, ***p<0.001, ****p<0.0001.

See also Figure S4, S5 and Videos S5 and S6, as well as Excel Table S1.

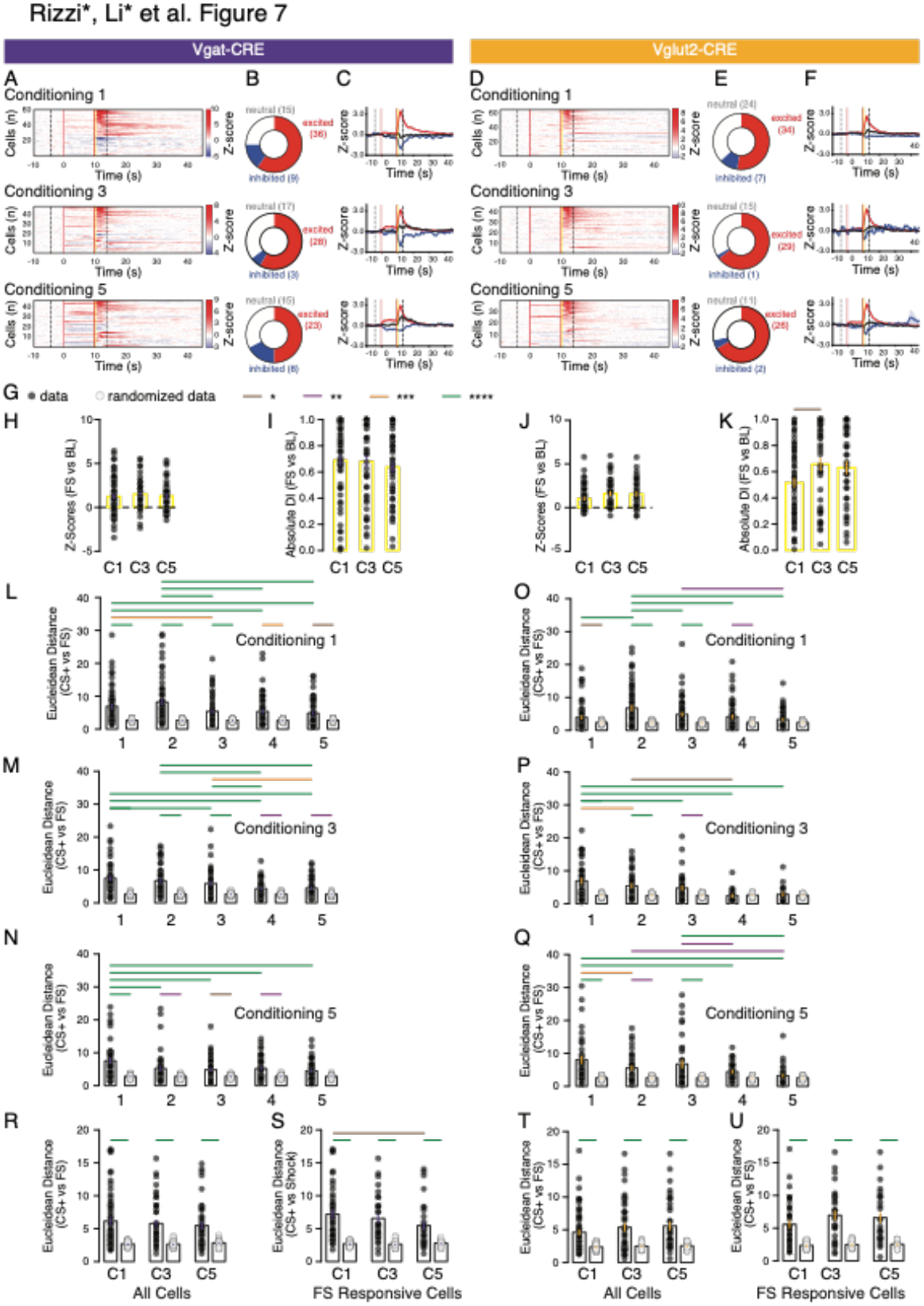
Rizzi*, Li* et al. Figure 7
Vgat-CRE
Vglut2-CRE
Conditioning 1
Conditioning 3
Conditioning 5
Cells (n)
Z-score
Time (s)
neutral (15)
excited (36)
inhibited (9)
neutral (17)
excited (28)
inhibited (3)
neutral (15)
excited (23)
inhibited (8)
neutral (24)
excited (34)
inhibited (7)
neutral (15)
excited (29)
inhibited (1)
neutral (11)
excited (26)
inhibited (2)
data
randomized data
Z-Scores (FS vs BL)
Absolute DI (FS vs BL)
C1 C3 C5
Euclidean Distance (CS+ vs FS)
Euclidean Distance (CS+ vs Shock)
All Cells
FS Responsive Cells

Figure 7: Lateral VTA Vgat- and Vglut2- expressing cells are both sensitive to FS but only Vgat- positive cells consolidate the association between FS and predictive auditory cues.

(A) Z-score heatmaps of average calcium transients of individual Vgat-expressing cells at the presentation of CS+ followed by the FS (start depicted by the vertical yellow bar) on C1, C3 and C5 days. The black dashed lines depict the start (related to baseline) and end (related to FS) of the 4 sec time windows used for response classification.

(B) Pie-chart quantifications of all Vgat-positive cells to the FS on C1, C3 and C5 days. The excited, inhibited and and non-responsive neurons are depicted in red, blue and white/grey; respectively.

(C) Z-score average curves of the calcium transients (SEM shaded) of characterized Vgat-expressing cells at the FS presentation on C1, C3 and C5 days.

(D) Z-score heatmaps of average calcium transients of individual Vglut2-expressing cells at the presentation of CS+ followed by the FS.

(E) Pie-chart quantifications of all Vglut2-positive cells-based FS responsivity on C1, C3 and C5 days.

(F) Z-score average curves of the calcium transients (SEM shaded) of characterized Vglut2-expressing cells surrounding the FS presentation on C1, C3 and C5 days.

(G) Key for statistical comparisons and data sets in H-U. *$p<0.05$, **$p<0.01$, ***$p<0.001$, ****$p<0.0001$.

(H) Z-score of FS responses in recorded Vgat-expressing cells on C1, C3 and C5 days.

(I) Absolute discrimination index of Vgat-positive cells to FS across days.

(J) Z-score of the FS responses in Vglut2-expressing cells on C1, C3 and C5 days.

(K) Absolute discrimination index of Vglut2-positive cells to FS.

(L) Similarity index measured as Euclidean distance between the distribution of calcium activity 4 sec after CS+ presentation and 4 sec after FS presentation across the 5 CS+/FS pair presentation (1 to 5) during C1 in Vgat-positive cells.

(M) Euclidean distance between CS+ and FS responses of Vgat-expressing cell responses within C3.

(N) Eucleidean distance between CS+ and FS responses in recorded Vgat-positive cells throughout C5.

(O) Eucleidean distance between CS+ and FS responses in recorded Vglut2-expressing cells throughout C1.
(P) Eucleidean distance between CS+ and FS responses in Vglut2-positive cells during C3.
(Q) Eucleidean distance between CS+ and FS responses in Vglut2-expressing cells on C5.
(R) Euclidean distance between CS+ and shock responses in all Vgat- positive cells across days (C1, C3 and C5 days) and compared to randomized data points of the baseline calcium activity.
(S) Euclidean distance between CS+ and FS responses in Vgat-FS responsive cells across days (C1, C3 and C5 days) as compared to bootstrapped data.
(T) Euclidean distance between CS+ and FS responses in all recorded Vglut2- cells across days (C1, C3 and C5 days) as compared to randomized data.
(U) Euclidean distance between CS+ and FS responses in Vglut2-FS responsive cells across days (C1, C3 and C5 days) as compared to bootstrapped data.
Data are represented as mean +/- SEM.
See also Excel Table S1.

STAR Methods

RESOURCE AVAILABILITY

Lead Contact

Further information and requests for resources and reagents should be directed to and will fulfilled by the lead contact, Dr. Kelly Tan (kelly.tan@unibas.ch).

Materials Availability

This study did not generate new unique reagents.

Data and Code Availability

All data generated and codes created during the current study are available from the lead contact upon reasonable request.

EXPERIMENTAL MODEL AND SUBJECT DETAILS

Adult (6-10 weeks old at the start of experimentation) male and female ChAT-CRE (B6;129S6-Chat<tm2(cre)Lowl>/J,JAX),Vglut2-Cre (B6.Cg-Slc17a6<tm2(cre)Lowl>Unc/J, UNC/JAX), Vgat-Cre (B6.Cg-Slc32a1<tm2(cre)Lowl>/J, JAX), and wildtype (WT) C57BL/6 mice were bred and genotyped in-house. Animals were housed in temperature-controlled facilities under a 12-hour light/dark cycle (7am to 7pm light) with food and water provided *ad libitum*. All experimental procedures were approved by the Institutional Animal Care Office of the University of Basel and the Cantonal Veterinary Office under the License Number 2742.

METHOD DETAILS

Surgery

General: Mice were anesthetized with Isoflurane (5% for induction and 1.5% for maintenance) in O_2 (Provet/Primal Healthcare, EZ Anesthesia Systems) and placed onto the stereotaxic frame (World Precision Instruments). Lidocaine (0.2mg/kg) (Steuli Pharma) was injected subcutaneously above the skull. The skin was disinfected with 70% ethanol and Betadine (Mundipharma) before drilling a hole above the target area

and specific constructs were injected into the target areas using a piston operated injector (Narishige). Optic fiber and gradient-index lens implantation were carried out after injection during the same surgical session to minimize the stress to the animals. After surgical interventions, in cases of anatomical mapping or *in vitro* patch-clamp recording investigations, mice were stitched with tissue absorptive silk sutures (SABANA) and provided with temporary silicone (Smooth-On). When a GRIN-lens was implanted, a fixed headcap was built from layers consisting of super-glue (Cyberbond) and UV-light curable glue (Loctite), then secured to the skin with Vetbond tissue adhesive glue (3M). Finally, when optic fibers were implanted, super-glue and dental cement (Lang) were used to secure them to the skull via small screws. Buprenorphine (Reckitt Benckiser) pain killers were administered (0.1g/kg) post-surgery as needed.

Optogenetic manipulations: Young adult male and female (6-8 weeks) Vgat- and Vglut2- positive mice and their CRE-negative littermates were operated on as described above, to express a CRE-dependent opsin construct (AAV5-Ef1α-DIO-eArch3.0-EYFP or AAV5-Ef1α-DIO-ChR2-H134R-EYFP, UNC Vector Core) bilaterally (150nl/side) in the lVTA (-3.1mm from the Bregma, ± 0.5mm to the midline, and 4.25mm below the surface of the brain) and to place optic fibers (>70% light transmittance, 200*μ*m diameter 0.39NA optic fibers fixed by epoxy to 1.25mm wide 6.4mm long ceramic ferrules, Thorlabs, Sparta et al., 2012) bilaterally above either the parafasicular thalamic nucleus (Pf, -2.3mm from the Bregma, ±1.15mm to the midline, and 3mm below the surface of the brain, 5 degrees away from the vertical axis) or the dorsal striatum (DMS, +0.65mm from the Bregma, ± 1.7mm to the midline, and 2.5mm).

Calcium Imaging: Adult male and female (8-10 weeks) WT mice were surgically operated on as described above, to express a virus containing calcium indicators (in WT mice: AAV1.CaMk2a.GCaMP6m.WPRE.SV40, Ready to Image Inscopix virus and in Vgat- and Vglut2-CRE mice : AAVdj/8.hEf1A.GCaMP6f.WPRE.bGHp, Zurich Viral Core Facility) unilaterally (200nl) in between the VTA and the SN (15 degree angle, -3.1mm from the Bregma, ± 0.8mm to the midline, and 4.25mm below the surface of the brain) and to place a 600-μm-diameter (7.3mm long) or 1000-μm-diameter (9mm long) gradient refractive index (GRIN) lens (Inscopix) at the same coordinates, guided by a

sterile needle. The lens was then secured with UV-light curable glue (Henkel). A custom-made head bar (2cm long, 0.4cm wide, 0.1cm tall) was placed and together fixed with the GRIN lens to the brain with a combination of super-glue (Cyberbond) and dental cement (Lang). Lens clearing was assessed 4-8 weeks post infection. Mice were restrained by the implanted head bars to a fixed plexiglass running wheel (15cm diameter) and a baseplate attached miniaturized microscope (miniscope) suited for the nVoke2 system (Inscopix) was lowered to the GRIN lens until the best focal plane has been reached. Once the conditions were visually determined to be satisfactory, the mice were placed under Isoflurane anesthesia on a stereotaxic frame and the baseplate was secured to the headcap. The GRIN lens is held in place using a UV-light curable flowable composite glue (Kerr).

Anatomical mapping

Rabies tracing: To map the monosynaptic inputs onto DMS-CINs neurons, the avian receptor restricted replication depleted modified rabies system was used (Leinweber et al., 2017). Adult ChAT-CRE mice were first injected bilaterally (300nl/side) with the CRE dependent helper virus for the monosynaptic retrograde rabies system, AAV2/1-Ef1α-DIO-TVA920-T2A-CVS11G (FMI) into the DMS, followed by EnvA-SADG-GCaMP6s into the same site three days later. The animals were sacrificed after ten days. Mice were injected intraperitoneally (ip) with pentobarbital (0.3mg/kg) (Esconarkon, Steuli Pharama AG) diluted in sterile saline and transcardially perfused with 1X phosphate buffered saline buffer (PBS) and 4% paraformaldehyde (PFA) (Sigma Aldrich) solution prepared in 1X PBS. Brains were extracted, post-fixed in 4% PFA in 1X PBS overnight, and then immersed in 30% sucrose in 1X PBS for at least 2 days. Sections were prepared (60 m) using a cryostat (Leica 1950 CM) and mounted for confocal imaging.

Anterograde tracing: To map the projections of lVTA GABAergic and glutamatergic neurons to the DMS-CINs neurons and to the Pf, Vgat- and Vglut2-CRE were injected with the CRE-dependent fluorescent construct (AAV2/1-phSyn1-FLEX-tdTomato-T2A-SypEGFP, Salk Institute) between the VTA and the SN. The CRE expressing infected cells and their processes are labeled with tdTomato and their presynaptic terminals

with EGFP. The animals were sacrificed after 4 to 6 weeks. Brain sections were prepared as mentioned above.

Retrobeads tracing: To validate the projection of the Pf to the DMS, red fluorescent microspheres (RetroBeads, Lumafluor) were injected bilaterally (150nl/side) into the DMS of adult WT mice. They were sacrificed after 10 days of expression and brain sections prepared as described above.

***In vitro* electrophysiology.** Acute coronal slices (200μm) containing the lVTA, the DMS or the Pf were prepared using a vibrotome (Leica VT1200S) in iced-cold cutting solution (in mM: NMDG 92, KCl 2.5, NaHPO4 1.25, $NaHCO_3$ 30, HEPES 20, Glucose 25, Thiourea 2, Na-Ascorbate 5, Na-Pyruvate 3, MgSO4.7H2O 10, $CaCl_2$.4H2O 0.5, and N-acetyl Cystein 10, pH 7.3, Osmolarity 290-300 mOsm). Slices were incubated in ACSF solution (in mM: NaCl 92, KCl 2.5, NaH2PO4 1.25, NaHCO3 30, HEPES 20, Glucose 25, Thiourea 2, Na-ascorbate 5, Na-Pyruvate 3, MgSO4.7H_2O 2, $CaCl_2$.4H20 2, pH 7.3, Osmolarity 290-300 mOsm) at 31^oC. Slices were then transferred to the recording chamber, super-fused with Ringer's solution (in mM: NaCl 119, KCl 2.5, NaH2PO4 1.25, NaHCO3 24, Glucose 12.5, CaCl2.4H2O 2 and MgSO4.7H2O, pH 7.3 Osmolarity 290-300 mOsm) at 2ml/min bubbled with 95% O_2 and 5% CO_2. Neurons were visualized with an infrared (IR) camera on an Olympus scope U-TV1X-2 and whole cell patch clamp recordings (multiclamp 700B amplifier) were performed. The internal solutions for voltage clamp recordings contained (in mM excitatory transmission: KGluconate 140, Creatine Phosphate 10, $MgCl_2$ 2, KCl 5, Na_2ATP 4, Na_3GTP 0.3, HEPES 10 and EGTA 0.2, pH 7.3, osmolarity 300 and for inhibitory transmission: KGluconate 30, KCl 100, Creatin Phosphate 10, MgCl2 4, Na2ATP 3.4, Na3GTP 0.1, EGTA 1.1 and HEPES 5, pH7.3, osmolarity 289) and for current clamp recordings contained (in mM: KGluconate 130, Creatin Phosphate 10, MgCl2 4, Na2ATP 3.4, Na3GTP 0.1, EGTA 1.1 and HEPES 5, pH7.3, osmolarity 289).
ChR2 stimulation was done with 2 pulses of 5msec 473nm blue light, 50msec apart with a Cool-LED pE-100 mounted on the microscope. Picrotoxin (PTX) was used at 100μM, kynureic acid (KA) at 2mM, TetrodoToxin (TTX) at 500nM and 4-amino pyridine (AP) at 300μm.

Histology

Immunohistochemistry: IVTA or DMS-containing slices were washed (3x3 mins) with 1X Tris-buffered saline (TBS) with 0.1% Tween-20 (Sigma Aldrich), permeabilized (20mins) with 1X TBS with 0.1% Tween-20 and Triton-X100 (Sigma Aldrich), blocked (120 mins) with 1% Bovine Serum Albumin (Sigma Aldrich) in 1X TBS with 0.1% Tween-20, stained overnight with the primary antibody (Rabbit anti-TH, Sigma Aldrich T8700, 1:500 or Goat anti-ChAT, EMD Millipore AB144P, 1:200), washed, stained (120 minutes) with the secondary antibody (Goat anti-Rabbit conjugated to AlexaFlour555, Invitrogen A21429, 1:500 or Donkey anti-Goat conjugated to AlexaFlour647, abcam ab150131, 1:500), washed, mounted on glass slides (Superfrost Plus, Thermo Scientific), immersed by DAPI containing ProLong Gold Antifade mounting solution (Invitrogen) and covered with borosilicate cover glass (VWR).

Fluorescent in situ hybridization (FISH): Adult male and female wildtype C57BL/6 mice were anesthetized with pentobarbital (0.3mg/kg) (Esconarkon, Steuli Pharama AG). Brain were extracted and quickly frozen on aluminum foil over dry ice. Brains were kept overnight at -80^{o}C. Thin 20μm fresh frozen brain sections containing the IVTA were manually prepared with the aid of a cryostat and placed onto glass slides. Selected slices were fixed for 30 minutes using 4% PFA in 1X PBS, dehydrated with increasing concentrations of ethanol (50%, 70%, 100%, 100%), surrounded by hydrophobic barriers (ImmEdge, Vector Laboratories), before proceeding with the RNAscope Fluorescent Multiplex (ACD, Biotechne) Assay to label the mRNAs for tyrosine hydroxylase (TH, ref 317621), vesicular glutamate transporter-2 (Vglut2, Slc17a6, ref 319171), CaMK2a (ref 445231), and vesicular GABA transporter (Vgat, Slc32a1, ref 319191). Processed slides were immersed in ProLong Diamond Antifade mounting solution (Invitrogen) and covered with borosilicate cover glass.

Brain clearing: To visualize the monosynaptic inputs onto DMS-CINs in 3-dimensions, a modified CUBIC-L/RA (clear, unobstructed brain imaging cocktails and computational analysis) brain clearing method (Tainaka et al., 2018) was utilized. Anatomically labeled mice were similarly transcardially perfused as described above. Immediately

after perfusion, brains were washed in shaking cold (4°C) 1X PBS (3x3 mins) before being post-fixed in 4% PFA in 1X PBS under refrigeration (4°C) for 48 hours. Fixed brains were split sagittally along the midline and individually submerged into an eppendorf tube (5ml) filled with pre-heated (to 37 °C) CUBIC-L solution (10% w/w N-butyldiethanolamine, 10%w/w triton X-100, in H_2O, Sigma Aldrich) and kept at 37 °C under continuous shaking. CUBIC-L solutions were refreshed every 5 days until the sample is cleared (~10 days). The cleared hemispheres were then transferred to CUBIC-RA solution (45% w/w antipyrine, 30%w/w N-methylnicotinamide, in H_2O, Sigma Aldrich, refractive index=1.5) and again kept at 37°C under continuous shaking, with the CUBIC-RA solution being refreshed every 2 days until the hemispheres is completely transparent (~ 4 days).

Microscopy

Confocal Imaging: To visualize fluorescent labeling of markers in brain sections, glass mounted brain sections were imaged with a Zeiss LSM700/800 upright confocal microscope with the ZEN Black image acquisition software (v2010, Zeiss), using the PLAN APO 20X objectives (0.8 NA, air) with the fixed wavelength 405nm, 488nm, 555nm, and 639nm lasers. Images were stitched with the acquisition software, further post-processed in FIJI (v2.0.0), and quantifications were conducted by experienced experimenters using the Adobe Illustrator (v2018).

Lightsheet Imaging: To visualize 3-D cleared hemispheres with monosynaptic inputs onto DMS ChAT neurons, CUBIC-L/RA processed anatomically labelled hemispheres were placed in a Zeiss Z1 lightsheet microscope with a PLAN APO 5X objective (0.16 NA, air) and the fixed wavelength 488nm and 561nm lasers to detect the fluorescently labeled mapping and autofluorescence respectively. The samples were imaged with a mounted PCO sCMOS camera in full frame (1920x1920 pixels) with an optical thickness of 12μm and exposure time of 200ms using the ZEN Black image acquisition software (v2010, Zeiss). The images were then first post-processed, fused at maximal intensity with Zen Lightsheet (Zeiss), stitched and visualized using the Arivis Vision 4D (v3.01, Arivis).

Behavior

Fear conditioning: Mice were individually handled (5mins per day for 3 consecutive days) to habituate them to the experimenter. In the subsequent days following the last handling day, mice were trained (1 session/day) for 5 consecutive days. The animals were then placed into a plexiglass walled box (20cm wide, 22.5 cm long, 11.5cm tall) with an electrical gridded floor (Med Associates Inc) covered with black stripes (context A). Beddings were placed below. The bedding was replaced in between each animal and the box was cleaned between each animal with 70% ethanol. During each training session, the baseline contextual freezing activity was recorded for 2 minutes. Then 5 presentations of auditory conditioned stimulus (85dB, 7 or 12 kHz, counterbalanced) paired to an immediate 2s electric (0.6mA) shock (CS+) or without (CS-) each were presented for 10s in a randomized order, separated by a randomized inter-trial interval (ITI) with a duration between 50 and 150s. The animals were tested in the subsequent day following the last training day. They were placed into another plexiglass walled box (20cm wide, 25cm long, 15cm tall) covered with black polka-dots (context B) and cleaned with 1% acetic acid between each animal. The baseline contextual freezing to the new environment was also recorded for 2 minutes, following which, 4 instances of CS- and 4 of CS+ tones (85dB, 30s) were presented in sequential order separated with a randomized ITI with a duration between 70 and 130s.

Videos were captured by a camera (The Imaging Source) from above at a fixed sampling rate (10Hz) and recorded mice were tracked with a behavioral acquisition and analysis software ANYMAZE (v5.23, Stoeling) that also controlled the delivery of tones (with Logitech speakers) and electric shocks (Med Associates Inc shock delivery box) with the TTL (time to live)-based master control box.

Freezing episodes lasting more than 1s were detected with the acquisition software and visually confirmed. The resulting freezing values and the timestamps of the CS presentations were exported.

Optogenetic manipulations: During the training days, animals were restrained and the protruding optic fibers were bilaterally connected to custom-made optic cables (Thorlabs) that were connected via a commutator (Doric) to a 532-nm laser source (SUNON). The lasers are controlled by the behavioral acquisition software via a TTL

master box that also controls the presentation of auditory tones and the delivery of electric shocks. The laser power was measured using the power meter (Thorlabs PM100A) and individually adjusted for each animal such that the power emitted from the optic fiber reaches 10mW. The lasers were turned ON continuously during the CS+ tone presentation throughout all five training days in both the control and experimental groups.

Calcium Imaging: On each day of behavioral experimentation, the miniscope mounted mouse was placed in the behavioral chamber and the lVTA calcium transients were recorded continuously with the nVoke2 (Inscopix) at a 20Hz sampling rate. The acquisition software ANYMAZE (Stoeling) captures the behavioral movements of the recorded mouse with a camera (The Imaging Source) and simultaneously controls the presentation of auditory tones and the delivery of the electric shocks. Parameters such as the LED-power, the gain, and the electronic focus were adjusted on a mouse-to-mouse basis. The alignment of these recordings was made possible by a set of TTL triggers that were delivered by the behavioral acquisition software at the start and the end of the fear conditioning paradigm to the calcium imaging acquisition source. The behavioral paradigm included two pre-training sessions over two days where mice were presented to the contexts and tones in order to record a baseline activity to these cues. The mice were assessed for baseline contextual activity (context B in pre-training day 1 and context A in pre-training day 2) for 5 minutes and then to the two tones (30 seconds in pre-training day 1 and 10 seconds in pre-training day 2) three times each in a randomized order separated with a randomized ITI (between 50 and 150s in pre-training day 1 and between 70 and 130s in the pre-training day 2). In the day following the last pre-training day, the discriminative auditory cued fear conditioning paradigm was run as described previously with the exception that the CS- tone was pre-defined as the 7kHz tone and the CS+ tone pre-defined as the 12kHz tone. In addition to the resulting freezing values throughout the behavioral experimentation and the timestamps of the CS presentations, the recorded calcium transients (F/F) with respect to time were exported.

Analysis

Freezing: The proportion of time mice spent freezing during the baseline contextual condition or during tone presentations were analyzed using custom-written Matlab (v2018b, Mathworks) scripts and visually verified. Statistical comparisons in the proportion of freezing between the control and experimental groups and/or across experimental days were made and plotted using Prism (v8.2.1, GraphPad).

Calcium Imaging: Acquired calcium transients from the nVoke2 were first processed in the Inscopix Data Processing Software (IDPS, Inscopix), where the traces were pre-processed, spatially filtered, and motion corrected. Individuals cells were identified using the principle component (PCA) and independent component (ICA) analyses with no spatial or temporal down-sampling. Manual ROIs were used when the identification of cells with PCA/ICA analyses were suboptimal. Different ROIs were analysed across days. Cells were visually verified by their maximal intensity projection visualizations and the placement of the region of interest (ROI) in these visualizations. Traces with abnormal physiological calcium transients (ie; transients lasting over minutes) were excluded. Time-stamped traces were exported to Matlab (v2018b, Mathworks), where custom-written scripts were used from there onwards. Calcium transients were first standardized (per trace per day), aligned to the presentation of external stimuli (tones, FS) and then binned (500ms bins). Calcium activity surrounding the onset of tones (CS+ or CS-) were extracted (10s before and 45s after) and normalized to the baseline window (10s before tone onset). Average traces were generated and the average transients during the baseline period before the tone onset (10s) were compared to the initial period of tone presentation (also 10s). Cells were characterized either as excited (Wilcoxon rank-sum test $p < 0.01$ and mean delta z-score > 0), inhibited (Wilcoxon rank-sum test $p < 0.01$ and mean delta z-score < 0), or nonresponsive (Wilcoxon rank-sum test $p > 0.01$). Shock responsive cells were characterized in the same manner by comparing the calcium activity 4s before CS+ presentation and 4s after the onset of the FS. To investigate the responsiveness of the overall population activity of Vgat- and Vglut2- expressing lVTA cells to the auditory cues and FS throughout the fear conditioning paradigm, an average trace of all recorded cells within each recording session was generated and comparisons were made as described above.

To examine whether cells could discriminate the presence of cues (CS-, CS+, or shock) or between cues (such as CS- from CS+), receiver operating characteristic analysis were used to calculate a discrimination index (DI, DI = (Area Under the ROC Curve – 0.5) x 2) from the distribution of activity during either cue presentation and during the corresponding baseline or from the distribution of activity during CS- presentation and the distribution of activity during CS+ presentation, respectively.

To investigate whether the calcium activity pattern during the CS+ presentation is shaped towards the activity pattern of its paired aversive stimulus (shock), Euclidean distance (ED) as a measure of similarity is used and is calculated from the distribution of activity during first 4s of CS+ presentation and 4s following the shock onset for each pair across the training days. The onset of the shock was randomly shuffled across the trace 1000 times and an average randomized ED is generated for each CS+/shock pairing per trace. Comparisons were made between the data-driven CS+/shock ED and randomized data-driven CS+/shock ED within and across training days.

QUANTIFICATION AND STATISTICAL ANALYSIS

Statistical comparisons for the proportion of time spent freezing across days in the baseline contextual period or during tone presentations across different control and experimental groups were conducted with two-way analysis of variance (ANOVA) with multiple comparisons analyses following Bonferroni's corrections. Comparisons between behavioral discrimination to aversive paired and non-paired tones between control and experimental groups were done using unpaired t-tests. Comparisons for contextual freezing across days in the calcium imaging animals were tested with the one-way ANOVA with Bonferroni's multiple comparisons tests. Comparisons between cued freezing across days were made with two-way ANOVA with Bonferroni's multiple comparisons tests. Behavioral discrimination across days in these animals were made with paired t-tests. In the analysis of the calcium imaging data, the comparison between calcium transients during tone or FS presentations and time periods before were made with the Wilcoxon rank-sum test (significance level = 0.01). Comparisons between cue responses and DI across days were tested with the Kruskal-Wallis test with post-hoc Dunn's multiple comparisons analyses. Within-day comparisons were made with Wilcoxon matched pairs signed-rank test. To examine the changes in the Euclidean

distance between CS+ and FS pairings within and across conditioning days, the data sets (do not meet the normality assumption as tested by the Shapiro-Wilk test but are lognormal verified by the same test) were first log-transformed and then tested with two-way ANOVA with multiple comparisons analyses following Bonferroni's corrections. The significance level unless otherwise noted is set at 0.05.

References:

Aosaki, T., Tsubokawa, H., Ishida, A., Watanabe, K., Graybiel, A.M., and Kimura, M. (1994). Responses of tonically active neurons in the primate's striatum undergo systematic changes during behavioral sensorimotor conditioning. Journal of Neuroscience *14*, 3969–3984.

Apicella, P. (2002). Tonically active neurons in the primate striatum and their role in the processing of information about motivationally relevant events. European Journal of Neuroscience *16*, 2017–2026.

Apicella, P., Legallet, E., and Trouche, E. (1997). Responses of tonically discharging neurons in the monkey striatum to primary rewards delivered during different behavioral states. Exp Brain Res *116*, 456–466.

Bennett, B.D., Callaway, J.C., and Wilson, C.J. (2000). Intrinsic Membrane Properties Underlying Spontaneous Tonic Firing in Neostriatal Cholinergic Interneurons. J. Neurosci. *20*, 8493–8503.

Brown, M.T.C., Tan, K.R., O'Connor, E.C., Nikonenko, I., Muller, D., and Lüscher, C. (2012). Ventral tegmental area GABA projections pause accumbal cholinergic interneurons to enhance associative learning. Nature *492*, 452–456.

Cai, Y., and Ford, C.P. (2018). Dopamine Cells Differentially Regulate Striatal Cholinergic Transmission across Regions through Corelease of Dopamine and Glutamate. Cell Rep *25*, 3148-3157.e3.

Chuhma, N., Zhang, H., Masson, J., Zhuang, X., Sulzer, D., Hen, R., and Rayport, S. (2004). Dopamine neurons mediate a fast excitatory signal via their glutamatergic synapses. J. Neurosci. *24*, 972–981.

Chuhma, N., Mingote, S., Moore, H., and Rayport, S. (2014). Dopamine neurons control striatal cholinergic neurons via regionally heterogeneous dopamine and glutamate signaling. Neuron *81*, 901–912.

Cohen, J.Y., Haesler, S., Vong, L., Lowell, B.B., and Uchida, N. (2012). Neuron-type-specific signals for reward and punishment in the ventral tegmental area. Nature *482*, 85–88.

Ding, J., Peterson, J.D., and Surmeier, D.J. (2008). Corticostriatal and Thalamostriatal Synapses Have Distinctive Properties. Journal of Neuroscience *28*, 6483–6492.

Doig, N.M., Magill, P.J., Apicella, P., Bolam, J.P., and Sharott, A. (2014). Cortical and thalamic excitation mediate the multiphasic responses of striatal cholinergic interneurons to motivationally salient stimuli. J. Neurosci. *34*, 3101–3117.

Ghosh, K.K., Burns, L.D., Cocker, E.D., Nimmerjahn, A., Ziv, Y., Gamal, A.E., and Schnitzer, M.J. (2011). Miniaturized integration of a fluorescence microscope. Nat Methods *8*, 871–878.

Grewe, B.F., Gründemann, J., Kitch, L.J., Lecoq, J.A., Parker, J.G., Marshall, J.D., Larkin, M.C., Jercog, P.E., Grenier, F., Li, J.Z., et al. (2017). Neural ensemble dynamics underlying a long-term associative memory. Nature *543*, 670–675.

de Jong, J.W., Afjei, S.A., Pollak Dorocic, I., Peck, J.R., Liu, C., Kim, C.K., Tian, L., Deisseroth, K., and Lammel, S. (2019). A Neural Circuit Mechanism for Encoding Aversive Stimuli in the Mesolimbic Dopamine System. Neuron *101*, 133-151.e7.

Kawaguchi, Y., Aosaki, T., and Kubota, Y. (1997). Cholinergic and GABAergic interneurons in the striatum. Nihon Shinkei Seishin Yakurigaku Zasshi *17*, 87–90.

Klug, J.R., Engelhardt, M.D., Cadman, C.N., Li, H., Smith, J.B., Ayala, S., Williams, E.W., Hoffman, H., and Jin, X. (2018). Differential inputs to striatal cholinergic and parvalbumin interneurons imply functional distinctions. Elife *7*.

Lapper, S.R., and Bolam, J.P. (1992). Input from the frontal cortex and the parafascicular nucleus to cholinergic interneurons in the dorsal striatum of the rat. Neuroscience *51*, 533–545.

Leinweber, M., Ward, D.R., Sobczak, J.M., Attinger, A., and Keller, G.B. (2017). A Sensorimotor Circuit in Mouse Cortex for Visual Flow Predictions. Neuron *95*, 1420-1432.e5.

Matsumoto, N., Minamimoto, T., Graybiel, A.M., and Kimura, M. (2001). Neurons in the thalamic CM-Pf complex supply striatal neurons with information about behaviorally significant sensory events. Journal of Neurophysiology *85*, 960–976.

Morales, M., and Margolis, E.B. (2017). Ventral tegmental area: cellular heterogeneity, connectivity and behaviour. Nat. Rev. Neurosci. *18*, 73–85.

Petreanu, L., Huber, D., Sobczyk, A., and Svoboda, K. (2007). Channelrhodopsin-2-assisted circuit mapping of long-range callosal projections. (Nature Publishing Group).

Reynolds, J.N.J., and Wickens, J.R. (2004). The corticostriatal input to giant aspiny interneurons in the rat: a candidate pathway for synchronising the response to reward-related cues. Brain Res. *1011*, 115–128.

Root, D.H., Mejias-Aponte, C.A., Qi, J., and Morales, M. (2014). Role of glutamatergic projections from ventral tegmental area to lateral habenula in aversive conditioning. J. Neurosci. *34*, 13906–13910.

Root, D.H., Barker, D.J., Estrin, D.J., Miranda-Barrientos, J.A., Liu, B., Zhang, S., Wang, H.-L., Vautier, F., Ramakrishnan, C., Kim, Y.S., et al. (2020). Distinct Signaling by Ventral Tegmental Area Glutamate, GABA, and Combinatorial Glutamate-GABA Neurons in Motivated Behavior. Cell Rep *32*, 108094.

Schultz, W. (2017). Reward prediction error. Curr. Biol. *27*, R369–R371.

Schultz, W., Dayan, P., and Montague, P.R. (1997). A neural substrate of prediction and reward. Science *275*, 1593–1599.

Sparta DR, Stamatakis AM, Phillips JL, Hovelsø N, van Zessen R, Stuber GD. (2012). Construction of implantable optical fibers for long-term optogenetic manipulation of neural circuits. Nat Protoc. *7,* 12-23.

Stamatakis, A.M., Jennings, J.H., Ung, R.L., Blair, G.A., Weinberg, R.J., Neve, R.L., Boyce, F., Mattis, J., Ramakrishnan, C., Deisseroth, K., et al. (2013). A Unique Population of Ventral Tegmental Area Neurons Inhibits the Lateral Habenula to Promote Reward. Neuron *80*, 1039–1053.

Tainaka, K., Murakami, T.C., Susaki, E.A., Shimizu, C., Saito, R., Takahashi, K., Hayashi-Takagi, A., Sekiya, H., Arima, Y., Nojima, S., et al. (2018). Chemical Landscape for Tissue Clearing Based on Hydrophilic Reagents. Cell Rep *24*, 2196-2210.e9.

Tan, K.R., Yvon, C., Turiault, M., Mirzabekov, J.J., Doehner, J., Labouèbe, G., Deisseroth, K., Tye, K.M., and Lüscher, C. (2012). GABA neurons of the VTA drive conditioned place aversion. Neuron *73*, 1173–1183.

Tritsch, N.X., Ding, J.B., and Sabatini, B.L. (2016). Dopaminergic neurons inhibit striatal output through non-canonical release of GABA. Nature *490*, 262–266.

Ungless, M.A., Magill, P.J., and Bolam, J.P. (2004). Uniform inhibition of dopamine neurons in the ventral tegmental area by aversive stimuli. Science *303*, 2040–2042.

Wall, N.R., De La Parra, M., Callaway, E.M., and Kreitzer, A.C. (2013). Differential Innervation of Direct- and Indirect-Pathway Striatal Projection Neurons. Neuron *79*, 347–360.

Wickersham, I.R., Lyon, D.C., Barnard, R.J.O., Mori, T., Finke, S., Conzelmann, K.-K., Young, J.A.T., and Callaway, E.M. (2007). Monosynaptic restriction of transsynaptic tracing from single, genetically targeted neurons. Neuron *53*, 639–647.

Zhang, Y.-F., and Cragg, S.J. (2017). Pauses in Striatal Cholinergic Interneurons: What is Revealed by Their Common Themes and Variations? Front Syst Neurosci *11*, 80.

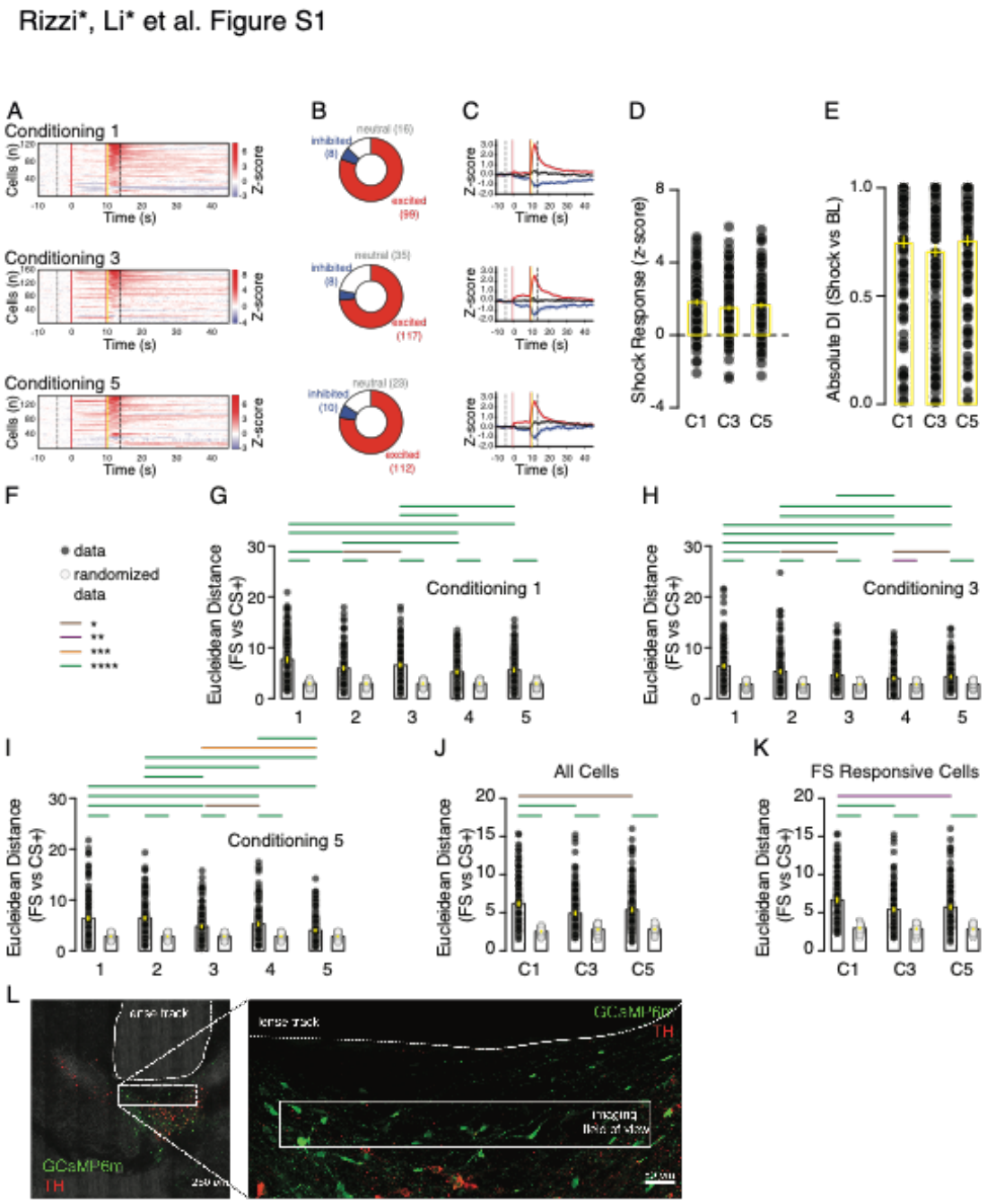
Rizzi*, Li* et al. Figure S1
A
Conditioning 1
Conditioning 3
Conditioning 5
Cells (n)
Time (s)
Z-score
B
neutral (16)
inhibited (8)
excited (99)
neutral (35)
inhibited (8)
excited (117)
neutral (23)
inhibited (10)
excited (112)
C
Z-score
Time (s)
D
Shock Response (z-score)
C1 C3 C5
E
Absolute DI (Shock vs BL)
C1 C3 C5
F
data
randomized data
*
**
***
****
G
Conditioning 1
Euclidean Distance (FS vs CS+)
H
Conditioning 3
I
Conditioning 5
J
All Cells
K
FS Responsive Cells
L
GCaMP6m
TH
imaging field of view

Figure S1: Lateral VTA neurons encode the association between CS+ and the foot-shock (related to Figure 1).

(A) Z-score heatmaps of average calcium transients at the presentation of CS+ followed by the FS on C1, C3 and C5 days. The black dashed lines depict the start (related to baseline) and end (related to FS) of the 4 sec time windows used for response classification.

(B) Pie-chart quantifications of all recorded cells to FS on C1, C3 and C5 days. The exited, inhibited and and non-responsive neurons are depicted in red, blue and white/grey; respectively.

(C) Z-score average curves of the calcium transients of characterized cells at FS presentation on C1, C3 and C5 days.

(D) Z-score of FS responses on C1, C3 and C5 days.

(E) Discrimination index of all recorded cell to FS.

(F) Key for statistical comparisons and data sets in G to K *p<0.05, **p<0.01, ***p<0.001, ****p<0.0001.

(G) Similarity index measured as Euclidean distance between the distribution of calcium activity 4 sec after CS+ presentation and 4 sec after the shock presentation across the 5 CS+/FSpair presentation (1 to 5) on C1 day.

(H) Euclidean distance between the CS+ and FS responses on C3 day.

(I) Euclidean distance between CS+ and FS responses on C5 day.

(J) Euclidean distance between CS+ and FS responses in all recorded cells across days (C1, C3 and C5 days) and compared to randomized data points of the baseline calcium activity.

(K) Euclidean distance between CS+ and shock responses in FS responsive cells across days (C1, C3 and C5 days) as compared to bootstrapped data.

(L) Confocal images of lVTA sections showing GCaMP6m-expressing neurons (green) and the lense track. The slices were counter-stained against TH (red).

Data are represented as mean +/- SEM.

See also Excel Table S1.

Rizzi*, Li* et al. Figure S2

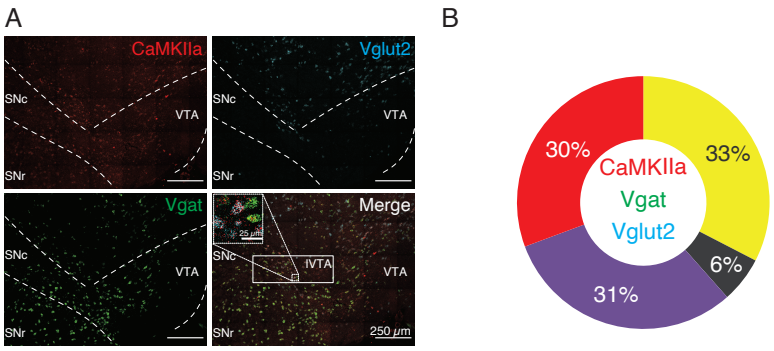

Figure S2. IVTA CaMK2a-positive cells co-express Vgat or Vglut2 (related to Figure 1).

A) Example confocal images of a representative coronal section containing the IVTA with FISH labeling of the mRNAs for CaMK2a (red), Vglut2 (cyan), Vgat (green), as well as the merged image of all three. The white rectangle on the merged image delineates IVTA. The dotted rectangle highlights a zoomed-in image (top left or the merge).

B) Pie chart quantification of IVTA CaMK2a expressing cells that either co-express Vgat or Vglut2 (887 cells, 3 mice).

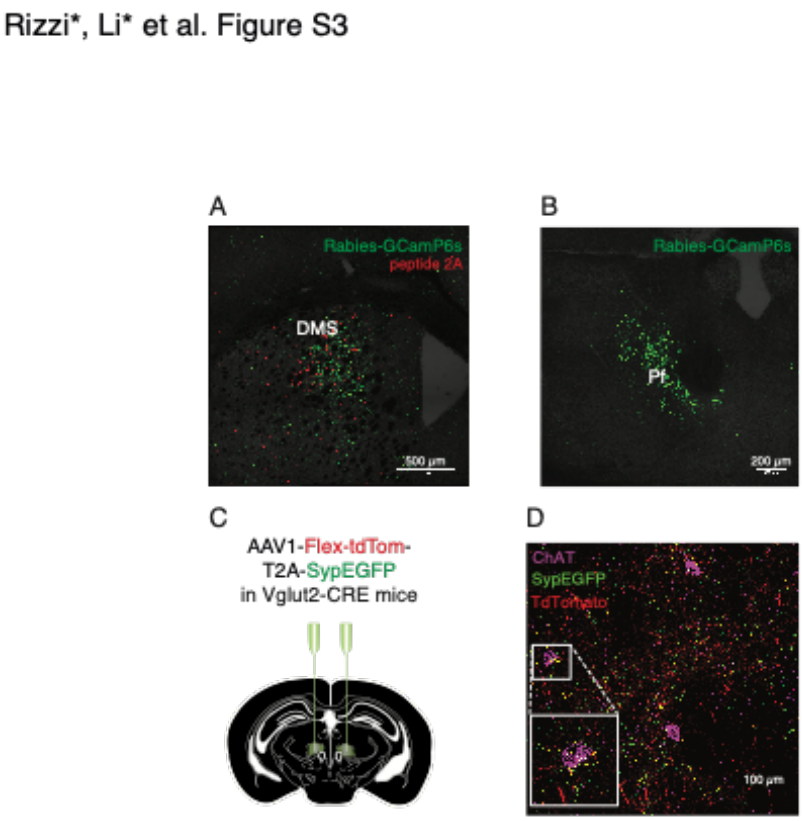

Figure S3: Pf thalamic cells provide monosynaptic excitatory inputs onto dmCINs (related to Figure 2 and 4).

(A) Example confocal image of the DMS showing starter cells in the pseudotype-rabies mapping experiment in Figure 2 (Rabies-GCaMP6s, peptide 2A in red).

(B) Example confocal image of monosynaptic input cells in the Pf expressing rabies-GCaMP6s.

(C) Schematic reporting the bilateral injection of AAV1-Flex-tdTomato-T2A-SypEGFP in the Pf of Vglut2-CRE mice.

(D) Example confocal merge image of the staining for ChAT (magenta) in coronal section of the DMS showing Pf-Vglut2 positive axons (red) and synaptophysin apposition (green) on ChAT positive cell bodies (magenta).

Rizzi*, Li* et al. Figure S4

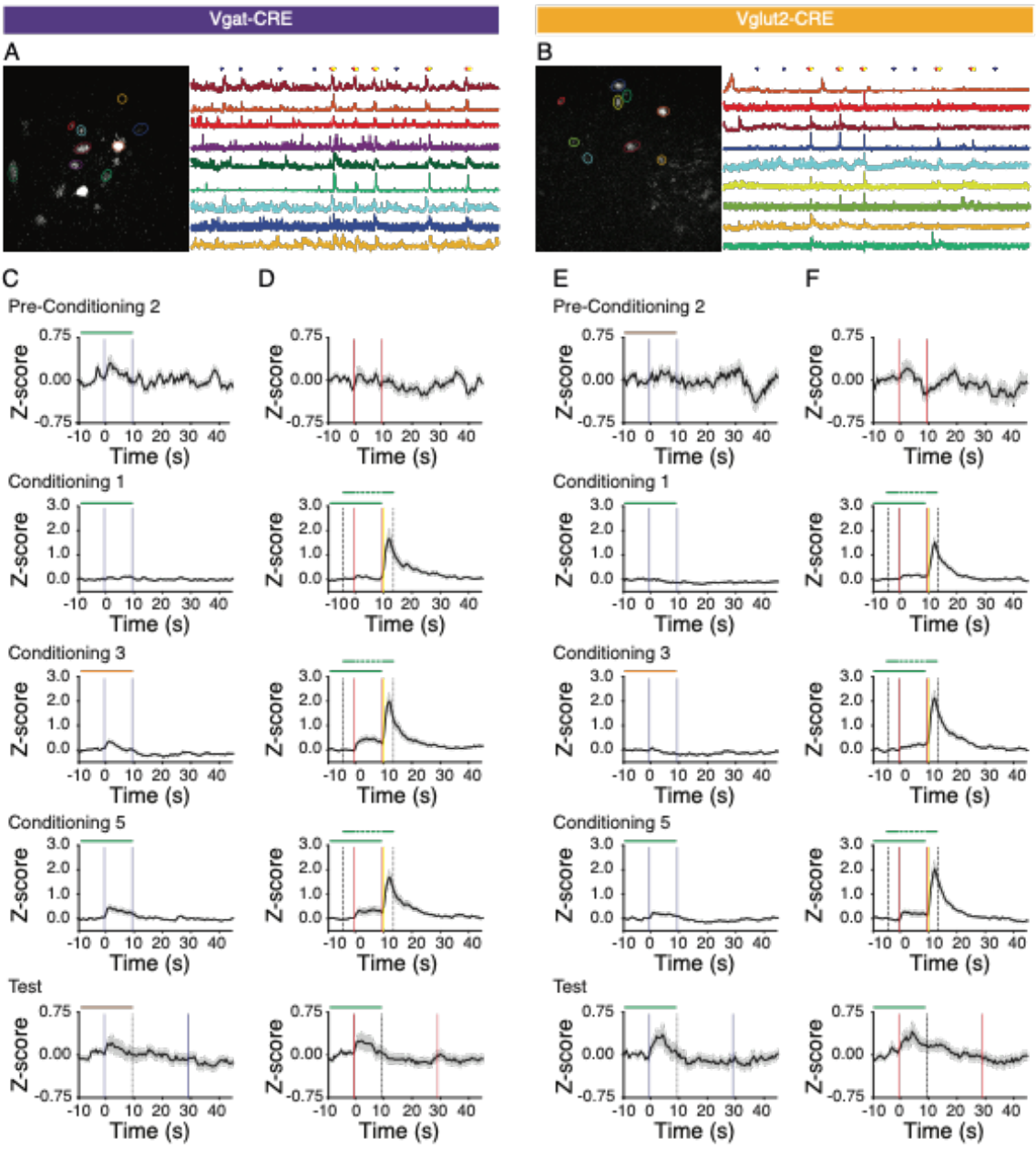

Figure S4: Lateral VTA Vgat- and Vglut2- ensemble calcium activities encode fear predictive cues following fear fear conditioning (related to Figure 6 and 7).

(A) Representative maximal projection image of the field of view obtained from the miniaturized microscope with detected GCaMP6f- expressing lVTA Vgat cells labeled in different colors (left) along with corresponding calcium transient traces of the color identified individual cells during C5 (right). Presentations of CS-, CS+ and FS are depicted in blue, red and yellow; respectively.

(B) Representative maximal projection image of lVTA Vglut2- positive cells (left) with calcium transient traces of the color-coded individual cells during C5 (right).

(C) Z-score curves of the average calcium transients (SEM shaded) of all Vgat-expressing cells at the CS- presentation (depicted between blue vertical bars) on the P2, C1, C3, C5 and T days (analysis window depicted by dotted black bar).

(D) Z-score curves of the average calcium transients (SEM shaded) of all Vgat-expressing cells at the CS+ presentation (denoted by red vertical bars) on the P2, C1, C3, C5 and T days. The start of the FS is depicted by the vertical yellow bar and the FS analysis window is represented by the dotted black bars.

(E) Z-score curves of the average calcium transients (SEM shaded) of all Vglut2-expressing cells at the CS- presentation on the P2, C1, C3, C5 and T days.

(F) Z-score curves of the average calcium transients (SEM shaded) of all Vglut2-expressing cells at the CS+ presentation on the P2, C1, C3, C5 and Tdays.

Data are represented as mean +/- SEM. *p<0.05, **p<0.01, ***p<0.001, ****p<0.0001. See also Excel Table S1 and Videos S5 and S6.

Rizzi*, Li* et al. Figure S5

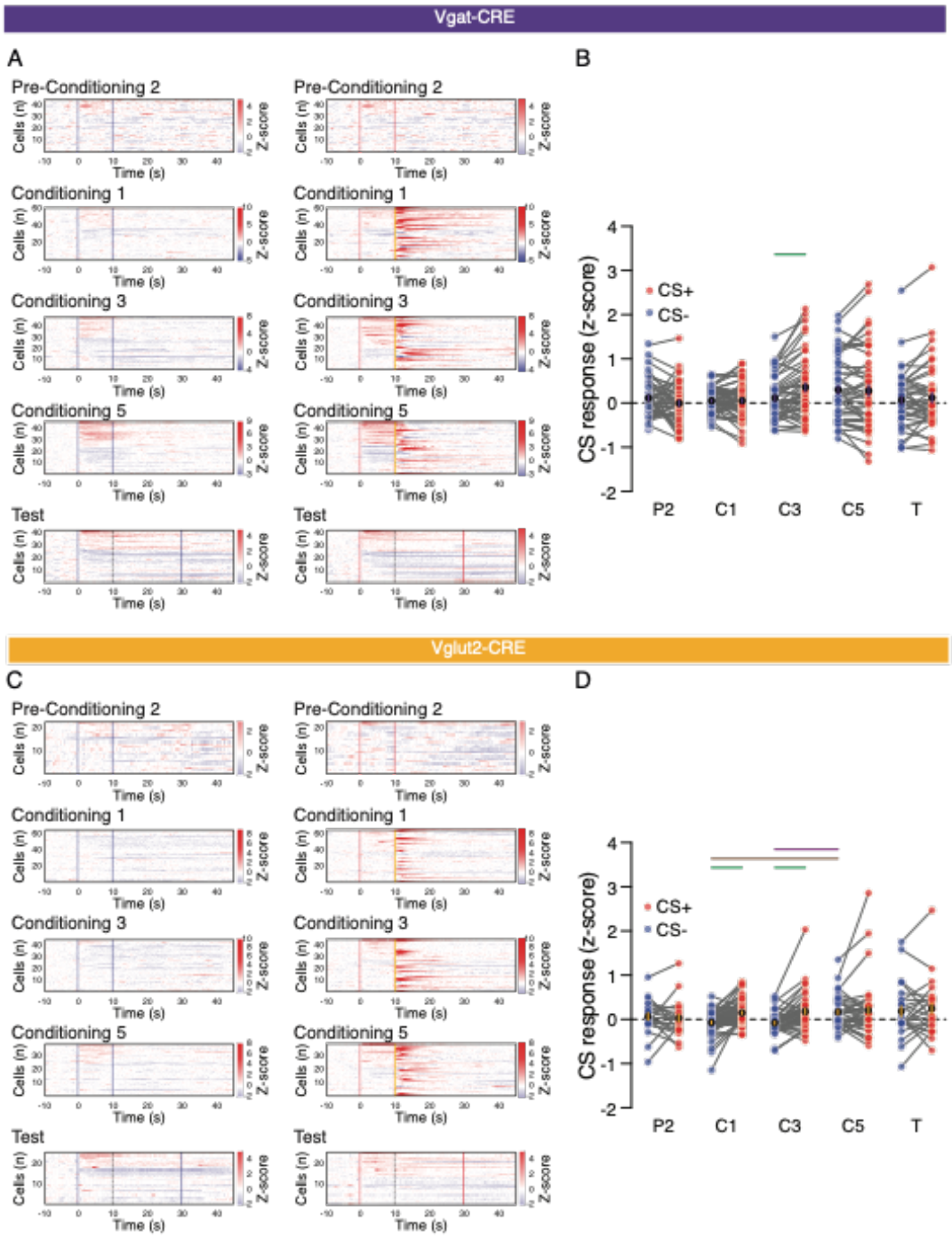

Figure S5: Individual lVTA Vgat- and Vglut2- positive cells encode auditory cues through fear conditioning (related to Figure 6 and 7).

(A) Z-score heatmaps of average calcium transients of individual recorded lVTA Vgat-expressing cells at the presentation of the CS- (vertical blue bars) and CS+ (vertical red bars) on P2, C1,C3, C5 and the T days. The vertical black dashed line depicts the end of the time window used for response classification on the test day.

(B) Summary graph reporting the Z-score of the tone responses of Vgat-expressing cells on P2, C1, C3, C5 and T days.

(C) Z-score heatmaps of average calcium transients of Vglut2-positive cells at the presentation of the CS- and CS+ on P2, C1,C3, C5 and the T days.

(D) Summary graph reporting the Z-score of the tone responses of Vglut2-expressing cells on P2, C1, C3, C5 and T days.

Data are represented as mean +/- SEM. *p<0.05, **p<0.01, ***p<0.001, ****p<0.0001. See also Excel Table S1 as well as Videos S5 and S6.

Video S1: Population activity in the lateral VTA during fear conditioning (related to Figure 1). Example calcium transient observed under the field of view during the conditioning session 5.

Video S2: Input connectivity onto dmCINs (related to Figure 2). 3D reconstruction of a ChAT-CRE mouse brain that was cleared after expression of rabies-GCaMP6s in the DMS.

Video S3: Mouse behavior during optogenetic manipulation on C1 day (related to Figure 5).

Video S4: Mouse behavior during optogenetic manipulation on the test day (related to Figure 5).

Video S5: Lateral VTA Vgat- expressing neuronal population calcium activity during fear conditioning (related to Figure 6 and 7). Example calcium transient observed under the field of view during the conditioning session 5.

Video S6: Lateral VTA Vglut2- expressing neuronal population calcium activity during fear conditioning (related to Figure 6 and 7). Example calcium transient observed under the field of view during the conditioning session 5.

Excel Table S1. Statistical analyses (related to Figure 1, 5-7, S1, S4-5).

2.1 Lateral VTA GABAergic and Glutamatergic modulation of conditioned learning

	Mice	test	effect	Posthoc	Posthoc	Posthoc	Posthoc	Posthoc	Posthoc
Fig 1E	8 mice	one-way repeated measures ANOVA with post-hoc Bonferroni's test	Training $F_{(3,21)} = 8.627$ $p = 0.0006$	P1 vs C5 $p = 0.0293$	P2 vs C5 $p = 0.0005$	C5 vs T $p = 0.0069$			
Fig 1F	8 mice	two-way repeated measures ANOVA with post-hoc Bonferroni's test	training $F_{(1,14)} = 279.4$ $p < 0.0001$	CS- P2 vs T $p < 0.0001$	CS+ P2 vs T $p < 0.0001$				
			tone effect $F_{(1,14)} = 44.82$ $p < 0.0001$	T CS- vs CS+ $p < 0.0001$					
Fig 1G	8 mice	paired t-test	$t_7 = 6.342$ $p = 0.004$						
Fig 1O	8 mice 80-160 cells	Kruskal-Wallis test with post-hoc Dunn's test	CS- training effect $H = 17.36$ $p = 0.0016$	C3 vsT $p = 0.0118$	C5 vs T $p = 0.0030$				
			CS+ training effect $H = 26.26$ $p < 0.0001$	P2 vs C3 $p = 0.0017$	C1 vs C3 $p = 0.0014$	C3 vs T $p = 0.0023$			
Fig 1O	8 mice 80-160 cells	Wilcoxon matched-pairs signed rank sign test		C3 CS- vs CS+ $W_{160} = 6428$ $p < 0.0001$	C5 CS- vs CS+ $W_{145} = 2835$ $p = 0.0049$	T CS- vs CS+ $W_{80} = 936$ $p = 0.0244$			
Fig 1P	8 mice 80-160 cells	Kruskal-Wallis test with post-hoc Dunn's test	CS- training effect $H = 28.80$ $p < 0.0001$	P2 vs C3 $p = 0.0007$	P2 vs C5 $p < 0.0001$	C1vs C3 $p = 0.0192$	C1 vs C5 $p = 0.0036$		
			CS+ training effect $H = 46.09$ $p < 0.0001$	P2 vs C3 $p < 0.0001$	P2 vs C5 $p < 0.0001$	P2 vs T $p = 0.0010$	C1 vs C3 $p = 0.0006$	C1 vs C5 $p = 0.0001$	C1 vs T $p = 0.0404$
Fig 1Q	8 mice 80-160 cells	Kruskal-Wallis test with post-hoc Dunn's test	training effect $H = 26.32$ $p < 0.0001$	C1 vs C3 $p = 0.0131$	C1 vs C5 $p = 0.0001$	C1 vs T $p = 0.0002$			

Table S1: Statistical analysis related to Figure 1

	Mice	test	effect	Posthoc Bonferroni	Posthoc Bonferroni	Posthoc Bonferroni	Posthoc Bonferroni	Posthoc Bonferroni
Fig 5F	10 mice	two-way repeated measures ANOVA	Time $F_{(2,16)} = 39.95$ $p < 0.0001$	Ctrl C1 vs C5 $p = 0.0003$	Ctrl C5 vs T $p = 0.0014$	Arch C1 to C5 $p < 0.0001$	Arch D5 to T $p < 0.0001$	
Fig 5G	10 mice	two-way repeated measures ANOVA	interaction effect $F_{(1,8)} = 18.76$ $p = 0.0025$	Arch CS- vs Ctrl CS- $p = 0.001$				
			tone effect $F_{(1,8)} = 87.69$, $p < 0.0001$	Arch CS- vs Ctrl CS- $p = 0.001$	WT CS- vs CS+ $p < 0.0001$			
Fig 5H	10 mice	unpaired t-test	$t_8 = 4.331$ $p = 0.0025$					
Fig 5J	10 mice	two-way repeated measures ANOVA	time effect $F_{(2,16)} = 50.32$ $p < 0.0001$	Ctrl C1 vs C5 $p = 0.0002$	Ctrl C5 vs T $p = 0.0004$	Arch C1 vs C5 $p < 0.0001$	Arch C5 vs T $p < 0.0001$	
Fig 5K	10 mice	2-way repeated measures ANOVA	tone effect $F_{(1,8)} = 41.52$ $p = 0.0002$	Arch CS- vs CS+ $p = 0.002$	Ctrl CS- vs CS+ $p = 0.0072$			
Fig 5L	10 mice	unpaired t-test	$t_8 = 0.6902$ $p = 0.5096$					
Fig 5N	10 mice	two-way repeated measures ANOVA	interaction effect $F_{(2,16)} = 8.176$ $p = 0.0036$	Ctrl C1 vs C5 $p < 0.0001$	Ctrl C5 vs T $p = 0.0002$			
			genotype effect $F_{(18)} = 5.709$ $p = 0.0439$	C5 Ctrl vs Arch $p = 0.0003$				
Fig 5O	10 mice	two-way repeated measures ANOVA	tone effect $F_{(1,8)} = 89.89$ $p < 0.0001$	CS- Arch vs Ctrl $p = 0.014$	Arch CS- vs CS+ $p = 0.0001$	Ctrl CS- vs CS+ $p = 0.0009$		
Fig 5P	10 mice	unpaired t-test	$t_8 = 2.309$ $p = 0.0249$					
Fig 5R	11 mice	2-way repeated measure	tone effect $F_{(1,9)} = 7.28$ $p = 0.0245$	Ctrl C1vs C5 $p = 0.0003$	Ctrl C5 vs T $p = 0.0004$	Arch C1 vs C5 $p < 0.0001$	Arch C5 vs T $p < 0.0001$	Ctrl C5 vs Arch C5

		s ANOVA						p = 0.0059
Fig 5S	11 mice	2-way repeated measure s ANOVA	tone effect $F_{(1,9)} = 5.718$ p = 0.0405	CS+ Arch vs Ctrl p = 0.0339	WT CS- vs CS+ p = 0.0231			
Fig 5T	11 mice	unpaired t-test	$t_9 = 2.275$ p = 0.049					

Table S2: Statistical analysis related to Figure 5

	Mice	test	effect	Posthoc	Posthoc	Posthoc	Posthoc
Fig 6D	3 mice	one-way repeated measures ANOVA with post-hoc Bonferroni's test	Vgat-CRE $F_{(3,6)} = 8.846$ $p = 0.0127$	P1 vs C5 $p = 0.0407$	P2 vs C5 $p = 0.0196$		
Fig 6D	3 mice	one-way repeated measures ANOVA with post-hoc Bonferroni's test	Vglut2-CRE $F_{(3,6)} = 11.32$ $p = 0.0070$	P1 vs C5 $p = 0.0213$	P2 vs C5 $p = 0.0139$	C5 vs T $p = 0.0243$	
Fig 6E	3 mice	two-way repeated measures ANOVA with post-hoc Bonferroni's test	Vgat-CRE training $F_{(1,4)} = 28.49$ $p = 0.0059$	CS- P2 vs T $p = 0.0157$	CS+ P2 vs T $p = 0.0009$		
			Vgat-CRE tone effect $F_{(1,4)} = 7.644$ $p = 0.0506$	T CS- vs CS+ $p = 0.0481$			
Fig 6E	3 mice	two-way repeated measures ANOVA with post-hoc Bonferroni's test	Vglut2-CRE training $F_{(1,4)} = 325.8$ $p < 0.0001$	CS- P2 vs T $p = 0.0012$	CS+ P2 vs T $p < 0.0001$		
			Vglut2-CRE tone effect $F_{(1,4)} = 16.71$ $p = 0.0150$	T CS- vs CS+ $p = 0.0130$			
Fig 6F	3 mice	Vgat-CRE paired t-test	$t_2 = 2.181$ $p = 0.1610$				
Fig 6F	3 mice	Vglut2-CRE paired t-test	$t_2 = 2.957$ $p = 0.0979$				
Fig 6O	3 mice 42-60 cells	Kruskal-Wallis test with post-hoc Dunn's test	Vgat-CRE CS- training effect $H = 28.24$ $p < 0.0001$	P2 vs C5 $p = 0.003$	C1 vs C5 $p < 0.0001$		
			Vgat-CRE CS+ training effect $H = 32.82$ $p < 0.0001$	P2 vs C3 $p = 0.0009$	P2 vs C5 $p < 0.0001$	C1 vs C3 $p = 0.0073$	C1 vs C5 $p = 0.0004$

Fig 6P	3 mice 42-60 cells	Kruskal-Wallis test with post-hoc Dunn's test	training effect H = 3.244 p = 0.5178				
Fig 6Q	3 mice 22-65 cells	Kruskal-Wallis test with post-hoc Dunn's test	Vglut2-CRE CS- training effect H = 7.754 p = 0.1010				
			Vglut2-CRE CS+ training effect H = 16.70 p = 0.0022	C1 vs C3 p = 0.0194	C1 vs C5 p = 0.0427	C1 vs T p = 0.0382	
Fig 6R	3 mice 22-65 cells	Kruskal-Wallis test with post-hoc Dunn's test	Vglut2-CRE training effect H = 19.80 p = 0.0005	C1 vs C3 p = 0.0053	C1 vs T p = 0.0155	C3 vs C5 p = 0.0473	

Table S3: Statistical analysis related to Figure 6

	Mice	test	effect	Posthoc	Posthoc	Posthoc	Posthoc	Posthoc	Posthoc
Fig 7H	3 mice 46-60 cells	Kruskal-Wallis test with post-hoc Dunn's test	training effect H = 1.333 p = 0.5136						
Fig 7I	3 mice 46-60 cells	Kruskal-Wallis test with post-hoc Dunn's test	training effect H = 1.634 p = 0.4418						
Fig 7J	3 mice 39-65 cells	Kruskal-Wallis test with post-hoc Dunn's test	training effect H = 4.685 p = 0.0961						
Fig 7K	3 mice 39-65 cells	Kruskal-Wallis test with post-hoc Dunn's test	training effect H = 7.520 p = 0.0233	C1 vs C3 p = 0.0324					
Fig 7L	3 mice 60 cells	two-way repeated measures ANOVA with post-hoc Bonferroni's test	pairing effect $F_{(4,472)}$ = 14.55 p < 0.0001	1 vs 3 p =0.0002	1 vs 4 and 1 vs 5 p < 0.0001	2 vs 3, 2 vs 4, and 2 vs 5 all p < 0.0001			
			randomization effect $F_{(1,118)}$ = 41.52 p < 0.0001	Pairs 1, 2, and 3 all p < 0.0001			Pair 4 p = 0.0002	Pair 5 p = 0.0216	
Fig 7M	3 mice 48 cells	two-way repeated measures ANOVA with post-hoc Bonferroni's test	pairing effect $F_{(4,376)}$ = 16.45 p < 0.0001	1 vs 3, 1 vs 4, 1 vs 5 all p < 0.0001		2 vs 4 and 2 vs 5, p < 0.0001		3 vs 4 p < 0.0001	3 vs 5 p = 0.0006
			randomization effect $F_{(1,94)}$ = 44.61 p < 0.0001	Pairs 1, 2, and 3 all p < 0.0001			Pair 4 p = 0.0094	Pair 5 p = 0.0028	
Fig 7N	3 mice 46 cells	two-way repeated measures ANOVA with post-hoc Bonferroni's test	pairing effect $F_{(4,360)}$ = 7.283 p < 0.0001	All companions with pair 1 p < 0.0001					
			randomization effect $F_{(1,90)}$ = 20.37 p < 0.0001	Pair 1 p < 0.0001	Pair 2 p = 0.0085	Pair 3 p = 0.0407	Pair 4 p = 0.019		
Fig 7O	3 mice	two-way repeated	pairing effect $F_{(4,512)}$ = 10.45 p < 0.0001	1 vs 2 p < 0.0001	2 vs 3, 2 vs 4, and 2 vs 5 all p < 0.0001				3 vs 5 p = 0.0018

	65 cells	measures ANOVA with post-hoc Bonferroni's test	randomization effect $F_{(1,128)} = 31.02$ $p < 0.0001$	Pair 1 $p = 0.0210$	Pair 2 and Pair 3 $p < 0.0001$	Pair 4 $p = 0.0066$			
Fig 7P	3 mice 45 cells	two-way repeated measures ANOVA with post-hoc Bonferroni's test	pairing effect $F_{(4,259)} = 6.612$ $p < 0.0001$	1 vs 2 $p = 0.0004$	1 vs 3, 1 vs 4, 1 vs 5 all $p < 0.0001$			2 vs 4 $p = 0.0433$	
			randomization effect $F_{(1,88)} = 19.50$ $p < 0.0001$	Pair 1 $p < 0.0001$	Pair 2 $p = 0.0001$	Pair 3 $p = 0.0032$			
Fig 7Q	3 mice 39 cells	two-way repeated measures ANOVA with post-hoc Bonferroni's test	pairing effect $F_{(4,304)} = 9.352$ $p < 0.0001$	1 vs 2 $p = 0.0009$	1 vs 4 and 1 vs 5 $p < 0.0001$	2 vs 5 $p = 0.0015$	3 vs 4 $p = 0.0020$	3 vs 5 $p < 0.0001$	
			randomization effect $F_{(1,76)} = 24.58$ < 0.0001	Pair 1 $p < 0.0001$	Pair 2 $p = 0.0015$	Pair 3 $p < 0.0001$			
Fig 7R	3 mice 46-60 cells	two-way repeated measures ANOVA with post-hoc Bonferroni's test	training effect $F_{(2,302)} = 16.45$ $p = 0.9449$						
			randomization effect $F_{(1,302)} = 146.6$ $p < 0.0001$	All pairs $p < 0.0001$					
Fig 7S	3 mice 31-45 cells	two-way repeated measures ANOVA with post-hoc Bonferroni's test	training effect $F_{(2,208)} = 1.537$ $p = 0.2175$	C1 vs C5 $p = 0.0157$					
			randomization effect $F_{(1,208)} = 141.5$ $p < 0.0001$	All pairs $p < 0.0001$					
Fig 7T	3 mice 39-65 cells	two-way repeated measures ANOVA with post-hoc Bonferroni's test	training effect $F_{(2,292)} = 0.2956$ $p = 0.7443$						
			randomization effect $F_{(1,292)} = 72.88$ $p < 0.0001$	All pairs $p < 0.0001$					

Fig 7U	3 mice 28-41 cells	two-way repeated measures ANOVA with post-hoc Bonferroni's test	training effect $F_{(2,192)} = 2.342$ $p = 0.0989$						
			randomization effect $F_{(1,192)} = 953.9$ $p < 0.0001$	All pairs $p < 0.0001$					

Table S4: Statistical analysis related to Figure 7

2.1 Lateral VTA GABAergic and Glutamatergic modulation of conditioned learning

	Mice	test	effect	Posthoc	Posthoc	Posthoc	Posthoc	Posthoc	Posthoc
Fig S1D	8 mice 123-160 cells	Kruskal-Wallis test with post-hoc Dunn's test	training effect $H = 3.883$ $p = 0.1435$						
Fig S1E	8 mice 123-160 cells	Kruskal-Wallis test with post-hoc Dunn's test	training effect $H = 0.4650$ $p = 0.7925$						
Fig S1G	8 mice 123 cells	two-way repeated measures ANOVA with post-hoc Bonferroni's test	pairing effect $F_{(4,976)} = 15.56$ $p < 0.0001$	1 vs 2, 1 vs 4, 1 vs 5 all $p < 0.0001$		2 vs 3 $p = 0.0402$	2 vs 4 $p < 0.0001$	3 vs 4, 3 vs 5 both $p < 0.0001$	
			randomization effect $F_{(1,244)} = 108.5$ $p < 0.0001$	all comparisons $p < 0.0001$					
Fig S1H	8 mice 160 cells	two way repeated measures ANOVA with post-hoc Bonferroni's test	pairing effect $F_{(4,1272)} = 31.20$ $p < 0.0001$	all comparisons with pair 1 $p < 0.001$		2 vs 3 $p = 0.0184$	2 vs 4 and 2 vs 5 both $p < 0.0001$	3 vs 4 $p < 0.0001$	4 vs 5 $p = 0.0030$
			randomization effect $F_{(1,318)} = 78.23$ $p < 0.0001$	pairs 1, 2, 3, and 5 all $p < 0.0001$				pair 4 $p = 0.0074$	
Fig S1I	8 mice 145 cells	two way repeated measures ANOVA with post-hoc Bonferroni's test	pairing effect $F_{(4,1152)} = 27.68$ $p < 0.0001$	1 vs 3, 1 vs 4, 1 vs 5 all $p < 0.0001$		all comps. with pair 2 $p < 0.0001$	3 vs 4 $p = 0.0470$	3 vs 5 $p = 0.0004$	4 vs 5 $p < 0.0001$
			randomization effect $F_{(1,288)} = 104.7$ $p < 0.0001$	pairs 1, 2, 3, and 4 all $p < 0.0001$				pair 5 $p = 0.0133$	
Fig S1J	8 mice 123-160 cells	two way repeated measures ANOVA with post-hoc Bonferroni's test	time effect $F_{(2,850)} = 2.597$ $p = 0.0015$	C1 vs C3 $p < 0.0001$	C1 vs C5 $p = 0.0187$				
			randomization effect $F_{(1,850)} = 513.5$ $p < 0.0001$	for all comparisons $p < 0.0001$					
Fig S1K	8 mice 107-125 cells	two way repeated measures ANOVA with post-hoc	time effect $F_{(2,702)} = 7.488$ $p = 0.0015$	C1 vs C3 $p < 0.0001$	C1 vs C5 $p = 0.0062$				
			randomization effect	for all comparisons $p < 0.0001$					

		Bonferroni's test	$F_{(1,702)} = 496.5$ $p < 0.0001$	

Table S5: Statistical analysis related to Figure S1

	Comparison	test	effect	effect	effect	effect	effect
Fig S3E	Vgat-CRE Baseline (20 bins) vs CS- (20 bins)	Wilcoxon rank sum test	PreD2 rank sum = 275 p < 0.0001	C1 rank sum = 242 p < 0.0001	C3 rank sum = 301 p = 0.0033	C5 rank sum = 210 p < 0.0001	T rank sum = 303 p = 0.0040
Fig S3F	Vgat-CRE Baseline (20 bins) vs CS+ (20 bins)	Wilcoxon rank sum test	PreD2 rank sum = 400 p = 0.7972	C1 rank sum = 263 p < 0.0001	C3 rank sum = 210 p < 0.0001	C5 rank sum = 210 p < 0.0001	T rank sum = 242 p < 0.0001
Fig S3F	Vgat-CRE Baseline (8 bins) vs CS+ (8 bins)	Wilcoxon rank sum test		C1 rank sum = 36 p < 0.0001	C3 rank sum = 36 p < 0.0001	C5 rank sum = 36 p < 0.0001	
Fig S3G	Vglut2-CRE Baseline (20 bins) vs CS- (20 bins)	Wilcoxon rank sum test	PreD2 rank sum = 315 p = 0.0106	C1 rank sum = 552 p < 0.0001	C3 rank sum = 532 p = 0.0010	C5 rank sum = 210 p < 0.0001	T rank sum = 233 p < 0.0001
Fig S3H	Vglut2-CRE Baseline (20 bins) vs CS+ (20 bins)	Wilcoxon rank sum test	PreD2 rank sum = 360 p = 0.1806	C1 rank sum = 210 p < 0.0001	C3 rank sum = 210 p < 0.0001	C5 rank sum = 212 p < 0.0001	T rank sum = 211 p < 0.0001
Fig S3H	Vglut2-CRE Baseline (8 bins) vs CS+ (8 bins)	Wilcoxon rank sum test		C1 rank sum = 36 p < 0.0001	C3 rank sum = 36 p < 0.0001	C5 rank sum = 36 p < 0.0001	

Table S6: Statistical analysis related to Figure S3

	Mice	test	effect	Posthoc Dunn	Posthoc Dunn
Fig S4B	3 mice 42-60 cells	Kruskal-Wallis test with post-hoc Dunn's test	CS- training effect H = 1.690 p = 07926		
			CS+ training effect H= 6.763 p = 0.1489		
Fig S4B	3 mice 42-60 cells	Wilcoxon matched-pairs signed rank sign test		C3 CS- vs CS+ W_{48} = 780 p < 0.0001	
Fig S4D	3 mice 22-65 cells	Kruskal-Wallis test with post-hoc Dunn's test	CS- training effect H = 17.35 p = 0.0017	C1 vs C5 p = 0.0293	C3 vs C5 p = 0.0043
			CS+ training effect H= 3.881 p = 0.4224		
Fig S4D	3 mice 22-65 cells	Wilcoxon matched-pairs signed rank sign test		C1 CS- vs CS+ W_{65} = 1479 p < 0.0001	C3 CS- vs CS+ W_{45} = 795 p < 0.0001

Table S7: Statistical analysis related to Figure S4

Title: Zona Incerta calcium dynamics underlying associative fear learning

Authors: Zhuoliang Li[1,2], Giorgio Rizzi[1,2,3], Kelly R. Tan[1,*]
Affiliations:

1. Biozentrum, University of Basel, Klingelbergstrasse 50/70, 4056, Basel, Switzerland
2. These authors contributed equally.
3. Current affiliation: Inscopix Inc, Palo Alto, California, United States

Abstract

Recent studies suggest that the Zona Incerta (ZI) plays a role in fear learning and recall. However, there is clear gap in knowledge as to whether the ZI can encode fear evoking threats and cues that predict them. Here, we subject mice to a classical fear conditioning paradigm while recording the *in-vivo* calcium dynamics of ZI neurons. We observed that ZI neurons can encode not only a fear evoking stimulus, but can also learn to encode predictive cues, associate them with the unconditioned fear evoking stimulus, and discriminate them from neutral non-predictive cues. Furthermore, differences in these learned responses are linked with the extent mice generalized fear. Our findings provide extensive evidence in the way ZI neurons encode aspects of fear learning and generalization.

Introduction

Fear is an emotional defensive behavioral response to a threatening stimulus[1,2]. To ensure survival, it is principally important to react not only to innately threatening stimuli but also those that predicts them[1,2]. The classical and robust Pavlovian fear conditioning paradigm where an initially neutral stimulus evokes fear following its association with an innately threatening stimulus have often been used to experimentally study the neural basis for learned fear[3,4]. A wide range of brain regions have been thus far shown to play a role in this robust learned fear response[4] including the amygdala[5,6], prefrontal cortex[7,8], hippocampus[9,10], lateral ventral tegmental area[11], and periaqueductal gray[12]. More recently, the Zona Incerta (ZI) has also been implicated.

Despite an early report where the electrolytic lesion of the ZI in rats impaired their ability to avoid the shock-paired context[13], the link between the ZI and fear has been largely overlooked since. In the past handful of years, the interest into the role that the ZI plays in fear has been renewed. Specifically, the optogenetic activation and inactivation of the abundant GAD2-expressing ZI neurons during fear recall of a previously shock-paired auditory cue reduced and potentiated conditioned freezing, respectively[14]. This finding is corroborated by a clinical observation where patients with Parkinson's Disease receiving deep brain stimulation in the ZI self-reported improved fear recognition[15]. On the other hand, it is also reported that the tetanus toxin mediated blockade of synaptic transmission of all ZI neuronal types non-specifically or just ones expressing parvalbumin impaired freezing to a shock-paired tone during fear acquisition, fear recall, as well as fear recall of an already learned shock-paired tone[16]. In more complex fear conditioning paradigms involving both neutral and shock-

paired tones, the chemogenetic activation and inactivation of the ZI non-specifically during fear recall modulated fear generalization by impairing and improving discrimination between the two tones, respectively[17].

In spite of the seemingly conflicting findings among recent studies, they all suggest that the manipulation of the ZI impacts fear, either during acquisition, recall, and/or generalization. However, there is close to no knowledge about the activity of the ZI neurons and specifically whether they can encode threatening stimuli and cues that predict them during fear acquisition as well as recall. In this study, we use the head mounted miniaturized microscope to image the calcium dynamics of ZI neurons in freely moving mice as they perform in a fear conditioning paradigm. We observed in both the populational level and the longitudinally tracked cells that most of the ZI neurons are excited by footshocks (FS), become more responsive to both neutral (CS-) and shock-paired (CS+) tones after learning, and can learn to discriminate between the two tones. Interestingly, ZI neurons of mice that developed high and low fear generalization discriminated between the CS+ and CS- differently. Together, our findings provide important insights into the dynamics of the ZI neurons throughout fear conditioning and recall.

Results

To investigate whether the ZI neurons can encode the association between a threatening stimulus and its predictive cues, we recorded the calcium dynamics of ZI neurons as a proxy for neuronal activity while mice performed in a classical fear conditioning paradigm. We surgically injected a virus containing the calcium indicator GCaMP6m (AAV1-CAMKIIα-GCaMP6m) into the ZI and implanted a gradient refractive index (GRIN) lens above (Fig. 1A). The calcium transients of the ZI neurons were concomitantly imaged while mice performed in a fear conditioning task where one of the two neutral pre-exposed auditory tones (CS+) was repeatedly presented with an aversive FS (unconditioned stimulus) while the other without (CS-) over 5 consecutive conditioning days and tested for fear recall in a neutral context (Fig. 1B). The mice exhibited comparably low levels of freezing to the neutral context as well as the conditioning context before any shocks were delivered (Fig. 1C). CS+ and CS- tones evoked low and similar levels of freezing before conditioning and mice froze significantly more to the CS+ than the CS- during on the test day after conditioning (Fig. 1D), hence showing that they have learned that the CS+ rather than CS- is predictive of the FS. Interestingly, unique cells showed cue related calcium transients during the task (Fig. 1A). To profile cells, we first investigated whether they were responsive to cues by comparing their activity during the cue window against the baseline period before (ranksum test, $p< 0.05$). We then asked whether these responses can be discriminated from the intrinsic spontaneous activity within the recording session. To do so, we compared the discrimination index (DI) of these responses with that of randomly sampled cue and baseline windows (receiver-operating characteristic analysis with bootstrapping, $\alpha = 0.05$). Throughout learning,

while both the proportion of CS- (Fig. 1E-H) and CS+ (Fig. 1I-L) responsive cells increased and more responses became distinguishable, the majority of cells were inhibited by the CS- and excited by the CS+ on the test day. Furthermore, the amplitude and discriminability of the inhibition to the CS- (Fig. 1M-N) and excitation to the CS+ (Fig. 1O-P) became increasingly potentiated throughout learning and peaked on the test day.

The sharp contrast in the way the majority of ZI neurons responded to the CS- and the CS+ after learning led us to speculate that they discriminate between the two tones. To test this hypothesis, we compared the activity of ZI neurons between the two tones (Fig. S1A-D). While many ZI neurons responded differently to the CS- and the CS+ even before conditioning (Fig. S1C), the majority of these differences were weak and indistinguishable from randomly sampled differences in activity (Fig. S1D). Interestingly, with learning, there was a clear shift in how cells responded to the CS+ as compared to the CS-, with the majority of cells exhibiting higher activity during the CS+ than the CS- on the test day (Fig. S1C) and a noticeable portion of these differences now distinguishable (Fig. S1D). In addition, this shift coincided with an increase in the amplitude (Fig. 1Q) and the discriminability (Fig. 1R) between the activity during the CS+ and the CS- windows within these cells.

In addition to predictive cues, we also investigated whether ZI neurons are modulated by the FS (Fig. S1E-M). We observed that the majority of ZI neurons were strongly excited by the FS (Fig. S1G) and can discriminate them (Fig. S1H). While the proportion of FS excited cells (Fig. S1G) and the amplitude of these responses (Fig. S1I) remained high from the first to last conditioning days, more excitatory responses were indistinguishable from the whole trace on the last conditioning day (Fig. S1H)

accompanied by a significant drop in their discriminability (Fig. S1J). Lastly, to examine whether ZI neurons can associate predictive cues with FS, we investigated the similarity between CS+ and FS responses by calculating the Euclidean distance (ED) between the two[11,18]. Indeed, the ED between CS+ and FS responses became smaller (thus more similar) across pairings (Fig. S1K-L) on both conditioning days, suggesting an association between the two responses. However, the lack of any change in the ED between CS+ and FS+ responses across the first and last conditioning days (Fig. S1M) suggest that this association may not be consolidated.

So far, we have observed on a population level across all recorded cells that ZI neurons can encode predictive cues as well as FS, discriminate between CS+ from CS-, and associate CS+ with FS. To strengthen our findings, we identified longitudinally tracked cells across all analyzed days with spatial alignment (Fig. 2A) and investigated changes in their response profiles throughout fear learning. To do so, we classified cells based on their responses to cues on the last day they were presented (T for CS-/CS+ and C5 for FS) and examined how they behaved beforehand. Expectedly, we observed similar proportion of longitudinally tracked cells responsive to CS- (Fig. 2B-E) and CS+ (Fig. 2F-I) on the test day as compared to the populational analyses (Fig. 1). Notably, there was a great deal of heterogeneity and plasticity in how cells responded to CS- and the CS+ across days (Fig 2D-E, H-I). Interestingly, the amplitude (Fig. 2L) and the DI (Fig. 2M) of the average excitatory responses to CS+ increased gradually across fear learning and peaked during the test day, coinciding with a gradual increase in freezing to the CS+ (Fig. 1D). On the other hand, the corresponding changes to the average inhibitory responses to the CS- were more drastic and appeared only on the test day (Fig. 2B, J-K).

The contrast in the way that the CS- and the CS+ responses were modulated across fear learning drove us to question whether cells gradually learned to differentiate between the two tones. On the contrary, cells on average responded similarly to the CS- and the CS+ (Fig. 3A-F) across fear conditioning and only clearly distinguishable from one another on the test day (Fig. 3E-F), coinciding with the differences in freezing between the CS- and the CS+ across the paradigm (Fig. 1D). Lastly, to address the association between the CS+ and the FS, we also observed in longitudinally tracked cells that the majority of ZI neurons remained excited to FS throughout learning (Fig. 3G-O) and could associate between the CS+ and the FS within conditioning days (Fig. 3M-N). In contrast to the populational level (Fig. S2I), we observed that CS+ and FS responses became more similar from the first to last conditioning days (Fig. 3O), suggesting that they were indeed consolidated.

These data in both the populational level and in longitudinally tracked cells provide convincing evidence that the ZI neurons encode threatening stimuli, can learn to encode cues that predict them, and discriminate fear-predictive cues from neutral ones. Yet, it is still unclear whether the activity of ZI neurons is influenced by the extent of fear learning that took place. Individual differences in fear acquisition and recall have been well documented in humans[19] and to a lesser extent in rodents[20–22]. Moreover, the ZI has been reported to modulate fear generalization[17]. We, therefore, investigated whether the response profile of ZI neurons differed between mice that exhibited higher fear generalization (FG) from the ones with lower generalization (fear not generalized, FnG). To do so, we stratified our data (Fig. 4, S2-4) into two groups based on the extent mice exhibited generalized freezing to the CS- on the test day (cutoff 50% freezing). FG and FnG mice both exhibited similar contextual freezing

levels throughout (Fig. 4A) while only the FG mice displayed an increased freezing to the CS- after learning (Fig. 4B), reflective of fear generalization that is modality specific. On the other hand, both groups increased their freezing to the CS+ (Fig. 4C), indicating that they both learned that the CS+ is predictive of the FS. When we examined the response profiles of FG and FnG mice to the CS- (Fig. S2A-H), the CS+ (Fig. 2I-P), we observed that more ZI cells became excited to the CS+ and the magnitude of these excitations potentiated after fear learning in both groups (Fig. S2I-P). Similarly, the majority of the ZI neurons in both groups were excited by the FS (Fig. S3). However, while the responsive cells to the CS- became proportionally more inhibited in the FnG mice, this shift was not observed in the FG mice (Fig. S2A-H). Consequently, this difference was maintained in the way that the CS+ was differentiated from the CS- (Fig. 4D-H, S4). While both groups displayed bi-directional differences in how they responded to the CS+ with respect to the CS- before learning, the ZI neurons in FnG mice learned to become strongly biased, only exhibiting higher CS+ activity to the CS- (Fig. 4D-H). In contrast, this learned bias is weaker in the FG mice where there were still cells that respond more strongly to the CS- than the CS+ on the test day (Fig. 4D-H). These data together demonstrates that the activity dynamics of ZI neurons do not only encode aspects of fear learning but also is reflective of the extent that mice generalized fear.

Discussion

A growing number of studies highlighted the importance of the ZI in associative fear learning[13,14,16,17], without much inquiry into whether the ZI can encode the necessary underlying cues and whether these representations change over learning. We imaged ZI neurons in freely moving mice while they performed in a fear conditioning task. We observed that the majority of the ZI neurons are excited by the threatening and fear evoking FS, supporting claims that the ZI is sensitive to stressful stimuli[23]. The ZI neurons are also modulated by auditory cues and these representations are plastic across fear learning. ZI cells associate the CS+ with the FS and become gradually more excited (in both proportions and magnitude) after learning, coinciding with a gradual increase in CS+ evoked freezing. This finding is in conflict with a previous report where no plasticity was observed in the *in vivo* extracellular activity of ZI cells to successive presentations of CS+ during fear conditioning[14]. However, the previous study only reported the absolute change in activity across multiple CS+ windows without taking into account how these cells behaved immediately before and how CS+ modulated this activity. Furthermore, the low number of units (only 12 total) recoded and differences in the behavioral task (ie. having the mice restrained in a head-fixed position, only one conditioning session) could also contribute to the discrepancy. In sharp contrast to the CS+, ZI cells learn to become inhibited by the CS- and consequently, mainly discriminate between the CS+ and the CS- by exhibiting higher activity towards the CS+.

Our observations suggest that the ZI neurons are strongly activated by fear-evoking stimuli and once a fear association is learned, activated by fear-predictive cues which produces high levels of evoked freezing while inhibited by neutral cues

with low freezing. These findings closely support studies where loss-of-function manipulations in the ZI impaired freezing to fear predictive cues during recall[13,16] rather than the report where the inactivation of ZI GAD2-expressing cells enhanced freezing[14]. Future studies should focus on the gain-of-function side and investigate whether entraining the activity of the ZI to cues in the absence of aversive stimuli is sufficient to evoke cued fear. In behavioral paradigms with both fear-predictive and neutral cues, based on our findings, a general increase in the excitability of ZI neurons would reduce the effect size of CS+ excitation and potentiate CS- inhibition, consequently resulting in a reduction in freezing to both CS+ and CS-. Conversely, a general decrease in the excitability would enhance freezing to both cues. Indeed, these scenarios were observed in a previous study where chemogenetic tools were applied prior to fear recall[17], supporting our theory.

In addition, we provide substantial evidence supporting the role of the ZI in fear generalization[17] with the response profiles of ZI neurons dependent on the extent mice generalized fear. In contrast to the FnG mice where ZI neurons learned to differentiate CS+ from CS- in a biased manner (consistently being more activated by the CS+), the response profiles of ZI cells in the FG mice are more heterogenous.

Avoiding cues predictive of strong threats is essential for survival. It is no surprise that many brain areas are hardwired to encode this association[5–12]. Recent studies suggest that the ZI may play a role in associative fear learning[13–17], we provide valuable insights into the way ZI neurons encode important aspects of conditioned fear and fear generalization.

Methods

Animals

Adult (6-8 weeks old) male C57BL/6 mice were bred in house and kept in a temperature-controlled facility under a 12-hour light/dark cycle (7am to 7pm, light period) with standard chow and water provided ad libitum. All experimental procedures were conducted during the light period. All experimental procedures were approved by the Institutional Animal Care Office of the University of Basel and the Cantonal Veterinary Office of Basel under the license number 2742.

Surgery

Mice were anesthetized with Isoflurane (5% for induction, 1.5% for maintenance, Provet Healthcare, EZ Anesthesia Systems) in O_2 and placed onto the stereotaxic frame (World Precision Instruments). The eyes were covered by a custom mixed eye lube composed of vegetable oil and petroleum jelly (Vaseline). Lidocaine (0.2mg/kg, Stueli Pharma) was injected (subcutaneous) above the skull. The skin was disinfected through successive applications of Betadine (Mundipharma) and ethanol (70%, Sigma-Aldrich). Hair above the skull were shortened with surgical scissors (Fine Science Tools). Incisions were made to expose the skull and then thoroughly cleaned with hydrogen peroxide (3%, Sigma-Aldrich), ethanol, and saline (Braun). The skull was etched with surgical blades (Swann-Morton) before drilling holes above the ZI (1.3mm posteriorly to the Bregma, 0.7mm laterally to the midline, 4.9mm below the surface of the skull[24]). Viral construct containing the GCaMP6m (AAV1-CaMKIIα-GCaMP6m-WPE-SV40, Ready to Image Virus, Inscopix) was injected (250nl) into the ZI with a piston operated injector system (Narishige). Mice were stitched with tissue

absorptive silk sutures (SABANNA) and allowed to recover for 2 weeks before implantation. The mice were prepared as previously described. Two small holes were drill anterior to the Bregma and screws were inserted. A needle (26-guage, Braun) was stereotaxically lowered (0.1mm) above the ZI and then a GRIN (0.6mm diameter, 7.3mm long, Inscopix) lens already integrated with a baseplate was implanted at the same location. A custom metal head-bar (0.4cm wide, 2cm long) was placed on the side and pointing to the posterior direction. The lens was fixed to the skull with a combination of adhesive (Pattex) and light-curable (Kulzer, Kerr) glue and secured together with the head-bar to the skull with a fixed headcap built from dental cement (Kulzer). Buprenorphine (Reckitt Benckiser) was administered (intraperitoneal, 0.1g/kg) as necessary to alleviate pain.

Fear Conditioning with Calcium Imaging

Implanted were checked bi-weekly until the area below the lens have cleared and GCaMP6m labeled cells can be visualized. To do so, mice were held by the head-bar on a custom-built running wheel while the miniscope (Inscopix) is attached. ZI calcium transients were recorded by the nVoke2 (Inscopix) system and visualized through the Inscopix Data Acquisition Software (IDAS). Once cells could be visualized, mice were individually handled and habituated to the experimental room (5 mins per day for 3 consecutive days). Following the last handling day, mice were subjected to a 7-day fear conditioning protocol (pre-conditioning, 5 conditioning days, and test day). On each day, the miniscope is first attached and mice were then placed into either a plexiglass box (20cm wide, 25cm long, 15cm tall) covered with polka-dots (context A, pre-conditioning/test days, cleaned with 1% acetic acid) or a different (context B,

conditioning days, cleaned with 70% ethanol) plexiglass box (20cm wide, 22.5cm long, 11.5cm tall) with metal gridded floors (Med Associates Inc) and bedding below (replaced between each animal). In each session, a baseline period was first recorded to measure the contextual freezing. Auditory tones (7kHz CS-, 12kHz CS+) were presented (85 dB all tones, 30s/3 times each in pre-conditioning day and 10s/5 times each for conditioning days and 10s/4 times each on the test day) in a randomized order (except for the test day where CS- are presented consecutively and followed by CS+) with a randomized inter-tone interval (ITI) with a 100s average duration (70-130s for pre-conditioning and test days and 50-150s for conditioning days). The duration, number of tones, and ITI were designed to vary and randomized when feasible to reduce expectation and the likelihood that mice attribute either of these factors as fear predictive. Shocks (2s, 0.6mA) were delivered immediately following the CS+ presentations during the conditioning days. These cues were controlled and delivered by ANYMAZE (Stoeling). Videos were captured by a camera (The Imaging Source) placed from above (or at a 45-degree angle) at a fixed sampling rate (30Hz) and freezing was detected with ANYMAZE (1s minimum). Calcium transients were recorded by IDAS. The synchronization between the behavioral and calcium recordings were made possible by the delivery of a short TTL (time-to-live) pulse at the start and end of the fear conditioning protocol and is recorded by the IDAS. Timestamps for all CS- and CS+ presentations are recorded in ANYMAZE and also by IDAS through TTL pulses delivered by ANYMAZE. The resulting files with the timestamped freezing detection, as well as the behavioral and calcium recordings were exported for further analyses.

Histology

Mice were anesthetized with a lethal injection (intraperitoneal) of pentobarbital (0.3mg/kg, Stueli Pharrma). Mice were laid flat on a styrofoam board and pinned down with needles (32G, Braun). Incisions were made to expose the heart. Mice were then perfused with a cold phosphate buffered saline (PBS, Sigma, 25mL) solution and equal volume of 4% paraformaldehyde (PFA, Sigma) fixative in PBS. The head was removed and post-fixed for at least 48 hours in the PFA fixative. The brain was then carefully extracted and immersed in 30% sucrose (Sigma) in PBS until complete submersion. Sections were prepared with a cryostat (Leica 1950CM) and mounted on glass slides (Superfrost Plus, Thermo Scientific) in a DAPI containing mounting solution (ProLong God Antifade, Invitrrogen) and covered with borosilicate cover glass (VWR).

Imaging

To verify the expression of GCaMP6m and the placement of the lens, mounted sections were imaged with a Zeiss LSM700 upright confocal microscope controlled by the ZEN Black acquisition software (Zeiss). Images were acquired with a 20x (PLAN APO, 0.8NA, air) or 40x (PLAN APO, 1.3NA, oil) objectives. Fixed wavelength (405nm, 488nm) lasers were used to visualize DAPI and GCaMP6m, respectively. Simultaneous differential interference contrast imaging was used to visualize the anatomical landmarks. Images were processed with FIJI.

Analysis

Freezing: The proportion of time mice spent freezing in the baseline contextual freezing window as well as during tone presentations were analyzed with a custom-written script in MATLAB (Mathworks) and verified visually with the behavioral video.

Calcium Imaging: Acquired calcium recordings were first processed with the Inscopix Data Processing Software (IDPS) to extract calcium transients from unique individual cells. The video is pre-processed, spatially filtered, and motion corrected. Individual traces were extracted from the video with the principal component (PCA) and independent component (ICA) analysis algorithms with no downsampling. Traces with abnormal physiological transients (ie. peaks lasting over minutes) or abnormal maximal intensity projection visualizations (ie. multiple cells) were excluded. For the identification of longitudinally tracked cells, processed traces and cell maps across all analyzed days (pre-conditioning P, conditioning day 1 C1, conditioning day 5 C5, and test day T) were longitudinally registered with a spatial alignment algorithm and manually verified.

Files containing the individual traces and the general-purpose input/output (GPIO) traces were extracted and fed through a custom-written script in MATLAB. Calcium transients were denoised, normalized (per trace per day), and then binned (500ms). Tone (CS- and CS+) presentations were identified through timestamps recorded in the corresponding GPIO traces and the normalized activity in the surrounding windows (10s before tone and 45s after) were extracted. Within day average traces were generated for each cell and tone. To characterize if a cell is responsive to a tone, the average activity during the baseline (10s before onset) window is compared (Wilcoxon's rank sum test) with that of the tone (only the first 10s is considered for pre-

conditioning day). Cells are classified as either excited ($p< 0.05$, tone baseline delta > 0), inhibited ($p< 0.05$, tone baseline delta < 0), or non-responsive ($p> 0.05$). Shock responses were characterized in the manner by comparing activity during the baseline (4s before CS+ onset) window and a 4s period after shock onset (shock analysis window). To take into account a minority of transient shock responses where the majority of rise as well as decay were captured within the analysis window, a shortened baseline window (2s) was compared with the same period within the shock analysis window in a rolling manner. To determine if cells can differentiate CS+ from CS-, comparisons were made between the two tone windows.

In addition, to identify whether the observed responses could be discriminated from spontaneous fluctuations intrinsic to the recorded cell, the distributions of activity within all cue and baseline (or another cue) windows were concatenated and analyzed using the receiver operating characteristic analysis to calculate the discrimination index (DI = (Area Under the ROC curve – 0.5) x 2) between the cue and the baseline. To model spontaneous fluctuations, the calcium trace was circularly shifted 1000 times by a random integer and DIs were similarly calculated for each cue. Cue responses that can be positively (DI > 97.5^{th} percentile of shifted DIs), negatively (DI < 2.5^{th} percentile of shifted DIs), or not discriminated from spontaneous fluctuations were identified ($\alpha = 0.05$).

To investigate whether the CS+ responses throughout conditioning can become shifted towards that of the US (FS), the similarity between each CS+ and US pairing within each conditioning day is compared by examining the Euclidean distance (ED) between the two (shock analysis window and the first 4s of CS+ window). To examine whether this shift could be consolidated across days, the day average ED were

compared across days. In order to verify that potential changes in ED across pairings or across days are not influenced by random fluctuation, randomly shifted (1000 times) ED were calculated for each pairing and comparisons were made between the data-driven and random ED within and across conditioning days.

For populational analyses, cells were pooled across mice within days and analyzed. Analyzed data are stratified between mice that developed high (FG, >50% freezing to CS- on T) and low (FNG, <50% freezing to CS- on T) levels of fear generalization. For longitudinally tracked cells, cells were first characterized by their response to cues on the last day they were presented (T for tones and C5 for FS) and traced back in time.

Statistics

Statistical comparisons for the contextual freezing across days in all mice were conducted with one-way analysis of variance (ANOVA) and two-ways ANOVA in comparisons where FG and FNG mice were separated. Tones evoked freezing across days were analyzed with the two-ways ANOVA. Comparisons of tone (both CS- and CS+) response amplitude and DI across days in the populational analyses were made with the one-way ANOVA for each type of response individually and with the two-way ANOVA for the longitudinally tracked cells. Similar comparisons for shock responses were conducted with unpaired two-tail t-tests. All comparisons involving the Euclidean distance between CS+ and FS were made with the two-way ANOVA. When applicable, Bonferroni's multiple comparisons tests were applied. The significance level is always set at 0.05. All statistical comparisons (except the classification of cell responses using the Wilcoxon Ranksum test, computed with MATLAB) were performed by Prism (Graphpad).

References:

1. Blanchard, D. C. & Blanchard, R. J. Chapter 2.4 Defensive behaviors, fear, and anxiety. in *Handbook of Behavioral Neuroscience* (eds. Blanchard, R. J., Blanchard, D. C., Griebel, G. & Nutt, D.) vol. 17 63–79 (Elsevier, 2008).

2. LeDoux, J. Rethinking the emotional brain. *Neuron* **73**, 653–676 (2012).

3. Maren, S. Neurobiology of Pavlovian fear conditioning. *Annu Rev Neurosci* **24**, 897–931 (2001).

4. Tovote, P., Fadok, J. P. & Lüthi, A. Neuronal circuits for fear and anxiety. *Nature Reviews Neuroscience* **16**, 317–331 (2015).

5. Ciocchi, S. *et al.* Encoding of conditioned fear in central amygdala inhibitory circuits. *Nature* **468**, 277–282 (2010).

6. Grewe, B. F. *et al.* Neural ensemble dynamics underlying a long-term associative memory. *Nature* **543**, 670–675 (2017).

7. Courtin, J. *et al.* Prefrontal parvalbumin interneurons shape neuronal activity to drive fear expression. *Nature* **505**, 92–96 (2014).

8. Cummings, K. A. & Clem, R. L. Prefrontal somatostatin interneurons encode fear memory. *Nat Neurosci* **23**, 61–74 (2020).

9. Tang, J., Wagner, S., Schachner, M., Dityatev, A. & Wotjak, C. T. Potentiation of amygdaloid and hippocampal auditory-evoked potentials in a discriminatory fear-conditioning task in mice as a function of tone pattern and context. *Eur J Neurosci* **18**, 639–650 (2003).

10. Xu, C. *et al.* Distinct Hippocampal Pathways Mediate Dissociable Roles of Context in Memory Retrieval. *Cell* **167**, 961-972.e16 (2016).

11. Rizzi, G., Li, Z., Hogrefe, N. & Tan, K. R. Lateral ventral tegmental area GABAergic and glutamatergic modulation of conditioned learning. *Cell Rep* **34**, 108867 (2021).

12. Tovote, P. *et al.* Midbrain circuits for defensive behaviour. *Nature* **534**, 206–212 (2016).

13. Loskutova, L. V., Vinnitskii, I. M. & Il'yuchenok, R. Yu. Participation of the zona incerta in mechanisms of the conditioned avoidance reaction. *Neurosci. Behav. Physiol.* **11**, 60–62 (1981).

14. Chou, X.-L. *et al.* Inhibitory gain modulation of defense behaviors by zona incerta. *Nat Commun* **9**, 1151 (2018).

15. Burrows, A. M. *et al.* Limbic and motor function comparison of deep brain stimulation of the zona incerta and subthalamic nucleus. *Neurosurgery* **70**, 125–130; discussion 130-131 (2012).

16. Zhou, M. *et al.* A central amygdala to zona incerta projection is required for acquisition and remote recall of conditioned fear memory. *Nat. Neurosci.* **21**, 1515–1519 (2018).

17. Venkataraman, A. *et al.* Modulation of fear generalization by the zona incerta. *Proc. Natl. Acad. Sci. U.S.A.* **116**, 9072–9077 (2019).

18. Taylor, J. A. *et al.* Single cell plasticity and population coding stability in auditory thalamus upon associative learning. *Nat Commun* **12**, 2438 (2021).

19. MacNamara, A. *et al.* Neural correlates of individual differences in fear learning. *Behav Brain Res* **287**, 34–41 (2015).

20. Bush, D. E. A., Sotres-Bayon, F. & LeDoux, J. E. Individual differences in fear: isolating fear reactivity and fear recovery phenotypes. *J Trauma Stress* **20**, 413–422 (2007).

21. Graham, B. M. & Richardson, R. Individual differences in the expression of conditioned fear are associated with endogenous fibroblast growth factor 2. *Learn Mem* **23**, 42–45 (2016).

22. Duvarci, S., Bauer, E. P. & Paré, D. The bed nucleus of the stria terminalis mediates inter-individual variations in anxiety and fear. *J Neurosci* **29**, 10357–10361 (2009).

23. Liu, K. *et al.* Lhx6-positive GABA-releasing neurons of the zona incerta promote sleep. *Nature* **548**, 582–587 (2017).

24. Keith, F. B. J. & Paxinos, G. *The Mouse Brain in Stereotaxic Coordinates*. (Elsevier Inc., 2007).

Acknowledgements

We thank the past and current members of the Tan Lab for constructive input, the Biozentrum Imaging Facility for microscopy training, and the Inscopix team for technical support in regards to the calcium imaging experiments.

Author Contributions

Z. Li, G. Rizzi, and K.R. Tan all contributed to the experimental design. G.Rizzi conducted the calcium imaging experiments. Z. Li performed all analyses and prepared the manuscript. K.R. Tan provided supervision and corrected the manuscript.

Competing Interests

The authors declare no competing interests.

Materials & Correspondence

All requests for materials and code should be addressed to K.R. Tan.

Figures

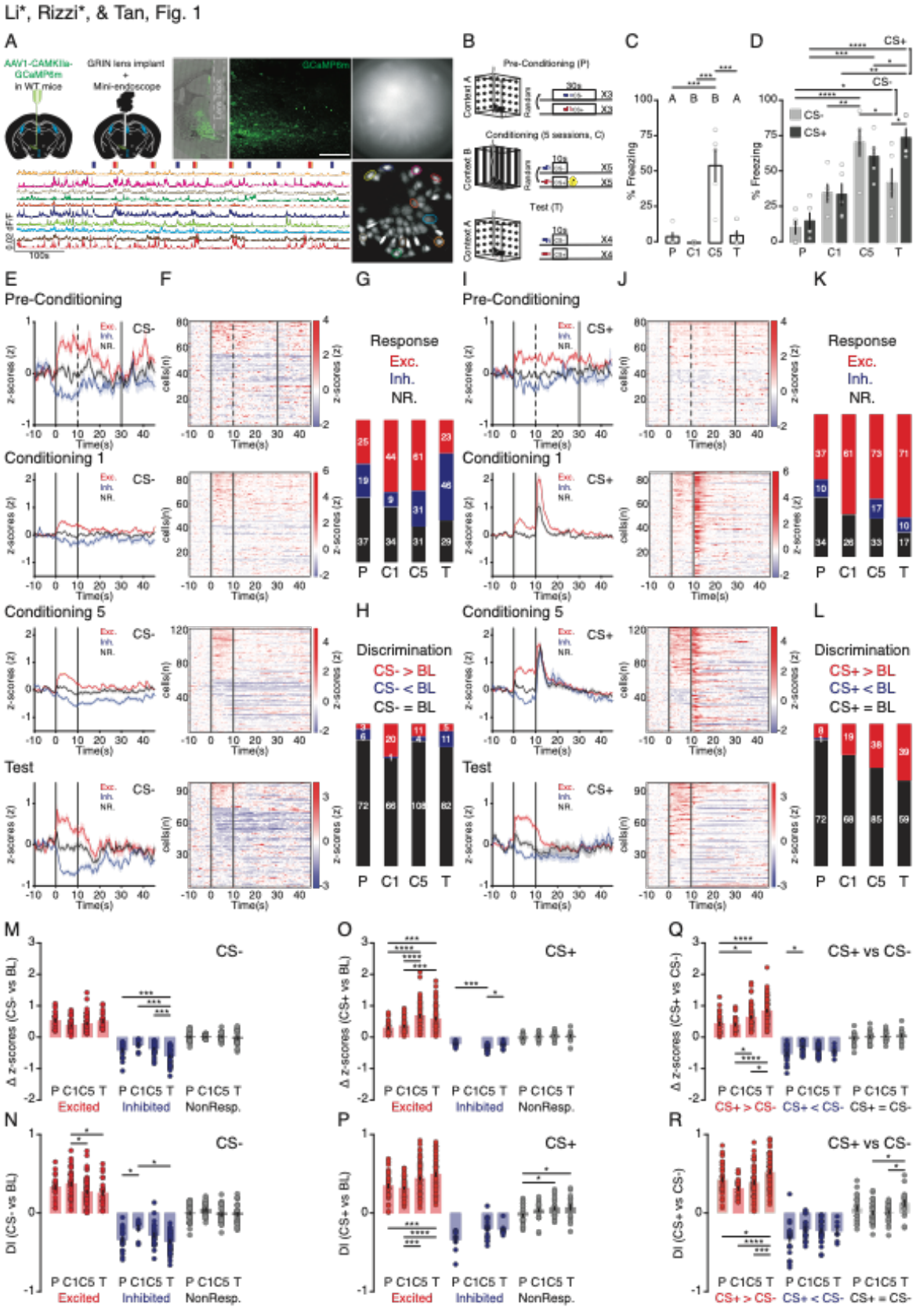
Li*, Rizzi*, & Tan, Fig. 1
A
B
C
D
E
F
G
H
I
J
K
L
M
N
O
P
Q
R
Pre-Conditioning
Conditioning 1
Conditioning 5
Test
CS-
CS+
Response
Exc.
Inh.
NR.
Discrimination
CS- > BL
CS- < BL
CS- = BL
CS+ > BL
CS+ < BL
CS+ = BL
CS+ vs CS-
Excited
Inhibited
NonResp.
P C1 C5 T

Figure 1. ZI neurons are bi-directionally modulated by auditory cues and are plastic across over fear conditioning.

A) Design to visualize calcium dynamics in ZI neurons: injection of GCaMP6m containing virus, GRIN lens implant, low and high magnification confocal image of ZI containing slice with GCaMP6m expression in the ZI and lens track above (500 and 100μm scale bar, respectively), raw and maximal projection images of field-of-view with example traces.

B) Fear conditioning paradigm.

C) Bar graph of contextual fear across P, C1, C5, and T.

D) Bar graph of cued fear across P, C1, C5, and T.

E) Average traces ($\pm$ SEM, shaded) of categorized cells responding to the CS- (black bars) across P, C1, C5, and T.

F) Heatmap of CS- responses across P, C1, C5, and T.

G) Stacked bar chart depicting the proportion of categorized responses to CS- across P, C1, C5, and T.

H) Stacked bar chart showing the proportion of CS- responses that can be discriminated from intrinsic fluctuations within the whole trace across P, C1, C5, and T.

I) Average traces of categorized cells responding to the CS+ across P, C1, C5, and T.

J) Heatmap of CS+ responses across P, C1, C5, and T.

K) Stacked bar chart depicting the proportion of categorized responses to CS+ across P, C1, C5, and T.

L) Stacked bar chart with the proportion of CS+ responses that can be discriminated from intrinsic fluctuations across P, C1, C5, and T.

M) Bar graph of the amplitude of CS- responses across P, C1, C5, and T.

N) Bar graph of the DI of CS- responses across P, C1, C5, and T.

O) Bar graph of the amplitude of CS+ responses across P, C1, C5, and T.

P) Bar graph of the DI of CS+ responses across P, C1, C5, and T.

Q) Bar graph of the amplitude difference between CS+ and CS- responses across P, C1, C5, and T.

R) Bar graph of the DI between CS+ and CS- responses across P, C1, C5, and T.

Data are presented as mean $\pm$ SEM *p<0.05, **p<0.01, ***p<0.001, ****p<0.0001, 81-123 cells from 5 mice.

Li*, Rizzi*, & Tan, Fig. 2

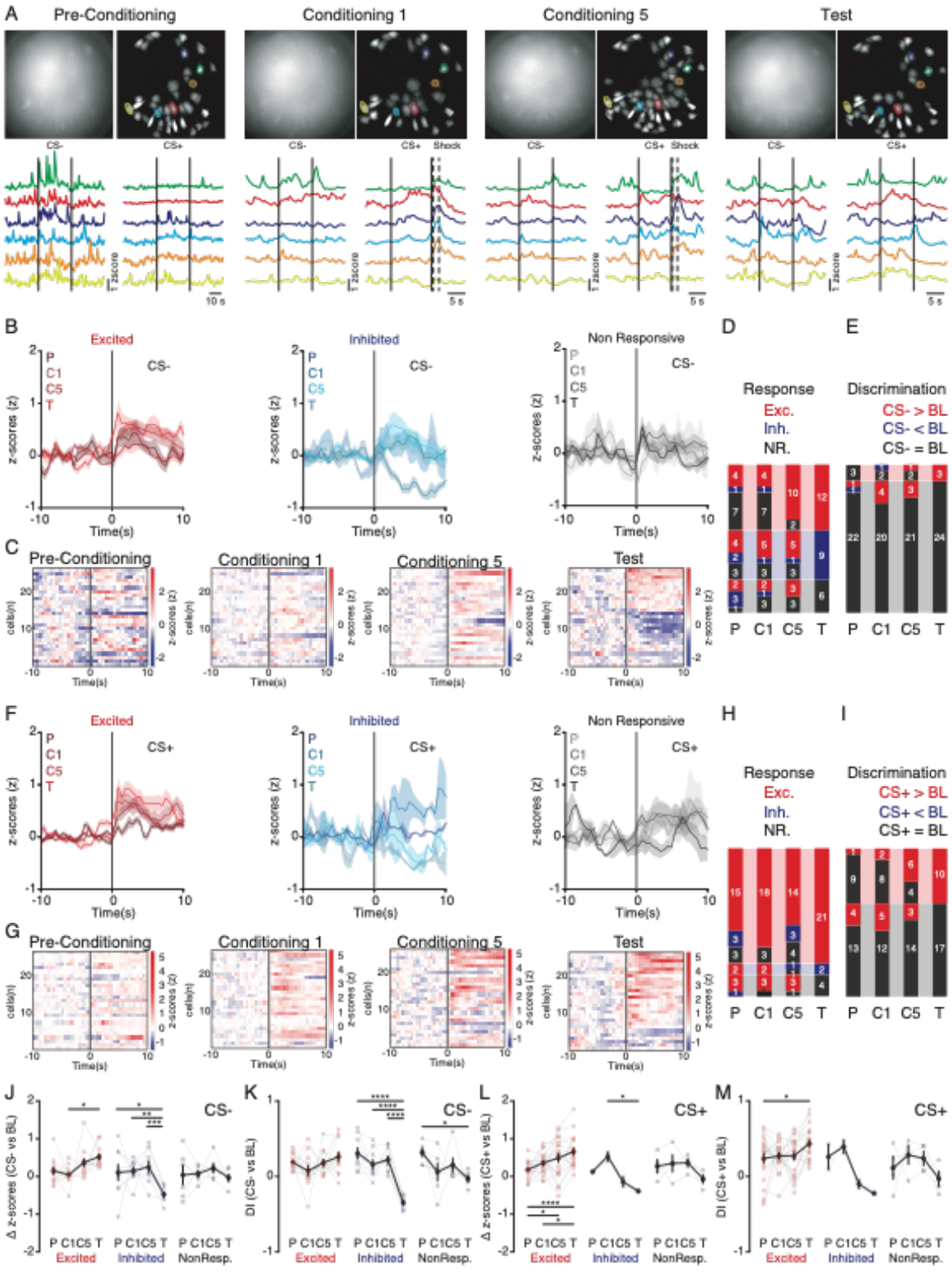

Figure 2. Fear learning gradually potentiate ZI excitatory responses to predictive cues.

A) Example longitudinally tracked cells across P, C1, C5, and T: example raw and maximal projection images with example cell traces (black bars represent tones and shock windows).

B) Average traces of T day CS- responsive cells tracked across P, C1, C5, and T.

C) Heatmaps of tracked CS- responses across P, C1, C5, and T.

D) Stacked bar chart of the proportion of CS- responsive cells on the T day and their response profiles before.

E) Stacked bar chart with the proportion of CS- responses that can be discriminated from spontaneous activity across P, C1, C5, and T.

F) Average traces of T day CS+ responsive cells tracked across P, C1, C5, and T (black bar denotes tone onset).

G) Heatmaps of tracked CS+ responses across P, C1, C5, and T.

H) Stacked bar chart showing the proportion of CS+ responsive cells on the T day and how they responded days prior.

I) Stacked bar chart depicting the proportion of CS+ responses that can be discriminated from intrinsic cell activity across P, C1, C5, and T days.

J) Line graph summarizing the tracked changes in amplitude of CS- responses across P, C1, C5, and T days.

K) Line graph showing the tracked changes in the DI of CS- responses across P, C1, C5, and T days.

L) Line graph depicting the tracked changes in the amplitude of CS+ responses across P, C1, C5, and T days.

M) Line graph with the tracked DI of CS+ responses across P, C1, C5, and T days. Data are presented as mean ± SEM *p<0.05, **p<0.01, ***p<0.001, ****p<0.0001, 27 cells from 2 mice.

Li*, Rizzi*, & Tan, Fig. 3

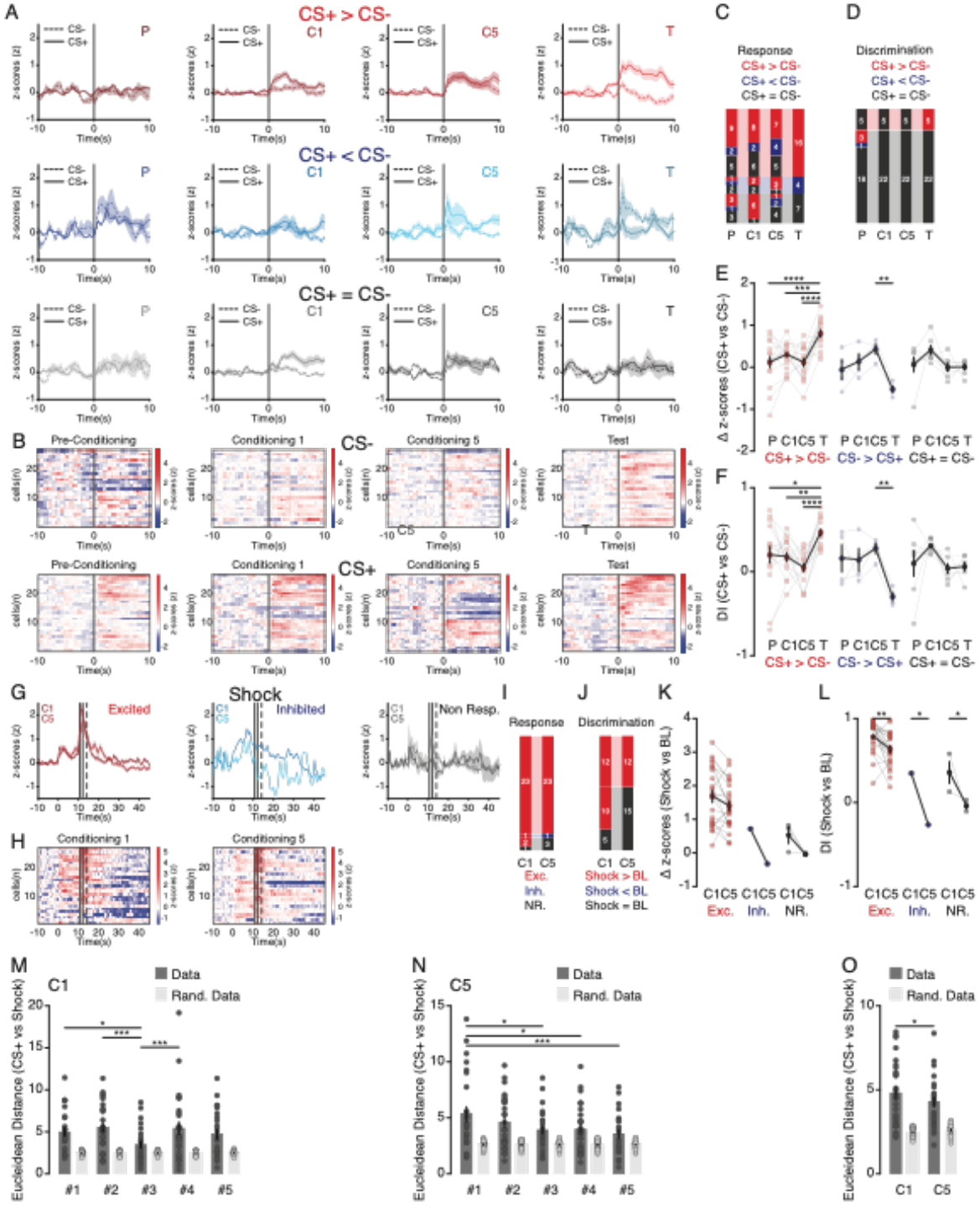

Figure 3. ZI neurons associate CS+ with footshocks and learn to discriminate between CS+ from CS-.

A) Average traces of cells that are differentially modulated by CS+ and CS- on the T day tracked across P, C1, C5, and T days (black bar denote tone onset).

B) Heatmaps of tracked responses to CS+ and CS- across P, C1, C5, and T.

C) Stacked bar chart of proportion of cells that are differentially modulated by CS+ and CS- during the T day and their bias during the days before.

D) Stacked bar chart showing the proportion of cells whose discrimination between CS+ and CS- is grossly different from disparity among spontaneous activity across P, C1, C5, and T days.

E) Line graph summarizing the tracked amplitude difference between CS+ and CS- responses across P, C1, C5, and T days.

F) Line graph depicting the tracked changes in DI between CS+ and CS- across P, C1, C5, and T days.

G) Average traces of shock responsive cells on the C5 and their shock responses also during the first conditioning day (solid and dotted bar denotes shock and shock analysis windows, respectively).

H) Heatmaps of tracked shock responses across C1 and C5.

I) Stacked bar chart with the proportion of shock responsive cells on C5 and their response profile on C1.

J) Stacked bar chart of the proportion of shock responses that can be discriminated from intrinsic trace fluctuations across C1 and C5.

K) Line graph summarizing the tracked changes in the amplitude of shock responses across C1 and C5.

L) Line graph with the tracked changes in the DI of shock responses across C1 and C5.

M) Bar graph with the Euclidean Distance between the CS+ and FS pairings during C1.

N) Bar graph of the Euclidean Distance between the CS+ and FS pairings on C5.

P) Bar graph depicting the average Euclidean Distance between the CS+ and FS pairings tracked across C1 and C5.

Data are presented as mean $\pm$ SEM *p<0.05, **p<0.01, ***p<0.001, ****p<0.0001, 27 cells from 2 mice.

Li*, Rizzi*, & Tan, Fig. 4

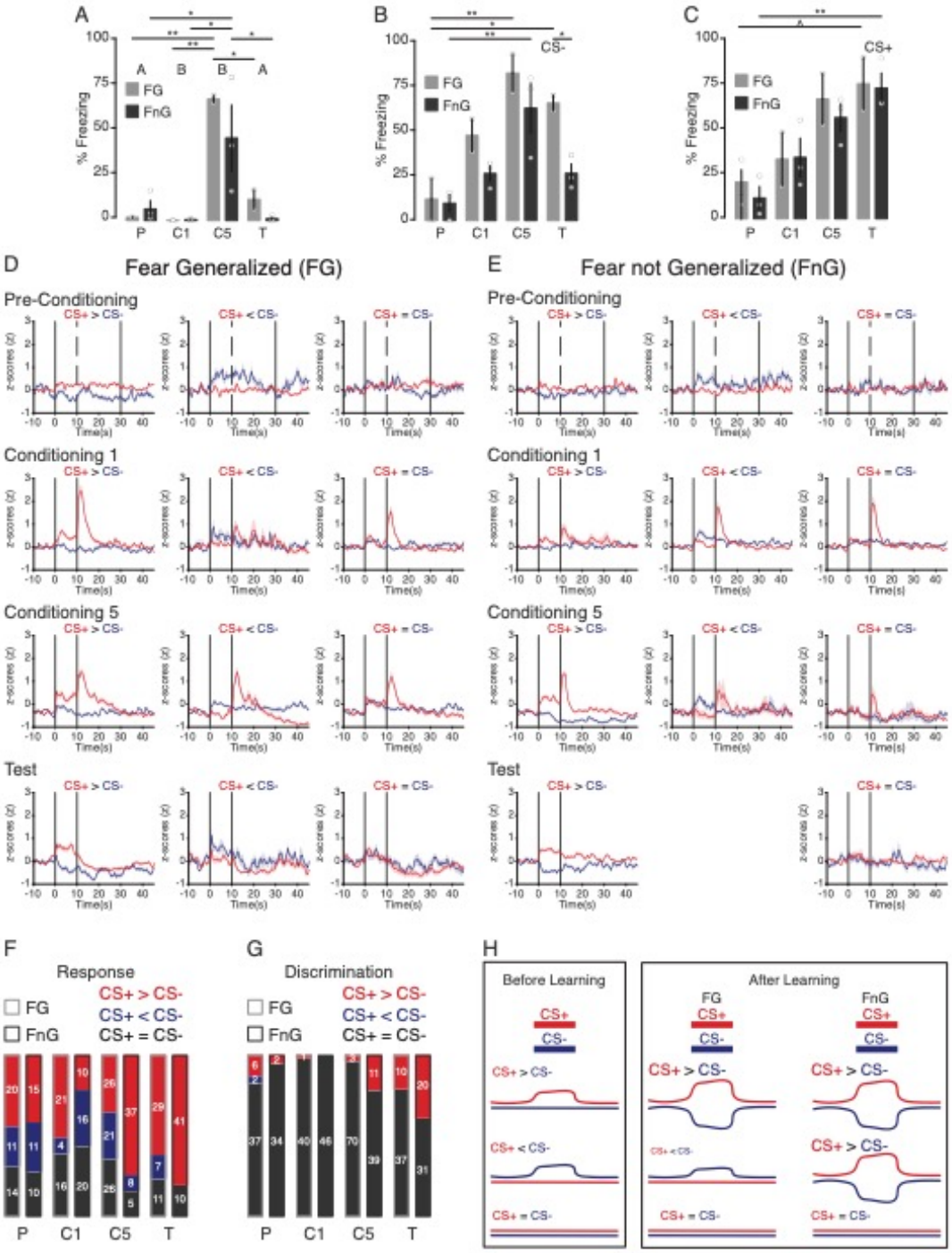

Figure 4. ZI neurons in fear generalized and not generalized mice differentially learn to discriminate between CS+ and CS-

A) Bar graph of contextual fear between fear generalized and not generalized mice across P, C1, C5, and T.

B) Bar graph with proportion of time spent freezing during the CS- in fear generalized and not generalized mice across P, C1, C5, and T.

C) Bar graph showing the proportion of freezing during the CS+ in fear generalized and not generalized mice across P, C1, C5, and T.

D) Average traces of cells differentially modulated by CS+ and CS- in fear generalized mice across P, C1, C5, and T.

E) Average traces of cells that respond differentially to CS+ and CS- in mice that did not developed fear generalization across P, C1, C5, and T.

F) Stacked bar chart showing the proportion of cells differentially modulated by CS+ and CS- in fear generalized and not generalized mice across P, C1, C5, and T.

G) Stacked bar chart depicting the proportion of cells whose discrimination between CS+ and CS- are significantly different from that of intrinsic activity fluctuations in fear generalized and not generalized mice across P, C1, C5, and T.

H) Model highlighting the differences in CS+ and CS- discrimination in fear generalized and not generalized mice following fear conditioning.

Data are presented as mean $\pm$ SEM ^p = 0.0572 (trend), *p<0.05, **p<0.01, ***p<0.001, ****p<0.0001, 41-73 cells (fear generalized, 2 mice) and 36-51 cells (fear not generalized, 3 mice).

Li*, Rizzi*, & Tan, Fig. S1

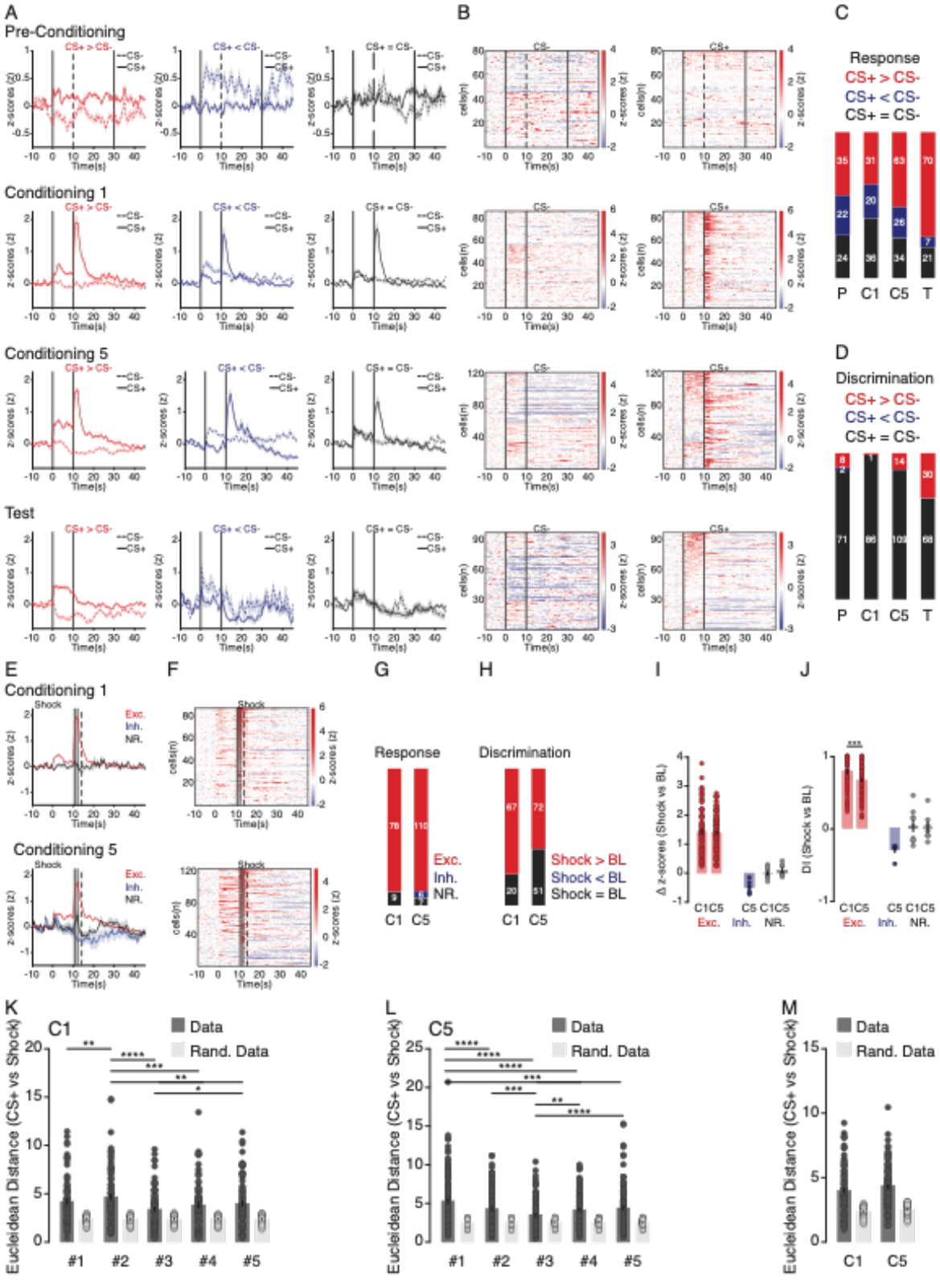

Figure S1. On the population level, the representations of CS+ and CS- become more distinguishable while that of the CS+ and footshocks become more similar.

A) Average traces of cells that are differentially modulated by CS+ and CS- in P, C1, C5, and T days (black bars denote tone windows).

B) Heatmaps of cell responses to CS+ and CS-, sorted by the difference between CS+ and CS- modulations in P, C1, C5, and T days.

C) Stacked bar chart of proportion of cells differentially modulated by CS+ as compared to CS- in P, C1, C5, and T days.

D) Stacked bar chart of proportion of cells whose discrimination between CS+ and CS- is significantly distinct from intrinsic activity fluctuations in P, C1, C5, and T days.

E) Average traces of shock responsive cells in C1 and C5 days (solid and dotted bar denotes shock and shock analysis windows, respectively).

F) Heatmaps of shock responses in C1 and C5.

G) Stacked bar chart showing proportion of shock responses in C1 and C5.

H) Stacked bar chart of shock responses that can be discriminated from spontaneous activity in C1 and C5.

I) Bar plot depicting the amplitude of shock responses in C1 and C5.

J) Bar plot denoting the DI of shock responses in C1 and C5.

K) Bar graph with the Euclidean distance between CS+ and FS pairings within C1.

L) Bar graph of the Euclidean distance between CS+ and FS pairings within C5.

M) Bar graph presenting the average Euclidean distance between CS+ and FS pairings in C1 and C5.

Data are presented as mean $\pm$ SEM *p<0.05, **p<0.01, ***p<0.001, ****p<0.0001, 81-123 cells from 5 mice.

Li*, Rizzi*, & Tan, Fig. S2

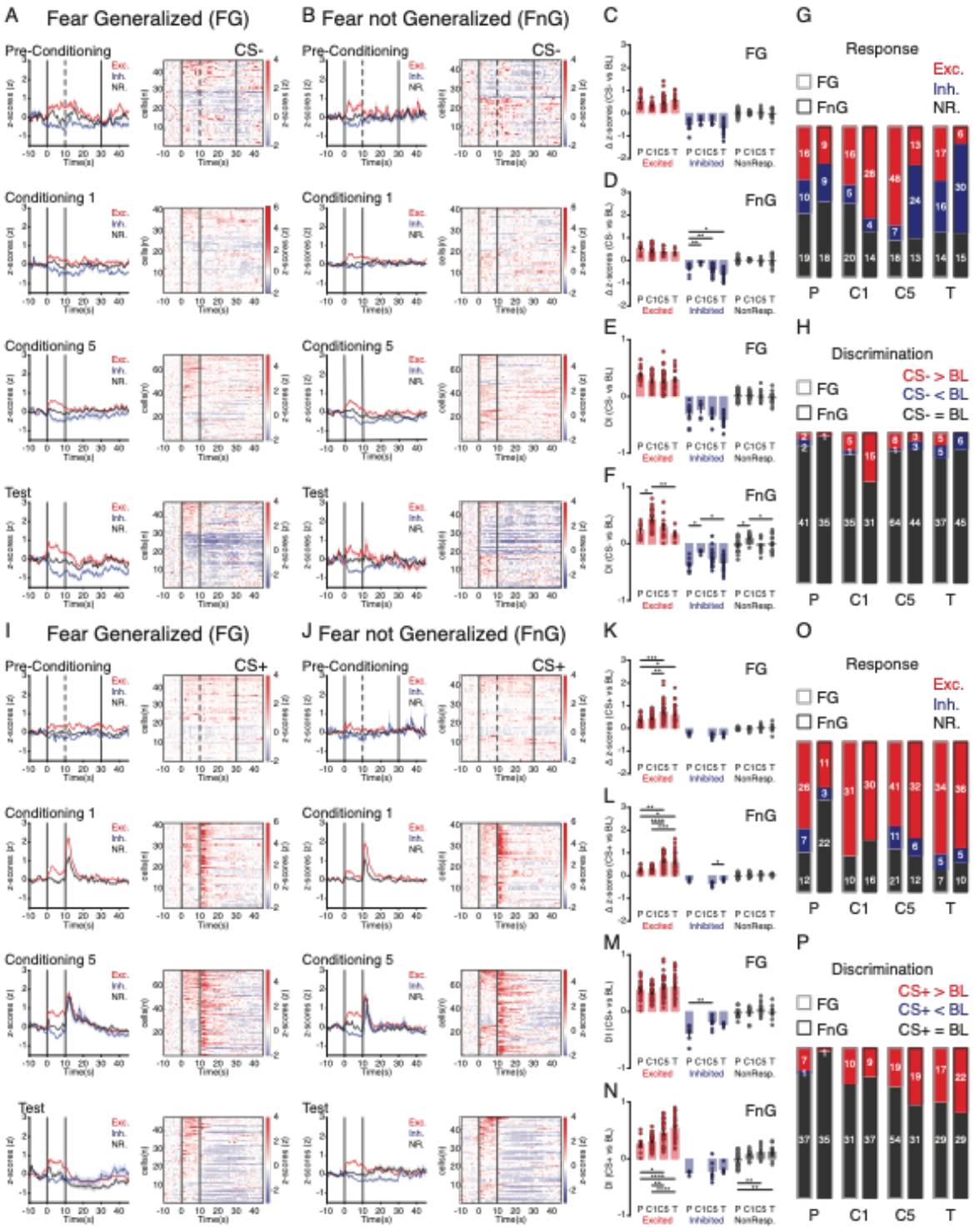

Figure S2. ZI neurons of fear generalized and not generalized mice encode CS+ similarly but differentially encode CS-.

A) Average traces and heatmaps of CS+ responses from fear generalized mice in P, C1, C5, T days (black bars depict tone windows).

B) Average traces and heatmaps of CS+ responses from mice that did not generalized fear.

C) Bar graph with the amplitude of CS+ responses from mice that generalized fear.

D) Bar graph with the DI of CS+ responses of mice that generalized fear.

E) Bar graph with the amplitude of CS+ responses from mice that did not generalized fear.

F) Bar graph with the DI of CS+ responses of mice that did not generalized fear.

G) Stacked bar chart with proportion of CS+ responsive cells between fear generalized and not generalized mice.

H) Stacked bar chart with proportion of cells that can discriminate CS+ responses from spontaneous activity fluctuations between fear generalized and not generalized mice.

I) Average traces and heatmaps of CS- responses from fear generalized mice in P, C1, C5, T days.

J) Average traces and heatmaps of CS- responses from mice that did not generalized fear.

K) Bar graph with the amplitude of CS- responses from mice that generalized fear.

L) Bar graph with the DI of CS- responses of mice that generalized fear.

M) Bar graph with the amplitude of CS- responses from mice that did not generalized fear.

N) Bar graph with the DI of CS- responses of mice that did not generalized fear.

O) Stacked bar chart with proportion of CS- responsive cells between fear generalized and not generalized mice.

P) Stacked bar chart with proportion of cells that can discriminate CS- responses from spontaneous activity fluctuations between fear generalized and not generalized mice. Data are presented as mean ± SEM *p<0.05, **p<0.01, ***p<0.001, ****p<0.0001, 41-73 cells (fear generalized, 2 mice) and 36-51 cells (fear not generalized, 3 mice).

Li*, Rizzi*, & Tan, Fig. S3

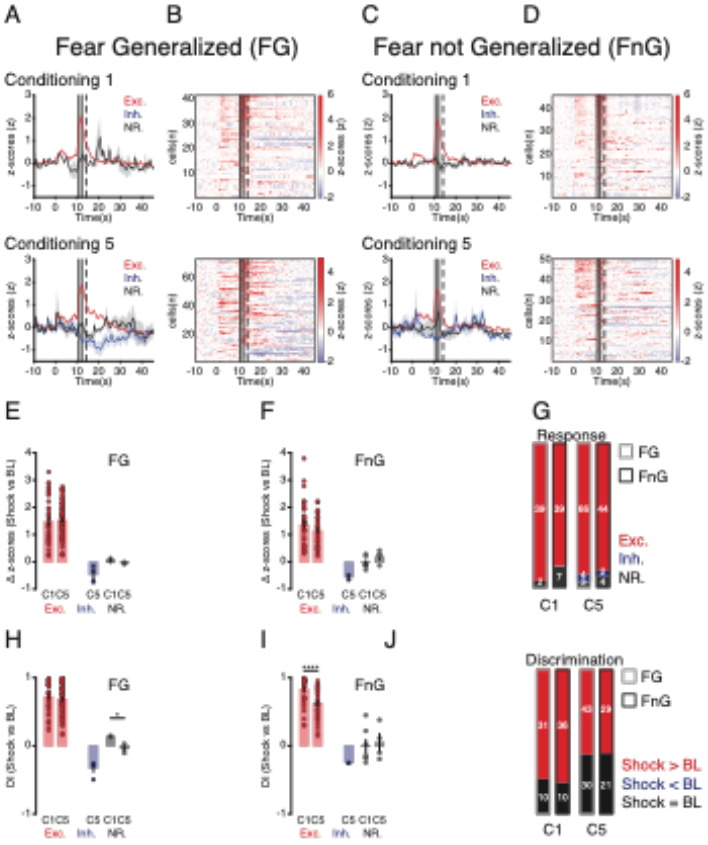

Figure S3. ZI neurons of both fear generalized and not generalized mice are strongly excited by footshocks.

A) Average traces of shock responses (solid and dotted lines denote shock and shock analysis windows) of fear generalized mice in C1 and C5 days.

B) Heatmaps of shock responses from fear generalized mice in C1 and C5 days.

C) Average traces of shock responses in mice that did not generalized fear on C1 and C5.

D) Heatmaps of shock responses in mice that did not generalize fear on C1 and C5.

E) Bar graph summarizing the amplitude of shock responses from fear generalized mice on C1 and C5 days.

F) Bar graph of the amplitude of shock responses from mice that did not generalized fear on C1 and C5.

G) Stacked bar chart showing the proportion of shock responsive cells between fear generalized and not generalized mice on C1 and C5.

H) Bar graph with the DI of shock responses in fear generalized mice on C1 and C5 days.

I) Bar graph depicting the DI of shock responses in mice that did not generalized fear on C1 and C5.

J) Stacked bar chart highlighting the proportion of shock responses that can be discriminated from spontaneous activity in mice that generalized and did not generalized fear on C1 and C5.

Data are presented as mean $\pm$ SEM *p<0.05, **p<0.01, ***p<0.001, ****p<0.0001, 41-73 cells (fear generalized, 2 mice) and 36-51 cells (fear not generalized, 3 mice).

Li*, Rizzi*, & Tan, Fig. S4

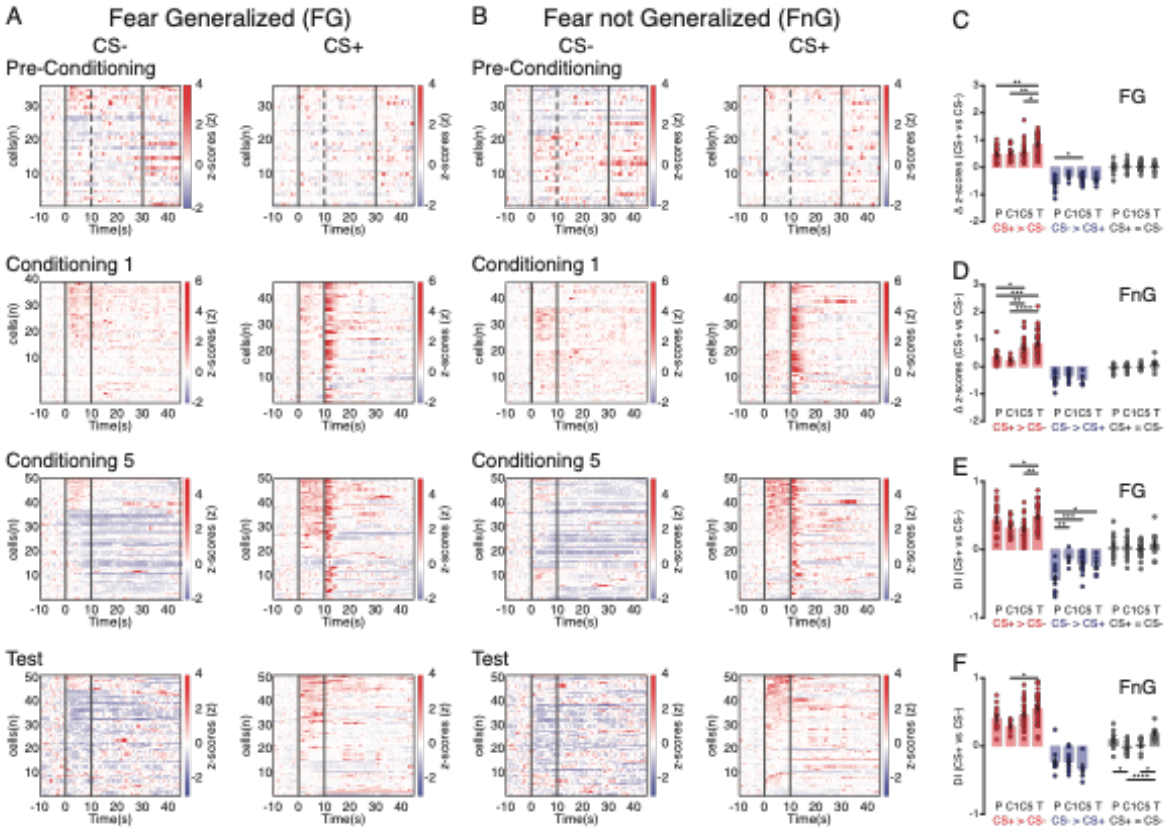

Figure S4. The magnitude of positive discrimination between CS+ and CS- is potentiated in the ZI neurons of both fear generalized and not generalized mice.

A) Heatmaps of CS+ and CS- responses from fear generalized mice in P, C1, C5, and T days, sorted by magnitude of differences between CS+ and CS- modulations (black bars highlight tone windows).

B) Heatmaps of CS+ and CS- responses from mice that did not develop fear generalization in P, C1, C5, and T days, sorted by magnitude of differences between CS+ and CS- modulations.

C) Bar graph of differences in CS+ and CS- modulations of fear generalized mice in P, C1, C5, and T days.

D) Bar graph of differences in activity between CS+ and CS- observed from mice that did not develop fear generalization in P, C1, C5, and T days.

E) Bar graph of DI between CS+ and CS- responses in fear generalized mice on P, C1, C5, and T days.

F) Bar graph of DI between CS+ and CS- responses in mice that did not generalized fear on P, C1, C5, and T days.

Data are presented as mean $\pm$ SEM *p<0.05, **p<0.01, ***p<0.001, ****p<0.0001, 41-73 cells (fear generalized, 2 mice) and 36-51 cells (fear not generalized, 3 mice).

Table S1. Statistical Information for Figure 1.

Fig. 1C	One-way ANOVA				
		SS	DF	MS	$F_{(DFn, DFd)}$	P Value
	Days	9975	3	3325	$F_{(3, 12)} = 17.27$	0.0001
	Residual	2311	12	192.6		
	Bonferroni's Multiple Comparisons Test					
				t	DF	P Value
	P vs C5			5.723	12	0.0006
	C1 vs C5			6.205	12	0.0003
	C5 vs T			5.636	12	0.0007
Fig. 1D	Two-way ANOVA					
		SS	DF	MS	$F_{(DFn, DFd)}$	P Value
	Interaction	2442	3	814.0	$F_{(3, 24)} = 3.825$	0.0227
	Tones	415.3	1	415.3	$F_{(1, 8)} = 0.9093$	0.3682
	Days	17232	3	5744	$F_{(3, 24)} = 26.99$	<0.0001
	Animal	3654	8	456.8	$F_{(8, 24)} = 2.146$	0.0708
	Residual	5107	24	212.8		
	Bonferroni's Multiple Comparisons Test					
				t	DF	P Value
	CS- vs. CS+					
	T			3.055	32.00	0.0181
	CS-					
	P vs C5			6.514	24.00	<0.0001
	P vs T			3.415	24.00	0.0136
	C1 vs C5			3.886	24.00	0.0042
	C5 vs T			3.099	24.00	0.0294
	CS+					
	P vs C5			4.935	24.00	0.0003
	P vs T			6.377	24.00	<0.0001
	C1 vs C5			2.906	24.00	0.0465
	C1 vs T			4.349	24.00	0.0013
Fig. 1M	One-way ANOVA					
	Excited Cells					
		SS	DF	MS	$F_{(DFn, DFd)}$	P Value
	Days	0.5301	3	0.1767	$F_{(3, 149)} = 3.021$	0.0317
	Residual	8.714	149	0.05849		
	Inhibited Cells					
		SS	DF	MS	$F_{(DFn, DFd)}$	P Value
	Days	1.620	3	0.5400	$F_{(3, 101)} = 10.07$	<0.0001
	Residual	5.418	101	0.05364		
	Bonferroni's Multiple Comparisons Test					
				t	DF	P Value
	P vs T			2.845	101	0.0323
	C1 vs T			4.293	101	0.0002
	C5 vs T			4.272	101	0.0003
	NonResponsive Cells					
		SS	DF	MS	$F_{(DFn, DFd)}$	P Value
	Days	0.06614	3	0.02205	$F_{(3, 127)} = 1.076$	0.3618
	Residual	2.602	127	0.02049		
Fig. 1N	One-way ANOVA					
	Excited Cells					
		SS	DF	MS	$F_{(DFn, DFd)}$	P Value
	Days	0.3503	3	0.1168	$F_{(3, 149)} = 4.184$	0.0071
	Residual	4.158	149	0.02791		
	Bonferroni's Multiple Comparisons Test					
				t	DF	P Value
	C1 vs C5			3.176	149	0.0109
	C1 vs T			2.694	149	0.0473
	Inhibited Cells					
		SS	DF	MS	$F_{(DFn, DFd)}$	P Value
	Days	0.2764	3	0.09213	$F_{(3, 101)} = 5.215$	0.0022
	Residual	1.784	101	0.01767		
	Bonferroni's Multiple Comparisons Test					

				t	DF	P Value
	P vs C1			2.705	101	0.0482
	C1 vs T			3.464	101	0.0047
				NonResponsive Cells		
		SS	DF	MS	$F_{(DFn, DFd)}$	P Value
	Days	0.1114	3	0.03713	$F_{(3, 127)} = 3.220$	0.0250
	Residual	1.465	127	0.01153		
Fig. 1O				One-way ANOVA		
				Excited Cells		
		SS	DF	MS	$F_{(DFn, DFd)}$	P Value
	Days	5.547	3	1.849	$F_{(3, 238)} = 17.41$	<0.0001
	Residual	25.27	238	0.1062		
				Bonferroni's Multiple Comparisons Test		
				t	DF	P Value
	P vs C5			5.739	238	<0.0001
	P vs T			4.347	238	0.0001
	C1 vs C5			5.687	238	<0.0001
	C1 vs T			4.066	238	0.0004
				Inhibited Cells		
		SS	DF	MS	$F_{(DFn, DFd)}$	P Value
	Days	0.1112	2	0.05561	$F_{(2, 34)} = 6.316$	0.0047
	Residual	0.2994	34	0.008806		
				Bonferroni's Multiple Comparisons Test		
				t	DF	P Value
	P vs C5			3.163	34	0.0098
	C5 vs T			2.676	34	0.0341
				NonResponsive Cells		
		SS	DF	MS	$F_{(DFn, DFd)}$	P Value
	Days	0.06975	3	0.02325	$F_{(3, 106)} = 2.271$	0.0845
	Residual	1.085	106	0.01024		
Fig. 1P				One-way ANOVA		
				Excited Cells		
		SS	DF	MS	$F_{(DFn, DFd)}$	P Value
	Days	1.242	3	0.4140	$F_{(3, 238)} = 12.33$	<0.0001
	Residual	7.993	238	0.03358		
				Bonferroni's Multiple Comparisons Test		
				t	DF	P Value
	P vs T			3.995	238	0.0005
	C1 vs C5			3.887	238	0.0008
	C1 vs T			5.496	238	<0.0001
				Inhibited Cells		
		SS	DF	MS	$F_{(DFn, DFd)}$	P Value
	Days	0.1384	2	0.06921	$F_{(2, 34)} = 4.964$	P=0.0128
	Residual	0.4741	34	0.01394		
				Bonferroni's Multiple Comparisons Test		
				t	DF	P Value
	P vs C5			3.023	34	0.0142
				NonResponsive Cells		
		SS	DF	MS	$F_{(DFn, DFd)}$	P Value
	Days	0.1812	3	0.06041	$F_{(3, 106)} = 4.299$	P=0.0066
	Residual	1.490	106	0.01405		
				Bonferroni's Multiple Comparisons Test		
				t	DF	P Value
	P vs C5			3.153	106	0.0126
	P vs T			2.805	106	0.0359
Fig. 1Q				One-way ANOVA		
				CS+ > CS- Cells		
		SS	DF	MS	$F_{(DFn, DFd)}$	P Value
	Days	5.979	3	1.993	$F_{(3, 195)} = 16.83$	<0.0001
	Residual	23.10	195	0.1184		
				Bonferroni's Multiple Comparisons Test		
				t	DF	P Value
	P vs C5			2.853	195	0.0288
	P vs T			5.697	195	<0.0001

	C1 vs C5			3.114	195	0.0128
	C1 vs T			5.845	195	<0.0001
	C5 vs T			3.327	195	0.0063
				CS+ < CS- Cells		
		SS	DF	MS	$F_{(DFn, DFd)}$	P Value
	Days	0.4990	3	0.1663	$F_{(3, 71)} = 3.631$	0.0169
	Residual	3.252	71	0.04581		
				Bonferroni's Multiple Comparisons Test		
				t	DF	P Value
	P vs C1			3.265	71	0.0101
				CS+ = CS- Cells		
		SS	DF	MS	$F_{(DFn, DFd)}$	P Value
	Days	0.1090	3	0.03633	$F_{(3, 111)} = 1.349$	0.2621
	Residual	2.988	111	0.02692		
Fig. 1R				One-way ANOVA		
				CS+ > CS- Cells		
		SS	DF	MS	$F_{(DFn, DFd)}$	P Value
	Days	1.179	3	0.3928	$F_{(3, 195)} = 11.13$	<0.0001
	Residual	6.884	195	0.03530		
				Bonferroni's Multiple Comparisons Test		
				t	DF	P Value
	P vs T			2.793	195	0.0345
	C1 vs T			5.262	195	<0.0001
	C5 vs T			4.171	195	0.0003
				CS+ < CS- Cells		
		SS	DF	MS	$F_{(DFn, DFd)}$	P Value
	Days	0.2025	3	0.06751	$F_{(3, 71)} = 2.476$	0.0684
	Residual	1.936	71	0.02727		
				CS+ = CS- Cells		
		SS	DF	MS	$F_{(DFn, DFd)}$	P Value
	Days	0.2587	3	0.08623	$F_{(3, 111)} = 4.749$	0.0037
	Residual	2.016	111	0.01816		
				Bonferroni's Multiple Comparisons Test		
				t	DF	P Value
	C1 vs T			3.416	111	0.0053
	C5 vs T			3.150	111	0.0126

Table S2. Statistical Information for Figure 2.

Fig. 2J	Two-way ANOVA				
	SS	DF	MS	$F_{(DFn, DFd)}$	P Value
Interaction	3.815	6	0.6358	$F_{(6, 72)} = 4.359$	P=0.0008
Responses	1.535	2	0.7677	$F_{(2, 24)} = 6.240$	P=0.0066
Days	0.9829	3	0.3276	$F_{(3, 72)} = 2.246$	P=0.0902
Animals	2.953	24	0.1230	$F_{(24, 72)} = 0.8435$	P=0.6716
Residual	10.50	72	0.1459		
	Bonferroni's Multiple Comparisons Test				
			t	DF	P Value
Excited					
C1 vs T			3.015	72.00	0.0213
Inhibited					
P vs T			3.227	72.00	0.0113
C1 vs T			3.441	72.00	0.0058
C5 vs T			4.023	72.00	0.0008
Fig. 2K	Two-way ANOVA				
	SS	DF	MS	$F_{(DFn, DFd)}$	P Value
Interaction	1.890	6	0.3151	$F_{(6, 72)} = 7.581$	<0.0001
Responses	0.1793	2	0.08965	$F_{(2, 24)} = 5.606$	0.0101
Days	1.298	3	0.4328	$F_{(3, 72)} = 10.41$	<0.0001
Animals	0.3838	24	0.01599	$F_{(24, 72)} = 0.3848$	0.9947
Residual	2.993	72	0.04156		
	Bonferroni's Multiple Comparisons Test				
			t	DF	P Value
Inhibited					
P vs T			6.808	72.00	<0.0001
C1 vs T			5.278	72.00	<0.0001
C5 vs T			5.919	72.00	<0.0001
NonResponsive					
P vs T			2.922	72.00	0.0279
Fig. 2L	Two-way ANOVA				
	SS	DF	MS	$F_{(DFn, DFd)}$	P Value
Interaction	2.748	6	0.4580	$F_{(6, 72)} = 4.581$	P=0.0005
Responses	1.448	2	0.7238	$F_{(2, 24)} = 3.138$	P=0.0616
Days	0.6836	3	0.2279	$F_{(3, 72)} = 2.279$	P=0.0867
Animals	5.535	24	0.2306	$F_{(24, 72)} = 2.307$	P=0.0035
Residual	7.198	72	0.09997		
	Bonferroni's Multiple Comparisons Test				
			t	DF	P Value
Excited					
P vs C5			3.175	72.00	0.0132
P vs T			4.851	72.00	<0.0001
C1 vs T			3.073	72.00	0.0180
Inhibited					
C1 vs T			2.888	72.00	0.0307
Fig. 2M	Two-way ANOVA				
	SS	DF	MS	$F_{(DFn, DFd)}$	P Value
Interaction	1.092	6	0.1819	$F_{(6, 72)} = 3.488$	P=0.0044
Responses	0.6017	2	0.3008	$F_{(2, 24)} = 3.771$	P=0.0377
Days	0.3981	3	0.1327	$F_{(3, 72)} = 2.544$	P=0.0628
Animals	1.915	24	0.07979	$F_{(24, 72)} = 1.530$	P=0.0860
Residual	3.755	72	0.05216		
	Bonferroni's Multiple Comparisons Test				
			t	DF	P Value
Excited					
P vs T			2.854	72.00	0.0338

Table S3. Statistical Information for Figure 3.

Fig. 3E	Two-way ANOVA				
	SS	DF	MS	$F_{(DFn, DFd)}$	P Value
Interaction	6.164	6	1.027	$F_{(6, 72)} = 7.963$	<0.0001
Responses	1.805	2	0.9027	$F_{(2, 24)} = 4.511$	0.0217
Days	0.5693	3	0.1898	$F_{(3, 72)} = 1.471$	0.2297
Animals	4.803	24	0.2001	$F_{(24, 72)} = 1.551$	0.0793
Residual	9.290	72	0.1290		
	Bonferroni's Multiple Comparisons Test				
			t	DF	P Value
CS+ > CS-					
P vs T			5.403	72.00	<0.0001
C1 vs T			4.327	72.00	0.0003
C5 vs T			5.476	72.00	<0.0001
CS- > CS+					
C5 vs T			3.738	72.00	0.0022
Fig. 3F	Two-way ANOVA				
	SS	DF	MS	$F_{(DFn, DFd)}$	P Value
Interaction	2.157	6	0.3596	$F_{(6, 72)} = 5.860$	<0.0001
Responses	0.3858	2	0.1929	$F_{(2, 24)} = 3.054$	0.0658
Days	0.1825	3	0.06082	$F_{(3, 72)} = 0.9913$	0.4019
Animals	1.516	24	0.06317	$F_{(24, 72)} = 1.030$	0.4431
Residual	4.418	72	0.06136		
	Bonferroni's Multiple Comparisons Test				
			t	DF	P Value
CS+ > CS-					
P vs T					0.0210
C1 vs T					0.0081
C5 vs T					<0.0001
CS- > CS+					
C5 vs T					0.0094
Fig. 3K	Two-way ANOVA				
	SS	DF	MS	$F_{(DFn, DFd)}$	P Value
Interaction	0.3629	2	0.1815	$F_{(2, 24)} = 1.014$	0.3777
Responses	11.70	2	5.849	$F_{(2, 24)} = 5.930$	0.0081
Days	1.294	1	1.294	$F_{(1, 24)} = 7.233$	0.0128
Animals	23.67	24	0.9864	$F_{(24, 24)} = 5.514$	<0.0001
Residual	4.294	24	0.1789		
Fig. 3L	Two-way ANOVA				
	SS	DF	MS	$F_{(DFn, DFd)}$	P Value
Interaction	0.1521	2	0.07606	$F_{(2, 24)} = 2.861$	0.0768
Responses	2.382	2	1.191	$F_{(2, 24)} = 23.29$	<0.0001
Days	0.5055	1	0.5055	$F_{(1, 24)} = 19.01$	0.0002
Animals	1.228	24	0.05115	$F_{(24, 24)} = 1.924$	0.0579
Residual	0.6380	24	0.02658		
	Bonferroni's Multiple Comparisons Test				
			t	DF	P Value
Excited			3.531	24.00	0.0051
Inhibited			2.662	24.00	0.0410
NonResponsive			2.976	24.00	0.0197
Fig. 3M	Two-way ANOVA				
	SS	DF	MS	$F_{(DFn, DFd)}$	P Value
Interaction	36.74	4	9.184	$F_{(4, 208)} = 3.066$	0.0175
Pairs	36.89	4	9.223	$F_{(4, 208)} = 3.079$	0.0172
Days	369.6	1	369.6	$F_{(1, 52)} = 38.91$	<0.0001
Data Types	493.9	52	9.497	$F_{(52, 208)} = 3.171$	<0.0001
Residual	623.0	208	2.995		
	Bonferroni's Multiple Comparisons Test				
			t	DF	P Value
Data					
#1 vs #3			3.238	208.0	0.0281
#2 vs #3			4.367	208.0	0.0004

	#3 vs #4			4.143	208.0	0.0010
Fig. 3N	Two-way ANOVA					
		SS	DF	MS	$F_{(DFn, DFd)}$	P Value
	Interaction	27.23	4	6.806	$F_{(4, 208)} = 3.093$	0.0168
	Pairs	27.57	4	6.892	$F_{(4, 208)} = 3.131$	0.0158
	Days	184.8	1	184.8	$F_{(1, 52)} = 33.26$	<0.0001
	Data Types	289.0	52	5.558	$F_{(52, 208)} = 2.525$	<0.0001
	Residual	457.8	208	2.201		
	Bonferroni's Multiple Comparisons Test					
				t	DF	P Value
	Data					
	#1 vs #3			3.521	208.0	0.0106
	#1 vs #4			3.384	208.0	0.0171
	#1 vs #5			4.486	208.0	0.0002
Fig. 3O	Two-way ANOVA					
		SS	DF	MS	$F_{(DFn, DFd)}$	P Value
	Interaction	3.169	1	3.169	$F_{(1, 52)} = 4.541$	0.0378
	Days	1.193	1	1.193	$F_{(1, 52)} = 1.710$	0.1967
	Data Types	107.7	1	107.7	$F_{(1, 52)} = 46.56$	<0.0001
	Animals	120.3	52	2.313	$F_{(52, 52)} = 3.315$	<0.0001
	Residual	36.28	52	0.6978		
	Bonferroni's Multiple Comparisons Test					
				t	DF	P Value
	Data					
	C1 vs C5			2.431	52.00	0.0370

Table S4. Statistical Information for Figure 4.

Fig. 4A	Two-way ANOVA				
	SS	DF	MS	$F_{(DFn, DFd)}$	P Value
Interaction	506.2	3	168.7	$F_{(3, 9)} = 0.8414$	0.5048
Groups	223.1	1	223.1	$F_{(1, 3)} = 1.467$	0.3125
Days	10345	3	3448	$F_{(3, 9)} = 17.20$	0.0005
Animals	456.2	3	152.1	$F_{(3, 9)} = 0.7582$	0.5451
Residual	1805	9	200.5		
	Bonferroni's Multiple Comparisons Test				
			t	DF	P Value
Generalized					
P vs C5			4.664	9.000	0.0071
C1 vs C5			4.784	9.000	0.0060
C5 vs T			3.955	9.000	0.0200
Not Generalized					
P vs C5			3.433	9.000	0.0448
C1 vs C5			3.944	9.000	0.0203
C5 vs T			3.902	9.000	0.0217
Fig. 4B	Two-way ANOVA				
	SS	DF	MS	$F_{(DFn, DFd)}$	P Value
Interaction	822.5	3	274.2	$F_{(3, 9)} = 1.490$	0.2822
Groups	2034	1	2034	$F_{(1, 3)} = 9.276$	0.0556
Days	9372	3	3124	$F_{(3, 9)} = 16.98$	0.0005
Animals	657.9	3	219.3	$F_{(3, 9)} = 1.192$	0.3667
Residual	1656	9	184.0		
	Bonferroni's Multiple Comparisons Test				
			t	DF	P Value
Gen vs Not Gen					
T			3.098	12.00	0.0369
Generalized					
P vs C5			5.194	9.000	0.0034
P vs T			3.958	9.000	0.0199
Not Generalized					
P vs C5			4.803	9.000	0.0058
Fig. 4C	Two-way ANOVA				
	SS	DF	MS	$F_{(DFn, DFd)}$	P Value
Interaction	104.6	3	34.88	$F_{(3, 9)} = 0.1244$	0.9433
Groups	128.1	1	128.1	$F_{(1, 3)} = 0.4609$	0.5459
Days	10034	3	3345	$F_{(3, 9)} = 11.93$	0.0017
Animals	833.7	3	277.9	$F_{(3, 9)} = 0.9910$	0.4399
Residual	2524	9	280.4		
	Bonferroni's Multiple Comparisons Test				
			t	DF	P Value
Generalized					
P vs T			3.280	9.000	0.0572
Not Generalized					
P vs T			4.493	9.000	0.0090

Table S5. Statistical Information for Figure S1.

Fig. S1I	Unpaired t-test (two-tailed)				
	Excited				
			t	DF	P Value
			0.3997	186	0.6898
	NonResponsive				
			t	DF	P Value
			1.071	14	0.3021
Fig. S1J	Unpaired t-test (two-tailed)				
	Excited				
			t	DF	P Value
			3.732	186	0.0003
	NonResponsive				
			t	DF	P Value
			0.1251	14	0.9022
Fig. S1K	Two-way ANOVA				
		SS	DF	MS	$F_{(DFn, DFd)}$	P Value
	Interaction	42.57	4	10.64	$F_{(4, 648)} = 5.582$	0.0002
	Pairs	40.99	4	10.25	$F_{(4, 648)} = 5.375$	0.0003
	Days	601.7	1	601.7	$F_{(1, 162)} = 62.82$	<0.0001
	Data Types	1552	162	9.578	$F_{(162, 648)} = 5.024$	<0.0001
	Residual	1235	648	1.906		
	Bonferroni's Multiple Comparisons Test					
				t	DF	P Value
	Data					
	#1 vs #2			3.887	648.0	0.0011
	#2 vs #3			6.434	648.0	<0.0001
	#2 vs #4			4.068	648.0	0.0005
	#2 vs #5			3.501	648.0	0.0050
	#3 vs #5			2.933	648.0	0.0347
Fig. S1L	Two-way ANOVA					
		SS	DF	MS	$F_{(DFn, DFd)}$	P Value
	Interaction	106.7	4	26.68	$F_{(4, 960)} = 9.833$	<0.0001
	Pairs	106.1	4	26.52	$F_{(4, 960)} = 9.771$	<0.0001
	Days	1002	1	1002	$F_{(1, 240)} = 147.8$	<0.0001
	Data Types	1627	240	6.779	$F_{(240, 960)} = 2.498$	<0.0001
	Residual	2605	960	2.714		
	Bonferroni's Multiple Comparisons Test					
				t	DF	P Value
	Data					
	#1 vs #2			4.645	960.0	<0.0001
	#1 vs #3			8.758	960.0	<0.0001
	#1 vs #4			5.409	960.0	<0.0001
	#1 vs #5			4.279	960.0	0.0002
	#2 vs #3			4.113	960.0	0.0004
	#3 vs #4			3.349	960.0	0.0084
	#3 vs #5			4.479	960.0	<0.0001
Fig. S1M	Two-way ANOVA					
		SS	DF	MS	$F_{(DFn, DFd)}$	P Value
	Interaction	0.8574	1	0.8574	$F_{(1, 416)} = 0.5354$	0.4648
	Days	5.714	1	5.714	$F_{(1, 416)} = 3.568$	0.0596
	Data Types	298.6	1	298.6	$F_{(1, 416)} = 186.5$	0.0001
	Residual	666.2	416	1.601		

Table S6. Statistical Information for Figure S2.

Fig. S2C	One-way ANOVA				
	Excited Cells				
		SS	DF	MS	$F_{(DFn, DFd)}$	P Value
	Days	2.851	3	0.9505	$F_{(3, 129)} = 8.019$	<0.0001
	Residual	15.29	129	0.1185		
	Bonferroni's Multiple Comparisons Test					
				t	DF	P Value
	P vs C5			4.462	129	0.0001
	P vs T			3.149	129	0.0122
	C1 vs C5			3.305	129	0.0074
	Inhibited Cells					
		SS	DF	MS	$F_{(DFn, DFd)}$	P Value
	Days	0.04030	2	0.02015	$F_{(2, 20)} = 2.299$	0.1263
	Residual	0.1753	20	0.008765		
	NonResponsive Cells					
		SS	DF	MS	$F_{(DFn, DFd)}$	P Value
	Days	0.04152	3	0.01384	$F_{(3, 46)} = 1.091$	0.3626
	Residual	0.5838	46	0.01269		
Fig. S2D	One-way ANOVA					
	Excited Cells					
		SS	DF	MS	$F_{(DFn, DFd)}$	P Value
	Days	2.991	3	0.9971	$F_{(3, 105)} = 11.08$	<0.0001
	Residual	9.452	105	0.09002		
	Bonferroni's Multiple Comparisons Test					
				t	DF	P Value
	P vs C5			3.720	105	0.0019
	P vs T			3.122	105	0.0139
	C1 vs C5			4.809	105	<0.0001
	C1 vs T			4.034	105	0.0006
	Inhibited Cells					
		SS	DF	MS	$F_{(DFn, DFd)}$	P Value
	Days	0.09436	2	0.04718	$F_{(2, 11)} = 5.439$	0.0228
	Residual	0.09542	11	0.008675		
	Bonferroni's Multiple Comparisons Test					
				t	DF	P Value
	C5 vs T			2.977	11	0.0378
	NonResponsive Cells					
		SS	DF	MS	$F_{(DFn, DFd)}$	P Value
	Days	0.04491	3	0.01497	$F_{(3, 56)} = 1.734$	0.1704
	Residual	0.4834	56	0.008632		
Fig. S2E	One-way ANOVA					
	Excited Cells					
		SS	DF	MS	$F_{(DFn, DFd)}$	P Value
	Days	0.2309	3	0.07697	$F_{(3, 129)} = 2.395$	0.0713
	Residual	4.147	129	0.03214		
	Inhibited Cells					
		SS	DF	MS	$F_{(DFn, DFd)}$	P Value
	Days	0.1648	2	0.08239	$F_{(2, 20)} = 7.756$	0.0032
	Residual	0.2125	20	0.01062		
	Bonferroni's Multiple Comparisons Test					
				t	DF	P Value
	P vs C5			3.900	20	0.0027
	NonResponsive Cells					
		SS	DF	MS	$F_{(DFn, DFd)}$	P Value
	Days	0.04365	3	0.01455	$F_{(3, 46)} = 1.184$	0.3264
	Residual	0.5655	46	0.01229		
Fig. S2F	One-way ANOVA					
	Excited Cells					
		SS	DF	MS	$F_{(DFn, DFd)}$	P Value
	Days	1.337	3	0.4456	$F_{(3, 105)} = 13.49$	<0.0001
	Residual	3.469	105	0.03304		
	Bonferroni's Multiple Comparisons Test					

			t	DF	P Value
	P vs C5		3.206	105	0.0107
	P vs T		4.642	105	<0.0001
	C1 vs C5		3.404	105	0.0056
	C1 vs T		5.437	105	<0.0001
			Inhibited Cells		
		SS	DF	MS	$F_{(DFn, DFd)}$	P Value
	Days	0.006836	2	0.003418	$F_{(2, 11)} = 0.1722$	0.8440
	Residual	0.2184	11	0.01985		
			NonResponsive Cells		
		SS	DF	MS	$F_{(DFn, DFd)}$	P Value
	Days	0.2463	3	0.08208	$F_{(3, 56)} = 6.236$	0.0010
	Residual	0.7371	56	0.01316		
			Bonferroni's Multiple Comparisons Test		
			t	DF	P Value
	P vs C5		3.366	56	0.0083
	P vs T		3.538	56	0.0049
Fig. S2K			One-way ANOVA		
			Excited Cells		
		SS	DF	MS	$F_{(DFn, DFd)}$	P Value
	Days	0.6006	3	0.2002	$F_{(3, 93)} = 2.907$	0.0388
	Residual	6.404	93	0.06886		
			Inhibited Cells		
		SS	DF	MS	$F_{(DFn, DFd)}$	P Value
	Days	0.6134	3	0.2045	$F_{(3, 34)} = 3.180$	0.0363
	Residual	2.186	34	0.06430		
			NonResponsive Cells		
		SS	DF	MS	$F_{(DFn, DFd)}$	P Value
	Days	0.04239	3	0.01413	$F_{(3, 67)} = 0.7430$	0.5302
	Residual	1.274	67	0.01902		
Fig. S2L			One-way ANOVA		
			Excited Cells		
		SS	DF	MS	$F_{(DFn, DFd)}$	P Value
	Days	0.1186	3	0.03953	$F_{(3, 52)} = 1.009$	0.3965
	Residual	2.038	52	0.03919		
			Inhibited Cells		
		SS	DF	MS	$F_{(DFn, DFd)}$	P Value
	Days	1.172	3	0.3907	$F_{(3, 63)} = 8.275$	0.0001
	Residual	2.975	63	0.04722		
			Bonferroni's Multiple Comparisons Test		
			t	DF	P Value
	P vs T		2.824	63	0.0380
	C1 vs T		4.013	63	0.0010
	C5 vs T		3.387	63	0.0073
			NonResponsive Cells		
		SS	DF	MS	$F_{(DFn, DFd)}$	P Value
	Days	0.04816	3	0.01605	$F_{(3, 56)} = 0.6895$	0.5623
	Residual	1.304	56	0.02328		
Fig. S2M			One-way ANOVA		
			Excited Cells		
		SS	DF	MS	$F_{(DFn, DFd)}$	P Value
	Days	0.1678	3	0.05595	$F_{(3, 93)} = 2.240$	0.0888
	Residual	2.323	93	0.02498		
			Inhibited Cells		
		SS	DF	MS	$F_{(DFn, DFd)}$	P Value
	Days	0.1528	3	0.05093	$F_{(3, 34)} = 2.570$	0.0704
	Residual	0.6738	34	0.01982		
			NonResponsive Cells		
		SS	DF	MS	$F_{(DFn, DFd)}$	P Value
	Days	0.02642	3	0.008807	$F_{(3, 67)} = 1.070$	0.3677
	Residual	0.5513	67	0.008229		
Fig. S2N			One-way ANOVA		
			Excited Cells		
		SS	DF	MS	$F_{(DFn, DFd)}$	P Value

	Days	0.5478	3	0.1826	$F_{(3, 52)} = 6.860$	0.0006
	Residual	1.384	52	0.02662		
			Bonferroni's Multiple Comparisons Test			
				t	DF	P Value
	P vs C1			3.169	52	0.0154
	C1 vs T			3.597	52	0.0043
			Inhibited Cells			
		SS	DF	MS	$F_{(DFn, DFd)}$	P Value
	Days	0.2126	3	0.07086	$F_{(3, 63)} = 4.564$	0.0059
	Residual	0.9782	63	0.01553		
			Bonferroni's Multiple Comparisons Test			
				t	DF	P Value
	P vs C1			3.069	63	0.0190
	C1 vs T			2.823	63	0.0381
			NonResponsive Cells			
		SS	DF	MS	$F_{(DFn, DFd)}$	P Value
	Days	0.1678	3	0.05594	$F_{(3, 56)} = 3.773$	0.0155
	Residual	0.8303	56	0.01483		
			Bonferroni's Multiple Comparisons Test			
				t	DF	P Value
	P vs C1			2.871	56	0.0346
	C1 vs T			2.306	56	0.0276

Table S7. Statistical Information for Figure S3.

Fig. S3E	Unpaired t-test (two-tailed)		
	Excited		
	t	DF	P Value
	0.3641	103	0.7165
	NonResponsive		
	t	DF	P Value
	2.637	3	0.0778
Fig. S3F	Unpaired t-test (two-tailed)		
	Excited		
	t	DF	P Value
	0.8760	103	0.3831
	NonResponsive		
	t	DF	P Value
	3.480	3	0.04
Fig. S3H	Unpaired t-test (two-tailed)		
	Excited		
	t	DF	P Value
	1.415	81	0.1610
	NonResponsive		
	t	DF	P Value
	1.734	9	0.1170
Fig. S3I	Unpaired t-test (two-tailed)		
	Excited		
	t	DF	P Value
	4.828	81	<0.0001
	NonResponsive		
	t	DF	P Value
	0.3542	9	0.7313

Table S8. Statistical Information for Figure S4.

Fig. S4C	One-way ANOVA				
	CS+ > CS- Cells				
	SS	DF	MS	$F_{(DFn, DFd)}$	P Value
Days	2.150	3	0.7166	$F_{(3, 92)} = 6.987$	0.0003
Residual	9.436	92	0.1026		
	Bonferroni's Multiple Comparisons Test				
			t	DF	P Value
P vs T			3.763	92	0.0018
C1 vs T			3.785	92	0.0016
C5 vs T			3.128	92	0.0141
	CS+ < CS- Cells				
	SS	DF	MS	$F_{(DFn, DFd)}$	P Value
Days	0.3983	3	0.1328	$F_{(3, 39)} = 3.129$	0.0365
Residual	1.655	39	0.04242		
	Bonferroni's Multiple Comparisons Test				
			t	DF	P Value
P vs C5			2.817	39	0.0454
	CS+ = CS- Cells				
	SS	DF	MS	$F_{(DFn, DFd)}$	P Value
Days	0.03386	3	0.01129	$F_{(3, 63)} = 0.3686$	0.7759
Residual	1.929	63	0.03061		
Fig. S4D	One-way ANOVA				
	CS+ > CS- Cells				
	SS	DF	MS	$F_{(DFn, DFd)}$	P Value
Days	4.479	3	1.493	$F_{(3, 99)} = 11.49$	<0.0001
Residual	12.87	99	0.1300		
	Bonferroni's Multiple Comparisons Test				
			t	DF	P Value
P vs C5			2.960	99	0.0231
P vs T			4.368	99	0.0002
C1 vs T			3.554	99	0.0035
C5 vs T			4.759	99	<0.0001
	CS+ < CS- Cells				
	SS	DF	MS	$F_{(DFn, DFd)}$	P Value
Days	0.1783	2	0.08915	$F_{(2, 29)} = 1.821$	0.1799
Residual	1.420	29	0.04896		
	CS+ = CS- Cells				
	SS	DF	MS	$F_{(DFn, DFd)}$	P Value
Days	0.1488	3	0.04959	$F_{(3, 44)} = 2.238$	0.0971
Residual	0.9751	44	0.02216		
Fig. S4E	One-way ANOVA				
	CS+ > CS- Cells				
	SS	DF	MS	$F_{(DFn, DFd)}$	P Value
Days	0.6091	3	0.2030	$F_{(3, 92)} = 6.376$	0.0006
Residual	2.930	92	0.03184		
	Bonferroni's Multiple Comparisons Test				
			t	DF	P Value
C1 vs T			3.176	92	0.0122
C5 vs T			3.808	92	0.0015
	CS+ < CS- Cells				
	SS	DF	MS	$F_{(DFn, DFd)}$	P Value
Days	0.4995	3	0.1665	$F_{(3, 39)} = 7.551$	0.0004
Residual	0.8600	39	0.02205		
	Bonferroni's Multiple Comparisons Test				
			t	DF	P Value
P vs C1			3.532	39	0.0065
P vs C5			4.332	39	0.0006
P vs T			2.889	39	0.0377
	CS+ = CS- Cells				
	SS	DF	MS	$F_{(DFn, DFd)}$	P Value
Days	0.04211	3	0.01404	$F_{(3, 63)} = 0.6254$	0.6012
Residual	1.414	63	0.02244		

Fig. S4F						
	One-way ANOVA					
	CS+ > CS- Cells					
		SS	DF	MS	$F_{(DFn, DFd)}$	P Value
	Days	0.6799	3	0.2266	$F_{(3, 99)} = 6.929$	0.0003
	Residual	3.238	99	0.03271		
	Bonferroni's Multiple Comparisons Test					
				t	DF	P Value
	C1 vs T			4.127	99	0.0005
	CS+ < CS- Cells					
		SS	DF	MS	$F_{(DFn, DFd)}$	P Value
	Days	0.1013	3	0.03378	$F_{(3, 28)} = 1.408$	0.2611
	Residual	0.6716	28	0.02399		
	CS+ = CS- Cells					
		SS	DF	MS	$F_{(DFn, DFd)}$	P Value
	Days	0.3304	3	0.1101	$F_{(3, 44)} = 10.07$	<0.0001
	Residual	0.4813	44	0.01094		
	Bonferroni's Multiple Comparisons Test					
				t	DF	P Value
	P vs C1			3.073	44	0.0218
	C1 vs T			5.252	44	<0.0001
	C5 vs T			3.252	44	0.0132

Title

- **Zona Incerta subpopulations differentially encode and modulate anxiety**
- **Zona Incerta cells modulate anxiety**

Teaser: Zona Incerta, an anxiety sensor and modulator.

Authors

Zhuoliang Li,[1] Giorgio Rizzi,[1,2] Kelly R. Tan,[1*]

Affiliations

1. Biozentrum, University of Basel, Klingelbergstrasse 50/70, 4056, Basel, Switzerland
2. Current affiliation: Inscopix Inc, Palo Alto, California, United States

Abstract

Despite recent clinical observations linking the Zona Incerta (ZI) to anxiety, little is known about whether and how the ZI processes anxiety. Here, we subject mice to anxious experiences and observe an increase in ZI cfos-labelled neurons and single-cell calcium activity as well as an efficient effect of ZI infusion of diazepam, a classical anxiolytic drug. We further identify that somatostatin- (SOM), calretinin- (CR), and vesicular glutamate transporter-2 (Vglut2)-expressing cells display unique electrophysiological profiles; yet they similarly respond to anxiety-provoking stimuli and to diazepam. Interestingly, optogenetic manipulations reveal that each of these ZI neuronal populations triggers specific anxiety-related behavioral phenotypes. Activation of SOM-expressing neurons induced anxiety while in stark contrast, photo-activation of CR-positive cells and photo-inhibition of Vglut2-expressing neurons produce anxiolysis. Furthermore, activation of CR- and Vglut2-positive cells provokes rearing and jumps, respectively. Our findings provide the first experimental evidence that ZI subpopulations encode and modulate different components of anxiety.

Introduction

Anxiety is a negative emotional state triggered by potential threats and generates autonomic responses, avoidance and stress-like behaviors (*1*, *2*). Several brain regions, including the amygdala (*3–5*), the bed nucleus of stria terminalis (*5*, *6*), the medial prefrontal cortex (*7*, *8*), the hippocampus (*4*, *8*, *9*), and the hypothalamus (*9*, *10*) have been reported to play an important role in anxiety. Very recently, the understudied Zona Incerta (ZI) has also been associated with it. Specifically, Parkinson's disease patients treated with deep brain stimulation (DBS) in the ZI self-reported lower levels of anxiety (*11*, *12*). However, there is little to no experimental evidence supporting these interesting clinical observations.

Located between the thalamus and the hypothalamus, the ZI is an elongated string-like structure that has been implicated in a wide range of functions, varying from neuronal development (*13*), hormonal regulation (*14*, *15*), ingestion (*16–18*), sleep (*19*, *20*), sensory processing (*21*, *22*) and pain (*23*). More recently, a stream of research showcased the implication of the ZI in emotionally related experiences and adaptive defensive behaviors. Exposure to stressful events such as sleep deprivation was shown to potentiate the expression of the immediate early gene cfos in the ZI (*20*). Furthermore, electrical stimulation in the ZI induced pupil dilation (*24*), increased the blood flow to the extremities (*24*) and the heart rate (*25*); all of these are physiological reactions similar to that of the acute stress response (*2*). In addition, ZI loss of function impaired mice in their ability to respond to cues predictive of incoming threat. Specifically, mice with ZI electrolytic lesions displayed reduced avoidance in a conditioned avoidance response test (*26*). Similarly, ZI tetanus toxin infusion to block synaptic transmission decreased the ability to associate a predictive cue with the negative outcome in a fear conditioning task for mice (*27*). In contrast, optogenetic inactivation of ZI Vgat-expressing cells during the presentations of loud tones exacerbated the triggered flight response (*28*). These previous studies imply that the ZI could be influenced by negative cues and modulate adaptative responses. However, how the ZI senses stressful stimuli when mice experience anxiety triggering states is not known.

Most of the current knowledge on the ZI was gained from non-specific manipulations, yet the ZI is a highly heterogenous structure. Indeed, histological

investigations revealed diverse cell types possessing the capacity to release chemical signaling molecules such as glutamate, GABA, neuropeptides, and potentially dopamine (tyrosine hydroxylase- expressing cells) (*29*, *30*). While the GABAergic neurons are abundant in number and thoroughly expressed across the ZI, the existence of somatostatin (SOM), calretinin (CR), calbindin (CB), parvalbumin (PV), and vasopressin (VIP) indicate diversity within the GABAergic cells (*29–31*). Such biochemical heterogeneity may explain why the ZI has been implicated in quite a wide range of functions (*30*).

Here we aimed at investigating how the ZI neuronal population responds to stressful and anxious events. Based on a recent report that the rostral ZI modulates cue triggered defense behaviors (*28*), we speculated that the rostral ZI could also sense stressful anxiety provoking cues. So in our study, we targeted the rostral ZI (referred throughout as ZI). We first show that the ZI indeed encodes anxiety. We applied a three-steps strategy with histological labeling against cfos and *in-vivo* calcium recordings as mice experience anxious conditions; as well as the assessment of the efficacy of a pharmacological anxiety-relieving drug directly infused in the ZI. We then focused on two GABAergic subpopulations, the SOM- and CR-expressing neurons, along with the glutamatergic ones. They exhibit distinct electrophysiological properties. Although they are all activated by exposure to anxious conditions and are similarly modulated by diazepam, their bidirectional optogenetic modulation revealed distinct behavioral phenotypes. Specifically, activation of SOM-expressing cells induced anxiogenesis. Conversely, activation of CR-expressing neurons triggered anxiolysis and exploratory rearing. Finally, the activation of Vglut2-expressing cells induced flight-like jumps. Our data provide unprecedented information about how the ZI and some of its neuronal subpopulations encode anxiety related behaviors. Our study hence represents an important first step into understanding the neuronal and circuit basis of the clinical observation for ZI DBS to relieve anxiety in PD patients (*11*, *12*).

Results

Zona Incerta neurons encodes anxiety

Based on the recently reported clinical observations (*11*, *12*), we first verified and assessed that the ZI encodes anxiety. We performed three experiments among different levels of investigation. First, if indeed the ZI encodes anxiety, an anxious stimulus is expected to increase the expression of the immediate early gene cfos in the ZI. To test this hypothesis, we forced mice to experience a stay on an elevated rod, which is also exposed, meeting the two common criterions to trigger anxiety in rodents (*1*, *32*). Mice were hence placed on an elevated rod (100cm above ground, 3 cm in diameter, Figure 1A) for 30 minutes and brought back to their home cage for an additional 30 min before intracardiac perfusion. Control mice stayed in their home cage for 60 min (Figure 1B). Post-hoc immunostaining against cfos (Figure 1C-D) followed by quantification revealed a significantly higher number of cfos labelled neurons in the ZI of mice which experienced the elevated rod as compared to control mice (Figure 1E, elevated rod 3.38 ± 0.20 vs home cage 1.00 ± 0.14 cells, 951 and 243 cells respectively in 12 slices from 3 mice). These data confirm that an anxiety or stress triggering event increased the activity of ZI cells.

We next further investigated this with a higher temporal precision through *in vivo* calcium imaging. An AAV construct carrying the calcium indicator GCaMP6m gene was expressed in ZI neurons and a GRIN lens implanted slightly above (Figure 2A-B). To investigate changes in ZI populational activity due to shifts in anxiety levels, we needed an apparatus where mice can freely explore between areas with relatively high and low anxiety triggering values. While the elevated rod is a strong and unambiguous anxiogenic stimulus, it does not provide such a contrast. We therefore recorded the calcium dynamics of ZI neurons while mice explored an elevated platform (Figure 2C), adapted from the elevated plus maze (EPM) by blocking off the closed arms. This configuration allows mice to freely explore between the relatively safer (center) and anxiety triggering (open arms, especially the edges) areas and at the same time improves maneuverability of the miniscope mounted mice as well as maximizing the amount of time mice explored the anxiety-evoking edges. First, we observed that the mice spent more time in the center as compared to the edges (center 48.0 ± 3.3 vs edges 14.3 ± 3.3% time, Figure 2D). This is in line with the reported

values of the standard EPM (*33*), hence validates that our elevated platform task evokes anxiety-like phenotypes. Interestingly, we observed that a significant proportion of cells exhibited higher levels of activity when mice explored the safe center while other cells showed elevated calcium activity in the open edges (Figure 2E-F, Video S1[2]). To confirm and strengthen such observation we further analyzed and evaluated the correlation between neuronal activity with the absolute distance of the recorded animal away from the safe center. 23% of the imaged ZI cells displayed a positive correlation and were more active when mice explored the anxious edges as compared to the safer center (Figure 2G-I, +ve Corr 0.96 ± 0.07 vs not Corr 0.06 ± 0.04 z-scores, 128 cells from 5 mice). Conversely, 9% of the imaged cells exhibited a negative correlation and were less active when the animals were in the edges compared to the center (Figure 2G-I, -ve Corr -0.75 ± 0.06 vs not Corr 0.06 ± 0.04 z-scores). We also analyzed the calcium dynamics as mice transitioned into a safer or more anxious location (Figure 2J-M). To do so, we extracted from the cells exhibiting a positive, negative and no correlation (from Figure 2G-I), the calcium activity immediately before and after mice transitioned into and out of the edges (edge entry and exit respectively, Figure 2J-K) as well as the center (center exit and entry, Figure 2L-M). On average, the positively correlated neurons increased their activity when entering the edge or leaving the center (Figure 2J, edge entry, center/transition 0.00 ± 0.07 vs edge 0.32 ± 0.06 z-scores; Figure 2L, center exit, center 0.00 ± 0.03 vs edge/transition 0.15 ± 0.04 z-scores) and significantly decreased their activity when leaving the edge or entering the center (Figure 2K, edge exit, edge 0.00 ± 0.10 vs center/transition -0.36 ± 0.03 z-scores; Figure 2M, center entry, edge/transition 0.00 ± 0.03 vs center -0.20 ± 0.05 z-scores). Furthermore, the magnitude of these change was significantly larger than the not correlated cells during edge entry (Figure 2J, +ve Corr 0.32 ± 0.11 vs not Corr -0.07 ± 0.05 zscores) and edge exit (Figure 2K, +ve Corr -0.36 ± 0.13 vs not Corr -0.08 ± 0.05 zscores) but not during center entry (Figure 2M, +ve Corr -0.20 ± 0.04 vs not Corr -0.10 ± 0.04 zscores) or center exit (Figure 2L, +ve Corr 0.15 ± 0.03 vs not Corr 0.10 ± 0.04 zscores). On the other hand, the negatively correlated cells showed the opposite trend on average; reaching significant decreases

[2] Videos for Supplementary videos for Study 2.3 can be found in the line below
https://www.dropbox.com/sh/ta98df7nhuxstvu/AAA19l0szgxQ-k16oYunz2rFa?dl=0

in activity when the animals exited the edges (Figure 2J, edge entry, center/transition 0.00 ± 0.06 vs edge -0.259 ± 0.03 z-scores; Figure 2K, edge exit, edge 0.00 ± 0.03 vs center/transition 0.18 ± 0.07 z-scores; Figure 2L, center exit, center 0.00 ± 0.03 vs edge/transition -0.07 ± 0.04 z-scores; Figure 2M, center entry, edge/transition 0.00 ± 0.02 vs center -0.06 ± 0.02 z-scores). However, the magnitude of their responses did not different significantly from the not correlated cells (Figure 2J, edge entry, -ve Corr -0.26 ± 0.10 vs not Corr -0.07 ± 0.05 zscores; Figure 2K, edge exit, -ve Corr 0.18 ± 0.11 vs not Corr -0.08 ± 0.05 zscores; Figure 2L, center exit, -ve Corr -0.07 ± 0.08 vs not Corr 0.10 ± 0.04 zscores; Figure 2M, center entry, -ve Corr -0.06 ± 0.11 vs not Corr -0.10 ± 0.04 zscores). Corresponding increases and decreases in activity when mice entered more anxiety provoking and safer areas, respectively, provide further support that this subset of ZI neurons encode anxiety related information. To exclude a possible motor component, we correlated the calcium activity of individual ZI cells with the movement speed of the recorded mice. Of the cells that displayed positive and negative correlation with the mouse position on the platform, a majority of 69 and 91% were not correlated with the movement speed, respectively (Figure S1A-B, 20 of 29 and 10 of 11 cells). On average, the speed mice traveled in the center and the edges were similar (Figure S1C, center 0.038 ± 0.003 vs edges 0.024 ± 0.007 m/s) and thus further suggest that movement speed does not explain the differences in neuronal activity while mice were in these two areas. All together, these data reveal that a significant subset of ZI neurons is sensitive to anxiety-related cues irrespective of locomotion.

So far, we have shown that the ZI can detect changes in environments provoking relatively lower and higher levels of anxiety. We then wanted to assess the ability of the ZI to influence anxiety. We took a pharmacological approach where the anxiolytic properties of diazepam applied directly into the ZI was tested. The much smaller cannula implants posed little physical constraint on maneuverability and thus mice were tested in a standard paradigm for studying anxiety-like behaviors in mice (*34*). Of the two popular elevated mazes (the EPM and the EOM), the EOM was selected because it allows straightforward interpretations given the simple design with equally sized safe closed and anxiogenic open arms (*35*). Furthermore, to ensure that a potential anxiolysis effect is not overlooked, we used BALB/c mice for their relatively

heightened baseline levels of anxiety (*36*, *37*). Infusion cannulas were bilaterally implanted above the ZI (Figure 3A-B). Diazepam or vehicle infusions were made 30 min prior to placing mice in the EOM (Figure 3C). It was previously reported that diazepam (10mg/kg, provided intraperitoneally) was anxiolytic without affecting general locomotion (*38*) and thus we provided a dose ten times smaller for infusion. The order of the treatments was counterbalanced and reversed 2 weeks later. When mice received diazepam, they spent significantly more time in the open arms as compared to when they were treated with the vehicle (Figure 3D-E, Video S2, vehicle 130.8 ± 27.85 vs diazepam 219.9 ± 30.03s, 13 mice). They also made more entries into the open arms (Figure 3F, vehicle 24.38 ± 4.90 vs diazepam 37.92 ± 4.77 entries). In addition, we observed no significant differences across distance and immobility measures between diazepam and vehicle treated mice in the EOM (Figure S2). To make sure the diazepam mediated anxiolytic effects in the EOM were not cofounded by changes in locomotion, we investigated general locomotion with the open field test (OFT). Indeed, the distance traveled and the time mice spent immobile in the OFT were similar with both treatment conditions (Figure 3G-I, distance traveled, vehicle 43.76 ± 3.82 vs diazepam 46.33 ± 3.22; time immobile vehicle 50.05 ± 13.17 vs diazepam 64.39 ± 17.09s). These findings suggest that local diazepam treatment in the ZI reduces anxiety without impacting locomotion, further consolidating our biochemical and *in vivo* calcium imaging data.

To briefly summarize here, our multi-level experimental observations converge onto the ZI as a brain structure processing anxiety-related stimulus and modulating exploration into anxiety evoking environments.

Zona Incerta SOM-, CR- and Vglut2-expressing cells exhibit unique electrophysiological profiles and are all sensitive to anxious stimuli and diazepam.

So far, we have shown with complementary approaches that the ZI encodes anxiety. However, it is important to note that we observed subsets of ZI neurons displaying anxiety-induced cfos expression and anxiety-induced changes in calcium transients. Previous literature reported the cellular diversity within the ZI (*29–31*). We therefore wondered about the specific role an individual ZI subpopulation plays in the

encoding of anxiety. To address this question, we first examined the ZI biochemical diversity with FISH, focusing on the GABAergic and glutamatergic markers with Vgat and Vglut2, respectively. We report that Vgat-expressing cells are more abundant than Vglut2-expressing ones (Figure 4A-B; Vgat- only 78.8% and Vglut2- only 19.0%, 3390 cells from 3 mice). Probing against specific inhibitory markers namely somatostatin (SOM), calretinin (CR), and parvalbumin (PV) revealed that the SOM- and CR-expressing subpopulations are larger than the PV-expressing one (Figure 4C-D; SOM-only 36.6%, CR- only 53.2%, PV- only 2.0%, 1684 cells from 3 mice). Expectedly, SOM- and CR-expressing cells co-express Vgat (Figure S3).

We also investigated the co-expression of CaMKIIα with SOM- and CR- (Figure S4A-F) or with Vglut2- (Figure S4G-K) in the ZI in separate preparations. We observed that subsets of CaMKIIα- expressing cells also co-express SOM (16.3%), CR (26.4%) or Vglut2 (19.7%) (Figure S4A-K). With these data, we confirmed that the imaged neurons (GCaMP6m under the expression of CaMKIIα promoter) recorded in Figure 2 indeed included SOM-, CR- and Vglut2-expressing cell types.

Considering that SOM- and CR-expressing cells represent as sizable portion of the Vgat-positive neurons (as opposed to the PV-expressing cells, Figure 4 and S3), we sought to focus the study onto these 2 inhibitory sub-populations as well as the rare excitatory Vglut2-expressing one.

Next, we functionally characterized these ZI subpopulations performing *in-vitro* whole cell patch clamp recordings (Figure 4 E-M). To unequivocally study SOM-, CR-, and Vglut2-expressing cells, reporter lines (SOM-TOM and CR-TOM) or CRE-dependent EYFP (AAV5-DIO-EYFP) injected Vglut2-CRE-mouse line were used (Figure 4E-F). Despite exhibiting similar capacitance (Figure 4G, SOM 14.27 ± 0.80, CR 16.94 ± 2.16, Vglut2 15.15 ± 1.09 pF, 13-16 cells, 4-5 mice), resting membrane potential (Figure 4H, SOM -72.20 ± 2.12, CR -74.31 ± 3.37, Vglut2 -68.15 ± 2.88 mV), and action potential width (Figure 4I, SOM 8.46 ± 0.16, CR 8.46 ± 0.13, Vglut2 9.16 ± 0.47ms), SOM-expressing neurons are less excitable and display a higher rheobase (Figure 4J, SOM 41.33 ± 5.68, CR 23.13 ± 2.54, Vglut2 29.17 ± 3.362 pA) while Vglut2-expressing cells sustain higher maximum firing frequencies (Figure 4K-M, SOM 45.43 ± 5.34, CR 42.00 ± 6.38, Vglut2 105.20 ± 11.42 Hz).

In order to characterize further these three neuronal populations in a circuit mapping context, we first assessed their local connectivity probability and in a second step their long-range anatomical mapping.

We injected an AAV vector containing CRE-dependent ChR2 (AAV5-DIO-ChR2-EYFP) in the ZI of CR-, SOM-, and Vglut2-CRE mice (Figure S5A). We performed *in vitro* electrophysiology experiments in brain slices containing the ZI and recorded from ChR2 negative cells identified by the lack of a 400ms blue (473 nm) light induced desensitizing current. Local post-synaptically connected cells exhibited a brief 5ms light induced current response. We observed no (0 of 20 patched cells) locally connected cells to the SOM-expressing subpopulation (Figure S5B). In contrast, we observed 21.5% connected cells to the CR- expressing subpopulation (Figure S5D) and 59% connected cells to the Vglut2- subpopulation (Figure S5F). These connections are all monosynaptic as challenged by the successive bath application of tetrodotoxin (TTX) and 4-aminopyridine (4-AP) and are inhibitory and excitatory as abolished by subsequent bath application of picrotoxin (PTX) and kynureic acid (KA), respectively (Figure S5D-G).

We next identified SOM-, CR- and Vglut2-expressing cells' long range projections to other brain structures. To do so, we injected an AAV construct containing CRE-dependent tdTOM and synaptophysin-tagged EGFP (SypEGFP) into the ZI of SOM-, CR-, and Vglut2- CRE mice and comprehensively explored the diversity of the efferent projections across the brain (Figure S6). Across all three ZI subpopulations, the most noticeable tdTOM and SypEGFP signals were observed in the lateral habenula (LHb) and the periaqueductal grey (PAG) (Figure S6). Interesting, while CR- expressing ZI cells sparsely project to the dorsal medial PAG (dmPAG), the Vglut2- expressing cells densely project to the lateral as well as ventrolateral PAG (l/vlPAG), and the SOM-expressing cells project to all three (Figure S6).

We next assessed if SOM-, CR-, and Vglut2-expressing ZI neurons are activated by anxious conditions. The elevated rod experiment followed by cfos labeling was performed (Figure S7). Our quantification reports that co-expression of cfos with either SOM-, CR- or Vglut2- is significantly increased in the experimental mice as compared to the control ones (Figure S7B-P, SOM: elevated rod 3.50 ± 0.35 vs home cage 1.00 ± 0.18 cells, 3262 and 2458 cells total respectively in 12 slices from 3 mice;

CR: elevated rod 7.40 ± 1.39 vs home cage 1.00 ± 0.25 cells, 2074 and 1624 cells total, respectively; Vglut2: elevated rod 3.28 ± 0.30 vs home cage 1.00 ± 0.17 cells, 2538 and 1551 cells total, respectively). These data suggest that SOM-, CR-, and Vglut2-expressing cells are all activated by anxiety.

Finally, considering that the intra-ZI infusion of diazepam induced anxiolysis, we sought of verifying the sensitivity of our three neuronal cell types to diazepam. This was done through *in vitro* recordings of pharmacologically isolated inhibitory post-synaptic currents (IPSCs) onto SOM-, CR- and Vglut2-expressing cells were performed. The neurons were identified through the expression of TdTomato/EGFP (Figure 5A). Diazepam (1μM) potentiated the electrically evoked- IPSCs (Figure 5B, SOM: baseline -523.9 ± 96.29 vs diazepam -907.7 ± 175.3 pA; CR: baseline -232.9 ± 63.65 vs diazepam -500.3 ± 85.55 pA; Vglut2: baseline -342.0 ± 71.26 vs -669.0 ± 106.5 pA; 10-11 cells from 4-5 mice) without affecting the pair-pulse ratio in all three cell types (Figure 5B, SOM: baseline 1.11 ± 0.09 vs diazepam 0.91 ± 0.07; CR: baseline 0.95 ± 0.11 vs diazepam 0.85 ± 0.08; Vglut2: baseline 1.06 ± 0.07 vs diazepam 0.98 ± 0.06). The amplitude (Figure 5C, SOM: baseline -41.78 ± 5.07 vs diazepam -48.65 ± 6.27 pA; CR: baseline -44.54 ± 3.05 vs diazepam -50.08 ± 3.12 pA; Vglut2: baseline 40.79 ± 3.22 vs diazepam -47.54 ± 3.98 pA; 10-12 cells from 4-5 mice) and frequency (Figure 5C, SOM: baseline 0.05 ± 0.02 vs diazepam 0.09 ± 0.03 Hz; CR: baseline 0.04 ± 0.01 vs diazepam 0.06 ± 0.01 Hz; Vglut2: baseline 0.08 ± 0.02 vs diazepam 0.09 ± 0.02 Hz) of the spontaneous IPSCs were both increased. The IPSCs were blocked by picrotoxin (100μM). These *in vitro* electrophysiological data reveal that all three neuronal subpopulations are sensitive to diazepam.

Altogether, these findings suggest that SOM-, CR-, and Vglut2-expressing cells of the ZI are distinct neuronal sub-populations with specific functional intrinsic properties. However, they are all similarly activated by anxious stimuli and are sensitive to diazepam.

SOM-, CR-, and Vglut2-expressing Zona Incerta neurons trigger distinct anxiety-related traits

Despite being activated by elevation and allosterically modulated by diazepam; SOM-, CR- as well as Vglut2-expressing cells might still engage different components

of anxiety-related behaviors. To verify this hypothesis, we bidirectionally manipulated the activity of these three subpopulations while mice performed in the EOM task (Figure 6). To do so, we injected AAV vectors containing either CRE-dependent ChR2 (AAV5-DIO-ChR2-EYFP) or Arch (AAV5-DIO-Arch-EYFP) in the ZI of SOM-, CR-, and Vglut2- CRE mice and implanted optic fibers above the injection site (Figure 6A-B). Our experimental preparations were validated through *in-vitro* patch clamp recordings (Figure S8A-B). A short blue light illumination (400 msec, 473 nm) evoked desensitizing photocurrents in ChR2-positive SOM-, CR-, and Vglut2- positive ZI neurons (Figure S8C). Furthermore, either a 1 second continuous light pulse or a 10 second (40Hz) stimulation elicited firing activity that was reversed as soon as the stimulation was turned OFF (Figure S8D). Such a 40Hz blue light stimulation was efficient at significantly and sufficiently enhancing the firing activity of each three cell types (Figure S8D). In contrast, green light pulses (400 msec, 532nm) triggered hyperpolarizing photocurrents in Arch expressing SOM-, CR-, and Vglut2- positive cells, preventing evoked or spontaneous firing (Figure S8E-F).

At the behavioral level, mice performed the EOM task while the activity of SOM-, CR- and Vglut2-expressing cells was manipulated (1 min OFF, 1 min ON; 3 times, Figure 6C). Behavioral changes induced by light stimulation were reported as the difference in the performance during ON and OFF light stimulation. Activation of ChR2 in SOM- expressing ZI neurons significantly reduced both the amount of time spent in the open arm (Figure 6D, Ctrl 5.40 ± 5.47 vs ChR2 -9.53 ± 3.16s, 6-12 mice) and the number of entries made into the open arm (Figure 6E, Ctrl 0.83 ± 1.01 vs ChR2 -3.26 ± 0.65 entries). In stark contrast, optogenetic activation of CR-expressing neurons induced an opposite behavioral phenotype; with a significant increase of both the time spent in the open arm (Figure 6F, Ctrl 1.98 ± 4.47 vs ChR2 36.32 ± 13.83s, 5-8 mice) and the number of open arm entries (Figure 6G, -0.67 ± 0.33 vs 8.40 ± 4.49 entries). The optogenetic inhibition of either SOM- or CR- positive ZI neurons had little effect on the EOM performance (Figure 6D, SOM open arm time, Ctrl 5.40 ± 5.47 vs Arch 14.74 ± 2.89s; Figure 6E, SOM open arm entry, Ctrl 0.83 ± 1.01 vs Arch 1.13 ± 0.44 entries; Figure 6F, CR open arm time, Ctrl 1.98 ± 4.47 vs Arch 3.38 ± 3.74s; Figure 6G, CR open arm entry, -0.67 ± 0.33 vs 0.50 ± 0.78 entries). Interestingly, the light-induced inactivation of Vglut2-expressing cells increased the time mice spent in the

open arms (Figure 6H, Ctrl -6.64 ± 9.80 vs Arch 19.75 ± 5.14s, 5-6 mice) without affecting the number of open arm entries (Figure 6I, Ctrl 1.00 ± 0.32 vs Arch 2.33 ± 0.62 entries).

Importantly when mice were tested in the open field, the same light stimulations induced no significant change in locomotion (Figure S9) as reported by the distance travelled (Figure S9D, SOM: Ctrl -0.34 ± 0.35 vs ChR2 -1.82 ± 0.63 vs Arch 0.40 ± 0.57m; Figure S9F, CR: Ctrl -0.50 ± 0.67 vs ChR2 -0.03 ± 1.15 vs Arch 0.78 ± 0.65m; Figure S9H, Vglut2: Ctrl -0.27 ± 0.65 vs Arch 1.42 ± -0.83m) and the immobility time (Figure S9E, SOM: Ctrl -6.22 ± 6.90 vs ChR2 26.2 ± 10.29 vs Arch -2.51 ± 9.26s; Figure S9G, CR: Ctrl -7.22 ± 9.77 vs ChR2 8.28 ± 11.05 vs Arch -16.24 ± 8.11s; Figure S9I, Vglut2: Ctrl 11.18 ± 6.94 vs Arch -24.52 ± 14.03s). Photo-activation of Vglut2-expressing neurons was also tested. Due to the photo-triggered impressive jumps, testing mice in the EOM and the OFT was not possible. To measure such phenotype, mice were placed inside a closed transparent chamber (Figure 6J-K). Blue light stimulation (40Hz) triggered time locked jumps that were immediately stopped when the light stimulation was OFF (Figure 6L-M, Video S3, OFF 0.00 ± 0.00 vs ON 242.4 ± 24.60 jumps).

In order to verify that our light stimulation is restricted to Vglut2- expressing ZI cells, we conducted we reproduced the jumping phenotype in a separate cohort of Vglut2-CRE mice (Figure S10A-C, OFF 0.00 ± 0.00 vs ON 179.7 ± 56.81 jumps) and post-hoc stained slices containing the implant site against cfos. We observed that while cfos staining was sparsely observed in the ventral thalamus or the lateral hypothalamus, the majority of the cfos-positive neurons were concentrated within the ZI together with the ChR2-eYFP labelled cells (Figure S10D).

Finally, considering that ZI CR-ChR2 expressing mice exhibited an increased exploration in the EOM, we also tested them in the closed transparent chamber. Light stimulation significantly increased the number of rears (Figure 6N-O, Video S4, OFF 4.80 ± 1.72 vs ON 27.60 ± 7.38 rears). Such exploratory rearing behavior (*39*, *40*) provides an additional support that the activation of CR-expressing ZI neurons reduces anxiety. Furthermore, the activation of SOM-expressing neurons induced no clear-cut observable behavioral alterations (Video S5).

Together, our findings suggest that SOM-, CR- and Vglut2-expressing ZI subpopulations differentially modulate anxiety traits and related behaviors. Specifically, activation of SOM-expressing ZI neurons induces anxiogenesis while the activation of CR- expressing ZI neurons triggers anxiolysis and exploratory rears. Activation of Vglut2- expressing ZI neurons induces jumps and is contrasted by its inactivation, which is anxiolytic.

Discussion

With this study, we aimed at providing experimental evidence that the ZI encodes anxiety, in light of the interesting recent clinical observations reporting that ZI DBS treatment in PD reduces anxiety (*11*, *12*). Specifically, we showed that a powerful anxiety provoking stimulus such as the forced exposure on a narrow elevated rod activates ZI neurons as reported by their significant enhancement in cfos expression, adding to the growing literature that the ZI is sensitive to stressful experiences (*20*). Given the temporal limitations of such a biochemical investigation, we scrutinized the same question by examining the *in vivo* calcium dynamics of individual ZI neurons with a calcium indicator expressed under a CamKIIα promoter while mice explored an elevated platform. We revealed that a subset of ZI neurons is active in the open arm edges, and become more active when mice enter a more anxiogenic area and less to a safer one. These attributes cannot be solely explained by changes in motion as most movement speed correlated ZI cells are not correlated with anxiety. Supplementing this, the local infusion of a classical anxiolytic drug, diazepam directly into the ZI, reduced anxiety without affecting locomotion on the EOM and OFT, respectively.

It is worth noting that not all ZI cells show potentiated cfos expression or increased calcium activity following exposure to anxiogenic cues. These observations hint towards some underlying heterogeneities. Past literature provided comprehensive insights into the diversity of biochemical cell type markers expressed in the ZI (*29*–*31*), without much further characterization into their physiological and functional properties. In line with previous studies (*29*, *31*), we showed that cells expressing GABAergic markers are more prevalent over glutamatergic ones. We focused on two GABAergic subpopulations expressing Vgat with SOM or CR in addition to the rarer Vglut2-expressing cells and reported their unique intrinsic properties; leading the way with the electrophysiological profiling of genetically defined ZI subpopulations. Each of them co-express CamKIIα. Interestingly, SOM-expressing cells seem to not modulate local network activity whereas CR- and Vglut2- expressing neurons do act as interneurons, providing local inhibitory and excitatory modulations onto other ZI cells, respectively. Anatomically, all three ZI subpopulations send long-range projections innervating brain structures involved in emotionally relevant behaviors (*2*, *41*). Not only we confirmed the pathways ZI onto the LHb (*42*) and the PAG (*27*, *28*), but we also

delineate further that while CR- expressing cells innervate the dmPAG, Vglut2-positive cells project onto the l/vlPAG, and SOM- expressing neurons onto all three.

We also provide additional experimental evidence showing that they similarly respond to anxiety-related cues biochemically and to diazepam *ex vivo*; however, they drive specific and distinct actions. Indeed, optogenetic activation of SOM- expressing cells reduced exploration in the anxiogenic open arms while the activation of CR-expressing neurons as well as inhibition of Vglut2-expressing ZI cells increased it. These findings differ from previous reports where manipulation of the ZI did not influence anxiety. Specifically, non-selective inhibition of ZI neuronal activity with either tetanus toxin or chemogenetic manipulations was reported to not significantly affect exploration in the EPM (*27*) and OFT (*43*). Moreover, chemogenetic inhibition of Vgat-expressing neurons did not reduce anxiogenic center exploration in the OFT (*43*). These differences could potentially derive from the compensatory mechanisms following permanent impairments of the ZI by the tetanus toxin in the former study, the mild nature of center in the OFT to provoke anxiety by the latter investigation, or due to differences in the specificity of cells manipulated in both cases.

In addition, we observed that the photo-activation of Vglut2-expressing ZI cells induced time-locked jumps that were rapid, directed towards the walls of the chamber, and continuously changing in direction. While it is tempting to associate these light-induced jumps with compulsive repetitive jumping behavior observed in a genetic model of autism spectrum disorder (*44*) or in mice undergoing kindling seizures (*45*) given the multitude of jumps within a small period of time in all three cases. However, the jumps that we observed following the stimulation of Vglut2- positive ZI cells were not stationary but rather directed as an attempt to escape and continuously changing its direction once they fail to do so. The lack of additional motor disturbances prior to jumping further argues against the notion that these light-induced jumps were consequences of a seizure. Furthermore, the directed nature of these jumps resembles the active flight behavior observed in mice presented with an auditory tone that was previously paired with a strong aversive footshock (*46*). A recent report showed that the excitation of vlPAG promotes flight behavior (*47*). Interestingly we show that ZI Vglut2-expressing cells do project onto the vlPAG, hence we speculate that the observed flight-like jumps may be driven by the Vglut2-expressing ZI cells to

vlPAG sub-pathway. On the other hand, the activation of CR-expressing ZI cells promoted rearing, a rodent specific exploratory behavior (*48*, *49*) that is reduced in anxious animals following stressful experiences while elevated in animals with low anxiety states (*39*, *40*). Together with the anxiolytic effects observed in the EOM, the activation of CR-expressing ZI cells could provide the necessary foundations and partake in foraging (*18*) and hunting (*50*) behaviors, actions that have been previously attributed to the ZI. Finally, these behavioral alterations in anxiety-related behaviors that we observed with the optogenetic manipulations of its cell types are not concomitant with any significant changes in general locomotion, as is similarly reported by others (*27*, *28*, *43*).

While we bidirectionally manipulated the activity of SOM-, CR-, and Vglut2-expressing ZI neurons, the behavioral modifications were often unidirectional. Indeed, the inability for the inhibition of these cell types to produce significant opposing modulations in anxiety may potentially be attributed to the insufficient drive by Arch to completely shut down ongoing activity for prolonged periods of time in face of strong excitatory inputs.

Interestingly, photo-activation of SOM- and CR-expressing cells triggered opposite behavioral phenotype. This could potentially be due to the differences in their outgoing projections or underlying local connectivity. More specifically, it is tempting to speculate that CR-expressing cells may inhibit SOM- positive neurons, hence modulating and shifting the overall ZI dynamic to impact behavior. However, a much elaborated and systematic investigation into the ZI local connectivity including the identification of both the pre- and post-synaptic cells would be necessary to infer any circuit mechanisms.

Overall, our experimental findings support our hypothesis that the ZI plays an important role in anxiety. Indeed, through changes in the expression of activity dependent biochemical markers and neuronal activity, subsets of ZI cells detect changes in the environment triggering low and potentiated anxiety states. However, the ZI does not only have a sensory role but also actively influence anxiety-related behaviors, namely the exploration of exposed and elevated areas, when pharmacologically targeted. Interestingly through specific anatomical connections, ZI neuronal subpopulations engage in distinct actions to potentially generate a global

anxiety-related behavioral response. Specifically, the activation of SOM-expressing neurons promote avoidance of anxiogenic areas while the Vglut2- positive cells induce flight-like jumps. In stark contrast, the activation of CR-expressing cells drive exploration into anxiety provoking environments and also encourage rearing. Together, these findings provide converging evidence that the ZI and its neuronal subpopulations can sense anxiety-related information and influence anxiety-related states as well as behavioral outcomes.

Building on the clinical observations, our findings provide important experimental evidence to show that the ZI and its individual subpopulations encode anxiety and guide related behaviors. Our study hence provides valuable knowledge regarding the role of the ZI in anxiety and extends a positive outlook for the ZI as a therapeutic target for the treatment of anxiety.

Materials and Methods

Animals

Male and female SOM-CRE (B6-Sst<tm2.1(cre)Zjh>/J) (*51*), CR-CRE (B6(Cg)-Calb2<tm1(cre)Zjh>/J) (*51*), Vglut2-CRE (B6.Cg-Slc17a6<tm2(cre)Lowl>Unc/J, UNC) (*52*) and C57BL/6JRj mice were bred in-house. SOM-Tom and CR-Tom reporter lines were generated by crossing the respective Cre lines with the Ai9 transgenic line B6;129S6-Gt(ROSA)26Sor<tm9(CAG-tdTomato)Hze>/J) (*53*). All experimentation performed with transgenic mice involved mice of both sexes. No clear sex differences were observed and the data were thus pooled (Figure S11). BALB/cByJRj mice, previously shown to have elevated levels of anxiety (*36*, *37*), were purchased from Janvier Labs. All experimental procedures were approved by the Institutional Animal Care Office of the University of Basel and the Cantonal Veterinary Office under the License Number 2742.

Surgery

General

Mice were anesthetized with gas isoflurane (5% for induction and 1.5% for maintenance) in O_2 (Provet/Primal Healthcare, EZ Anesthesia Systems) and placed onto the stereotaxic frame (World Precision Instruments). Lidocaine (0.2mg/g) (Steuli Pharma) was injected subcutaneously above the skull. The skin was disinfected with 70% ethanol and Betadine (Mundipharma). A small incision along the anterior-posterior axis was made at the midline and then the skull was leveled. A small hole was drilled through the skull above the ZI, which consists of the regions Zona Incerta and Sub-incertal Nucleus in the mouse atlas (*54*) (1.3mm posteriorly to the Bregma, ±1.3mm laterally to the midline, and -4.87 mm deep from the surface of the skull at a 10 degrees angle away from the midline). Glass micropipettes (Drummond) were pulled with a vertical puller (Narishige). Viral vectors were ejected into the ZI with a pressure injector system controlled by a pulse generator (A.M.P.I.; 10-100ms, 20psi, at 0.333 Hz). The wound was either stitched together with tissue absorptive silk sutures (SABANA) or continued with additional implantations (optic fiber, cannula, or gradient refractive index lens). Buprenorphine (Bupaq P, Steuli Pharama AG) pain killers were administered (0.1μg/g) post-surgery as needed.

Calcium Imaging

Viruses (AAV1.Camk2a.GCaMP6m.WPRE.SV40, Ready to Image virus, Inscopix) were unilaterally (150nl) injected in the ZI and then a gradient refractive lens (GRIN lens; Inscopix; 600µm wide, 7.3mm long) was placed at the same coordinates. The lens was fixed with an UV-light curable glue (Henkel). A custom-made head bar (2cm long, 0.4cm wide, 0.1cm tall) was placed for future handling. A fixed headcap was built from layers consisting of super-glue (Cyberbond), UV-light curable glue (Loctite), and dental cement (Lang). Small screws were anchored into the skull to improve adhesion between the skull and the head cap. The headcap was secured to the skin with Vetbond tissue adhesive glue (3M). The implant was covered with temporary silicone gels (KauPo Smooth-On). The expression of the GCaMP6m and the clearing of the lens were assessed regularly starting from 2 weeks post-surgery. Once the conditions were visually determined to be satisfactory, the mice were placed under isoflurane anesthesia on the stereotaxic frame and the baseplate was secured to the headcap using a UV-light curable flowable composite glue (Kerr).

Cannula Implantation

Custom guide cannulas (460µm in diameter and 5.5mm in length, P1 Technologies) were bilaterally placed above the ZI. The cannulas were filled with a dummy cannula of the same length and covered by temporary silicone gel (KauPo).

Diazepam Infusion

Following surgical recovery (> 2 weeks), internal cannulas (100µm in inner diameter and 5.5mm in length, P1 Technologies) compatible with the guide cannulas were inserted. Freshly prepared diazepam (1mg/kg, Fagron) in vehicle (50% propylene glycol in sterile deionized H_2O, Sigma Aldrich) or vehicle were bilaterally infused into the ZI with the syringe pump (Harvard Apparatus) at 100nl/minute. The treatments were reversed after 2 weeks. The long gap is implemented to avoid potential acute re-exposure effects on anxiety-related behaviors in the behavioral paradigms involving elevated mazes (*55*, *56*). Following the end of all behavioral experiments, Red Retrobeads (Lumaflour) were infused via the same injection system

for anatomical validation. The mice were then sacrificed and histological preparations (see section on Histology) were made.

Preparation of Reporter Mice for cfos Screening or in vitro Recordings

To identify Vglut2+ ZI neurons whilst a reporter line is lacking, adult male and female (8-10 weeks) Vglut2-CRE mice were bilaterally injected with a virus expressing a CRE-dependent fluorescent protein (AAV5-EF1α-DIO-EYFP, UNC Vector Core, 300 nl/side). The virus was expressed for at least 2 weeks prior to histology or *in-vitro* electrophysiology experiments.

Anatomical tracing

Mice were injected with viruses that contained a CRE-dependent tdTOM with a synaptophysin-tagged EGFP (AAV1-phSyn-FLEX-tdTom-T2A-SypEGFP, UNC vector core, 100 nl/side). The virus was expressed for at least 3 weeks prior to perfusion and histology.

Optogenetics and Fiber Implantation

Mice were injected with viruses that contained a CRE-dependent opsin construct (AAV5-EF1α-DIO-eArch3.0-EYFP, AAV5-EF1α-DIO-ChR2-H134R-EYFP UNC/UZH Vector Cores) or a control fluorescent protein (AAV5-EF1α-DIO-EYFP, UNC Vector Core) bilaterally in the 5ZI (150nl/side). Optic fibers (>70% light transmittance, 200μm diameter 0.39NA optic fibers fixed by epoxy to 1.25mm wide 6.4mm long ceramic ferrules, Thorlabs, (*57*)) were bilaterally placed above the ZI (250μm).

***In vitro* electrophysiology**

Coronal mouse brain slices (180μm thick) containing the ZI were collected with a vibratome (Leica) in cooled artificial cerebrospinal fluid (ACSF) cutting solution (in mM: NMDG 92, KCl 2.5, NaH_2PO_4 1.25, $NaHCO_3$ 30, HEPES 20, Glucose 25, Thiourea 2, Na-ascorbate 5, Na-pyruvate 3, $CaCl_2 \cdot 2H_2O$ 0.5, $MgSO_4 \cdot 7H_2O$ 10, NAC 10; osmolarity of 290-300 mOsm) bubbled with 95% O_2 and 5% CO_2. The slices were kept in the holding ACSF solution (in mM: NaCl 92, KCl 2.5, NaH_2PO_4 1.25, $NaHCO_3$ 30, HEPES 20, Glucose 25, Thiourea 2, Na-ascorbate 5, Na-pyruvate 3, $CaCl_2 \cdot 2H_2O$

2, $MgSO_4 \cdot 7H_2O$ 2, NAC 10; pH 7.3; osmolarity of 290-300 mOsm) at 31 ^oC before transferred into the recording chamber containing the recording ACSF solution (in mM: NaCl 119, KCl 2.5, NaH_2PO_4 1.25, $NaHCO_3$ 24, Glucose 12.5, $CaCl_2 \cdot 2H_2O$ 2, $MgSO_4 \cdot 7H_2O$ 2; pH 7.3; osmolarity of 290-300 mOsm) bubbled with 95% O_2 and 5% CO_2. Visualized whole-cell patch recordings were performed to record cells from the ZI. We identified SOM-, CR-, and Vglut2- positive cells by the expression of TdTomato from reporter lines or virally introduced fluorescent proteins (AAV5-EF1α-DIO-EYFP, AAV5-EF1α-DIO-eArch3.0-EYFP, AAV5-EF1α-DIO-ChR2-H134R-EYFP) in each of the three cell-type specific CRE lines (SOM-CRE, CR-CRE, and Vglut2-CRE) visualized under an upright microscope (OLYMPUS) through PLANFL N 4X and 40X (OLYMPUS) objectives. The internal solution contained; for electrophysiological profiling and optogenetic tools validation (in mM: K-Gluconate 130, Creatine Phosphate 10, $MgCl_2$ 4, Na_2ATP 3.4, Na_3GTP 0.1, EGTA 1.1, HEPES 5; pH 7.3; osmolarity of 289 mOsm), for IPSC recordings as well as recording inhibitory transmission (in mM: K-Gluconate 30, KCl 100, Creatine Phosphate 10, $MgCl_2$ 4, Na_2ATP 3.4, Na_3GTP 0.1, EGTA 1.1, HEPES 5; pH 7.3; osmolarity of 289 mOsm), and for recording excitatory transmission (in mM: CsCl 130, NaCl 4, Creatine Phosphate 5, $MgCl_2$ 2, Na_2ATP 2, Na_3GTP 0.6, EGTA 1.1, HEPES 5, pH 7.3; osmolarity of 290 mOsm).

To investigate the ex vivo effect of diazepam, diazepam (1μM, Fagron) was subsequently washed in and blocked with picrotoxin (100μM). In separate slices, spontaneous inhibitory post-synaptic potentials were recorded and also subsequently bath applied with diazepam and blocked with picrotoxin. For the validation of optogenetic tools, light flashes (400ms) controlled by a pulse generator (A.M.P.I) were delivered from a microscope mounted LED (CoolLED) to evoke synaptic currents in voltage clamp mode held at resting membrane potential. To study the local connectivity, brief (5ms) light pulses (50ms apart) were delivered to evoke post-synaptic currents in non-ChR2 expressing cells. The concentrations of the pharmacological agents were applied at 500nM (TTX), 300μM (4-AP), 100μM (PTX), and 2mM (KA). In current clamp mode, blue light flashes (1s continuous and 10s at 40Hz) were used to evoke firing in ChR2-expressing cells and orange light flashes (1s continuous) were used to reduce electrically evoked (current injected) firing.

Histology

Immunohistochemistry

Mice received a lethal dose of pentobarbital (0.3mg/kg i.p.) (Steuli Pharama AG). Mice were fixed onto a Styrofoam board (with the back facing the board and the chest facing outwards) with 25-gauge needles (Braun) by the skin of their paws. The fixed mice is then placed at approximately 45 degrees. While clenching the chest skin with forceps, a vertical incision is made with surgical scissors (Fine Science Tools) to remove the outer skin. An incision is then made to expose and another to break open the diaphragm. Fat deposits around the heart are carefully removed with forceps. A small cut is made with a finer scissor to tear open the right atrium. The animals were then transcardially perfused with 25mL of phosphate buffered saline buffer (PBS) (Sigma Aldrich) followed by the same volume of 4% paraformaldehyde (PFA) (Sigma Aldrich) in PBS through the left ventricle. Brains were extracted and post-fixed in 4% PFA overnight then immersed in 30% sucrose in PBS until the brains has completely sunk to the floor of the container (complete absorption of sucrose). Sections were prepared (50μm) using a cryostat (Leica 1950 CM). Brain slices containing the ZI slices were first washed (3x3 mins) with 1X Tris-buffered saline (TBS) (Sigma Aldrich) with 0.1% Tween-20 (Sigma Aldrich), permeabilized for 20mins with 1X TBS with 0.1% Tween-20 and Triton-X100 (Sigma Aldrich) and blocked for 120 mins with 1% Bovine Serum Albumin (Sigma Aldrich) or 1% Bovine Serum Albumin with 10% Donkey Serum (Sigma Aldrich) in 1X TBS with 0.1% Tween-20. The brain slices were stained overnight in the blocking solution with the primary antibody (Rabbit anti-cfos, abcam ab7963, 1:500 and/or Goat anti-CR, swant CG1, 1:1000). In the following day, the brain slices were first washed and then stained for 120 minutes with the secondary antibody (Goat anti-Rabbit conjugated to AlexaFlour555, Invitrogen A21429, 1:500, Donkey anti-Rabbit conjugated to AlexaFlour488, Invitrogen A21206 1:500, or Donkey anti-Goat conjugated to AlexaFlour647, abcam ab150131, 1:500). The brain slices were again washed and then mounted on glass slides (Superfrost Plus, Thermo Scientific), immersed by DAPI containing ProLong Gold Antifade mounting solution (Invitrogen) and covered with borosilicate cover glass (VWR).

Fluorescent in-situ hybridization (FISH)

Mice were anesthetized with gas isoflurane. The brains were extracted and quickly frozen on aluminum foil over dry ice. Brains were kept overnight at -80°C. On the next day, the brains were equilibrated at -20°C in the cryostat for at least 30 minutes. Fresh frozen brain sections (20μm) containing the ZI were prepared and directly mounted onto glass slides. Selected slices were fixed for 30 minutes using 4% PFA in PBS, dehydrated with increasing concentrations of ethanol (50%, 70%, 100%, 100%), surrounded by hydrophobic barriers (ImmEdge, Vector Laboratories), before proceeding with the RNAscope Fluorescent Multiplex (ACD, Biotechne) Assay to label the mRNAs for vesicular GABA transporter (Vgat, Slc32a1, ref319191), vesicular glutamate transporter-2 (Vglut2, Slc17a6, ref319171), somatostatin (SOM, SST, ref482691), calretinin (CR, CALB2, ref313641), parvalbumin (PV, Pvalb, ref421931), and calcium/calmodulin dependent protein kinase II alpha (CaMKIIα, ref445231). Processed slides were immersed in ProLong Diamond Antifade mounting solution (Invitrogen) and covered with borosilicate cover glass.

Imaging

To visualize fluorescent IHC, FISH, or reporter protein labeling in brain sections, mounted sections were imaged with a Zeiss LSM700 upright confocal microscope controlled by the ZEN Black image acquisition software (v2010, Zeiss). PLAN APO 20X (0.8NA, air) and 40X (1.3NA, oil) objectives were used to take low and high magnification images, respectively. Fixed wavelength (405nm, 488nm, 555nm, and 639nm) lasers were utilized to visualize specific fluorescent signals while brightfield imaging was used for the anatomical features. For large throughput fluorescence imaging (anatomical tracing), mounted sections were imaged with a Zeiss Axio Scan Z1 with a Fluar 5X (0.25 NA, air) objective and filter sets suitable for imaging EGFP and tdTomato signals (38 and 43HE). Images were stitched with the acquisition software and further post-processed in FIJI (v2.0.0, ImageJ).

Behavior

General

Mice were brought into the testing room from the housing facilities on the experimental day and acclimatized for at least an hour before starting any experimentation or experimental preparations, such as connecting optic fibers to fiber implanted mice.

Elevated Rod Exposure for cfos Screening

Control and experimental mice were group-housed in their home cages and were brought from the housing room into the testing room. A 60 minutes acclimation period was allowed before mice were tested or directly transcardially perfused. The remaining mice were placed on an elevated rod (100cm tall, 3cm diameter) for 30 minutes and put back into the home cage for another 30 minutes before being perfused. It has been previously reported that increased cfos protein expression has been observed as little as 30 minutes following stimulus exposure (*58*, *59*). We chose a timeframe that could detect changes in cfos expression and as close to the stimulus exposure as possible. Soft packing foam was placed around the bottom of the elevated rod. Mice that fell were placed back into the home cage and excluded.

Elevated Platform Exposure for in-vivo Calcium Imaging

Mice were connected to the nVoke2 (Inscopix) system and recorded with the Inscopix data acquisition software with a 20Hz sampling rate while behaviorally recorded simultaneously from above using a camera (The Imaging Source) that is controlled by ANYMAZE (v5.23, Stoeling) and sampled up to 20Hz. The mice were then placed in the enclosed center of the elevated platform and recorded while freely moving for 5 minutes. The elevated platform is constructed by completely blocking the entrance of the closed arms of an elevated plus maze (arms with 7.5cm in width, 30cm in length separated by a center that is 7.5cm in width and in length and enclosed by 60cm tall cardboard pieces on the two sides not connected to the arms). This elevated platform maximizes and forces the recorded mice to explore the anxiogenic exposed open edges. The larger dimensions of this platform also provided more room for the recorded mice to maneuver.

Optogenetic Stimulation

The light power for optogenetic stimulation (473nm or 532nm) were adjusted with a power-meter (Thorlabs) such that the illumination at the tip of the optic fibers would be at around 10mW. To sufficiently activate ZI neurons with ChR2, 5msec pulses at 40Hz (473nm). Constant light (532nm) stimulation were used to drive the Arch3.0 mediated inhibition. The number of light stimulation periods were counterbalanced with periods where no light was provided in an alternating manner over 6 minutes with 1-minute bins.

Elevated O-Maze (EOM)

Cannula implanted mice that received intracranial infusion of either diazepam or vehicle (see Surgery/Diazepam Infusion) or fiber implanted mice that were attached to the laser cables (see Behavior/Optogenetic Manipulations) were placed on the open arm of the EOM (arms with 5cm in width; the maze is 55cm in diameter and 60cm above the ground) facing towards the closed arm (enclosed by two 15cm tall grey opaque plastic walls). The translucent floor allowed a camera mounted below facing upwards to record the shadow of the tested mice as it traveled along the EOM. Videos were recorded and tracked with ANYMAZE at a rate of up to 30Hz for either 10 minutes (infusion animals) or 6 minutes (optogenetics animals).

Open Field Test (OFT)

Mice were placed in the center of a rectangular OFT box (30cm in width and 45 cm in length, with 30cm tall walls) for either 10 minutes (infusion animals) or 6 minutes (optogenetics animals). Videos were recorded with a downward-facing camera from above with ANYMAZE in the same manner as mentioned previously.

Unique Behaviors in the Closed Chamber

Mice were placed in the center of a transparent plexi-glass rectangular box (25cm in width and 20cm in length, with 15cm tall walls) with a closed ceiling that had

a circular (5cm in diameter) hole that let out the fiber cables but not the mice for 6 minutes. Videos were recorded with a front-facing camera from the side with ANYMAZE in the same manner as mentioned previously. To test the extent of activated neurons following laser stimulation, a cohort of bilaterally implanted Vglut2-ChR2 expressing mice were stimulated in the closed chamber as mentioned above, returned to the home cage, transcardially perfused after 60 minutes and followed up with a post-hoc cfos immunohistochemistry staining.

Analysis

Calcium Imaging

The position of the center of the video recorded mouse and its movement speed were extracted from ANYMAZE together with the digital boundaries of the center and the open arms of the elevated platform. The behavioral trace was then exported to Matlab (v2018b, Mathworks) for further analysis.

Calcium transients recorded from the nVoke2 system were pre-processed in the Inscopix Data Processing Software (IDPS, v1.3, Inscopix). The time-stamped calcium traces were also exported to Matlab. Calcium transients and the behavioral traces were first aligned to each other. Calcium traces were denoised and standardized. Calcium and behavior traces were then both binned to 500ms windows. To examine the relationship between anxiety and the neuronal activity in the ZI, correlational analyses were made between the distance of the recorded mice to the enclosed center (center distance) and the calcium transients of the recorded cells. Center distance is an assessment for anxiety because the further the animal is from the center, the more exposed the animal is and thus the higher the level of anxiety. The center distance is calculated by subtracting the lengthwise position of the center of animal from that of the center of the platform and taking the absolute value. Pearson's correlation coefficient was calculated from the distribution of the binned calcium activity and center distance values. To characterize cells as being positively, negatively, or not correlated between these two parameters, a bootstrap test was performed by randomly shifting the calcium traces 1000 times in a circular manner and then calculating the correlation coefficient. Cells whose real correlation coefficient was negative and below the 5^{th} percentile or positive and above the 95^{th} percentile of the

random correlation coefficients w classified as negatively or positively correlated, respectively. Cells that did not fall into this range were classified as not correlated.

To further show that these correlated cells displayed activity with respect to the level of anxiety that the recorded mice experienced, the difference in activity between the time when the animals was in the center and the edges (defined as an area on extremities of the open arm with the same size as the center) was calculated for each cell and compared across groups. All recorded animals spent more time in the center as compared to the edges. To reduce sampling bias, the activity in the center was randomly sampled 1000 times to match the number of bins the animals spent in the edges and the averaged difference was reported.

To examine whether the correlated cells displayed changes in activity as the recorded animal transitioned between areas that are less anxiogenic to more anxiogenic and vice versa, calcium transients surrounding (2.5s before and after) the entry or the exit of the edge or the center were extracted, grouped, and compared. To visualize changes across cells and groups, transients were adjusted such that the average activity in the baseline window before the change in compartment is 0. The delta responses following each compartment change between positively, negatively, and not correlated cells were extracted and compared.

To show that the center distance correlated cells encoded anxiety rather than movement speed, the same correlation analysis was applied between calcium transients and movement speed for each cell. For each categorized (positively, negatively, and not correlated) center distance correlated cell groups, the proportion each of the three categories of movement speed correlated cells were shown.

Behavioral Paradigms

All parameters were extracted from ANYMAZE (EOM and OFT). Unique behaviors such as jumps and rears were visually identified and manually quantified.

Statistics

All statistical comparisons, unless otherwise noted, were analyzed with Prism (v8.4.3, GraphPad). The significance level was set at 5% (α = 0.05) in all cases. Student's t-test was used to make comparisons between two groups of data. The

unpaired design was utilized when the samples were independent from one another (number of cfos labelled ZI cells prepared from mice that were exposed to the elevated anxious experience or the control home conditions) while the paired design was applied in cases where repeated measures were made (activity of center distance cells before and after compartment change, effect of diazepam or vehicle on the performance in the EOM and OFT of the same mice, effect of diazepam on the recorded inhibitory currents onto ZI cells with respect to the baseline period before, and effect of photo-activation of CR- and Vglut2- ZI cells to respectively trigger rears and jumps as compared to periods in the same session where the light were off). One-way analysis of variance (ANOVA) with Bonferroni's multiple comparison tests were used to compare the differences across multiple (greater than two) independent samples (differences in activity between the center and the edge across the different center distance correlated groups, electrophysiological properties among the SOM-, CR-, and Vglut2-expressing ZI cells, and the differences in behavioral parameters among control, ChR2-, and Arch-expressing groups).

References and Notes

1. D. C. Blanchard, R. J. Blanchard, in *Handbook of Behavioral Neuroscience*, R. J. Blanchard, D. C. Blanchard, G. Griebel, D. Nutt, Eds. (Elsevier, 2008; http://www.sciencedirect.com/science/article/pii/S1569733907000057), vol. 17 of *Handbook of Anxiety and Fear*, pp. 63–79.

2. P. Tovote, J. P. Fadok, A. Lüthi, Neuronal circuits for fear and anxiety. *Nature Reviews Neuroscience*. **16**, 317–331 (2015).

3. K. M. Tye, R. Prakash, S.-Y. Kim, L. E. Fenno, L. Grosenick, H. Zarabi, K. R. Thompson, V. Gradinaru, C. Ramakrishnan, K. Deisseroth, Amygdala circuitry mediating reversible and bidirectional control of anxiety. *Nature*. **471**, 358–362 (2011).

4. A. C. Felix-Ortiz, A. Beyeler, C. Seo, C. A. Leppla, C. P. Wildes, K. M. Tye, BLA to vHPC inputs modulate anxiety-related behaviors. *Neuron*. **79**, 658–664 (2013).

5. S.-Y. Kim, A. Adhikari, S. Y. Lee, J. H. Marshel, C. K. Kim, C. S. Mallory, M. Lo, S. Pak, J. Mattis, B. K. Lim, R. C. Malenka, M. R. Warden, R. Neve, K. M. Tye, K. Deisseroth, Diverging neural pathways assemble a behavioural state from separable features in anxiety. *Nature*. **496**, 219–223 (2013).

6. J. H. Jennings, D. R. Sparta, A. M. Stamatakis, R. L. Ung, K. E. Pleil, T. L. Kash, G. D. Stuber, Distinct extended amygdala circuits for divergent motivational states. *Nature*. **496**, 224–228 (2013).

7. A. Adhikari, M. A. Topiwala, J. A. Gordon, Single units in the medial prefrontal cortex with anxiety-related firing patterns are preferentially influenced by ventral hippocampal activity. *Neuron*. **71**, 898–910 (2011).

8. N. Padilla-Coreano, S. S. Bolkan, G. M. Pierce, D. R. Blackman, W. D. Hardin, A. L. Garcia-Garcia, T. J. Spellman, J. A. Gordon, Direct Ventral Hippocampal-Prefrontal Input Is Required for Anxiety-Related Neural Activity and Behavior. *Neuron*. **89**, 857–866 (2016).

9. J. C. Jimenez, K. Su, A. R. Goldberg, V. M. Luna, J. S. Biane, G. Ordek, P. Zhou, S. K. Ong, M. A. Wright, L. Zweifel, L. Paninski, R. Hen, M. A. Kheirbek, Anxiety Cells in a Hippocampal-Hypothalamic Circuit. *Neuron*. **97**, 670-683.e6 (2018).

10. R. M. Cassidy, Y. Lu, M. Jere, J.-B. Tian, Y. Xu, L. R. Mangieri, B. Felix-Okoroji, J. Selever, Y. Xu, B. R. Arenkiel, Q. Tong, A lateral hypothalamus to basal forebrain neurocircuit promotes feeding by suppressing responses to anxiogenic environmental cues. *Sci Adv*. **5**, eaav1640 (2019).

11. A. M. Burrows, P. D. Ravin, P. Novak, M. L. B. Peters, B. Dessureau, J. Swearer, J. G. Pilitsis, Limbic and motor function comparison of deep brain stimulation of the zona incerta and subthalamic nucleus. *Neurosurgery*. **70**, 125–130; discussion 130-131 (2012).

12. A. Gourisankar, S. A. Eisenstein, N. T. Trapp, J. M. Koller, M. C. Campbell, M. Ushe, J. S. Perlmutter, T. Hershey, K. J. Black, Mapping movement, mood, motivation and mentation in the subthalamic nucleus. *R Soc Open Sci*. **5** (2018), doi:10.1098/rsos.171177.

13. J. Chen, A. R. Kriegstein, A GABAergic projection from the zona incerta to cortex promotes cortical neuron development. *Science*. **350**, 554–558 (2015).

14. M. K. Sanghera, J. Anselmo-Franci, S. M. McCann, Effect of medial zona incerta lesions on the ovulatory surge of gonadotrophins and prolactin in the rat. *Neuroendocrinology*. **54**, 433–438 (1991).

15. J. F. Murray, J. G. Mercer, R. A. Adan, J. J. Datta, C. Aldairy, K. M. Moar, B. I. Baker, M. J. Stock, C. A. Wilson, The effect of leptin on luteinizing hormone release is exerted in the zona incerta and mediated by melanin-concentrating hormone. *J. Neuroendocrinol.* **12**, 1133–1139 (2000).

16. L. L. Walsh, S. P. Grossman, Zona incerta lesions impair osmotic but not hypovolemic thirst. *Physiol. Behav.* **16**, 211–215 (1976).

17. B. A. Stamoutsos, R. G. Carpenter, L. Grossman, S. P. Grossman, Impaired feeding responses to intragastric, intraperitoneal, and subcutaneous injections of 2-

deoxy-D-glucose in rats with zona incerta lesions. *Physiol. Behav.* **23**, 771–776 (1979).

18. X. Zhang, A. N. van den Pol, Rapid binge-like eating and body weight gain driven by zona incerta GABA neuron activation. *Science*. **356**, 853–859 (2017).

19. M. Liu, C. Blanco-Centurion, R. Konadhode, S. Begum, D. Pelluru, D. Gerashchenko, T. Sakurai, M. Yanagisawa, A. N. van den Pol, P. J. Shiromani, Orexin gene transfer into zona incerta neurons suppresses muscle paralysis in narcoleptic mice. *J. Neurosci.* **31**, 6028–6040 (2011).

20. K. Liu, J. Kim, D. W. Kim, Y. S. Zhang, H. Bao, M. Denaxa, S.-A. Lim, E. Kim, C. Liu, I. R. Wickersham, V. Pachnis, S. Hattar, J. Song, S. P. Brown, S. Blackshaw, Lhx6-positive GABA-releasing neurons of the zona incerta promote sleep. *Nature*. **548**, 582–587 (2017).

21. J. C. Trageser, A. Keller, Reducing the uncertainty: gating of peripheral inputs by zona incerta. *J. Neurosci.* **24**, 8911–8915 (2004).

22. N. Urbain, M. Deschênes, Motor cortex gates vibrissal responses in a thalamocortical projection pathway. *Neuron*. **56**, 714–725 (2007).

23. R. Masri, R. L. Quiton, J. M. Lucas, P. D. Murray, S. M. Thompson, A. Keller, Zona incerta: a role in central pain. *J. Neurophysiol.* **102**, 181–191 (2009).

24. W. W. Kaelber, T. B. Smith, Projections of the zona incerta in the cat, with stimulation controls. *Exp. Neurol.* **63**, 177–200 (1979).

25. F. Benedetti, L. Colloca, M. Lanotte, B. Bergamasco, E. Torre, L. Lopiano, Autonomic and emotional responses to open and hidden stimulations of the human subthalamic region. *Brain Res. Bull.* **63**, 203–211 (2004).

26. L. V. Loskutova, I. M. Vinnitskii, R. Yu. Il'yuchenok, Participation of the zona incerta in mechanisms of the conditioned avoidance reaction. *Neurosci. Behav. Physiol.* **11**, 60–62 (1981).

27. M. Zhou, Z. Liu, M. D. Melin, Y. H. Ng, W. Xu, T. C. Südhof, A central amygdala to zona incerta projection is required for acquisition and remote recall of conditioned fear memory. *Nat. Neurosci.* **21**, 1515–1519 (2018).

28. X.-L. Chou, X. Wang, Z.-G. Zhang, L. Shen, B. Zingg, J. Huang, W. Zhong, L. Mesik, L. I. Zhang, H. W. Tao, Inhibitory gain modulation of defense behaviors by zona incerta. *Nat Commun*. **9**, 1151 (2018).

29. C. Kolmac, J. Mitrofanis, Distribution of various neurochemicals within the zona incerta: an immunocytochemical and histochemical study. *Anat. Embryol.* **199**, 265–280 (1999).

30. J. Mitrofanis, K. Ashkan, B. A. Wallace, A.-L. Benabid, Chemoarchitectonic heterogeneities in the primate zona incerta: clinical and functional implications. *J. Neurocytol.* **33**, 429–440 (2004).

31. C. Watson, C. R. P. Lind, M. G. Thomas, The anatomy of the caudal zona incerta in rodents and primates. *J. Anat.* **224**, 95–107 (2014).

32. G. Griebel, A. Holmes, 50 years of hurdles and hope in anxiolytic drug discovery. *Nature Reviews Drug Discovery*. **12**, 667–687 (2013).

33. R. J. Rodgers, A. Dalvi, Anxiety, defence and the elevated plus-maze. *Neurosci Biobehav Rev*. **21**, 801–810 (1997).

34. A. A. Walf, C. A. Frye, The use of the elevated plus maze as an assay of anxiety-related behavior in rodents. *Nat Protoc*. **2**, 322–328 (2007).

35. J. K. Shepherd, S. S. Grewal, A. Fletcher, D. J. Bill, C. T. Dourish, Behavioural and pharmacological characterisation of the elevated “zero-maze” as an animal model of anxiety. *Psychopharmacology (Berl)*. **116**, 56–64 (1994).

36. C. Belzung, G. Griebel, Measuring normal and pathological anxiety-like behaviour in mice: a review. *Behavioural Brain Research*. **125**, 141–149 (2001).

37. S. B. Sartori, R. Landgraf, N. Singewald, The clinical implications of mouse models of enhanced anxiety. *Future Neurol*. **6**, 531–571 (2011).

38. L. M. Behlke, R. A. Foster, J. Liu, D. Benke, R. S. Benham, A. J. Nathanson, B. K. Yee, H. U. Zeilhofer, E. Engin, U. Rudolph, A Pharmacogenetic "Restriction-of-Function" Approach Reveals Evidence for Anxiolytic-Like Actions Mediated by α5-Containing GABAA Receptors in Mice. *Neuropsychopharmacology*. **41**, 2492–2501 (2016).

39. J. N. Crawley, Neuropharmacologic specificity of a simple animal model for the behavioral actions of benzodiazepines. *Pharmacol Biochem Behav*. **15**, 695–699 (1981).

40. S. A. Krömer, M. S. Kessler, D. Milfay, I. N. Birg, M. Bunck, L. Czibere, M. Panhuysen, B. Pütz, J. M. Deussing, F. Holsboer, R. Landgraf, C. W. Turck, Identification of glyoxalase-I as a protein marker in a mouse model of extremes in trait anxiety. *J Neurosci*. **25**, 4375–4384 (2005).

41. H. Hu, Y. Cui, Y. Yang, Circuits and functions of the lateral habenula in health and in disease. *Nature Reviews Neuroscience*. **21**, 277–295 (2020).

42. I. Lazaridis, O. Tzortzi, M. Weglage, A. Märtin, Y. Xuan, M. Parent, Y. Johansson, J. Fuzik, D. Fürth, L. E. Fenno, C. Ramakrishnan, G. Silberberg, K. Deisseroth, M. Carlén, K. Meletis, A hypothalamus-habenula circuit controls aversion. *Molecular Psychiatry*. **24**, 1351–1368 (2019).

43. A. Venkataraman, N. Brody, P. Reddi, J. Guo, D. Gordon Rainnie, B. G. Dias, Modulation of fear generalization by the zona incerta. *Proc. Natl. Acad. Sci. U.S.A.* **116**, 9072–9077 (2019).

44. H. Won, H.-R. Lee, H. Y. Gee, W. Mah, J.-I. Kim, J. Lee, S. Ha, C. Chung, E. S. Jung, Y. S. Cho, S.-G. Park, J.-S. Lee, K. Lee, D. Kim, Y. C. Bae, B.-K. Kaang, M. G. Lee, E. Kim, Autistic-like social behaviour in Shank2-mutant mice improved by restoring NMDA receptor function. *Nature*. **486**, 261–265 (2012).

45. K. R. Stover, S. Lim, T.-L. Zhou, P. M. Stafford, J. Chow, H. Li, N. Sivanenthiran, S. Mylvaganam, C. Wu, D. F. Weaver, J. Eubanks, L. Zhang, Susceptibility to

hippocampal kindling seizures is increased in aging C57 black mice. *IBRO Rep*. **3**, 33–44 (2017).

46. J. P. Fadok, S. Krabbe, M. Markovic, J. Courtin, C. Xu, L. Massi, P. Botta, K. Bylund, C. Müller, A. Kovacevic, P. Tovote, A. Lüthi, A competitive inhibitory circuit for selection of active and passive fear responses. *Nature*. **542**, 96–100 (2017).

47. P. Tovote, M. S. Esposito, P. Botta, F. Chaudun, J. P. Fadok, M. Markovic, S. B. E. Wolff, C. Ramakrishnan, L. Fenno, K. Deisseroth, C. Herry, S. Arber, A. Lüthi, Midbrain circuits for defensive behaviour. *Nature*. **534**, 206–212 (2016).

48. C. Lever, S. Burton, J. O'Keefe, Rearing on hind legs, environmental novelty, and the hippocampal formation. *Rev Neurosci*. **17**, 111–133 (2006).

49. O. Sturman, P.-L. Germain, J. Bohacek, Exploratory rearing: a context- and stress-sensitive behavior recorded in the open-field test. *Stress*. **21**, 443–452 (2018).

50. Z.-D. Zhao, Z. Chen, X. Xiang, M. Hu, H. Xie, X. Jia, F. Cai, Y. Cui, Z. Chen, L. Qian, J. Liu, C. Shang, Y. Yang, X. Ni, W. Sun, J. Hu, P. Cao, H. Li, W. L. Shen, Zona incerta GABAergic neurons integrate prey-related sensory signals and induce an appetitive drive to promote hunting. *Nat. Neurosci.* **22**, 921–932 (2019).

51. H. Taniguchi, M. He, P. Wu, S. Kim, R. Paik, K. Sugino, D. Kvitsani, Y. Fu, J. Lu, Y. Lin, G. Miyoshi, Y. Shima, G. Fishell, S. B. Nelson, Z. J. Huang, A Resource of Cre Driver Lines for Genetic Targeting of GABAergic Neurons in Cerebral Cortex. *Neuron*. **71**, 995–1013 (2011).

52. L. Vong, C. Ye, Z. Yang, B. Choi, S. Chua, B. B. Lowell, Leptin Action on GABAergic Neurons Prevents Obesity and Reduces Inhibitory Tone to POMC Neurons. *Neuron*. **71**, 142–154 (2011).

53. L. Madisen, T. A. Zwingman, S. M. Sunkin, S. W. Oh, H. A. Zariwala, H. Gu, L. L. Ng, R. D. Palmiter, M. J. Hawrylycz, A. R. Jones, E. S. Lein, H. Zeng, A robust and high-throughput Cre reporting and characterization system for the whole mouse brain. *Nature Neuroscience*. **13**, 133–140 (2010).

54. F. B. J. Keith, G. Paxinos, *The Mouse Brain in Stereotaxic Coordinates* (Elsevier Inc., ed. 3rd, 2007).

55. M. N. Cook, M. Crounse, L. Flaherty, Anxiety in the Elevated Zero-Maze Is Augmented in Mice After Repeated Daily Exposure. *Behav Genet*. **32**, 113–118 (2002).

56. A. P. Carobrez, L. J. Bertoglio, Ethological and temporal analyses of anxiety-like behavior: the elevated plus-maze model 20 years on. *Neurosci Biobehav Rev*. **29**, 1193–1205 (2005).

57. D. R. Sparta, A. M. Stamatakis, J. L. Phillips, N. Hovelsø, R. van Zessen, G. D. Stuber, Construction of implantable optical fibers for long-term optogenetic manipulation of neural circuits. *Nat Protoc*. **7**, 12–23 (2011).

58. A. Chaudhuri, S. Zangenehpour, F. Rahbar-Dehgan, F. Ye, Molecular maps of neural activity and quiescence. *Acta Neurobiol Exp (Wars)*. **60**, 403–410 (2000).

59. X. Lin, C. A. Itoga, S. Taha, M. H. Li, R. Chen, K. Sami, F. Berton, W. Francesconi, X. Xu, c-Fos mapping of brain regions activated by multi-modal and electric foot shock stress. *Neurobiology of Stress*. **8**, 92–102 (2018).

Acknowledgments

General: We thank the past and current members of the Tan Lab for constructive input, the Biozentrum Imaging Facility for microscopy training, and the Inscopix team for technical support of the calcium imaging experiment.

Funding: This work was supported the Swiss National Science Foundation grants PPOOP3_150683 and BSSGIO_155830.

Author contributions: Z. Li, G. Rizzi, and K.R. Tan all contributed to the experimental design. G. Rizzi conducted the calcium imaging experiments. K.R. Tan conducted the electrophysiology experiments. Z. Li conducted all other experiments. Z. Li and K.R. Tan analyzed the data and prepared the manuscript.

Competing interests: The authors declare no competing interests.

Data and materials availability: All data needed to evaluate the conclusions in the paper are present in the paper and/or the Supplementary Materials.

Figures and Tables

Li et al. Figure 1

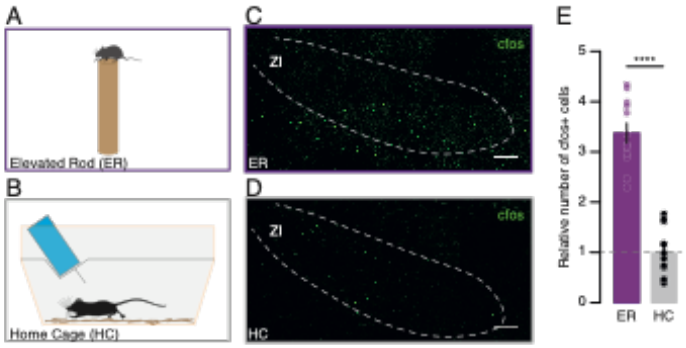

Figure 1. Anxious experience enhances ZI neuronal activation

A) Experimental setup where mice were placed on a narrow elevated rod.

B) Schematic of the control home cage condition.

C) Example confocal image of the immunohistochemical (IHC) staining against cfos (green) in the ZI-containing coronal brain slices from mice that were exposed to the anxious elevated rod experience (100μm scale bar).

D) Example confocal image of the IHC labeling of cfos in the ZI-containing coronal brain slices of mice that were left in the control home cage condition (100μm scale bar).

E) Bar graphs reporting the relative number of cfos labeled cells (normalized to the control mice) in the ZI for both experimental groups. Data are presented with the mean ± SEM.

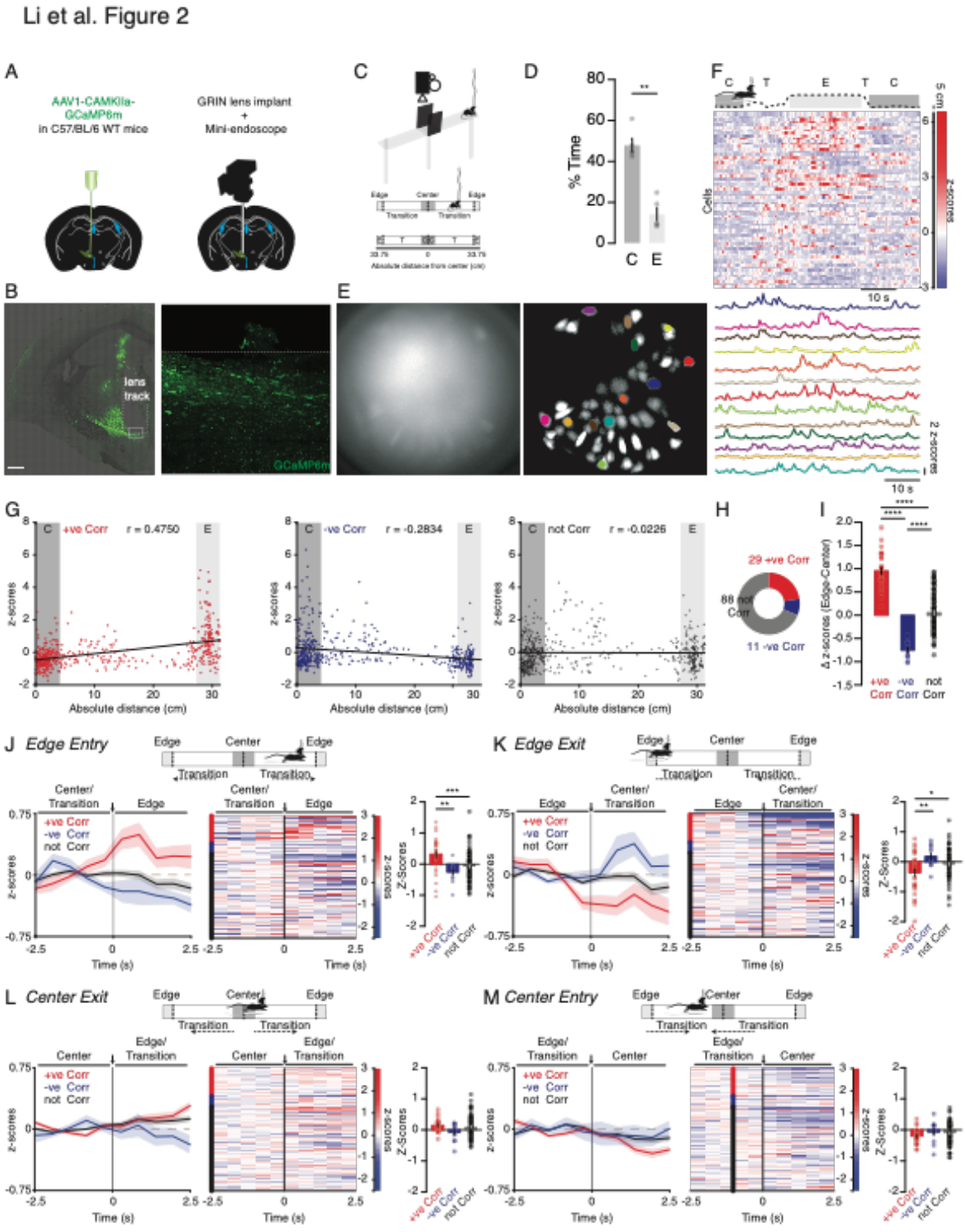
Li et al. Figure 2
A
AAV1-CAMKIIa-GCaMP6m in C57/BL/6 WT mice
GRIN lens implant + Mini-endoscope
B
lens track
GCaMP6m
C
D
% Time
C E
E
F
Cells
10 s
z-scores
G
+ve Corr r = 0.4750
-ve Corr r = -0.2834
not Corr r = -0.0226
Absolute distance (cm)
H
29 +ve Corr
88 not Corr
11 -ve Corr
I
Δ z-scores (Edge-Center)
+ve Corr
-ve Corr
not Corr
J Edge Entry
K Edge Exit
L Center Exit
M Center Entry
Time (s)
Z-Scores

Figure 2. ZI neurons are sensitive to anxiety-related cues

A) Surgical setup to express and visualize GCaMP6m in the ZI of wildtype C57BL/6 mice.

B) Example confocal image of a partial coronal section containing the GRIN lens tract and the GCaMP6m expressing (green) cells in the ZI (500 and 50μm scale bar, respectively).

C) Schematic of the elevated platform design, viewed from the side (left) and from above (right) with the compartments (edge, transition, and center) annotated along with the distance from the center to edges.

D) Bar graph reporting the percentage of time imaged mice explored in the center (C) and the open edges (E) of the elevated platform.

E) Example frame in the raw ZI calcium imaging recording video (left) and maximum intensity projection visualization of identified cells following data pre-processing (right) with example cells color coded.

F) Track plot of the center of a single mouse (top) as it traveled along the elevated platform with the different compartments highlighted. Time-locked heatmap of the calcium activity (represented in z-scores) of all recorded cells (middle) and traces from example cells (bottom; corresponding to ones labeled in Figure 2E) from the position-tracked mouse.

G) Scatterplots of example recorded cells with calcium activity positively (red), negatively (blue), and not (black) correlated to the distance of the recorded mouse from the center on the elevated platform.

H) Pie chart depicting the proportion of cells whose calcium activity positively, negatively, and not correlated to the center distance.

I) Bar graphs reporting the differences in calcium activity while mice were in the edges and in the center between the three types of center distance correlated cells.

J) Transient changes in activity of the three types of center distance correlated cells as mice entered the edge. Schematic of the positional change of the recorded mice from the center/transition area to the edge (top). Line plot (left) depicting the average activity of center distance correlated cells 2.5s before and after the positional change (align at 0s, denoted by the arrow). Heatmap (right) of the activity of all cells (grouped and sorted based on their correlation coefficient) before and after positional change.

The vertical bar to the left of the heatmap depict the group to which the cell belongs to (+ve Corr red, -ve Corr blue, not Corr black). Bar graphs (right) comparing the change in calcium activity between center distance correlated cells following the positional change.

K) Transient changes in activity of the three types of center distance correlated cells as mice exited the edge.

L) Transient changes in activity of the three types of center distance correlated cells as mice exited the center.

M) Transient changes in activity of the three types of center distance correlated cells as mice entered the center. Data are presented with the mean ± SEM.

Li et al. Figure 3

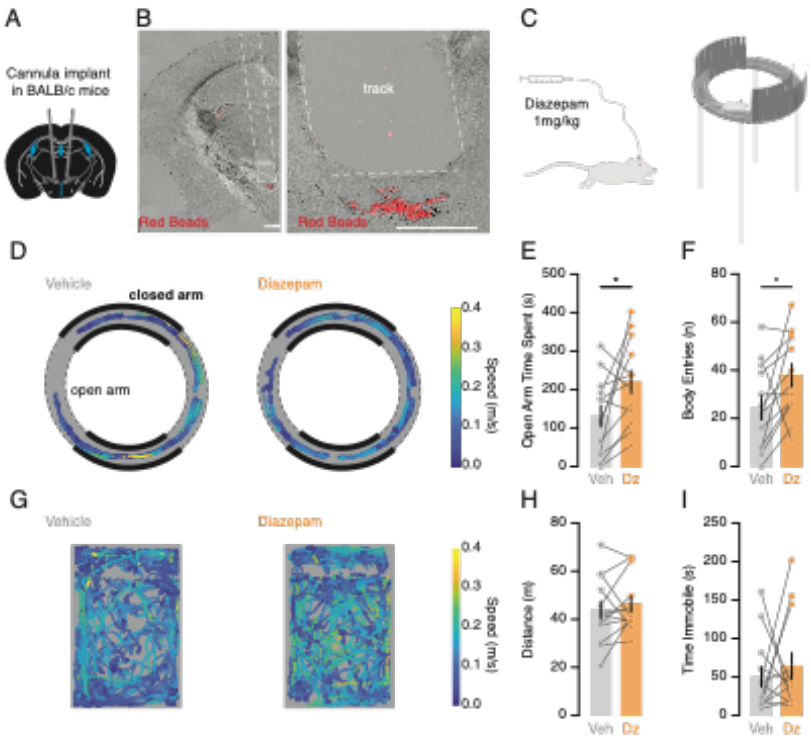

Figure 3. Local ZI diazepam infusion reduces anxiety without affecting movement

A) Surgical setup to place cannulas above the ZI.

B) Example confocal image of a partial coronal section containing the cannula tract with the red retrobeads in the ZI to show the extent of spread (500 and 250μm scale bar, respectively).

C) Schematic of the setup to directly infuse diazepam (1mg/kg) into the ZI or vehicle 30 minutes prior to testing the mouse on the EOM.

D) Track plot of a single example mouse on the EOM (dashed lines denote the open arms while the filled lines indicate the closed arms) after vehicle (left) and diazepam (right) infusion with the speed color-coded.

E) Bar graph of time the mice spent in the open arms after vehicle and diazepam infusions.

F) Bar graph depicting the number of times mice entered the open arm after vehicle and diazepam infusions.

G) Track plot of an example mouse in the OFT after vehicle (left) and diazepam (right) infusion with the speed color-coded.

H) Bar graph depicting the distance mice traveled after vehicle or diazepam infusions.

I). Bar graph showing the time mice spent immobile after vehicle or diazepam infusions.

Data are presented with the mean ± SEM.

Li et al. Figure 4

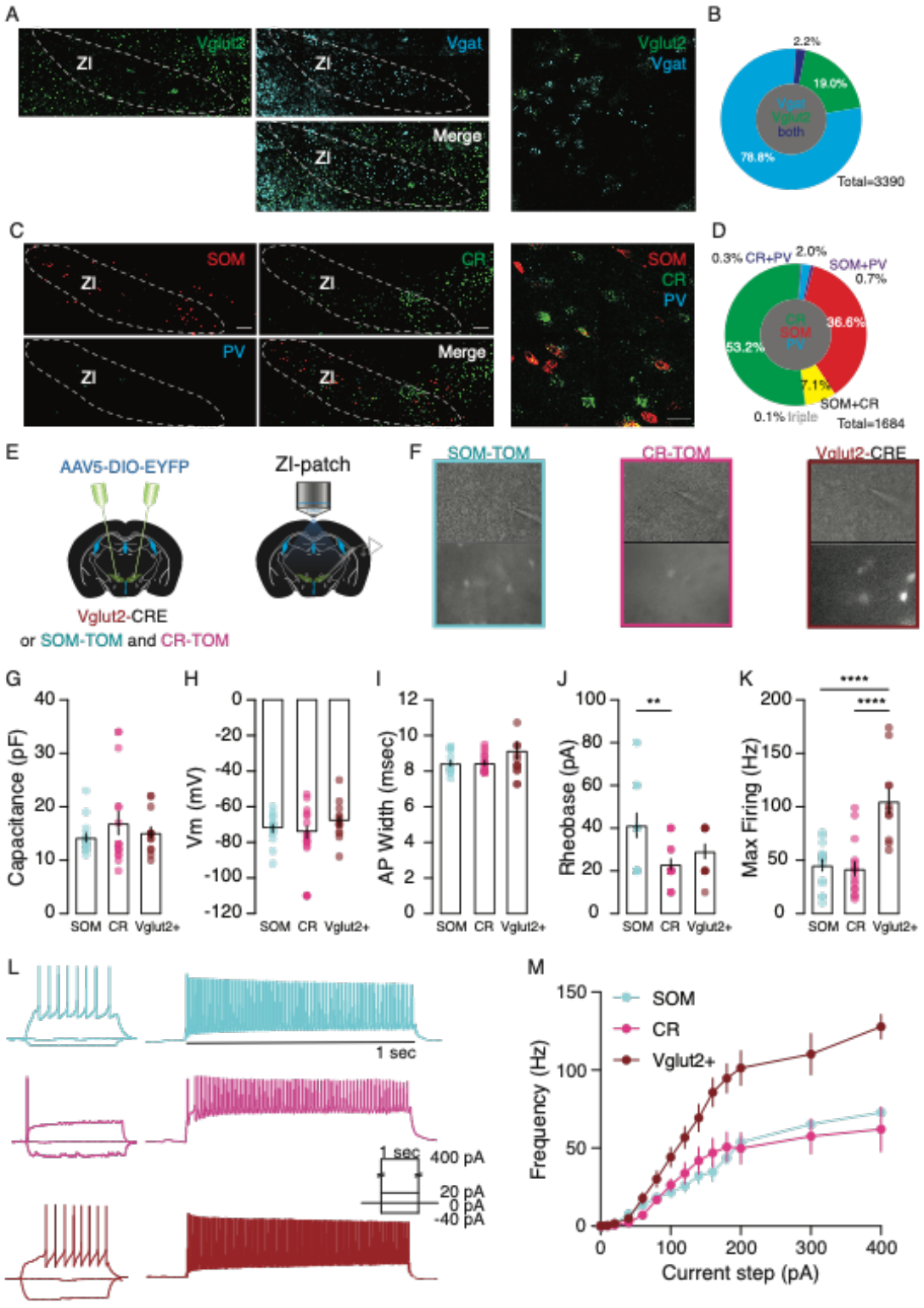

Figure 4. SOM-, CR-, and Vglut2-expressing ZI neurons display unique electrophysiological properties

A) Example confocal images of ZI-containing coronal brain slices with the FISH labeling of the mRNAs for Vglut2 (green) and Vgat (cyan) as well as the merged image (100μm and 25μm scale bar respectively).

B) Pie chart quantification of the proportion of cells in ZI expressing Vglut2, Vgat, or both (3390 cells total, 3 mice).

C) Example confocal images of the ZI-containing coronal brain sections with the FISH labeling of the mRNAs for SOM (red), CR (green), PV (cyan), and the merged (100μm and 25μm scale bar respectively).

D) Pie chart representation of the percentage of expressing the mRNAs for SOM, CR, PV, or any combination of the three (1684 cells total, 3 mice).

E) Schematic of the experimental procedure.

F) Example brightfield (top) and fluorescent (bottom) images of patched cells: SOM (cyan), CR (magenta), and Vglut2 (maroon).

G) Bar graphs reporting the capacitance from SOM-, CR-, and Vglut2-expressing ZI cells.

H) Bar graphs depicting the resting membrane potential (Vm) from SOM-, CR-, and Vglut2-expressing ZI cells.

I) Bar graphs of the action potential width from SOM-, CR-, and Vglut2-expressing ZI cells.

J) Bar graphs presenting the rheobase from SOM-, CR-, and Vglut2-expressing ZI cells.

K) Bar graphs summarizing the maximum firing frequency from SOM-, CR-, and Vglut2- expressing ZI cells.

L) Example current clamp recordings from SOM-, CR-, and Vglut2-expressing ZI cells upon various current step injections.

M) Summary input/output curve for SOM-, CR-, and Vglut2- positive cells. Data are presented with the mean ± SEM.

Li et al. Figure 5

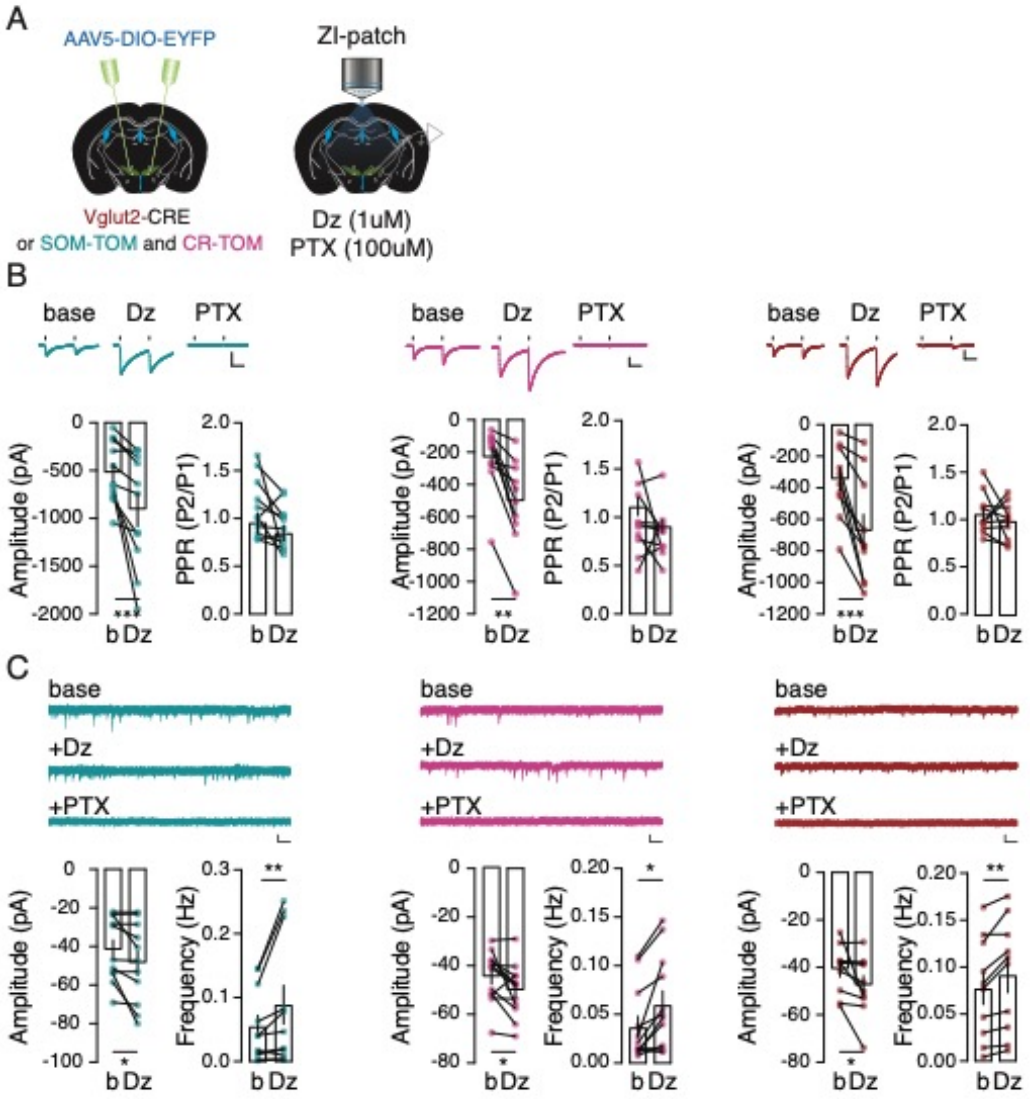

Figure 5. Diazepam potentiates inhibitory drive onto SOM-, CR-, and Vglut2-expressing ZI neurons

A) Schematic of the experimental setup.

B) Example IPSC from representative SOM- (cyan), CR- (magenta) and Vglut2- (maroon) expressing ZI cells during baseline (base) and following subsequent bath application of diazepam (Dz) and picrotoxin (PTX). The scale bars represent 100pA (vertical) and 25ms (horizontal). Bar graphs report the amplitude of the IPSCs and the paired-pulse ratio (PPR) both conditions.

C) Example sIPSCs recorded from representative SOM-, CR-, and Vglut2-expressing ZI cells during baseline (base) and during bath application of diazepam (Dz) and picrotoxin (PTX). The scale bars represent 30pA (vertical) and 500ms (horizontal). Bar graphs of the amplitude and the frequency of sIPSCs in the baseline and following diazepam application. Data are presented with the mean ± SEM.

Li et al. Figure 6

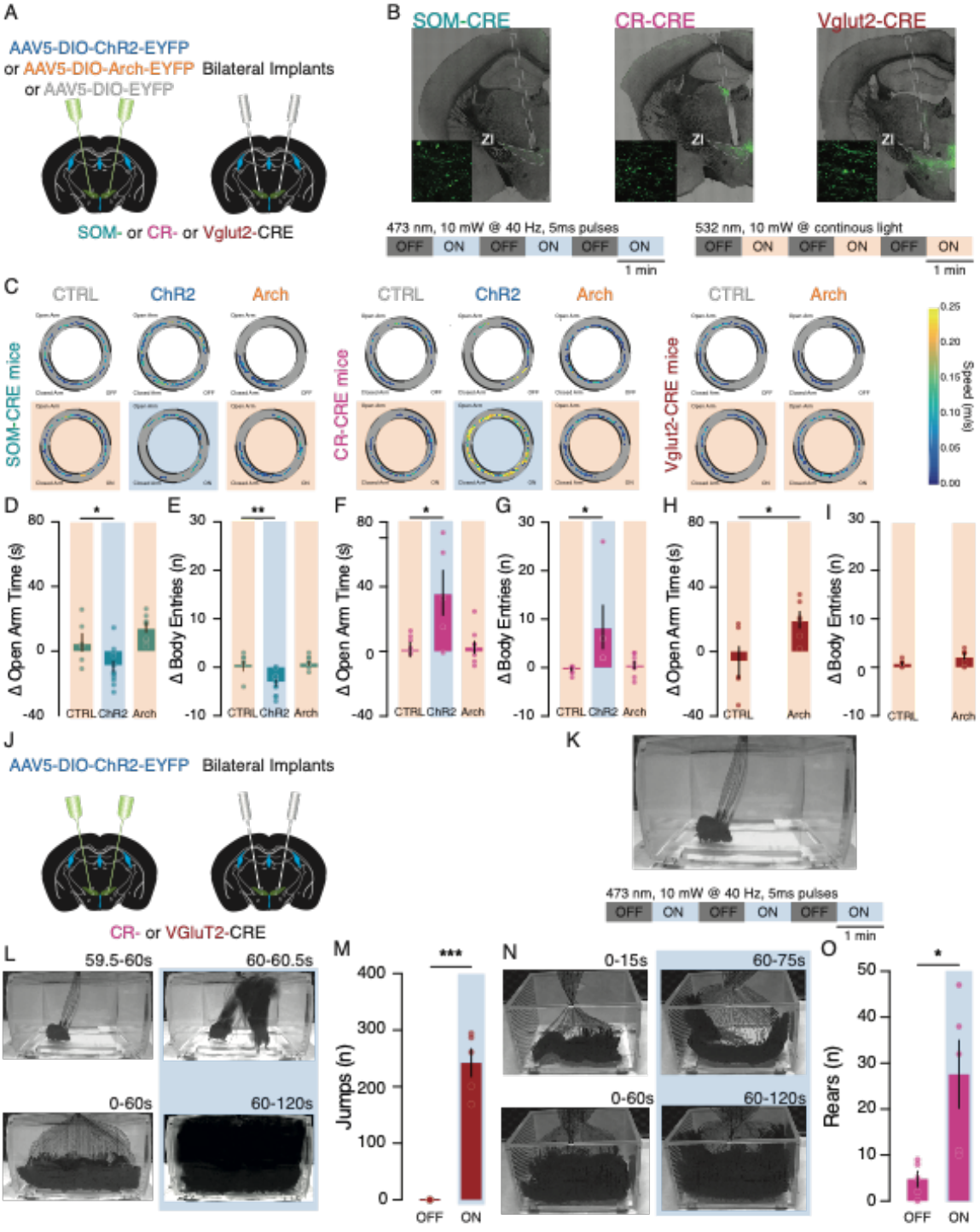

Figure 6. Optogenetic manipulation of SOM-, CR-, and Vglut2-expressing ZI neurons trigger distinct anxiety-related traits

A) Schematic of the experimental procedure.

B) Example confocal images of coronal brain slices with the expression of ChR2 in the SOM-, CR-, and Vglut2-expressing ZI cells and the optic fiber tracts above (100μm scale bar). The inserts are high magnification zoomed-in confocal images immediately below the tip of the optic tract depicting ChR2-expressing cells (25μm scale bar). Laser stimulation protocols for ChR2 mediated activation (bottom left) and Arch mediated inhibition (bottom right) of ZI cells.

C) Example track plots of the center of mice expressing control fluorescent protein, ChR2, and Arch in the SOM-, CR-, and Vglut2-expressing ZI cells on the EOM (dashed lines denote the open arms while the filled lines represent the closed arms). The periods when the laser stimulations were OFF are shown on top and ON are shown at the bottom and shaded with the speed color-coded.

D) Bar graph depicting the difference in the amount of time mice expressing the control construct, ChR2, and Arch in the SOM-expressing ZI cells spent in the open arm between periods when the laser was on and off.

E) Bar graph depicting the difference in the number of times mice expressing the control construct, ChR2, and Arch in the SOM-expressing ZI cells entered open arm between periods when the laser was on and off.

F) Bar graph depicting the difference in the amount of time CR-CRE mice spent in the open arm between periods when the laser was on and off.

G) Bar graph depicting the difference in the number of times CR-CRE mice entered open arm between periods when the laser was on and off.

H) Bar graph depicting the difference in the amount of time Vglut2-CRE mice spent in the open arm between periods when the laser was on and off.

I) Bar graph depicting the difference in the number of times Vglut2-CRE mice entered open arm between periods when the laser was on and off.

J) Surgical setup to express excitatory opsin (ChR2) in CR-, and Vglut2-expressing ZI cells and the implantation of optic fibers above.

K) Photograph of the closed transparent chamber and the laser stimulation protocol for the ChR2 mediated activation.

L) Example minimum intensity projection of a 0.5s and a 1-minute window before and after laser stimulation (blue-shaded) demonstrating the light triggered jumping behavior observed in the mice expressing ChR2 in the Vglut2-expressing ZI cells.
M) Bar graph presenting the cumulative number of jumps made by mice expressing ChR2 in the Vglut2-expressing ZI cells during the laser off and on periods.
N) Example minimum intensity projection of a 15s and a 1-minute window in the stimulation off and on period (blue-shaded) demonstrating the light induced increase in the rearing behavior observed in the mice expressing ChR2 in the CR-expressing ZI cells.
O) Bar graph presenting the cumulative number of rears made by mice expressing ChR2 in the CR-expressing ZI cells during the laser off and on periods. are presented with the mean ± SEM.

Supplementary Materials

Li et al. Figure S1

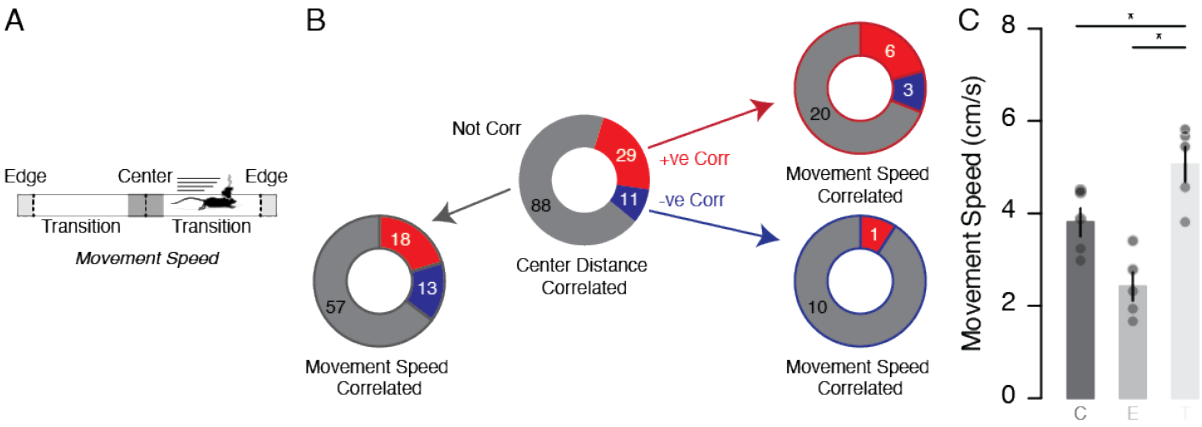

Figure S1. Anxiety sensitive ZI neurons are not sensitive to movement

A) Schematic of the top view of the elevated platform.

B) Pie chart depicting the proportion of center distance correlated cells (center; also reported in figure 2H). Proportion of positively (lined in red, top right), negatively (lined in blue, bottom right) and not (lined in black, bottom left) correlated center distance cell groups that show movement speed correlated activity.

C) Bar graphs reporting the average movement speed of the recorded mice in the center, the edges, and the transition areas. Data are presented with the mean ± SEM.

Li et al. Figure S2

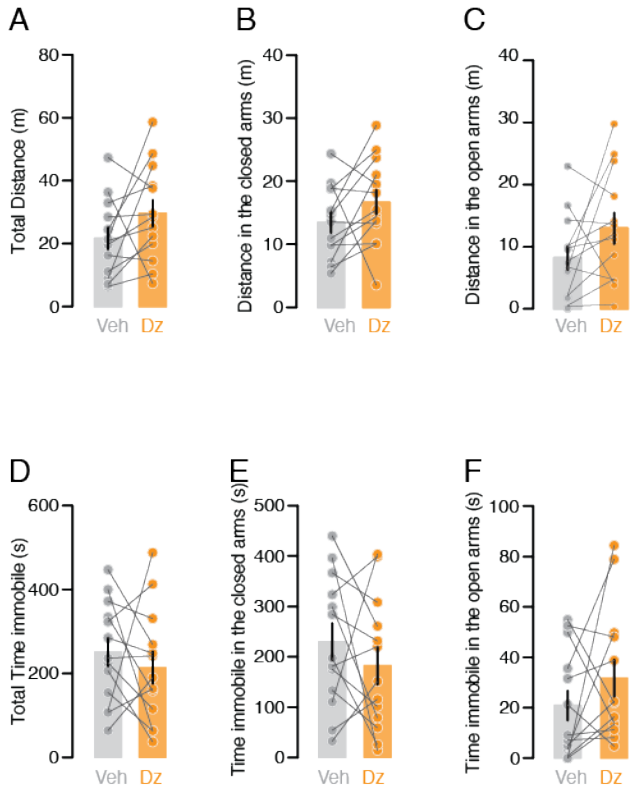

Figure S2. Local ZI diazepam infusion does not affect locomotor parameters on the EOM

A) Bar graph showing the total distance mice traveled after vehicle or diazepam infusions.

B) Bar graph depicting the distance mice traveled in the closed arms after vehicle or diazepam infusions.

C) Bar graph reporting the distance mice traveled in the open arms after vehicle or diazepam infusions.

D) Bar graph of the total time mice spent immobile after vehicle or diazepam infusions.

E) Bar graph comparing the total time mice spent immobile in the closed arms after vehicle or diazepam infusions.

F) Bar graph presenting the total time mice spent immobile in the open arms after vehicle or diazepam infusions. Data are presented with the mean ± SEM.

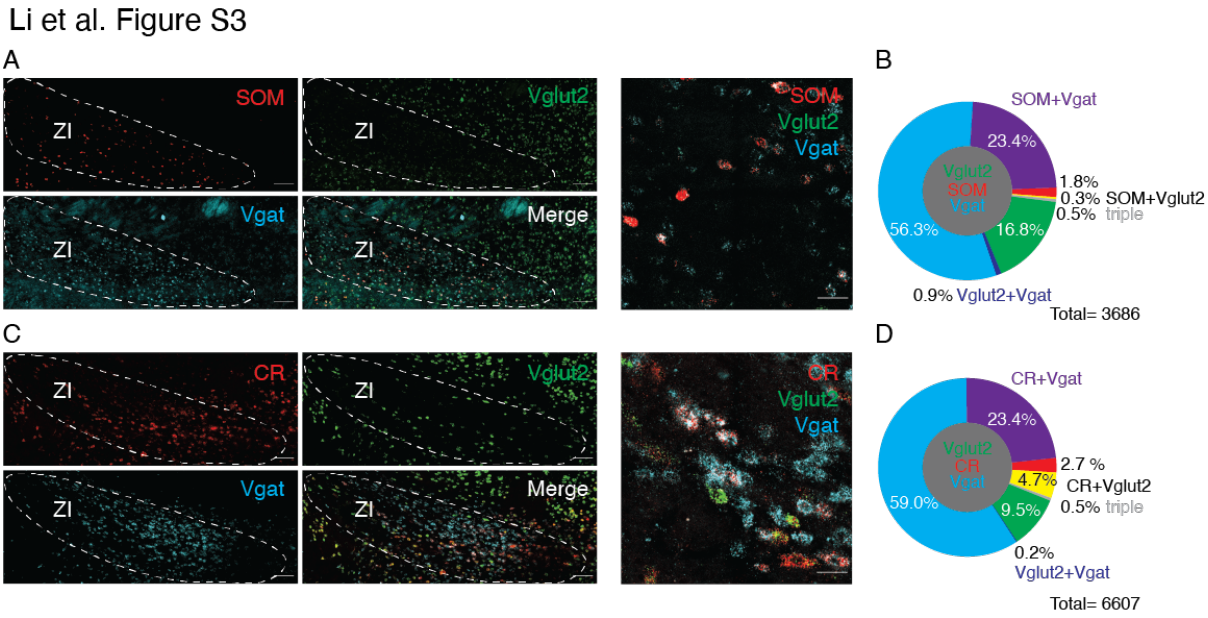

Figure S3. SOM- and CR-expressing ZI neurons co-express Vgat

A) Example confocal images of the ZI- containing brain slices with the FISH labeling of the mRNAs for SOM (red), Vglut2 (green), Vgat (cyan) as well as the merged image (100μm and 25μm scale bar respectively).

B) Pie chart quantification of the proportion of cells in ZI expressing SOM, Vglut2, Vgat, or any combination of all three (3686 cells, 3 mice).

C) Example confocal images of the ZI with the FISH labeling of the mRNAs for CR (red), Vglut2 (green), Vgat (cyan), and the merged image (100μm and 25μm scale bar respectively).

D) Pie chart representation of percentage of cells in the ZI with the labeling for CR, Vglut2, Vgat, or any combination of the three (6607 cells, 3 mice).

Li et al. Figure S4

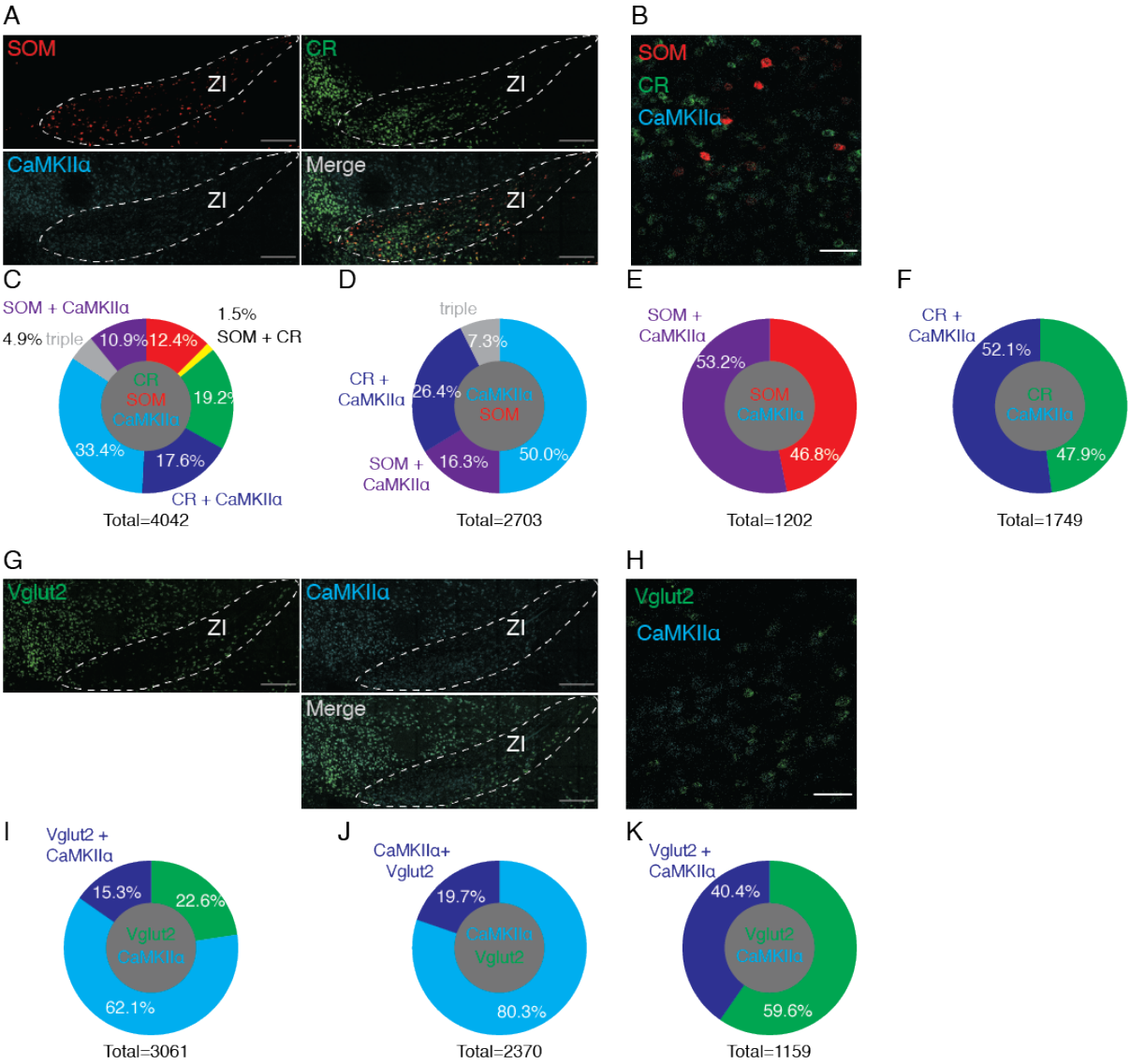

Figure S4. Subsets of SOM-, CR-, and Vglut2- expressing ZI neurons co-express CaMKIIα

A) Example confocal images of the ZI- containing brain slices with the FISH labeling of the mRNAs for SOM (red), CR (green), CaMKIIα (cyan) as well as the merged image (250μm scale bar).

B) High magnification confocal image with the three channels merged (50μm scale bar).

C) Pie chart representation of percentage of cells in the ZI with the labeling for SOM, CR, CaMKIIα, or any combination of the three (4042 cells, 3 mice).

D) Pie chart of percentage of CaMKIIα expressing cells in FigureS4C expressing SOM, CR, or SOM and CR (triple) (2703 cells total).

E) Pie chart representation of percentage of SOM expressing cells in FigureS4C expressing and not expressing CaMKIIα (1202 cells total).

F) Pie chart depiction of percentage of CR expressing cells in Figure S4C expressing and not expressing CaMKIIα (1749 cell total).

G) Example confocal images of the ZI- containing brain slices with the FISH labeling of the mRNAs for Vglut2 (green) and CaMKIIα (cyan) as well as the merged image (250μm scale bar).

H) High magnification confocal image with the two channels merged (50μm scale bar).

I) Pie chart presenting the percentage of cells in the ZI with the labeling for Vglut2, CaMKIIα, or both (3061 cells, 3 mice).

J) Pie chart showing the percentage of CaMKIIα expressing cells in FigureS4I expressing or not expressing Vglut2 (2370 cells total).

K) Pie chart of the percentage of Vglut2 expressing cells in FigureS4I expressing or not expressing CaMKIIα (1159 cells total).

Li et al. Figure S5

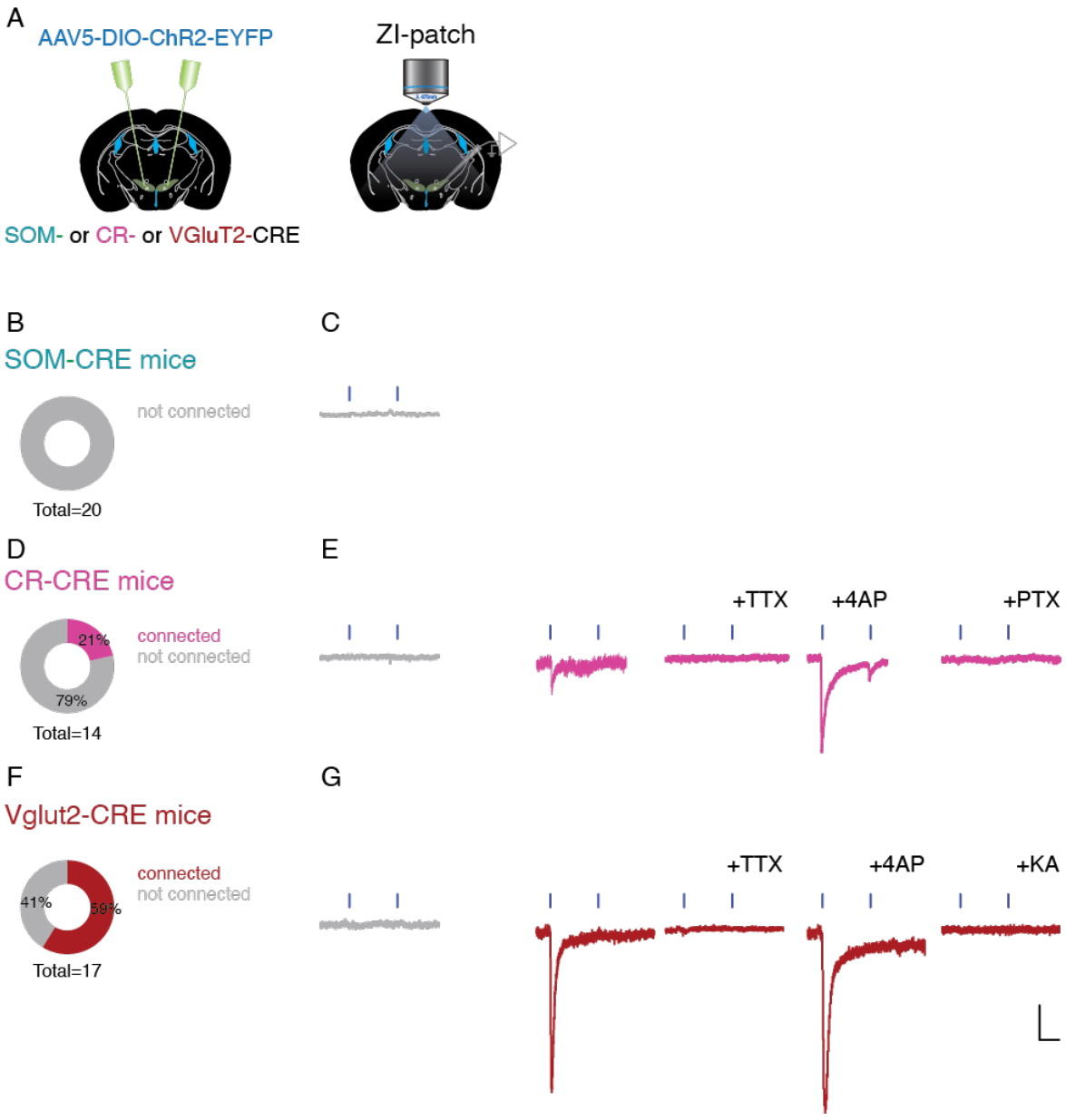

Figure S5. CR- and Vglut2- but not SOM- expressing ZI cells respectively provide local monosynaptic inhibitory and excitatory inputs

A) Schematic of the experimental procedure.

B) Pie chart presenting the percentage of ChR2- negative ZI cells that are monosynaptically innervated by ChR2-expressing SOM-positive ZI cells (20 cells, 5 mice).

C) Example current trace recorded in a ChR2- negative ZI cells (from Figure S5B) upon blue light (473nm; 5ms pulses 50ms apart) illumination displaying no evoked photocurrent.

D) Pie chart presenting the percentage of ChR2- negative ZI cells that receive monosynaptic inputs from ChR2-expressing CR-positive ZI cells (14 cells, 3 mice).

E) Example current trace recorded in a ChR2-negative ZI (from Figure S5D) upon blue light illumination displaying no evoked photocurrent (left, grey) and example traces of a ChR2-negative ZI that display a blue light-induced monosynaptic inhibitory photocurrent (right, magenta).

F) Pie chart reporting the percentage of ChR2-negative ZI cells that receive monosynaptic inputs from Vglut2-ChR2 ZI cells (17 cells, 3 mice).

G) Example current trace recorded in a ChR2-negative ZI (from Figure S5F) upon blue light illumination displaying no evoked photocurrent (left, grey) and example traces of a ChR2-negative ZI that display a blue light-induced monosynaptic excitatory photocurrent (right, maroon). The scale bar displayed (bottom right) represents 25pA vertically and 50ms horizontally.

Li et al. Figure S6

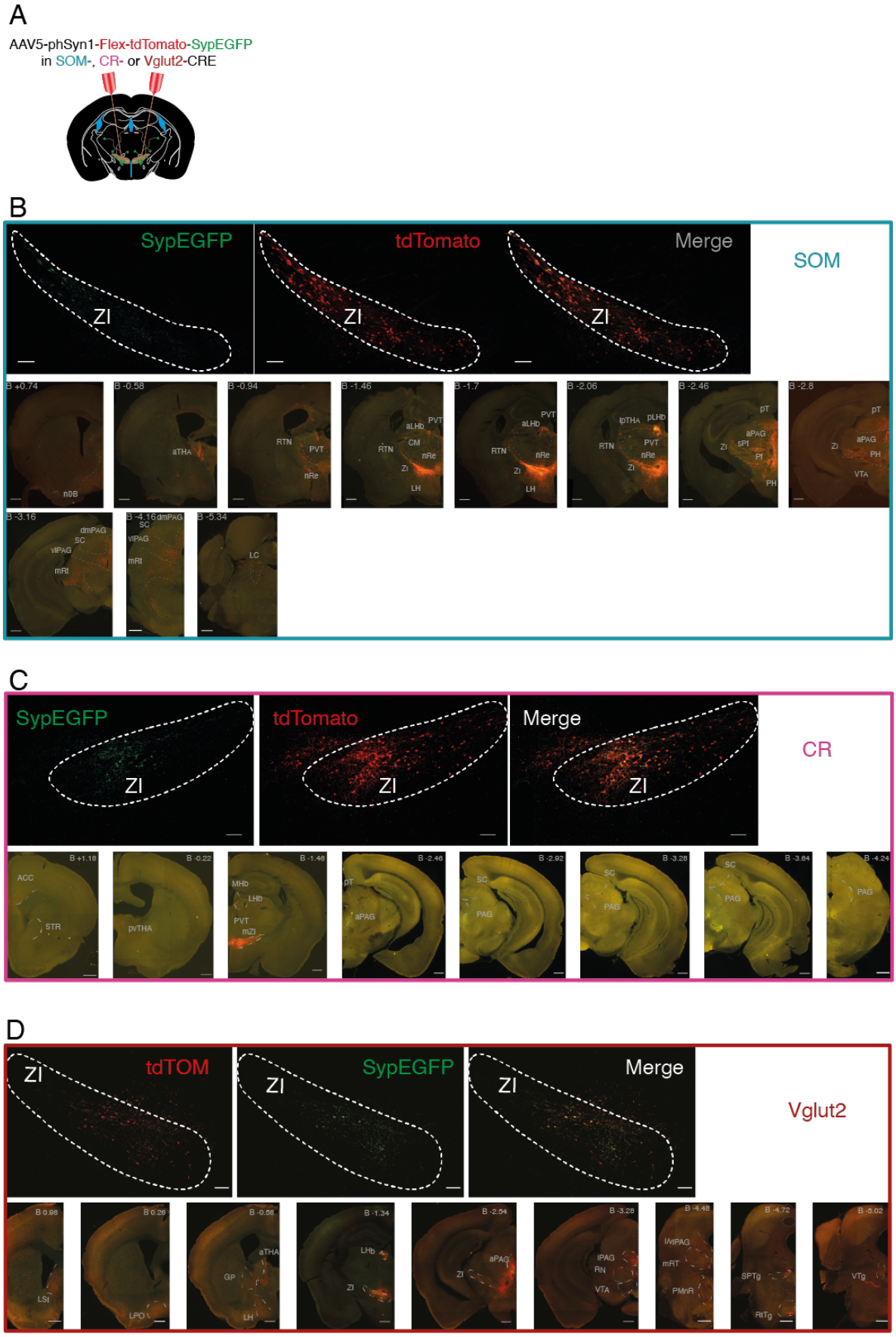

Figure S6. ZI SOM-, CR-, and Vglut2- expressing cells send differential and similar long-range projections across the brain

A) Schematic of the experimental procedure.

B) Example confocal images (top) of the ZI from a representative SOM-CRE mice with the synaptophysin tagged EGFP (green), tdTomato (red), and the merged (100μm, 3 mice). Fluorescent images (bottom) presenting brain sections from the representative mouse brain where noticeable fluorescent signals (tdTomato labelled axons and EGFP labelled axon terminals) were detected with the location with respect to the Bregma noted (upper left). The scale bar represents 500μm.

C) Example confocal images (top) of the ZI from a representative CR-CRE mice with the synaptophysin tagged EGFP, tdTomato, and the merged (100μm, 3 mice). Fluorescent images (bottom) presenting brain sections from the representative mouse brain where noticeable fluorescent signals were observed with Bregma coordinate noted (upper left). The scale bar represents 500μm.

D) Example confocal images (top) of the ZI from a representative Vglut2-CRE mice with the synaptophysin tagged EGFP, tdTomato, and the merged (100μm, 3 mice). Fluorescent images (bottom) presenting brain sections from the representative mouse brain where noticeable fluorescent signals were found with Bregma coordinate indicated (upper left). The scale bar represents 500μm.

Li et al. Figure S7

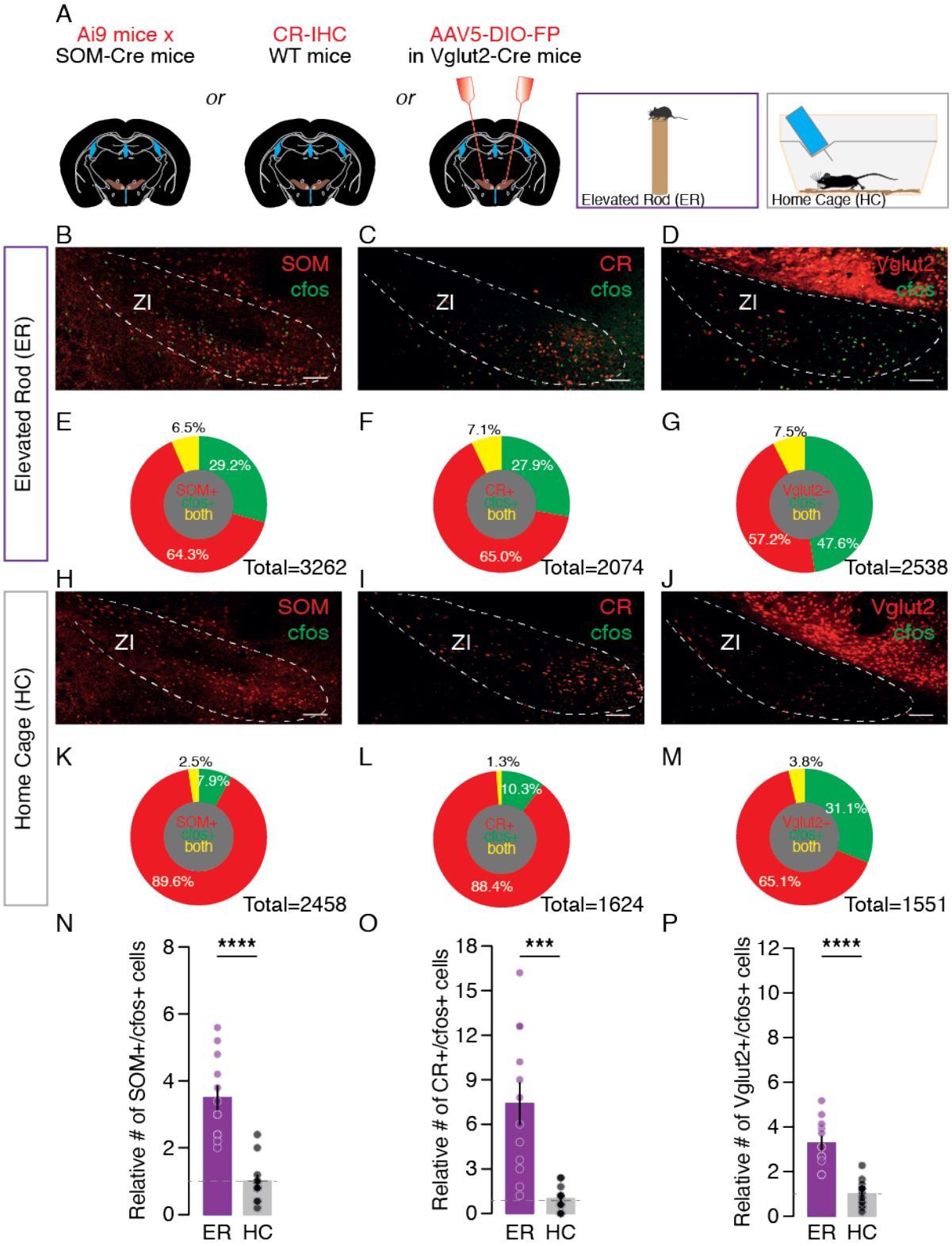

Figure S7. Anxious elevated experience activates ZI SOM-, CR-, and Vglut2-expressing cells.

A) Schematic of the experimental procedure.

B) Example confocal image of the ZI-containing brain section with SOM (red) and IHC labeling of cfos (green) in mice that were exposed to the anxious elevated rod experience (100μm scale bar).

C) Example confocal image of the ZI-containing brain slice with the IHC labeling of CR (red) and cfos (green) in mice that were exposed to the anxious elevated rod experience (100μm scale bar).

D) Example confocal image of the ZI with Vglut2 (red) and IHC labeling of cfos (green) in mice that were exposed to the anxious elevated rod experience (100μm scale bar).

E) Pie chart reporting the proportion of ZI cells (Figure S3B) labeled with SOM, cfos, or both (3262 cells, 3 mice)

F) Pie chart depicting the proportion of ZI cells (Figure S3C) labeled with CR, cfos, or both (2074 cells, 3 mice).

G) Pie chart of the proportion of ZI cells (Figure S3D) labeled with Vglut2, cfos, or both (2538 cells, 3 mice).

H) Example confocal image of the ZI with SOM (red) and the IHC labeling of cfos (green) in the ZI of mice that were left in the home cage (100μm scale bar).

I) Example confocal image of ZI-containing brain section with the IHC labeling against CR (red) and cfos (green) in mice that were left in the home cage (100μm scale bar).

J) Example confocal image of the ZI-containing brain slice with Vglut2 (red) and IHC labeling for cfos (green) in the mice that were left in the home cage (100μm scale bar).

K) Pie chart representation of the proportion of ZI cells (Figure S3H) labeled with SOM, cfos, or both (2458 cells, 3 mice).

L) Pie chart description of the proportion of ZI cells (Figure S3I) labeled with CR, cfos, or both (1624 cells, 3 mice);

M) Pie chart quantification of the proportion of ZI cells (Figure S3J) labeled with Vglut2, cfos, or both (1551 cells, 3 mice).

N) Bar graphs reporting the relative number of SOM+ and cfos+ labeled cells (normalized to the control mice) in the ZI for both experimental conditions.

O) Bar graphs presenting the relative number of CR+ and cfos+ labeled cells (normalized to the control mice) in the ZI for both experimental conditions.

P) Bar graphs comparing the relative number of Vglut2+ and cfos+ labeled cells (normalized to the control mice) in the ZI for both experimental groups. Data are presented with the mean ± SEM.

Li et al. Figure S8

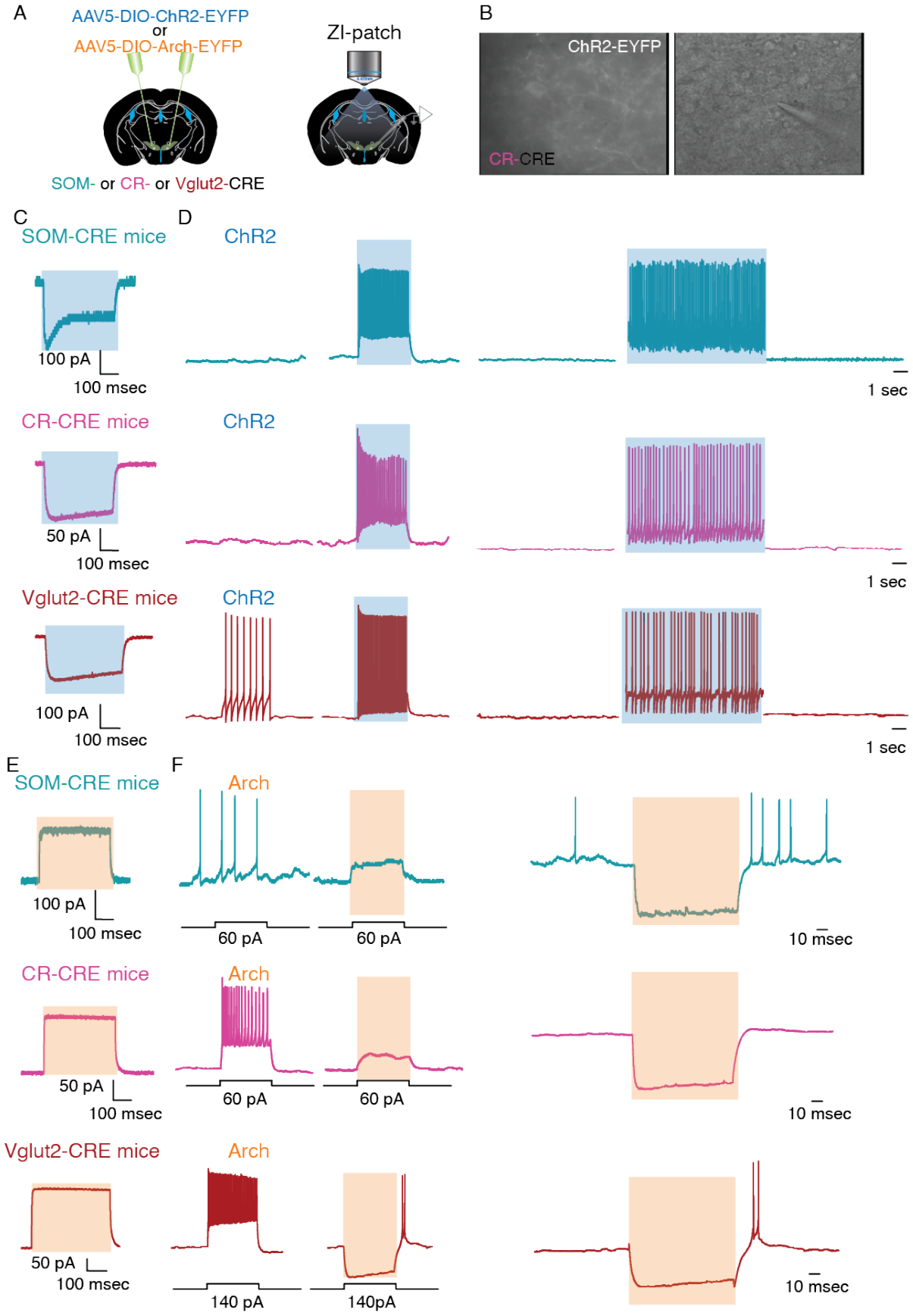

Figure S8. Validation of optogenetic tools in SOM-, CR-, and Vglut2-expressing ZI *in-vitro*

A) Schematic of the experimental procedure.

B) Example fluorescent and brightfield images of a patched ChR2 expressing ZI CR cell.

C) Example photocurrent recorded upon blue light (473nm; 400ms) illumination in representative ChR2 infected SOM- (cyan), CR- (magenta), and Vglut2- (maroon) expressing ZI cells.

D) Example traces of representative ChR2 infected SOM- (cyan), CR- (magenta), and Vglut2- (maroon) expressing ZI cells recorded in current clamp mode (I = 0) that shows a continuous blue light stimulation (1s) evokes time-locked increase in firing and a 10s blue light stimulation (5ms pulses, 40Hz) also induced sustained firing in all cells.

E) Example photocurrent recorded upon green light (532nm; 400ms) illumination in a representative Arch infected SOM- (cyan), CR- (magenta), and Vglut2- (maroon) expressing ZI cell.

F) Example traces of a representative Arch infected SOM- (cyan), CR- (magenta), and Vglut2- (maroon) expressing ZI cell recorded in current clamp mode that depicts a continuous green light stimulation (1s) suppresses evoked firing and hyperpolarizes neurons at rest.

Li et al. Figure S9

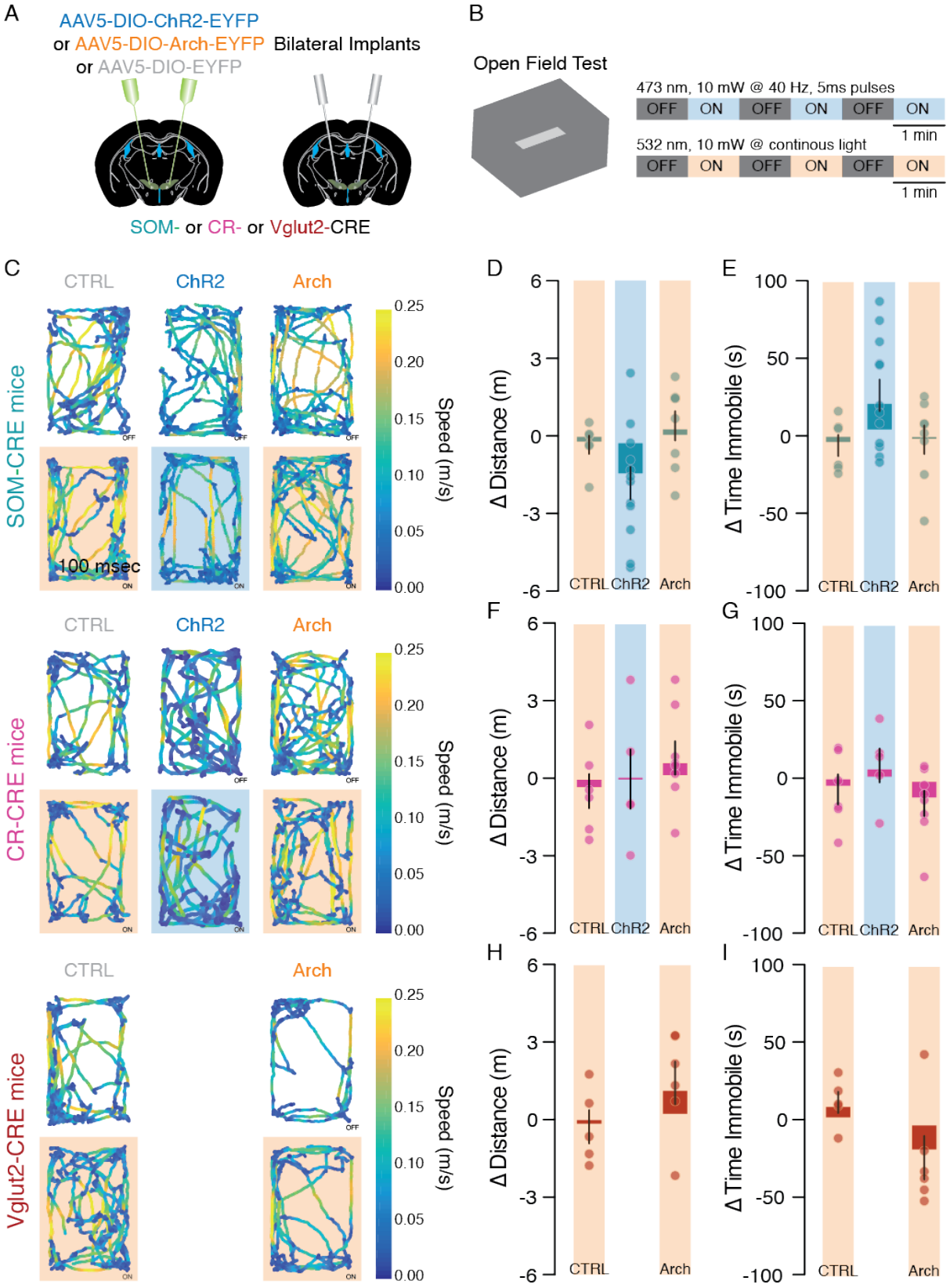

Figure S9. Bidirectional optogenetic manipulations of SOM-, CR-, and Vglut2-expressing ZI cells do not impact general locomotion.

A) Schematic of the experimental procedure.

B) Schematic of the open field test (OFT) box and the laser stimulation protocols for ChR2 mediated activation and Arch mediated inhibition.

C) Example track plots of the center of mice expressing control fluorescent protein, ChR2, and Arch in the SOM- (cyan), CR- (magenta), and Vglut2- (maroon) expressing ZI cells in the OFT during the periods when the laser stimulations were off and on (shaded) with the speed color-coded.

D) Bar graph reporting the difference in distance mice expressing the control construct, ChR2, and Arch in the SOM-expressing ZI cells traveled between periods when the laser was on and off.

E) Bar graph depicting the difference in the time mice expressing the control construct, ChR2, and Arch in the SOM-expressing ZI cells spent immobile between periods when the laser was on and off.

F) Bar graph presenting the difference in the distance mice expressing the control construct, ChR2, and Arch in the CR-expressing ZI cells traveled between periods when the laser was on and off.

G) Bar graph of the difference in the time mice expressing the control construct, ChR2, and Arch in the CR- expressing ZI cells spent immobile between periods when the laser was on and off.

H) Bar graph comparing the difference in the distance mice expressing the control construct and Arch in the Vglut2-expressing ZI cells traveled between periods when the laser was on and off.

I) Bar graph with the difference in the time mice expressing the control construct and Arch in the Vglut2-expressing ZI cells spent immobile between periods when the laser was on and off. Data are presented with the mean ± SEM.

Li et al. Figure S10

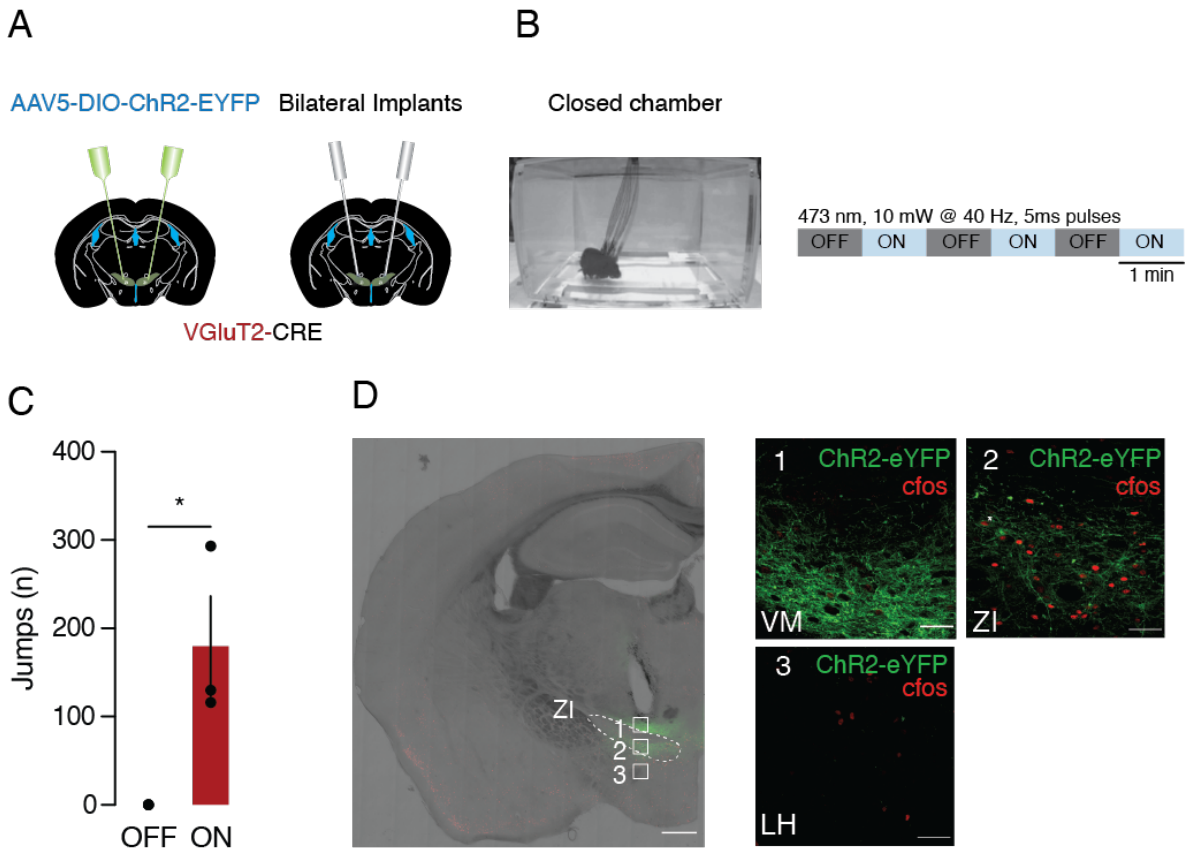

Figure S10. Histological validation of optogenetic stimulation range in the ZI of mice driven to jump by the activation of Vglut2- expressing ZI cells.

A) Schematic of the surgical procedure.

B) Schematic of the experimental procedure (left) with the stimulation protocol (right).

C) Bar graph reporting the number of jumps made by mice expressing ChR2 in ZI Vglut2-expressing cells during laser ON and OFF periods.

D) Example confocal images of coronal brain slices (left) with the expression of ChR2 (green) in the Vglut2- expressing ZI cells, the optic fiber above, and the post-hoc IHC labeling of cfos (red). The scale bar indicates 500μm. High magnification zoomed-in confocal images (right) in the ventromedial thalamus (VM, site 1), ZI (site 2, * indicates an example ChR2- expressing cells co-labeled with cfos), and LH (site 3). The scale bar measures 50μm.

Li et al. Figure S11

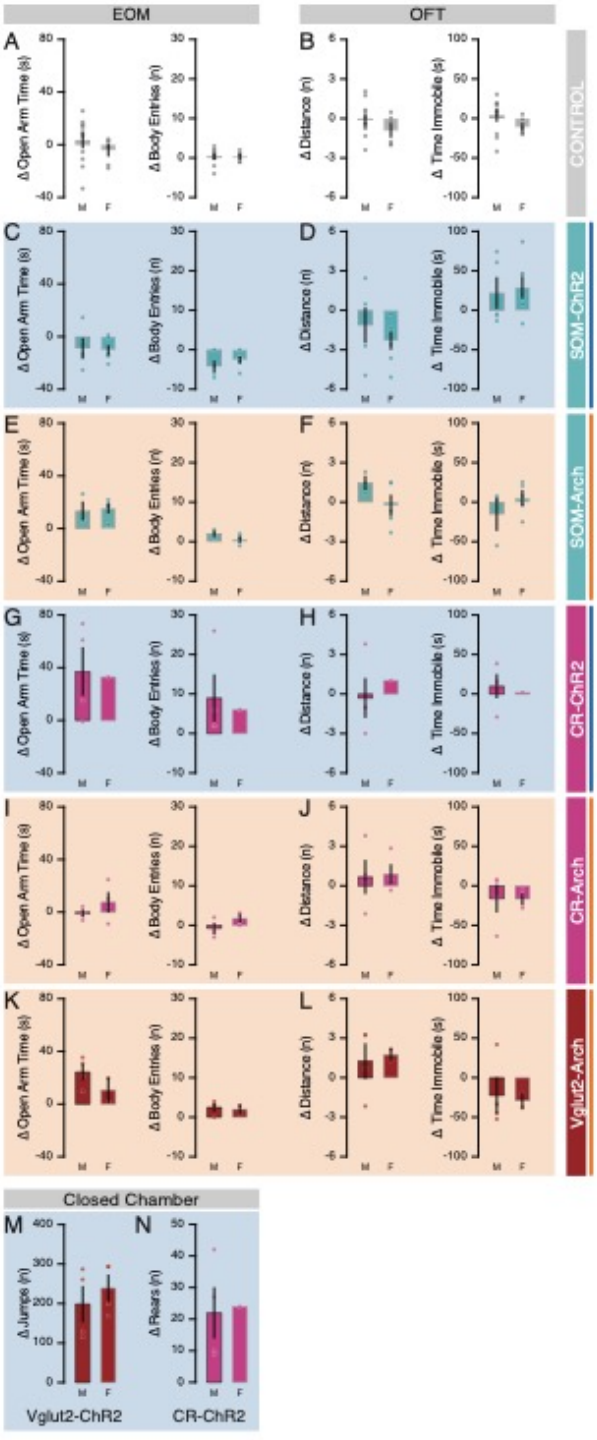

Figure S11. Sex comparisons for mice performance in the EOM, OFT, and the closed chamber.

A) Bar plot reporting the delta (ON – OFF) time spent in the open arms of the EOM (left) and the number of body entries into them (right) between male and female control mice during periods when the laser was on and off.

B) Bar plot of the delta distance traveled (left) and time immobile (right) in the OFT between male and female control mice.

C) Bar plot depicting the delta time spent in the open arms of the EOM (left) and the number of body entries into them (right) between male and female mice expressing ChR2 in SOM- positive ZI cells and receiving optogenetic stimulation.

D) Bar plot showing the delta distance traveled (left) and time immobile (right) in the OFT between male and female mice expressing ChR2 in SOM- positive ZI cells.

E) Bar plot showing the difference in the time spent in the open arms of the EOM (left) and the number of body entries into them (right) between male and female mice expressing Arch in SOM- positive ZI during periods when the laser was on and off.

F) Bar plot of the difference in distance traveled (left) and time immobile (right) in the OFT between male and female mice expressing Arch in SOM- positive ZI cells.

G) Bar plot reporting the difference in time spent in the open arms of the EOM (left) and the number of body entries into them (right) between male and female mice expressing ChR2 in CR- positive ZI cells during laser ON and OFF periods.

H) Bar plot of the difference in distance traveled (left) and time immobile (right) in the OFT between male and female mice expressing ChR2 in CR- positive ZI cells.

I) Bar plot depicting the delta time spent in the open arms of the EOM (left) and the number of body entries into them (right) between male and female mice expressing Arch in CR- positive ZI cells during laser ON and OFF periods

J) Bar plot showing the delta distance traveled (left) and time immobile (right) in the OFT between male and female mice expressing Arch in CR- positive ZI cells.

K) Bar plot showing the delta time spent in the open arms of the EOM (left) and the number of body entries into them (right) between male and female mice expressing Arch in Vglut2- positive ZI cells during periods when the laser was on and off.

L) Bar plot of the difference in distance traveled (left) and time immobile (right) in the OFT between male and female mice expressing Arch in Vglut2- positive ZI cells.

M) Bar plot depicting the delta number of jumps in the closed chamber made by male and female mice expressing ChR2 in the Vglut2- positive ZI cells during periods when the laser was on and off.

N) Bar plot reporting the delta number of rears in the closed chamber made by male and female mice expressing ChR2 in the CR- positive ZI cells during periods when the laser was on and off.

Video S1. Example calcium recording of ZI cells while the recorded mouse traveled between the enclosed center and the open edge of elevated platform.

Video S2. Local ZI infusion of diazepam increases open arm exploration in the EOM (4X speed).

Video S3. Optogenetic activation of Vglut2- ZI cells trigger time-locked jumps (4X speed).

Video S4. Optogenetic activation of CR- ZI cells promote rears (4X speed).

Video S5. Optogenetic activation of SOM- ZI cells do not elicit any peculiar behaviors (4X speed).

Table S1. Statistical Information for Figure 1.

Fig.1E	Unpaired two-tailed t-test		
	t	DF	P value
	9.859	22	<0.0001

Table S2. Statistical Information for Figure 2.

Fig. 2D	Paired t-test				
	t	DF	P value		
	5.949	4	P = 0.0040		
Fig.2I	One-way ANOVA				
		SS	DF	MS	$F_{(DFn, DFd)}$	P Value
	Cells	28.36	2	14.18	$F_{(2, 125)} = 89.30$	P<0.0001
	Residual	19.85	125	0.1588		
	Bonferroni's Multiple Comparisons Test					
				t	DF	P Value
		+ Corr vs - Corr		12.11	125	<0.0001
		+ Corr vs Non Corr		10.55	125	<0.0001
		- Corr vs Non Corr		6.341	125	<0.0001
Fig.2J	Two-way ANOVA (Average Traces)					
		SS	DF	MS	$F_{(DFn, DFd)}$	P value
	Interaction	0.4350	2	0.2175	$F_{(2, 24)} = 18.52$	P<0.0001
	Time	0.4350	2	0.2175	$F_{(2, 24)} = 18.52$	P<0.0001
	Cells	0.0001131	1	0.0001131	$F_{(1, 24)} = 0.009627$	P=0.9227
	Residual	0.2819	24	0.01175		
	Bonferroni's Multiple Comparisons Test					
				t	DF	P Value
		Non Corr		1.048	24.00	0.9151
		+ Corr		4.656	24.00	0.0003
		- Corr		3.778	24.00	0.0028
	One-way ANOVA (Delta Responses)					
		SS	DF	MS	$F_{(DFn, DFd)}$	P Value
	Cells	4.145	2	2.073	$F_{(2, 125)} = 9.598$	0.0001
	Residual	26.99	125	0.2159		
	Bonferroni's Multiple Comparisons Test					
				t	DF	P Value
		+ Corr vs - Corr		3.513	125	0.0019
		+ Corr vs Non Corr		3.929	125	0.0004
		- Corr vs Non Corr		1.259	125	0.6312

Fig.2K	Two-way ANOVA (Average Traces)					
		SS	DF	MS	$F_{(DFn, DFd)}$	P value
	Interaction	0.3637	2	0.1819	$F_{(2, 24)} = 12.04$	P=0.0002
	Time	0.3637	2	0.1819	$F_{(2, 24)} = 12.04$	P=0.0002
	Cells	0.05497	1	0.05497	$F_{(1, 24)} = 3.639$	P=0.0685
	Residual	0.3625	24	0.01510		
	Bonferroni's Multiple Comparisons Test					
				t	DF	P Value
	Non Corr			1.011	24.00	0.9669
	+ Corr			4.616	24.00	0.0003
	- Corr			2.322	24.00	0.0871
	One-way ANOVA (Delta Responses)					
		SS	DF	MS	$F_{(DFn, DFd)}$	P Value
	Cells	2.798	2	1.399	$F_{(2, 125)} = 5.438$	0.0054
	Residual	32.16	125	0.2573		
	Bonferroni's Multiple Comparisons Test					
				t	DF	P Value
	+ Corr vs - Corr			3.003	125	0.0097
	+ Corr vs Non Corr			2.580	125	0.0331
	- Corr vs Non Corr			1.597	125	0.3384
Fig.2L	Two-way ANOVA (Average Traces)					
		SS	DF	MS	$F_{(DFn, DFd)}$	P value
	Interaction	0.06600	2	0.03300	$F_{(2, 24)} = 7.353$	P=0.0032
	Time	0.06600	2	0.03300	$F_{(2, 24)} = 7.353$	P=0.0032
	Cells	0.02570	1	0.02570	$F_{(1, 24)} = 5.726$	P=0.0249
	Residual	0.1077	24	0.004487		
	Bonferroni's Multiple Comparisons Test					
				t	DF	P Value
	Non Corr			2.351	24.00	0.0818
	+ Corr			3.475	24.00	0.0059
	- Corr			1.682	24.00	0.3168
	One-way ANOVA (Delta Responses)					
		SS	DF	MS	$F_{(DFn, DFd)}$	P Value
	Cells	0.3849	2	0.1925	$F_{(2, 125)} = 2.133$	0.1228
	Residual	11.28	125	0.09025		
	Bonferroni's Multiple Comparisons Test					
				t	DF	P Value
	+ Corr vs - Corr			2.054	125	0.1263
	+ Corr vs Non Corr			0.7401	125	>0.9999

	- Corr vs Non Corr		1.778	125	0.2333
Fig.2M	Two-way ANOVA (Average Traces)				
		SS	DF	MS	$F_{(DFn, DFd)}$	P value
	Interaction	0.02361	2	0.01180	$F_{(2, 24)} = 3.127$	P=0.0621
	Time	0.02361	2	0.01180	$F_{(2, 24)} = 3.127$	P=0.0621
	Cells	0.1070	1	0.1070	$F_{(1, 24)} = 28.35$	P<0.0001
	Residual	0.09059	24	0.003775		
	Bonferroni's Multiple Comparisons Test				
				t	DF	P Value
	Non Corr			2.561	24.00	0.0515
	+ Corr			5.042	24.00	0.0001
	- Corr			1.619	24.00	0.3557
	One-way ANOVA (Delta Responses)				
		SS	DF	MS	$F_{(DFn, DFd)}$	P Value
	Cells	0.2396	2	0.1198	$F_{(2, 125)} = 1.212$	0.3010
	Residual	12.35	125	0.09881		
	Bonferroni's Multiple Comparisons Test				
				t	DF	P Value
	+ Corr vs - Corr			1.195	125	0.7030
	+ Corr vs Non Corr			1.432	125	0.4635
	- Corr vs Non Corr			0.3641	125	>0.9999

Table S3. Statistical Information for Figure 3.

Fig.3E	Paired two-tailed t-test		
	t	DF	P value
	2.608	12	0.0229
Fig.3F	Paired two-tailed t-test		
	t	DF	P value
	2.350	12	0.0367
Fig.3H	Paired two-tailed t-test		
	t	DF	P value
	0.8318	12	0.4316
Fig.3I	Paired two-tailed t-test		
	t	DF	P value
	0.5914	12	0.5652

Table S4. Statistical Information for Figure 4.

Fig.4G	One-way ANOVA				
		SS	DF	MS	$F_{(DFn, DFd)}$	P Value
	Cells	57.44	2	28.72	$F_{(2, 41)} = 0.8202$	P=0.4474
	Residual	1436	41	35.01		
	Bonferroni's Multiple Comparisons Test					
				t	DF	P Value
	SOM vs. CR			1.256	41	0.6488
	SOM vs. Vglut2+			0.3957	41	>0.9999
	CR vs. Vglut2+			0.8073	41	>0.9999
Fig.4H	One-way ANOVA				
		SS	DF	MS	$F_{(DFn, DFd)}$	P Value
	Cells	276.2	2	138.1	$F_{(2, 41)} = 1.141$	P=0.3295
	Residual	4964	41	121.1		
	Bonferroni's Multiple Comparisons Test					
				t	DF	P Value
	SOM vs. CR			0.5342	41	>0.9999
	SOM vs. Vglut2+			0.9705	41	>0.9999
	CR vs. Vglut2+			1.499	41	0.4246
Fig.4I	One-way ANOVA				
		SS	DF	MS	$F_{(DFn, DFd)}$	P Value
	Cells	4.712	2	2.356	$F_{(2, 41)} = 1.941$	P=0.1565
	Residual	49.76	41	1.214		
	Bonferroni's Multiple Comparisons Test					
				t	DF	P Value
	SOM vs. CR			0.01329	41	>0.9999
	SOM vs. Vglut2+			1.694	41	0.2935
	CR vs. Vglut2+			1.736	41	0.2700
Fig.4J	One-way ANOVA				
		SS	DF	MS	$F_{(DFn, DFd)}$	P Value
	Cells	2633	2	1317	$F_{(2, 40)} = 5.369$	P=0.0086
	Residual	9809	40	245.2		
	Bonferroni's Multiple Comparisons Test					
				t	DF	P Value
	SOM vs. CR			3.235	41	0.0073
	SOM vs. Vglut2+			2.006	41	0.1549
	CR vs. Vglut2+			1.010	41	0.9553
Fig.4K	One-way ANOVA				
		SS	DF	MS	$F_{(DFn, DFd)}$	P Value

	Cells	30865	2	15433	$F_{(2, 39)} = 19.98$	P<0.0001
	Residual	30122	39	772.3		
	Bonferroni's Multiple Comparisons Test					
				t	DF	P Value
	SOM vs. CR			0.3437	41	>0.9999
	SOM vs. Vglut2+			5.420	41	<0.0001
	CR vs. Vglut2+			5.809	41	<0.0001

Table S5. Statistical Information for Figure 5.

Fig.5B SOM Amplitude	Unpaired two-tailed t-test		
	t	DF	P value
	3.209	10	0.0094
Fig.5B SOM PPR	Unpaired two-tailed t-test		
	t	DF	P value
	2.090	10	0.0631
Fig.5B CR Amplitude	Unpaired two-tailed t-test		
	t	DF	P value
	5.022	9	0.0007
Fig.5B CR PPR	Unpaired two-tailed t-test		
	t	DF	P value
	0.9019	9	0.3906
Fig.5B Vglut2 Amplitude	Unpaired two-tailed t-test		
	t	DF	P value
	4.853	9	0.0009
Fig.5B Vglut2 PPR	Unpaired two-tailed t-test		
	t	DF	P value
	0.8453	9	0.4199
Fig.5C SOM Amplitude	Unpaired two-tailed t-test		
	t	DF	P value
	2.467	10	0.0333
Fig.5C SOM Frequency	Unpaired two-tailed t-test		
	t	DF	P value
	2.523	10	0.0302
Fig.5B CR Amplitude	Unpaired two-tailed t-test		
	t	DF	P value
	2.486	11	0.0302
Fig.5B CR Frequency	Unpaired two-tailed t-test		
	t	DF	P value
	3.609	11	0.0041

Fig.5B Vglut2 Amplitude	Unpaired two-tailed t-test		
	t	DF	P value
	2.321	9	0.0454
Fig.5B Vglut2 Frequency	Unpaired two-tailed t-test		
	t	DF	P value
	3.710	9	0.0048

Table S6. Statistical Information for Figure 6.

Fig.6D	One-way ANOVA				
	SS	DF	MS	$F_{(DFn, DFd)}$	P Value
Groups	2951	2	1476	$F_{(2, 23)} = 12.65$	P=0.0002
Residual	2682	23	116.6		
	Bonferroni's Multiple Comparisons Test				
			t	DF	P Value
Ctrl vs ChR2			2.764	23	0.0221
Ctrl vs Arch			1.601	23	0.2460
Fig.6E	One-way ANOVA				
	SS	DF	MS	$F_{(DFn, DFd)}$	P Value
Groups	117.0	2	58.50	$F_{(2, 23)} = 13.74$	P=0.0001
Residual	97.96	23	4.259		
	Bonferroni's Multiple Comparisons Test				
			t	DF	P Value
Ctrl vs ChR2			3.957	23	0.0013
Ctrl vs Arch			0.2617	23	>0.9999
Fig.6F	One-way ANOVA				
	SS	DF	MS	$F_{(DFn, DFd)}$	P Value
Groups	4151	2	2076	$F_{(2, 16)} = 6.377$	P=0.0092
Residual	5208	16	325.5		
	Bonferroni's Multiple Comparisons Test				
			t	DF	P Value
Ctrl vs ChR2			3.143	16	0.0126
Ctrl vs Arch			0.1428	16	>0.9999
Fig.6G	One-way ANOVA				
	SS	DF	MS	$F_{(DFn, DFd)}$	P Value
Groups	264.6	2	132.3	$F_{(2, 16)} = 4.806$	P=0.0232
Residual	440.5	16	27.53		
	Bonferroni's Multiple Comparisons Test				

		t	DF	P Value
	Ctrl vs ChR2	2.854	16	0.0230
	Ctrl vs Arch	0.4117	16	>0.9999
Fig.6H	Unpaired two-tailed t-test			
		t	DF	P value
		2.510	9	0.0333
Fig.6I	Unpaired two-tailed t-test			
		t	DF	P value
		1.809	9	0.1039
Fig.6M	Paired two-tailed t-test			
		t	DF	P value
		9.855	4	0.0006
Fig.6O	Paired two-tailed t-test			
		t	DF	P value
		3.692	4	0.0210

Table S7. Statistical Information for Figure S1.

Fig.S1C	Repeated Measures One-way ANOVA				
		SS	DF	MS	$F_{(DFn, DFd)}$	P Value
	Compartments	0.001745	2	0.0008727	$F_{(1.335, 5.338)} = 23.45$	P=0.0031
	Animals	0.0003733	4	9.333e-005	$F_{(4, 8)} = 2.507$	P=0.1250
	Residual	0.0002978	8	3.722e-005		
	Bonferroni's Multiple Comparisons Test					
				t	DF	P Value
	Center vs Edge			3.556	4	0.0710
	Center vs Transition			5.289	4	0.0184
	Edge vs Transition			5.415	4	0.0169

Table S8. Statistical Information for Figure S2.

Fig.S2A	Paired two-tailed t-test		
	t	DF	P value
	1.618	12	0.1317
Fig.S2B	Paired two-tailed t-test		
	t	DF	P value
	1.447	12	0.1735
Fig.S2C	Paired two-tailed t-test		
	t	DF	P value
	1.672	12	0.1204

Fig.S2D	Paired two-tailed t-test		
	t	DF	P value
	0.7537	12	0.4656
Fig.S2E	Paired two-tailed t-test		
	t	DF	P value
	1.008	12	0.3333
Fig.S2F	Paired two-tailed t-test		
	t	DF	P value
	1.184	12	0.2592

Table S9. Statistical Information for Figure S7.

Fig.S7N	Unpaired two-tailed t-test		
	t	DF	P value
	6.280	22	<0.0001
Fig.S7O	Unpaired two-tailed t-test		
	t	DF	P value
	4.538	22	0.0002
Fig.S7P	Unpaired two-tailed t-test		
	t	DF	P value
	6.541	22	<0.0001

Table S10. Statistical Information for Figure S9.

Fig.S9D	One-way ANOVA				
		SS	DF	MS	$F_{(DFn, DFd)}$	P Value
	Groups	25.25	2	12.63	$F_{(2, 23)} = 3.927$	P=0.0341
	Residual	73.94	23	3.215		
	Bonferroni's Multiple Comparisons Test					
				t	DF	P Value
	Ctrl vs ChR2			1.652	23	0.2243
	Ctrl vs Arch			0.7619	23	0.9077
Fig.S9E	One-way ANOVA					
		SS	DF	MS	$F_{(DFn, DFd)}$	P Value
	Groups	5970	2	2985	$F_{(2, 23)} = 3.395$	P=0.0511
	Residual	20223	23	879.2		
	Bonferroni's Multiple Comparisons Test					
				t	DF	P Value
	Ctrl vs ChR2			2.185	23	0.0787
	Ctrl vs Arch			0.2313	23	>0.9999

Fig.S9F	One-way ANOVA				
		SS	DF	MS	$F_{(DFn, DFd)}$	P Value
	Groups	5.927	2	2.963	$F_{(2, 16)} = 0.7476$	P=0.4894
	Residual	63.43	16	3.964		
	Bonferroni's Multiple Comparisons Test					
				t	DF	P Value
	Ctrl vs ChR2			0.3876	16	>0.9999
	Ctrl vs Arch			1.195	16	0.4988
Fig.S9G	One-way ANOVA					
		SS	DF	MS	$F_{(DFn, DFd)}$	P Value
	Groups	1850	2	925.1	$F_{(2, 16)} = 1.647$	P=0.2237
	Residual	8989	16	561.8		
	Bonferroni's Multiple Comparisons Test					
				t	DF	P Value
	Ctrl vs ChR2			1.080	23	0.5926
	Ctrl vs Arch			0.7047	23	0.9823
Fig.S9H	Unpaired two-tailed t-test					
				t	DF	P value
				1.557	9	0.1538
Fig. S9I	Unpaired two-tailed t-test					
				t	DF	P value
				2.133	9	0.0617

Table S11. Statistical Information for Figure S10.

Fig.S10C	Unpaired one-tailed t-test		
	t	DF	P value
	3.163	2	0.0436

Table S12. Statistical Information for Figure S11.

Fig.S11A	Unpaired two-tailed t-test (EOM; Open Time)		
	t	DF	P value
	0.9524	15	0.3560
	Unpaired two-tailed t-test (EOM; Body Entries)		
	t	DF	P value
	0.03414	15	0.9732
Fig. S11B	Unpaired two-tailed t-test (OFT; Distance)		
	t	DF	P value
	1,343	15	0.1992

	Unpaired two-tailed t-test (OFT; Time Immobile)		
	t	DF	P value
	1.488	15	0.1574
Fig.S11C	Unpaired two-tailed t-test (EOM; Open Time)		
	t	DF	P value
	0.2364	10	0.8179
	Unpaired two-tailed t-test (EOM; Body Entries)		
	t	DF	P value
	1.263	10	0.2353
Fig.S11D	Unpaired two-tailed t-test (OFT; Distance)		
	t	DF	P value
	0.9231	10	0.3777
	Unpaired two-tailed t-test (OFT; Time Immobile)		
	t	DF	P value
	0.3318	10	0.7469
Fig.S11E	Unpaired two-tailed t-test (EOM; Open Time)		
	t	DF	P value
	0.3185	6	0.7609
	Unpaired two-tailed t-test (EOM; Body Entries)		
	t	DF	P value
	1.750	6	0.1307
Fig.S11F	Unpaired two-tailed t-test (OFT; Distance)		
	t	DF	P value
	1,623	6	0.1558
	Unpaired two-tailed t-test (OFT; Time Immobile)		
	t	DF	P value
	1.079	6	0.3220
Fig.S11G	Unpaired two-tailed t-test (EOM; Open Time)		
	t	DF	P value
	0.1073	3	0.9213
	Unpaired two-tailed t-test (EOM; Body Entries)		
	t	DF	P value
	0.2335	3	0.8304
Fig.S11H	Unpaired two-tailed t-test (OFT; Distance)		
	t	DF	P value
	0.4094	3	0.7097
	Unpaired two-tailed t-test (OFT; Time Immobile)		
	t	DF	P value
	0.2527	3	0.8168

Fig.S11I	Unpaired two-tailed t-test (EOM; Open Time)		
	t	DF	P value
	1.155	6	0.2919
	Unpaired two-tailed t-test (EOM; Body Entries)		
	t	DF	P value
	1.868	6	0.1110
Fig.S11J	Unpaired two-tailed t-test (OFT; Distance)		
	t	DF	P value
	0.1593	6	0.8786
	Unpaired two-tailed t-test (OFT; Time Immobile)		
	t	DF	P value
	0.03281	6	0.9749
Fig.S11K	Unpaired two-tailed t-test (EOM; Open Time)		
	t	DF	P value
	1.341	4	0.2509
	Unpaired two-tailed t-test (EOM; Body Entries)		
	t	DF	P value
	0.3482	4	0.7453
Fig.S11L	Unpaired two-tailed t-test (OFT; Distance)		
	t	DF	P value
	0.2485	4	0.8160
	Unpaired two-tailed t-test (OFT; Time Immobile)		
	t	DF	P value
	0.2031	4	0.8490
Fig.S11M	Unpaired two-tailed t-test (Closed Chamber; Jumps)		
	t	DF	P value
	0.7490	6	0.4822
Fig.S10N	Unpaired two-tailed t-test (Closed Chamber; Rears)		
	t	DF	P value
	0.1141	3	0.9164

Final Comments

3.1 Overview

The three studies included in this thesis provide novel insights into our understanding of the brain circuitry underlying fear and anxiety. Here, we reported substantial evidence that structures classically not known for their roles in fear and anxiety, namely the lateral VTA and the ZI encode and modulate fear as well as anxiety (ZI only).

3.1a Ventral tegmental area and Zona Incerta, new members of the fear network

We report evidence that both the gabaergic and glutamatergic neurons of the lateral VTA as well as the ZI encode fear evoking footshocks and learned to encode cues predictive and non-predictive of fear. While further investigation is necessary to determine how the lateral VTA gabaergic and glutamatergic neurons as well as the ZI fit into the already established fear network, there are indications that they are related. VTA gabaergic and glutamatergic neurons have been shown to be anatomically connected with many of the regions described in the fear network[1–5], such as the prefrontal cortex, the amygdala, and the PAG. Similarly, we and others[6,7] have shown that the ZI is connected with the amygdala, the PAG, and the hypothalamus, regions already described in the fear network[8]. Furthermore, the blockade of synaptic transmission of ZI projections onto the amygdala has been shown to impair fear acquisition and recall[7], providing further verification that the ZI is a node in the currently described fear network. Fear is an important defensive response towards incoming threats and holds the key to survival, it is no surprise that they are widely and potentially redundantly encoded and modulated. While our findings report evidence that both the lateral VTA and the ZI should be considered and integrated as nodes within the currently described fear network, the relationship between these regions and their individual contributions to fear is still far from clear.

It is evident that all regions within the fear network are anatomically connected. While it is not fully known if they all reciprocally connected with each other. Many regions involved in the fear response are connected to the amygdala[8], including the lateral VTA[3,4] and ZI[6,7]. Even though the importance of the amygdala[8] in learned fear should not be overlooked, the manipulations of pathways that do not directly involve

the amygdala such as the lateral VTA to dSTR or lateral VTA to parafascicular thalamic nucleus (Pf) still impact fear learning. However, it is still possible that the amygdala is still affected further downstream.

At the current moment, it is impossible to know whether fear is controlled by a center within brain such the amygdala and then proliferated across the network or whether fear is controlled independently across multiple interconnected brain areas. One contributing factor to this debacle is that the role of different brain areas in fear is often studied on its own or with respect to a couple targets without considering the whole network holistically. A potential alternative approach would be to investigate the activity of all brain regions within the current fear network at the same time and examine how learned fear to predictive cues is acquired. To do so, simultaneous fiber photometry imaging of calcium dynamics across all nodes within the fear network[9] could be conducted while mice perform in a fear conditioning paradigm and combined with optogenetic manipulations. In this manner, the progression of learned fear acquisition within the fear network could be examined together. If the amygdala is the center of learned fear, it should be the first to associate the predictive cue with the footshock and any manipulation of the activity of the amygdala during this time should affect other nodes within the fear network. On the other hand, if different nodes within the fear network act more independently, the progression of learned fear should be comparable and the manipulation of activity of individual nodes should have little impact on how learned fear is associated in other areas. This approach could also be combined with selective targeting strategies such as the targeted recombination in active populations[10] to investigate functionally defined cell populations within areas investigated (such as ones activated by US or CS) to gain insights on potential determining factors that render populations encoding learned fear associations.

3.1b Clinical implications of the role of the Zona Incerta in fear generalization

Frustratingly and perhaps in a biased way, current research focuses mainly on how fear predictive cues and association between these cues and the US, are encoded over fear learning while fear non-predictive cues are glossed over[8,11]. This is particularly true in studies where learned fear is examined without a control fear non-predictive cue[6,7]. While it is important to understand the neural basis for learned fear,

it is equally important to understand how the discrimination between predictive and non-predictive cues is learned. Furthermore, fear generalization to a degree may be adaptive but overgeneralization is associated with anxiety disorders[12]. On a positive note, ZI neurons are particularly interesting. They seem to differentially learn to encode fear predictive (excited) and non-predictive cues (inhibited). Furthermore, this biased response profile seems to be less clear in mice that generalized fear. These findings could be clinically relevant and further investigations should examine whether individual differences in the ZI can influence the development of fear generalization as well as overgeneralization, thus contributing to pathologies where these characteristics are prominent such as the generalized anxiety-disorders[13], panic-disorders[14], or post-traumatic stress disorder[15,16]. On the other side of the coin, patients suffering from these disorders should be examined to see if the activity of the ZI or the responsiveness of the ZI to relevant stimuli such as natural and learned fear evoking cues or ones similar to them are abnormal.

3.1c Local Zona Incerta circuitry: potential self-regulating network for exploration and avoidance

The ZI is composed of biochemically diverse subpopulations of neurons[17,18]. We examined three biochemically distinct subpopulations, two inhibitory subpopulations expressing somatostatin (SOM) or calretinin (CR) as well as the rarer excitatory glutamatergic Vglut2- expressing cells. We have shown that specific subpopulations differentially modulate anxiety-like phenotypes. Specifically, the inhibitory cells acted in opposing manners where the activation of SOM- expressing ZI cells increased anxiety while the activation of CR- expressing cells reduced anxiety and promoted exploratory rearing. The activation of Vglut2- expressing induced fast jumps similar to escape-like behaviors and when inactivated reduced anxiety. While all three subpopulations projected long-range to many brain areas, some already noted in the fear and anxiety networks, CR- and Vglut2- expressing cells provided local inhibitory and excitatory inputs to other cells. Speculatively, it is possible that these ZI subpopulation regulate each other and select the most appropriate action during a potential conflict between the presence of an anxiogenic stimulus and the internal drive to explore for resource or to soothe curiosity.

Based on the current observed behavioral and electrophysiological characterizations, one can hypothesize that when the drive to explore outweighs the anxiogenic stimuli, CR- expressing cells promote exploration and inhibit SOM- and Vglut2- expressing cells from triggering avoidance or escape. On the other hand, when the need to get away from potential dangers outweighs the drive to explore, Vglut2-expressing cells could trigger escape through jumps and activate the SOM- cells to further promote avoidance. To test these hypotheses, one could first confirm these proposed connections by patching fluorescently labeled cells (expressing either SOM-, CR-, or Vglut2-) while at the same time activate local inputs from CR- or Vglut2-expressing cells with excitatory opsins and confirm the monosynaptic nature of this connection with pharmacology using tetrodotoxin and 4-aminopyridine.

Functionally, this hypothesis could be tested by designing a task where food deprived mice are placed in an environment littered with food in compartments that simultaneously is anxiogenic. Varying the duration of food deprivation and the magnitude of the anxiogenic stimuli could shift the balance between the drive for exploration to feed and the drive to stay away from potential threats. Pairs of ZI subpopulations could be differentially labeled with green or red calcium indicators. The calcium dynamics of different ZI subpopulations could then be recorded simultaneously with nVue (Inscopix) while the mice performed such a task to examine whether different subpopulations of ZI are in synchrony or in anti-synchrony in the presence of anxiogenic stimuli under different internal states with varying degrees of drive for exploration.

3.1d Zona Incerta and anxiety: implications for the treatment

The role of the ZI in anxiety is clinically relevant and should be further investigated. PD is classically recognized as a neurodegenerative disorder characterized by deliberating motor symptoms[19]. However, its association or comorbidity with anxiety and fear disorders such a phobias, are less well studied[20,21]. DBS of the ZI has been experimentally used and currently being tested with much success as a potential target for the treatment of motor symptoms PD[22] and have recently shown to also reduce anxiety and improve fear recognition[23,24]. While there is some indications that the ZI play a role in fear[6,7,25], the link between the ZI and anxiety

is largely unknown. We report evidence that the ZI and its subpopulations differentially impact anxiety. Based on our findings, it could be hypothesized that the DBS of the ZI either reduces the activity of the SOM- and Vglut2- expressing cells, activates CR-expressing ZI cells, or induces a combination of these changes. Future studies should investigate whether the activity of the ZI and its subpopulations are abnormal in patients suffering from anxiety disorders and whether the DBS in the ZI can reduce anxiety in the same way as it did for PD patients.

3.1e Zona Incerta: independent or intertwined roles in fear and anxiety

We provided evidence that the ZI encodes both learned fear and anxiety, without any insights on the relationship between the two. Future studies should investigate the relationship between ZI neurons that encode learned fear and those that encode anxiety. One approach would be to record the activity of ZI cells with calcium imaging while mice perform in a fear conditioning task followed by anxiety-related tasks such as the elevated mazes (or vice versa) and longitudinally track ZI cells throughout both sessions. Cells could be first characterized based on how they respond to footshocks or cues predictive and not-predictive of fear, then investigated to see how they respond to anxiety-related information.

Given that we have shown that unique biochemically defined ZI subpopulations impact anxiety differently. It would be worthwhile to take this information into account and examine how individual ZI subpopulations encode anxiety and fear. The same approach could be undertaken by labeling a different subpopulation each time through transgenic mouse lines expressing cre recombinase in either SOM-, CR-, or Vglut2-expressing cells and a cre dependent calcium indicator injected into the ZI. Moreover, to examine whether different ZI subpopulations can not only modulate anxiety differently but also learned fear, the activity of these three subpopulations could be manipulated with optogenetics during fear learning or recall to investigate whether they can modulate aspects of learned fear.

3.2 Closing remarks

Defensive responses such as fear and anxiety provide species with the necessary tools to defend against actual and potential threats. The network of brain

areas involved in fear and anxiety are complex and extensive. In this thesis, we report evidence that both the lateral Ventral Tegmental Area and the Zona Incerta should be integrated into the current fear network and the Zona Incerta into the anxiety network. We and many labs across the globe provide meaningful insights into how individual nodes or brain areas encode fear and anxiety and how individual connections or pathways modulate these responses. Going forward, more holistic and comprehensive investigations involving the network as a whole should be considered and likely will be paradigm-shifting.

References:

1. Breton, J. M. *et al.* Relative contributions and mapping of ventral tegmental area dopamine and GABA neurons by projection target in the rat. *J Comp Neurol* **527**, 916–941 (2019).

2. Ntamati, N. R., Creed, M., Achargui, R. & Lüscher, C. Periaqueductal efferents to dopamine and GABA neurons of the VTA. *PLoS One* **13**, e0190297 (2018).

3. Taylor, S. R. *et al.* GABAergic and glutamatergic efferents of the mouse ventral tegmental area. *J Comp Neurol* **522**, 3308–3334 (2014).

4. Hnasko, T. S., Hjelmstad, G. O., Fields, H. L. & Edwards, R. H. Ventral tegmental area glutamate neurons: electrophysiological properties and projections. *J Neurosci* **32**, 15076–15085 (2012).

5. Morales, M. & Margolis, E. B. Ventral tegmental area: cellular heterogeneity, connectivity and behaviour. *Nat Rev Neurosci* **18**, 73–85 (2017).

6. Chou, X.-L. *et al.* Inhibitory gain modulation of defense behaviors by zona incerta. *Nat Commun* **9**, 1151 (2018).

7. Zhou, M. *et al.* A central amygdala to zona incerta projection is required for acquisition and remote recall of conditioned fear memory. *Nat. Neurosci.* **21**, 1515–1519 (2018).

8. Tovote, P., Fadok, J. P. & Lüthi, A. Neuronal circuits for fear and anxiety. *Nature Reviews Neuroscience* **16**, 317–331 (2015).

9. Sych, Y., Chernysheva, M., Sumanovski, L. T. & Helmchen, F. High-density multi-fiber photometry for studying large-scale brain circuit dynamics. *Nat Methods* **16**, 553–560 (2019).

10. Guenthner, C. J., Miyamichi, K., Yang, H. H., Heller, H. C. & Luo, L. Permanent genetic access to transiently active neurons via TRAP: targeted recombination in active populations. *Neuron* **78**, 773–784 (2013).

11. Grewe, B. F. *et al.* Neural ensemble dynamics underlying a long-term associative memory. *Nature* **543**, 670–675 (2017).

12. Stegmann, Y. *et al.* Individual differences in human fear generalization-pattern identification and implications for anxiety disorders. *Transl Psychiatry* **9**, 307 (2019).

13. Lissek, S. *et al.* Generalized anxiety disorder is associated with overgeneralization of classically conditioned fear. *Biol Psychiatry* **75**, 909–915 (2014).

14. Lissek, S. *et al.* Overgeneralization of conditioned fear as a pathogenic marker of panic disorder. *Am J Psychiatry* **167**, 47–55 (2010).

15. Morey, R. A. *et al.* Fear learning circuitry is biased toward generalization of fear associations in posttraumatic stress disorder. *Transl Psychiatry* **5**, e700 (2015).

16. Lis, S. *et al.* Generalization of fear in post-traumatic stress disorder. *Psychophysiology* **57**, e13422 (2020).

17. Mitrofanis, J., Ashkan, K., Wallace, B. A. & Benabid, A.-L. Chemoarchitectonic heterogeneities in the primate zona incerta: clinical and functional implications. *J. Neurocytol.* **33**, 429–440 (2004).

18. Kolmac, C. & Mitrofanis, J. Distribution of various neurochemicals within the zona incerta: an immunocytochemical and histochemical study. *Anat. Embryol.* **199**, 265–280 (1999).

19. Poewe, W. *et al.* Parkinson disease. *Nat Rev Dis Primers* **3**, 17013 (2017).

20. Chen, J. J. & Marsh, L. Anxiety in Parkinson's disease: identification and management. *Ther Adv Neurol Disord* **7**, 52–59 (2014).

21. Gultekin, B. K., Ozdilek, B. & Bestepe, E. E. Social phobia in Parkinson's disease: Prevalence and risk factors. *Neuropsychiatr Dis Treat* **10**, 829–834 (2014).

22. Ossowska, K. Zona incerta as a therapeutic target in Parkinson's disease. *J Neurol* **267**, 591–606 (2020).

23. Burrows, A. M. *et al.* Limbic and motor function comparison of deep brain stimulation of the zona incerta and subthalamic nucleus. *Neurosurgery* **70**, 125–130; discussion 130-131 (2012).

24. Gourisankar, A. *et al.* Mapping movement, mood, motivation and mentation in the subthalamic nucleus. *R Soc Open Sci* **5**, (2018).

25. Venkataraman, A. *et al.* Modulation of fear generalization by the zona incerta. *Proc. Natl. Acad. Sci. U.S.A.* **116**, 9072–9077 (2019).

Acknowledgements

First, I would like to thank my boss, Prof. Dr. Kelly Tan for the amount of generous support that she has provided me over the course of my PhD, particularly with the design of projects, development of my surgical skills, and the preparation of manuscripts. In addition, I want to thank Kelly for the amount of *in-vitro* electrophysiological experiments that she performed for my projects as well as for keeping our promise before my arrival to the lab (that I do not have to perform in-vitro electrophysiology experiments if I don't want to); these things have greatly touched me. I would also like to thank the current and past members of the Tan lab for all the support and discussion that helped me grow as a person and a scientist. In particular, I would like to thank Dr. Giorgio Rizzi for helping me with all the calcium imaging experiments and peer-mentoring during the early years of my PhD.

I would also like to thank my PhD committee, Prof Dr. Fiona Doetsch and Prof. Dr. Manuel Mameli, for helping me shape my projects and keeping me on track. I would also like to thank Prof. Dr. Tania Barkat-Rinaldi, Prof. Dr. Jan Gründemann as well as their labs for always getting together formally and informally to discuss ongoing projects and technical details. To my previous mentors, particularly Prof. Dr. Fancis Bambico, thank you nourishing my curiosity and motivation for science.

I would like to also thank the Biozentrum Imaging Core Facility for helping me with microscopy training, troubleshooting, and last-minute emergencies. I would like to thank the Werner Siemens Foundations and the Biozentrum for providing me with a generous fellowship that funded the first three years of my PhD.

Lastly, I would like to thank my extended family (with the notable exception of my parents) for always supporting me and driving me to follow my dreams. Life is short and has no space for regrets. Your life belongs to you alone and no one else. Follow your hearts and never listen to those that try to persuade you away from your own paths just because it doesn't fit in their scheme.

To end on a positive note, thank you everyone for being a part of my PhD experience and helping me grow. It will be a memorable chapter of my life that I will always hold close to.

Zhuoliang Li (李卓良),
May 25th , 2021